



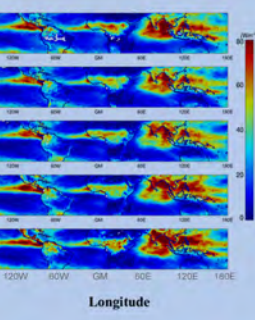
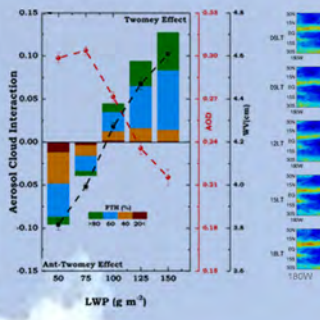
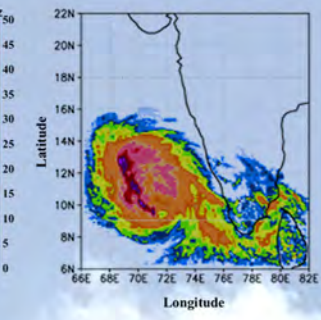
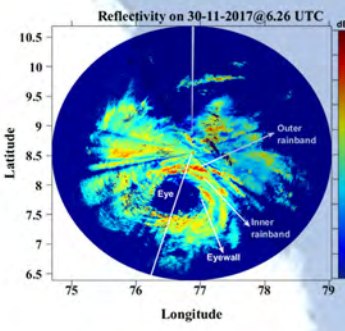
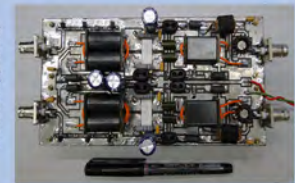
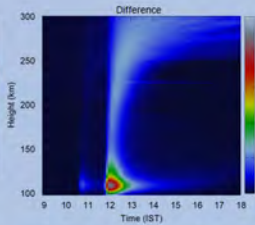
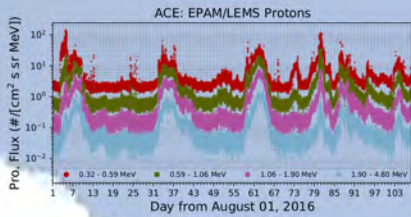
भौमिक एवं ग्रहीय पर्यावरण के उर्जा विज्ञान, गतिकी, एवं रसायन शास्त्र की वैज्ञानिक समझ, तथा समाज पर इनकी विवक्षा

Scientific understanding of the energetics, dynamics and chemistry of the terrestrial and planetary environments and implications to the society

वैज्ञानिक उपलब्धियाँ

SCIENTIFIC ACCOMPLISHMENTS

2020-2021



अंतरिक्ष भौतिकी प्रयोगशाला
विक्रम साराभाई अंतरिक्ष केंद्र
तिरुवनन्तपुरम

SPACE PHYSICS LABORATORY
Vikram Sarabhai Space Centre
Thiruvananthapuram



Scientific Advisory Committee of SPL

Chairman

Dr. T. K. Alex, Hon. Distinguished Professor, ISRO HQ

Alternate Chairman

Shri. S. Somanath, Director, IIST

Members

Dr. D. S. Ramesh, Director, IIG

Dr. Jyotiranjana S. Ray, Director, NCESS, Trivandrum

Shri. Uma Maheswaran, Scientific Secretary, ISRO HQ

Dr. Raj Kumar, Director, NRSC, Hyderabad

Dr. A K Patra, Director, NARL

Shri. Gopalakrishnan T., Deputy Director, AVN, VSSC

Dr. Tirtha Pratim Das, Director, SPO, ISRO HQ

Prof. K. Mohan Kumar, Emeritus Professor, CUSAT

Prof. Animesh Maitra, Calcutta University

Prof. S. K. Satheesh, Chairman, DCCC, IISc, Bangalore

Prof. R. Sridharan, Former Director, SPL (Emeritus Scientist, PRL)

Prof. P. Balarama Rao, Former Director, NARL

Dr. B. V. Krishna Murthy, Former Director, SPL

Prof. A. Jayaraman, Former Director, NARL

Dr. S. Seetha, Former Director, SSPO, ISRO HQ

Member Secretary

Dr. K. Rajeev, Director, SPL

Editorial Team

C. Vineeth, Mukunda M. Gogoi, S. Suresh Babu



वैज्ञानिक उपलब्धियाँ
Scientific Accomplishments
2020-2021

विक्रम साराभाई अंतरिक्ष केंद्र
Vikram Sarabhai Space Centre
भारतीय अंतरिक्ष अनुसंधान संगठन
Indian Space Research Organisation



ഭാരത സർക്കാർ
ബഹിരാകാശ വകുപ്പ്
വിക്രം സാരാഭായി ബഹിരാകാശ കേന്ദ്രം
GOVERNMENT OF INDIA
DEPARTMENT OF SPACE
VIKRAM SARABHAI SPACE CENTRE



भारत सरकार
अंतरिक्ष विभाग
विक्रम साराभाई अंतरिक्ष केंद्र
तिरुवनंतपुरम - 695 022, भारत
दूरभाष : 0471-2565567/2704412
फैक्स : 0471-2704105
ईमेल : director@vssc.gov.in

एस सोमनाथ/S. Somanath
विशिष्ट वैज्ञानिक व
Distinguished Scientist &
निदेशक/Director



Government of India
Department of Space
Vikram Sarabhai Space Centre
Thiruvananthapuram - 695 022, India
Phone : +91-471-2565567/2704412
Fax : +91-471-2704105
Email : director@vssc.gov.in
s_somanath@vssc.gov.in



MESSAGE

September 9, 2021

Space Physics Laboratory (SPL), VSSC has been doing pioneering research in the area of atmospheric, space and planetary science entwining spaceborne and ground-based observations complemented with theoretical modelling. SPL is also involved in the conceptualization and development of payloads for ISRO's planetary missions, sounding rocket experimental programs and orbital platform, in collaboration with entities of VSSC and other ISRO Centres. SPL is maintaining and operating a network of observatories, in collaboration with universities and national institutions, for the monitoring of atmospheric aerosols, boundary layer and space weather, spanning across the length and breadth of the country, adjoining islands, Himalayas and polar regions (Antarctic and Arctic), providing invaluable observations for science, policy and societal applications. SPL is also contributing to the capacity building through a vibrant academic program on doctoral and post-doctoral research.

It is heartening to note that during the 2020-21 period despite the difficult COVID-19 pandemic situation, SPL has made significant progress in the scientific activities with high quality publications in peer reviewed international journals with good impact factor. We had a successful RH-560 MkIII flight under the SOUREX-II program with TMA and scientific payloads for ionospheric studies. The payload development activities for the upcoming Aditya – L1 and Chandrayaan-3 missions are progressing very well. There is an active interest in SPL to participate in future scientific missions and also to build better instruments and infrastructure for scientific observations. I am happy to see that several of the SPL Scientists/Engineers are recognized at national and international levels for their scientific contributions. SPL has produced four PhDs in the last one year and supported several Masters students for their dissertational research.

SPL activities and achievements are reviewed annually by the national level Scientific Advisory Committee (SAC). I am sure the enriching scientific discussions during the forthcoming annual review by SPL - SAC will bring more focus and prioritization of the research activities.

Wishing SPL, an active and fruitful year ahead.

(S Somanath)

SCIENTIFIC DISCIPLINES AND ACTIVITIES



From the Director



Greetings from SPL!

On behalf of Team SPL, I am very happy to present the report of SPL's research activities and accomplishments during July 2020 to June 2021. The restrictions on regular office attendance for several weeks since July 2020 due to the Covid-19 pandemic were compensated with work from home. Through this we could make significant progress in the scientific activities, bring out major findings and further enhance the publication record in high impact factor journals – a bench-mark for any scientific institution. However, the pandemic and restrictions had an impact on the hardware development activities, which is being compensated.

The most remarkable scientific experiment during the reporting period was the Sounding Rocket Experiment (SOUREX) Phase-II conducted on 12 March 2021 using the RH560-MkIII flight from SDSC, SHAR which carried Trimethylaluminium (TMA) and the Electron density and Neutral Wind (ENWi) and Langmuir Probe (LP) payloads. This involved fast and high-resolution digital photography of the rocket-released TMA trail from four well-separated and carefully chosen ground stations (set up at Kavali, Gadanki, Kalpakkam, and Chennai, in addition to SHAR) to derive the altitude profiles of neutral winds in the 100-150 km region using triangulation of the drifting trails, and the altitude profiling of the electron density and neutral winds using LP and ENWi. This experiment was also supported with observations using ground-based radars and digital ionosondes at Thumba and NARL-Gadanki to explore the role of winds and shears in triggering the ionospheric irregularities. RH560-MKIII, the TMA and electronic payloads and the high-resolution digital photography were realized by the VSSC team led by ATVP project and SPL with deep involvement of several entities of VSSC, including MVIT, ASOE, AVN, MSA, MME, PCM, AERO, SPRE and strong support of SDSC, SHAR for all launch - related activities. The wind profiles derived from the imageries of drifting TMA trails show substantial neutral wind shears around the altitude of 135 km, a potential source for gravity wave generation; the electron density profiles could be obtained from 100 to 500 km altitude region.

In the microwave and boundary layer physics area, surface layer characterization under the IGBP-NOBLE project brought out the seasonal mean diurnal evolution of surface layer turbulence characteristics and heat flux as well as the similarity relationships over the semi-arid region at Anantapur (SK University) and the East Khasi Hill at Shillong (NESAC). A comprehensive analysis of 8-years of Micro Rain Radar observations at Thumba were used to derive the seasonal mean rain drop size distribution and Z-R relationship during convective and stratiform precipitations, which will further refine the estimation of rain rate from radar observations over similar regions. The attenuation of GSAT-14 Ka-band transponder signals at 20.2 GHz and 30.5 GHz due to precipitation were quantified in terms of rain rate and drop size distribution. Dependence of the backscattered signal from SCATSAT on the soil moisture content was estimated. Diurnal and seasonal variations of the occurrence of deep convective clouds (DCC) over the tropics estimated from the Megha-Tropiques

SAPHIR data showed distinctly different phases of DCC occurrence over continents and oceans. First direct observations of the diurnal variation of cloud radiative forcing over the tropics carried out using Megha-Tropiques-ScaRaB data revealed hitherto unknown features, including the almost similar zonal variations of the TOA net cloud radiative forcing over the equatorial region during El Niño and normal periods due to the near-cancellation of shortwave and longwave radiative effects.

In the domain of aerosols, trace gases and radiative forcing, the observational studies using satellite and ground based data sets and modelling studies have brought out important findings which are significant scientific contributions to the climate impact assessment over the Indian region. Multi-satellite observations of the indirect effects of aerosols over the northern Indian Ocean revealed the anti-Twomey effect due to enhanced aerosol loading during winter. Combining the ARFINET observations with space-borne LIDAR data, a novel approach was developed for assessing the vertical distribution of speciated aerosol absorption. Using model simulations, effect of aerosol induced snow darkening on the direct effect of aerosols over Himalayas and the amplification of South Asian haze by aerosol-water vapour interactions were estimated. Mixing state of aerosols in the South Asian outflow over the Indian Ocean and morphological characteristics of aerosols over the IGP were assessed based on multi-platform observations during different seasons. Detailed size segregated chemical characterization of aerosols, including trace metal analysis, were carried out over the peninsular Indian region during different air mass periods. Long-term changes in aerosol radiative properties over the Arctic region and multi-layer distribution of aerosol species in Himalayan snow-pack were studied for the assessment of aerosol-cryosphere interaction. The effects of nationwide COVID-19 lockdown on the aerosol and trace gas characteristics over the Indian region were investigated in detail.

In the Atmospheric Modelling studies, weather prediction support using COSMO model was extended to all the launch campaigns conducted from SHAR. A national level committee, appointed by Director, VSSC critically reviewed the revised Indian atmospheric model from surface to 1000 km for use in the design and analysis of missions from the Indian equatorial region, particularly SDSC, SHAR. After extensive discussions and clarifications, the committee recommended the model for launch vehicle design and applications. Performance evaluation of the COSMO model for the prediction of tropical cyclone trajectories for varying intensities of the storm showed a mean track error of about 50 km for the initial position of the storm, which increased to ~95 km for a lead time of 24 h and ~140 km for a lead time of 48 h. Impact of the implicit and explicit treatments of convection in the COSMO model for an intense convective episode associated with the passage of the very severe cyclonic storm 'Ockhi' and the impact of 'Ockhi' on the vertical structure of marine ABL were estimated. A detailed assessment of the vertical wind velocity profiles provided by 5 global Reanalyses data, which are being used extensively by the global community, was made by comparing with those from radar measurements over two tropical stations. This study brought out the major deficiencies in the vertical wind fields in the reanalysis data.

In atmospheric dynamics, an innovative approach has been employed to identify the source spectrum of gravity waves by means of ray tracing simulations and meteor radar observations. The long-term measurements of zonal winds in the mesosphere and lower thermosphere over low latitudes were analyzed to address an outstanding issue pertaining to the amplitude and period of the mesospheric quasi-biennial oscillation (QBO). The modulation of migrating diurnal tides by the stratospheric QBO has been investigated. Using multi-platform measurements carried out during the Indian Scientific Expeditions to Antarctica, stratosphere-troposphere exchange processes were investigated in details with ozone as a tracer element. By employing the balloon-borne cryogenic frost-point hygrometer measurements over three Indian locations, the effect of deep convection on the upper troposphere/lower stratosphere water vapour during the Indian summer monsoon was quantified. CloudSat and TRMM observations were synergistically employed to obtain the vertical profiles of latent heat associated with various cloud types. Rain rate estimates from the C-band

Doppler Weather Radar (DWR) at Thumba were validated and used for several scientific studies, including the investigations on the structure and dynamics of the tropical cyclone 'Ockhi'.

In the area of ionosphere-thermosphere-magnetosphere, observations of the thermosphere O(¹D) 630.0 nm dayglow over the dip equator during an X-class flare revealed that the dayglow had a four-fold enhancement after a time delay of ~45 minute; simulations using a quasi 2D ionospheric model could identify the mechanism responsible for this feature. The ionospheric nighttime enhancement of electron density, its characteristics and occurrence probability near equatorial ionization anomaly crest region in the Indian ionospheric sector were determined from the Total Electron Content (TEC) measurements carried out at the InSWIM network stations. Linkage of the variabilities in the post-sunset equatorial F-region zonal drift with the onset and duration of equatorial spread-F over the Indian longitudes have been examined using satellite data. An integrated parameter has been arrived at based on this, which is able to predict the peak vertical drift and growth rate of Rayleigh Taylor instability. The first estimations of gravity wave potential energy in the Martian thermosphere and its variations at different latitude bands have been obtained using MAVEN NGIMS data.

In the planetary science area, the observations of CHACE-2 on-board Chandrayaan-2 Orbiter since September 2019 covered all local times and provided the first global measurements of lunar exosphere composition; the number density of Ar-40 showed a distinct peak around sunrise and a secondary peak around sunset while the number density falls off on the night-side, in agreement with the condensable nature of Ar-40. Payload operations centre at SPL has quality checked and archived all the data from CHACE-2 recorded so far and provided the same for public release through the Pradan/ISSDC web portal of ISRO as per norms. Recurrent energetic electron and proton enhancements were observed near Earth and Mars in the presence of Corotating Interaction Regions (CIRs) in the heliosphere. Observations using MAVEN showed that the stealth CMEs can cause depletion of the night-time topside ionosphere of Mars; these observations have implications on the ion escape rates from the Martian upper atmosphere. Intense solar wind penetration up to ~300 km altitude was observed in the Martian atmosphere during a CME event, causing significant energization of ionospheric heavy ions.

The Atmosphere Technology Division (ATD) is playing a pivotal role for realizing the scientific ideas to experiments by designing and developing experimental systems for atmospheric, space and planetary exploration, in collaboration with the scientific groups. The 25-years old in-house developed HF Radar system is functioning well because of its meticulous maintenance and periodic augmentations, and proved its potential by observing the F-region plasma structures during the SOUREX-II experiment. The Digisonde system was refurbished in-house and is being operated with its full potential. Fabrication of the on-board electronics for the ChaSTE payload onboard Chandrayaan-3 Lander has been completed. Design of the front-end electronics for the solar occultation experiment payload as part of the Technology Development Programme and the development of a versatile user interface for automation of the High Vacuum Space Simulation Facility (HVSSF) are notable achievements. ATD is contributing to further strengthening of the ground-based observation network for ionospheric studies.

Development of the qualification and flight models of Aditya-L1-PAPA payload is progressing well at the Avionics entity of VSSC, in close coordination with SPL. The engineering model of PAPA was subjected to tests and calibration at the HVSSF to verify the energy, mass and angular resolutions as well as the field of view of the sensors. Detailed ion optics simulations were carried out as part of the design and development of a quadrupole mass spectrometer at VSSC. SPL has also contributed to the scientific aspects and ground segment planning for the magnetometer payload for Aditya-L1 being developed by LEOS, Bangalore. Integration and the T&E of the flight models of ChaSTE and RAMBHA-LP payloads onboard Chandrayaan-3 are progressing well. Several entities of VSSC, including MVIT, PCM, STR, AVN, SR, MME, AERO, CMSE and SPRE made major contributions to these developments. The front-end card of ChaSTE was provided by PRL, Ahmedabad.

We had a brain-storming meeting on the most relevant scientific problems and thrust areas for future research in atmospheric, space and planetary sciences during 21-22 January 2021. Eleven renowned experts from India, USA, Germany, UK, Sweden and Japan participated in this online meeting.

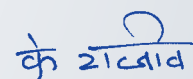
Many of our scientists have received national and international accolades this year also. These include the coveted Engineering Sciences Award of the International Academy of Astronautics, 2020 to Dr. Radhika Ramachandran. During the period of this report, there were **Seventy Three** peer-reviewed journal publications with an average impact factor of **3.48**. Four research fellows were awarded Ph.Ds. The scientific contributions further consolidate SPL's rightful position as a leading national institute of international repute in several areas of atmospheric, space and planetary science.

We are thankful to Dr. T. K. Alex (Chairman, SPL-SAC) and members of the Scientific Advisory Committee of SPL (SPL-SAC) who are playing a major role in bringing better focus to our scientific and technical activities. The scientific deliberations and presentations made to the SPL-SAC are enjoyable and rejuvenating, and we have made the best efforts to implement all the recommendations of the committee.

All our major scientific and technical goals, especially those involving multiple entities and centres, could be achieved only because of the visionary leadership at VSSC and ISRO. We are extremely thankful to Shri. S. Somanath, Director, VSSC for his detailed reviews, scientific temperament, very timely actions, unflinching support and inspiration for all the activities at SPL. We also thank all the Entity Chiefs of VSSC and Chiefs of our collaborating centres/institutions within and outside ISRO for their support and encouragements. We thank Shri. R. Umamaheswaran, Scientific Secretary, ISRO for his encouragements and strong support and taking care of our requirements at ISRO Hq. We are grateful to the critical reviews, inspiration and unflinching support received from Dr. K. Sivan, Chairman, ISRO for our scientific endeavours.

I thank the significant scientific contributions made by the members of SPL family for realizing our objectives, despite the Covid-19 restrictions – a sign of dedication and professionalism. I am particularly thankful to Dr. Radhika Ramachandran who was the director of SPL till January 2021 for her motivating leadership and major contributions. I thank the Editorial Team Dr. C. Vineeth, Dr. Mukunda M. Gogoi, and Dr. S. Suresh Babu, for bringing out this report in its present form.

09 September 2021



K. Rajeev
Director, SPL

पुरस्कार और सम्मान / Awards, Honours & Recognitions

RADHIKA RAMACHANDRAN

- Engineering Sciences Award of the International Academy of Astronautics, 2020

K. RAJEEV

- National Representative to Committee on Space Research (COSPAR) Council, 2020.
- Member, Research Advisory Committee, Indian Institute of Tropical Meteorology (IITM), Pune, Since 2020

S. SURESH BABU

- Fellow of the Indian Academy of Sciences (FASc), 2021.
- ISRO-ASI awards for Space Science and Applications - 2018.
- MoES National Award of Excellence in Atmospheric Science and Technology, 2020.
- Vice Chair, COSPAR Sub-Commission (A1) on Atmosphere, Meteorology and Climate 2021-2024.
- Member, INSA National Committee for Future Earth, Since 2020.
- Member of Executive Committee of Indian Geophysical Union (IGU), 2020-2022.
- Member, Academic Council, Central University of Rajasthan, Since 2020.

VIJAYAKUMAR S. NAIR

- SwarnaJayanti Fellowship of Department of Science and Technology for the period 2020-2025.
- Certificate of Excellence in Reviewing, Journal of Earth System Science, 2020.

GIRACH IMRAN ASATAR

- INSA Medal for Young Scientist from Indian National Science Academy, 2020.

KANDULA V. SUBRAHMANYAM

- Ministry of Earth Sciences Young Researcher Award for the year 2021.

AMBILI K. M.

- Swami Vivekanandan Yuva Prathibha Award in Science, Kerala State Youth Welfare Board 2018.

MUKUNDA M. GOGOI

- Guest Editor, Frontiers in Earth Science (Atmospheric Science), 2021.

PRAMITHA M.

- Inspire Faculty Position Awarded by Department of Science and Technology, 2021.

शैक्षणिक उत्कृष्टता / Academic Excellence

BEST PAPER AWARDS

KANDULA V. SUBRAHMANYAM

- National E-Symposium on Cloud and Precipitation Processes-2021, Organised by IMS Pune and IITM.

RENJU. R.

- Earth and Planetary Science Session, 33rd Kerala Science Congress (KSC), Scientist Category.

SISMA SAMUEL

- Earth and Planetary Science Session, 33rd Kerala Science Congress (KSC), Student Category.



पीएच.डी. से सम्मानित / Ph.D. Awarded



NITHIN MOHAN

- “Investigations on the Subsurface Thermophysical Properties of Venus based on the GMRT Observations of Thermal Radio Emissions”, Cochin University of Science and Technology (CUSAT), Kochi, September 2020 [Supervisors: Dr. S. Suresh Raju, Dr.Nizy Mathew].

NALINI K.

- “Spatio-temporal Variability of Atmospheric Carbon Dioxide over India and Design of Optimal Monitoring Network using Observations and Lagrangian Modelling”, Cochin University of Science and Technology (CUSAT), Kochi, November 2020 [Supervisor: Dr. Radhika Ramachandran].

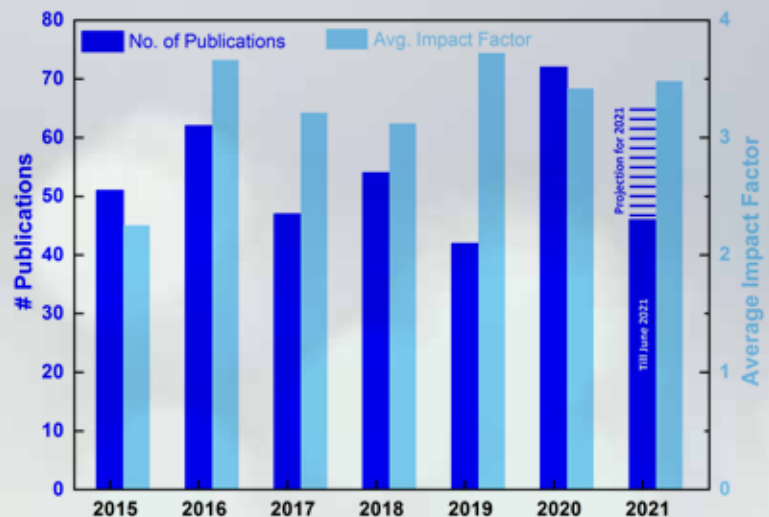
N. KOUSHIK

- “Investigations on the Role of Sudden Stratospheric Warming in High Latitude – Low Latitude Coupling in the Middle Atmosphere”, Cochin University of Science and Technology (CUSAT), Kochi, January 2021 [Supervisor: Dr. K. Kishore Kumar].

ASWINI A. R.

- “Characterisation of carbonaceous aerosols in distinct geographical environments over the Indian region”, Cochin University of Science and Technology (CUSAT), Kochi, April 2021. [Supervisors: Dr. Prashant Hegde, Dr. Prabha R. Nair].

प्रकाशनों / Publications

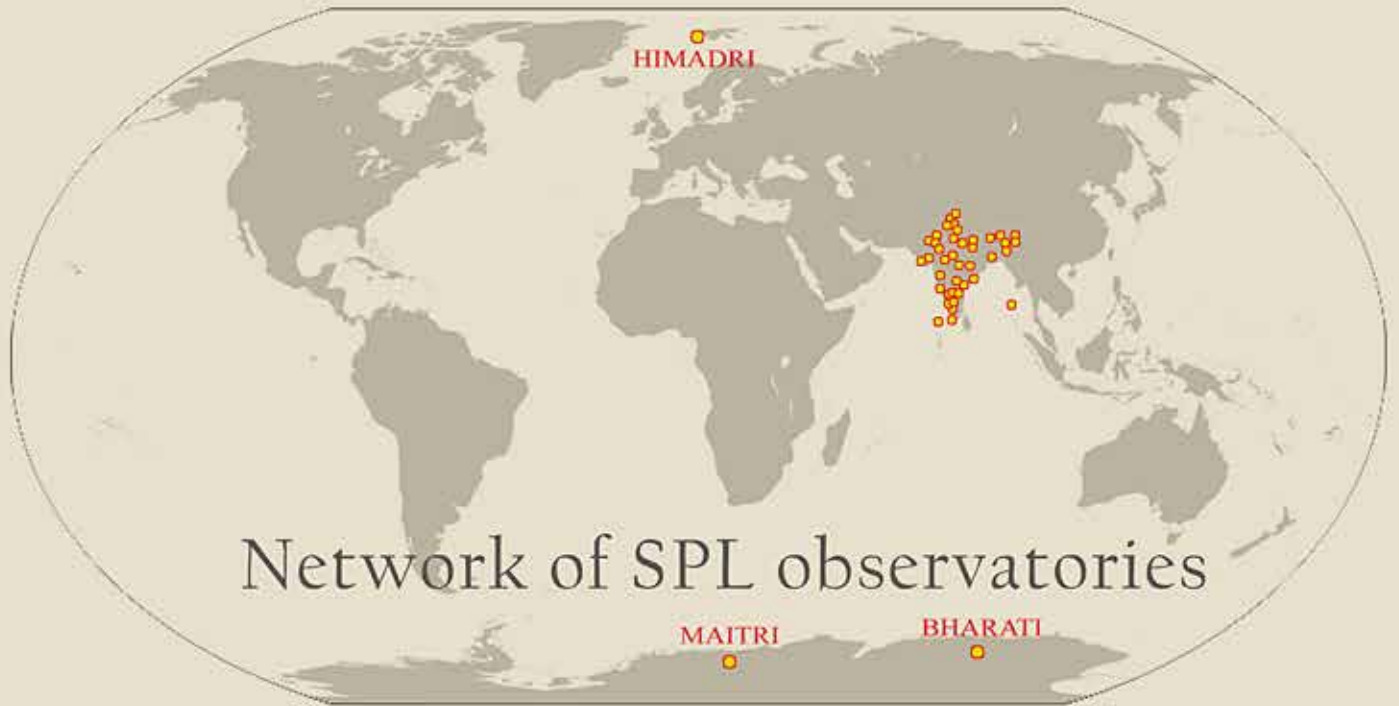


ISRO Story of the Week

- Megha-Tropiques ScaRaB/3 makes multi-year direct observations of the diurnal variation of cloud radiative forcing over tropics, 01 October, 2020.

अंतर्वस्तु / Contents

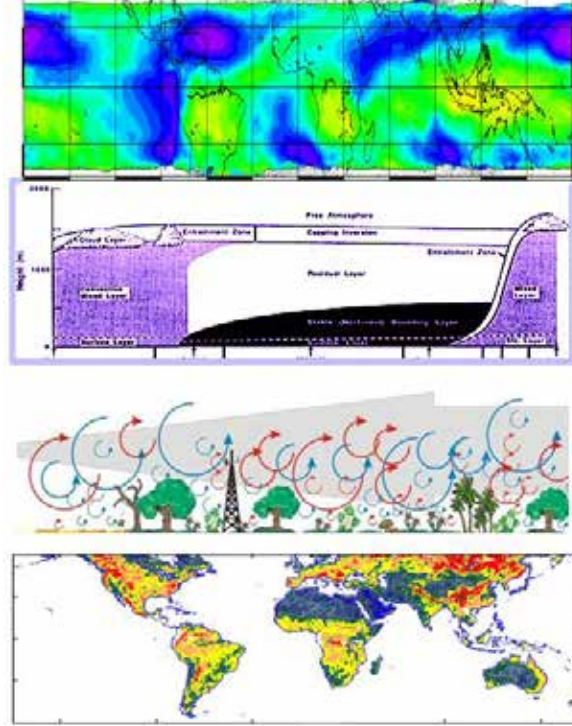
पुरस्कार और सम्मान / Awards, Honours and Recognitions	ix
शैक्षणिक उत्कृष्टता / Academic Excellence	ix
पीएच.डी. से सम्मानित / Ph.D. Awarded	x
प्रकाशनों / Publications	x
माइक्रोवेव एवं परिसीमा स्तर भौतिकी Microwave and Boundary Layer Physics	13
ऐरोसॉल, ट्रेस गैस तथा रेडिएटिव फोर्सिंग Aerosols Trace gases and Radiative Forcing	23
संख्यात्मक वायुमंडल प्रतिरूपण Numerical Atmosphere Modelling	45
वायुमंडलीय गतिकी शाखा Atmospheric Dynamics Branch	55
आयनमंडल तापमंडल एवं चुंबकमंडल भौतिकी Ionosphere Thermosphere Magnetosphere Physics	75
ग्रहीयविज्ञान शाखा Planetary Science Branch	87
वायुमंडल प्रौद्योगिकी प्रभाग Atmosphere Technology Division	97
योजना और समन्वय प्रकोष्ठ Planning and Co-ordination Cell	105
कार्यालय और प्रशासनिक सहायता Office and Administrative Support	106
शैक्षणिक परियोजनाएं Academic Projects	107



Network of SPL observatories

माइक्रोवेव एवं परिसीमा स्तर भौतिकी

MICROWAVE AND BOUNDARY LAYER PHYSICS



एमबीएलपी शाखा वायुमंडलीय परिसीमा परत (एबीएल) के पृष्ठीय अभिलक्षणों, संरचना एवं गतिकी तथा मुक्त क्षोभमंडल, मेघों, संवहन, अवक्षेपण के साथ इसके युग्मन और पृथ्वी एवं अन्य ग्रहीय पिंडों के माइक्रोवेव सुदूर संवेदन पर ध्यान केंद्रित करती है। इस शाखा के मुख्य लक्ष्य हैं: (i) पृष्ठ-वायु अन्त्योन्यक्रिया प्रक्रियाओं, एबीएल के दैनिक प्रादुर्भाव व प्रदूषक प्रकीर्णन में एबीएल प्रक्रियाओं की भूमिका सहित सुस्पष्ट भौगोलिक पर्यावरण के बारे में समझ को बढ़ाना (ii) मेघों, अवक्षेपण एवं भू-वायुमंडल प्रणाली की ऊर्जिकी से संबंधित समझ को सुधारना, एवं (iii) पृथ्वी की सतह के अंतरिक्षवाहित तथा भू-आधारित माइक्रोवेव सुदूर संवेदन से पृष्ठीय गुणधर्मों, वायुमंडलीय जल वाष्प, मेघ अभिलक्षणों एवं अवक्षेपण, तथा वायुमंडल के माध्यम से माइक्रोवेव संचरण पर उनके संभाव्य प्रभावों का अध्ययन।

The MBLP branch focuses on the surface characteristics, structure and dynamics of the atmospheric boundary layer (ABL) and its coupling with free-troposphere, clouds, convection, precipitation, and microwave remote sensing of the Earth and other planetary bodies. The main objectives are: (i) to improve the understanding of the ABL processes under distinct geographical environments, including surface-air interaction processes, diurnal evolution of ABL, and the role of ABL processes in pollutant dispersal (ii) improve the understanding on clouds, precipitation and energetics of the Earth-atmosphere system, and (iii) space-borne and ground-based microwave remote sensing of Earth's surface and atmosphere for deriving the surface properties, atmospheric water vapour, cloud characteristics and precipitation, including their potential impact on microwave propagation through the atmosphere.

वैज्ञानिक टीम / Science Team

राजीव के / Rajeev K.
सुरेश राजू सी / Suresh Raju C.*
सत्यमूर्ती वी / Sathiyamoorthy V.#
किरण कुमार एन वी पी / Kiran Kumar N.V.P.
मनोज कुमार मिश्रा / Manoj Kumar Mishra
निजी मात्यू / Nizy Mathew
संतोष एम / Santosh M.
रंजू आर / Renju R.

तकनीकी टीम / Technical Team

लाली पी टी / Lali P. T.
प्रमोद पी पी / Pramod P. P.
दिनकर प्रसाद वज्जा / Dinakar Prasad Vajja

अनुसंधान सहयोगी / Research Associates

शिवकुमार रेड्डी एन / Sivakumar Reddy N.⁵
लावण्या एस / Lavanya S.

अनुसंधान अध्येता / Research Fellows

सीस्मा सामुवेल / Sisma Samuel
अश्वती आर एस / Aswathy R.S.

* Relieved in November 2021

Joined in April 2021

\$ Relieved in February 2021

Atmospheric Boundary Layer under IGBP-NOBLE Project

Surface Layer Characteristics over Semi-Arid Region, Anantapur

Understanding of the surface layer characteristics, heat fluxes and turbulence is essential for improving the surface energy balance and surface layer parameterizations. The surface layer characteristics over semi-arid regions are least explored over the Indian region. The wintertime atmospheric surface-layer energy and momentum fluxes and turbulence characteristics over the semi-arid region Anantapur (14.62° N, 77.65° E) were investigated based on tower-mounted fast-response sonic anemometer observations. The observations consist of two-level sonic anemometers mounted at 10 m and 18 m at Sri Krishnadevaraya (SK) University, Anantapur under the IGBP-NOBLE Project. The data has been analysed with planar fit method for avoiding any sensor tilt errors. The stability parameter indicates systematic diurnal variation of surface layer instability, which builds up after 0730 LT and lasts till 1730 LT. The vertical flux of sensible heat attains its peak value of about 310 Wm⁻² around noon; this variation is in phase with the diurnal variation of the incoming shortwave radiative flux. The sensible heat flux is downward by about 15 Wm⁻² during night due to the colder surface and warmer atmosphere, which is associated with the nocturnal stable layer. Diurnal variations of Turbulent Kinetic Energy (TKE) and vertical flux of horizontal momentum show broad noon-time peak. A secondary pre-midnight peak is also observed in TKE and momentum flux between 2200-0000 LT, associated with the nocturnal turbulence arising from the wind shears (Fig.1). As seen from the stability parameter, this also weakens the nocturnal stability.

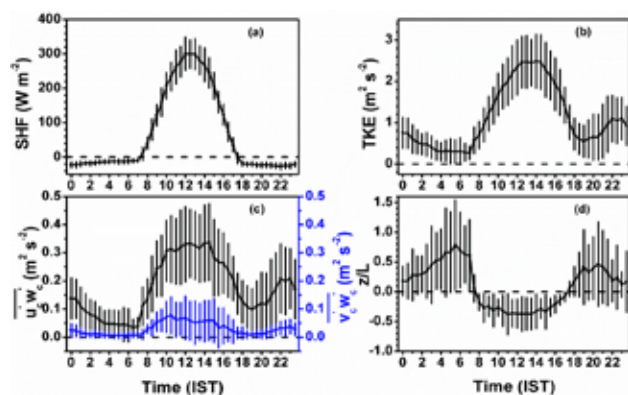


Figure 1: Diurnal variation of (a) sensible heat flux (SHF), (b) Turbulent Kinetic Energy (TKE), (c) vertical flux of horizontal momentum ($u'w'_c, v'w'_c$), and (d) stability parameter (z/L) over Anantapur during winter. Vertical bars indicate the standard deviations [Sivakumar Reddy et al., J. Atmos. Sol.-Terr. Phys., 2021].

Similarity Relationship

Figure 2 shows the scatter plots of scaled variables with the stability parameter (z/L) for both unstable and stable

conditions (where σ_{wc} is the standard deviation in the vertical wind component after tilt correction; u_* is the friction velocity). The non-dimensional wind variance with surface-layer stability parameter follows the 1/3 power law variation, conforming to the Monin-Obukhov similarity theory. The values of σ_{wc}/u_* decrease as z/L approaches near-neutral conditions, which tends to be nearly constant at about 1.29; this does not vary significantly within the stability range -1 to 1.2, indicating that is almost independent of z/L in this range. Overall, the variations of σ_{wc}/u_* with z/L observed in the unstable and stable conditions agree with the empirical fits observed over other regions (Fig.2), indicating the consistency in the similarity relationship over this semi-arid region with those at the other plain land regions.

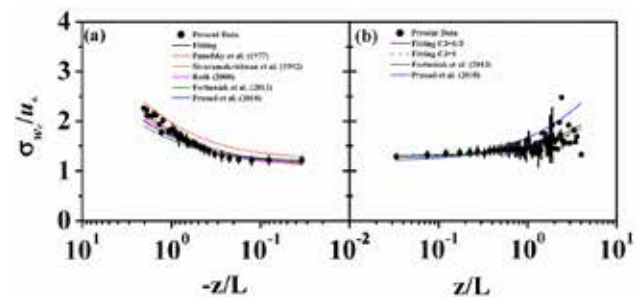


Figure 2: Variations of σ_{wc}/u_* as a function of z/L for (a) unstable ($z/L < 0$) and (b) stable conditions ($z/L > 0$) over the semi-arid region during winter. The error bars indicate one standard deviation within each bin. The bin size is determined in a logarithmic scale. [Sivakumar Reddy et al., J. Atmos. Sol.-Terr. Phys., 2021].

Atmospheric Surface Layer Variations over the East Khasi Hill in Northeast India

The seasonal variations of surface-layer characteristics over the east Khasi Hill in Northeast India are investigated based on micrometeorological observations using sensors mounted on 32-m meteorological tower installed at NESAC, Umiam (25.67°N, 91.91°E; 1040 m amsl), Shillong, under the IGBP-NOBLE project. Since the observations were carried out on a mountainous terrain, the data were subjected to planar-fit method of coordinate rotation for transforming the data to terrain following system. Mountainous topography and solar elevation angle have a significant influence on the wind circulation and energy exchange over this complex region where the noontime solar elevation and diurnal mean solar flux vary significantly with season. Effect of the mountain valley circulation is more prominent in the winter, pre-monsoon, and post-monsoon seasons, while the winds are primarily controlled by the synoptic circulation during summer monsoon season. The peak values of sensible heat flux (H) are found to be 219 ± 61 Wm⁻², 278 ± 120 Wm⁻², 152 ± 127 Wm⁻², and 166 ± 68 Wm⁻² during winter, pre-monsoon, summer monsoon and post-monsoon seasons respectively (Fig.3). Such high values of sensible heat flux over the complex terrain during pre-monsoon season are contributed by the higher solar insolation and the vertical

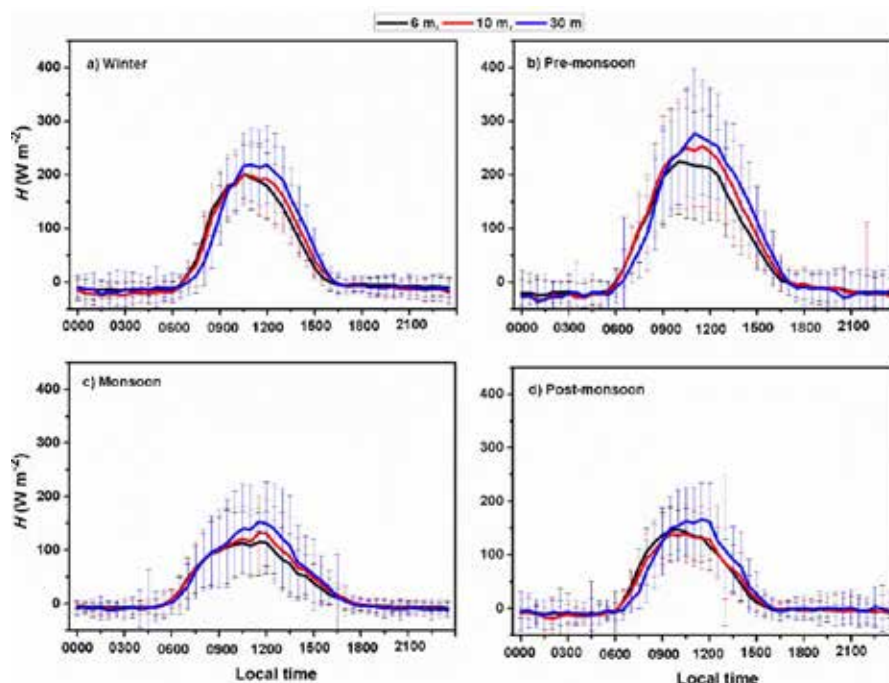


Figure 3: Multi-year seasonal mean diurnal variation (line) and standard deviation (vertical bar) of sensible heat flux (H) at the 6-m, 10-m, and 30-m heights during (a) winter, (b) pre-monsoon, (c) summer monsoon, and (d) post-monsoon seasons over NESAC, Shillong [Burman et al., *Theoretical and Applied Climatology*, 2021].

motions that dominated during the daytime. The peak values of momentum flux are found at about 2 to 3 h after the maximum value in sensible heat flux is attained. The average daytime turbulence kinetic energy was higher by 99%, 56%, 72%, and 93% than the respective night-time values during winter, pre-monsoon, summer monsoon and post-monsoon seasons respectively.

Precipitation Characteristics and Microwave Wave Propagation

Characteristics of the Raindrop Size Distribution

The measurement of raindrop size distribution (DSD) is important for understanding the microphysical processes in precipitation and improving the relationship between rain rate and radar reflectivity for accurate rainfall estimates from Doppler Weather Radar (DWR). Conventionally, for

the estimation of rainfall, DWRs operating at microwave frequencies assume an empirical relationship $Z=AR^b$, where A and b are constants. Several observational studies have demonstrated that the A and b coefficients vary with geographical locations, storms type and with precipitating systems. These discrepancies result in errors in the surface rainfall estimation by radars. Therefore, to improve the accuracy of rainfall estimation from radars, a wide range of DSD observations in the precipitating systems and storms should be examined. The major findings in this direction, obtained from the long-term (2007-2015 and 2018) observations of DSD over the coastal station Thumba are given below.

Seasonal Mean Droplet Size Distribution (DSD)

The precipitating systems observed over Thumba using disdrometer are classified into convective, transition and stratiform rain based on the ratio of mass-weighted mean

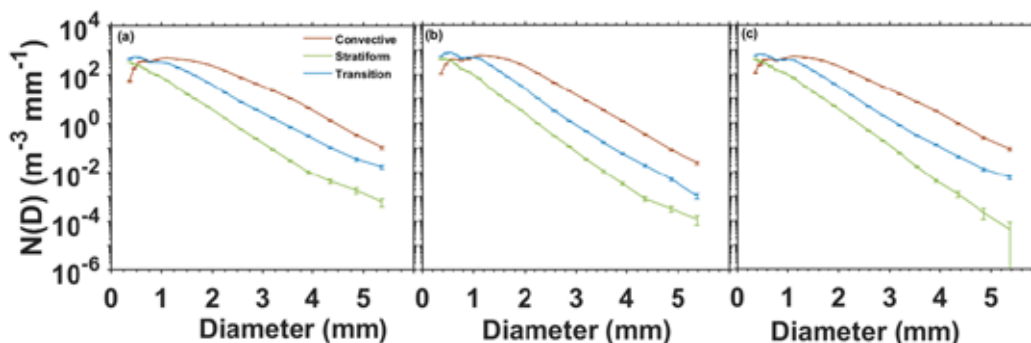


Figure 4: Average DSD during (a) pre-monsoon (b) summer monsoon and (c) post-monsoon seasons for the period 2007-2015 and 2018. Vertical bars indicate the standard deviations. [Lavanya and Kirankumar, *Atmos. Res.*, 2021].

diameter (D_m) and rain rate (R). This analysis shows distinct differences in DSD patterns in the convective, transition and stratiform rain types. In general, the mean DSD spectra for convective precipitation is found to be broad compared to that of the transition and stratiform rain types (Fig.4). The DSD spectra in the convective precipitation have relatively higher (smaller) number concentration of large (small) raindrops as compared to other precipitation types, resulting in larger D_m values than the other two rain regimes. The DSD spectra of stratiform precipitation show nearly exponential decrease with more number of small diameter drops irrespective of the season. The distinct shapes of DSD spectra observed in Fig.4 underline the physical processes occurring in different rain types over this region. The reduction of small drops (downward concavity of the DSD spectra) and increase in the concentration of larger drop sizes (higher D_m values) in the convective rain type is mainly due to evaporation. The DSD spectra for transition and stratiform rain are narrower

compared to that of the convective rain.

Z-R Relationship for Rainfall Estimation from Weather Radars

Figure 5 shows the scatter plots of the variation of radar reflectivity (Z) with rain rate (R) for different rain types during different seasons, estimated based on the disdrometer measured DSD. The parameters for Z-R relationship ($Z=AR^b$) derived for different rain types are depicted in Fig.5. The value of coefficient A (exponent b) is higher (lower) for stratiform (convective) rain type irrespective of the season. These values for transition rain regime are found to be in between the convective and stratiform rain regimes. The higher values of b (>1.68) in the convective and transition rain regime suggest that the rainfall is dominated by the size-controlled processes.

Attenuation Characteristics of GSAT-14/Ka-band Signals

Collocated and concurrent measurements of (i) the attenuation in the GSAT-14 Ka-band transponder signals at 20.2 GHz and 30.5 GHz using cross polarization Ka-band beacon receiver, (ii) atmospheric and cloud parameters using Microwave Radiometer Profiler (MRP), and (iii) rain parameters using Micro Rain Radar (MRR) and Laser Precipitation Monitor (LPM), carried out during the Asian summer monsoon season and convective rain events over the tropical coastal station, Thumba were used to investigate the impact of precipitation in the attenuation of Ka band signals from satellite (GSAT-14). The effect of rain rate (RR) and rain drop size distribution (DSD) for stratiform and convective precipitation on the attenuation of Ka-band signals has been examined and empirical relations between the attenuation in Ka-band signal at 20.2GHz and 30.5 GHz and the reflectivity have been formulated.

Figure 6 depicts the temporal evolution of the vertical distribution of relative humidity (RH) and cloud liquid

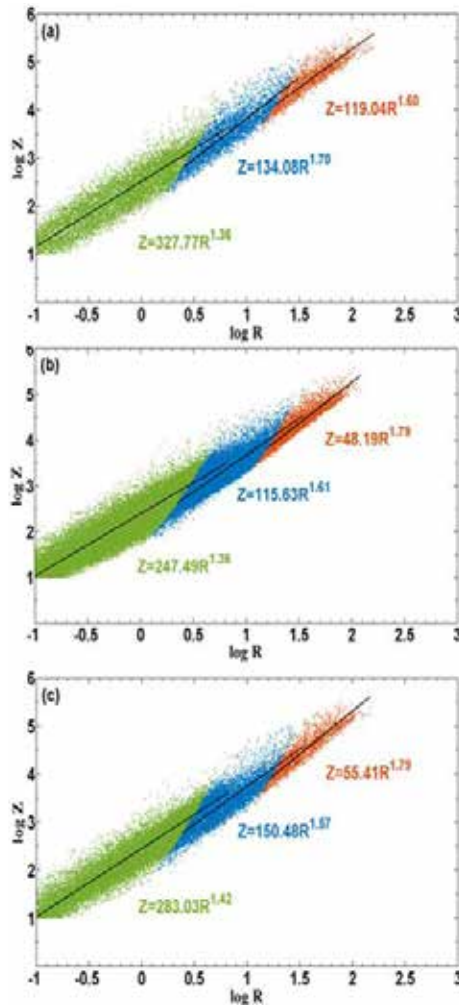


Figure 5: Scatter plots of log Z and log R for (a) pre-monsoon, (b) summer monsoon and (c) post-monsoon seasons. Brown, blue and green solid circles correspond to convective, transition and stratiform precipitation respectively. The black line represents the line of fit by using the A, b values derived from disdrometer data at Thumba [Lavanya and Kirankumar, Atmos. Res., 2021].

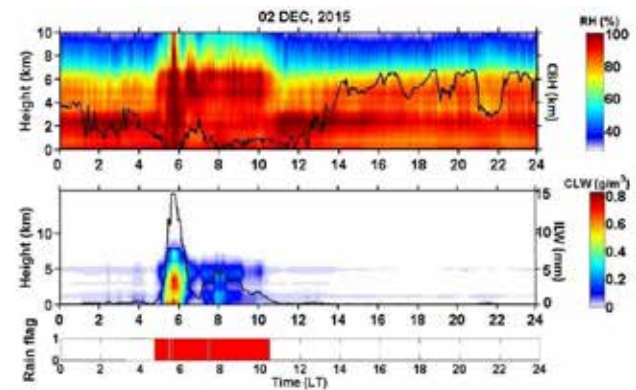


Figure 6. The temporal evolution of the vertical distribution of RH and cloud base height (CBH) (top panel), cloud liquid water content (CLW) and integrated liquid water content (ILW) (middle panel) and rain flag (bottom panel) during different phases of the mesoscale convective system (MCS) event on 2nd December 2015, obtained from MRP observations. [Renju et al, IEEE TAPS, 2021].

water content (CLW) during the occurrence of a mesoscale convective system (MCS) on 2nd December 2015, observed using the MRP. The genesis of the MCS, its evolution into a fully matured convective system, its decay and the post MCS meteorological conditions over the station are evident in the time variations of RH, cloud base height (CBH), CLW and integrated liquid water content (ILW). During this event, rain occurred for more than 5 hours (0500 to 1000 LT). The CLW showed an enhancement throughout the column with ILW >10 mm during the convective phase followed by a band of enhanced CLW at freezing point level (~5 km) with low ILW (<5 mm) during the stratiform phase of the MCS. Heavy precipitation of ~55 mm/hr with radar reflectivity value >38 dBZ, occurred during 0500 - 0600 LT, indicating the convective phase of the system followed by a stratiform rain.

The attenuation of signals in the 30.5 GHz and 20.2 GHz channels during the MCS is shown in Fig.7. Strong attenuation of 20-25 dB occurred at both channels during the convective phase (05:00 LT to 06:00 LT). During this period, intense rain with RR >30 mm/hr caused large scattering at 30.5 GHz leading to totally diminishing the signal whereas the 20.2 GHz channel showed a sharp peak in attenuation (>20 dB). The temporal pattern of the Ka-band signal attenuations match with the variations of CLW and ILW. During the stratiform part of the MCS, both channels showed attenuation <10 dB.

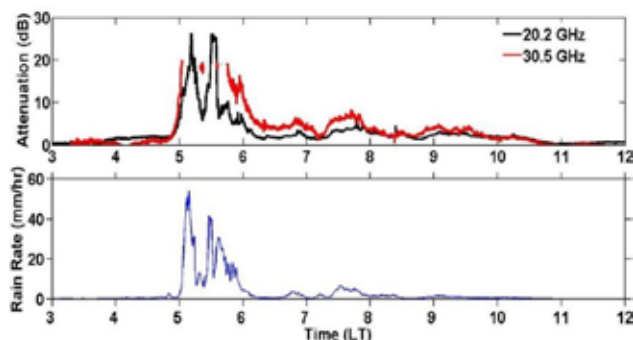


Figure 7. The temporal variations of Ka-band signal attenuation at 20.2 GHz (black line) and 30.5 GHz (red line) channels (top panel) and the corresponding rainfall (bottom panel) during the MCS event on 2nd December 2015 [Renju et.al, IEEE TAP, 2021].

Characterization of Ka-band Signal Attenuation

The attenuation characteristics of the Ka-band signal over Thumba were investigated during all rain events during 2018. The scatter plot of rain rate and attenuation at 30.5 GHz and 20.2 GHz channels are shown in Fig.8. It is found that, at 30.5 GHz, the path integrated attenuation varies from 0.2-3 dB for lower RR (<1 mm/hr) and increases exponentially with increase in RR. At 20.2 GHz, the attenuation and RR follow a linear trend with most probable attenuation of 0.1-2 dB for rain rate <12 mm/hr; the attenuation increases exponentially with further increase in RR. An exponential increase in attenuation with RR is observed for convective rain types (RR>12

mm/hr) for both frequencies. It has also been found that the signal attenuation varies significantly with drop size for both frequencies. Compared to 20.2 GHz, the attenuation at 30.5 GHz increases more rapidly with median volume diameter.

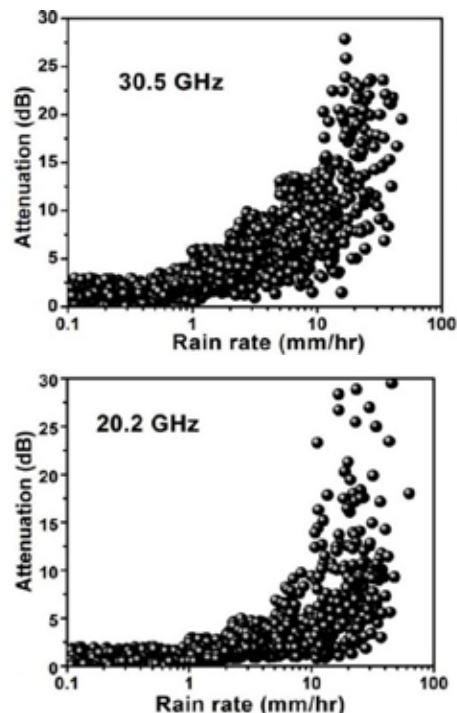


Figure 8. The scatter plots showing the dependence of attenuation at 30.5 GHz (left panel) and 20.2 GHz (right panel) channels on rain rate [Renju et.al, IEEE TAP, 2021].

Tropical Cloud Systems and Impact on Energetics

Spatial and Temporal Variations of Tropical Deep Convective Clouds using Megha-Tropiques/SAPHIR Observations

Deep convective clouds (DCCs) play a pivotal role in regulating the weather and climate of the earth-atmosphere system by modifying the radiation balance, thermodynamic structure, hydrological cycle and vertical and horizontal transfer of energy, moisture and momentum. The diurnal, seasonal and inter-annual cycles of DCCs over the tropics have been estimated using multi-year brightness temperature (TB) data obtained from SAPHIR payload, aboard the Megha-Tropiques (MT) satellite during the years 2011-2018. MT-SAPHIR provides the measurements at different local times over the entire tropics because of its low inclination orbit, which makes the study of the diurnal cycle of tropical DCCs possible from a single platform. The DCCs have been identified using the difference between TB measured by different channels of SAPHIR payload centred around 183.31 GHz. This methodology provides a unique opportunity to discern convective cores from the anvils. The total occurrence frequencies of DCCs are estimated for Northern Hemisphere (NH) spring (March

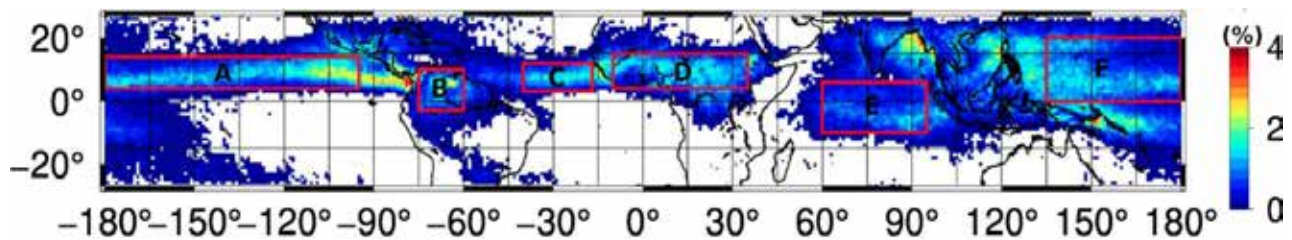


Figure 9: The frequency of occurrence of DCCs during NH summer and the regions identified to study the diurnal evolution. The regions identified for further analysis are: A-East Equatorial Pacific, B-Amazon region; C-Equatorial Atlantic; D-Central Africa; E-Equatorial Indian Ocean, and F-Western Pacific [Sisma et al., *Int. J. Rem. Sens.*, 2021].

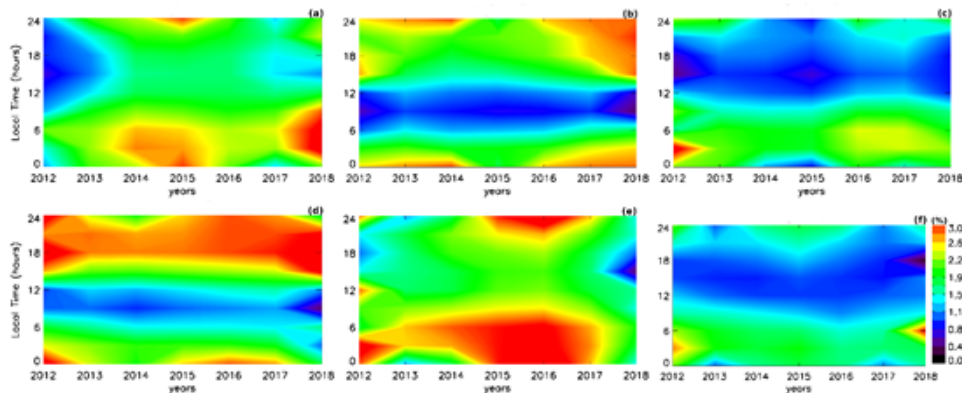


Figure 10: Diurnal variation of deep convective clouds over selected regions (marked A - F) for JJA marked in Fig.9 [Sisma et al., *Int. J. Rem. Sens.*, 2021].

to May), summer (June to August), autumn (September to November) and winter (December to February) seasons. The occurrence frequency of DCCs ranges from 0 to 4%, with the highest value occurring mostly over the ascending limbs of the Hadley and the Walker cells. Similarly, the lowest occurrence of DCC is over the descending limbs of the Hadley and the Walker cells. From the seasonal mean occurrence frequency maps, regions of large DCC occurrences are identified to study its diurnal evolution for each season (Fig.9).

The diurnal evolutions of DCCs over these regions during the NH summer are shown in Fig.10. The occurrence frequency of DCCs is maximum over the Asian summer monsoon region and the Pacific near to Central America during NH summer. The east equatorial Pacific (region 'A') exhibits a broad diurnal pattern with an early morning maximum with peak occurrence during 0300 to 0700 LT. During the El Niño period, a significant increase in the occurrence of DCC is evident due to the eastward movement of convective zones from the west Pacific to the east Pacific, resulting in an increased occurrence of 3% during the year 2015. The amplitude of the diurnal cycle is larger over the land compared to that over the oceanic regions, with the peak occurring between 1400 to 1900 LT. The large diurnal variability of land surface temperatures and lower tropospheric instability results in a clear diurnal pattern over the land compared to the ocean. Over the equatorial Atlantic (region 'C'), the maximum amplitude is in the early morning during 0000 to 0600 LT with a peak occurrence of 1.5%. Similarly, over the Indian Ocean

and the western Pacific, the amplitude of diurnal variation is significant. Overturning circulation during the Asian summer monsoon season has resulted in increased diurnal amplitude over the Indian Ocean region with a peak value ~3% between 0000 to 0600 LT.

Diurnal Variations of Cloud Radiative Forcing over Tropics using Megha-Tropiques-ScaRaB/3

Notwithstanding the long record of radiative flux observations using satellites and the fundamental work on global cloud radiative forcing (CRF), direct observations of the diurnal variations of CRF are very limited. The Megha-Tropiques ScaRaB observations of the broadband shortwave (SW) and longwave (LW) radiative fluxes at top of the atmosphere (TOA), together with its ability to make the measurements at different local times during its 51-day precession cycle, provide a unique opportunity to directly derive the diurnal variations of the SW and LW cloud radiative forcing (SWCRF and LWCRF) over the tropics.

Seasonal Mean Diurnal Variations of LWCRF and SWCRF

Figure 11 depict the multi-year (2012-2016) seasonal mean diurnal variations of LWCRF and SWCRF during the northern hemispheric (NH) summer season (June-August). Similar analysis was carried out for all other seasons as well. Fig.11 shows that the cloud occurrence and LWCRF are the largest over the Inter-Tropical Convergence Zone (ITCZ) and the ascending limbs of the Walker cell, while the least values of CRF occur at their descending limbs. In general, CRF has the largest magnitude during the local

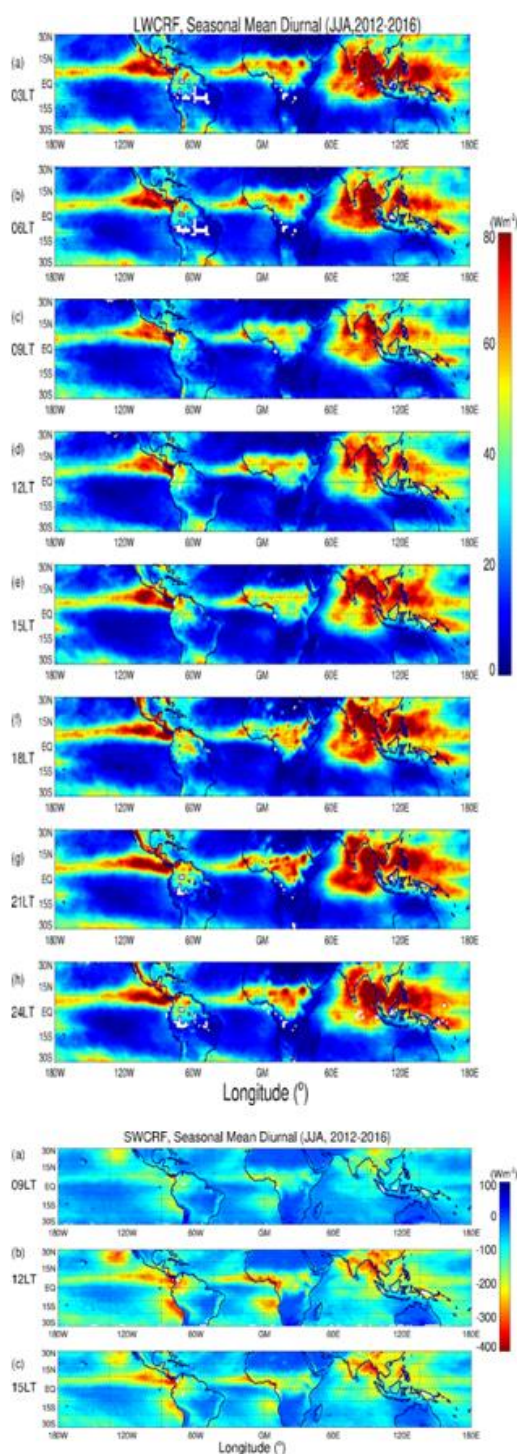


Figure 11 (Top panel): Multi-year (2012-2016) seasonal mean spatial variations of LWCRF (averaged at 3 hourly intervals) at different local times during NH summer (June-August). (Bottom panel): SWCRF averaged at 3 hourly intervals of 0800-1100 LT, 1100-1400 LT, 1400-1700 LT during NH summer (June-August). [Gupta et al., *Climate Dynamics*, 2020]

summer in each hemisphere. During all seasons, the largest magnitudes of LWCRF and SWCRF over the continents are observed at the deep convective regions: the Amazon, Central and Southern Africa and the Indian subcontinent. Over the continental convective regions, the diurnal peak

of LWCRF occurs during 1500-2100 LT while the diurnal minimum occurs at 0900-1200 LT. The peak-to-trough variations of LWCRF over these regions are generally in the range of 15-30 Wm^{-2} , while the evening peak values vary between 60-80 Wm^{-2} . The SWCRF is generally largest at ~ 12 LT. Though the convection over the monsoon trough and the Bay of Bengal are driven by the Asian summer monsoon circulation and occur within about 10° geographical distance, their diurnal phases (1800-2100 LT and 0000-0600 LT respectively) are remarkably different. The largest diurnal variation of LWCRF over the entire tropics ($35\text{-}55 \text{ Wm}^{-2}$) occurs over the Madagascar Island during the local summer. Over the oceanic regions, the largest values of LWCRF during NH summer are associated with the Asian summer monsoon circulation: the LWCRF over the northeast Bay of Bengal during this season, which witnesses the deepest convection over the entire globe, is $>75 \text{ Wm}^{-2}$ throughout the day. The equatorial regions of the western and the eastern Pacific also have LWCRF $> 75 \text{ Wm}^{-2}$ during the night. The magnitude of the diurnal variation of LWCRF over these regions varies in the range of 15 to 25 Wm^{-2} , which is nearly 20-30% of the respective mean LWCRF. The largest SWCRF ($<-300 \text{ Wm}^{-2}$ at 12 LT) is observed over the northeast Bay of Bengal and the subtropical oceanic regions of the northeast and the southeast Pacific and the southeast Atlantic, associated with the occurrence of marine stratocumulus. This study also indicates the nighttime strengthening of the Walker and Hadley cells.

Effect of El Niño on the Zonal Variations of LWCRF, SWCRF and NCRF

El Niño conditions prevailed from November 2014 to May 2016 (Oceanic Niño Index, $\text{ONI} > 0.5$), with moderate and strong phases of El Niño during May 2015 to April 2016 (ONI in the range of 1 to 2.6). Substantial zonal gradients are observed in SWCRF, LWCRF and NCRF (averaged over the equatorial region) in all seasons during the normal and El Niño periods (Fig.12). In general, the magnitude of the NCRF is quite small ($<10 \text{ Wm}^{-2}$) over the deep convective oceanic regions, while significantly negative NCRF is observed over the continental deep convective regions. This is primarily because of the phase of the diurnal variation of convection. During the normal periods, the western Pacific witnesses strong deep convection with large magnitudes of SWCRF and LWCRF, while the central and the eastern Pacific have relatively smaller magnitudes. In contrast, during the El Niño period, magnitudes of LWCRF and SWCRF decreases significantly (by 20 to 30 Wm^{-2}) over the western Pacific while their values increase considerably (by 20 to 40 Wm^{-2}) over the central and eastern Pacific. This is due to the eastward movement of the convective zone from the western Pacific to the central and the eastern Pacific during El Niño periods. Though significant spatial variations occur in the LWCRF and SWCRF between the normal and El Niño periods, zonal variations of NCRF during the El Niño and normal periods

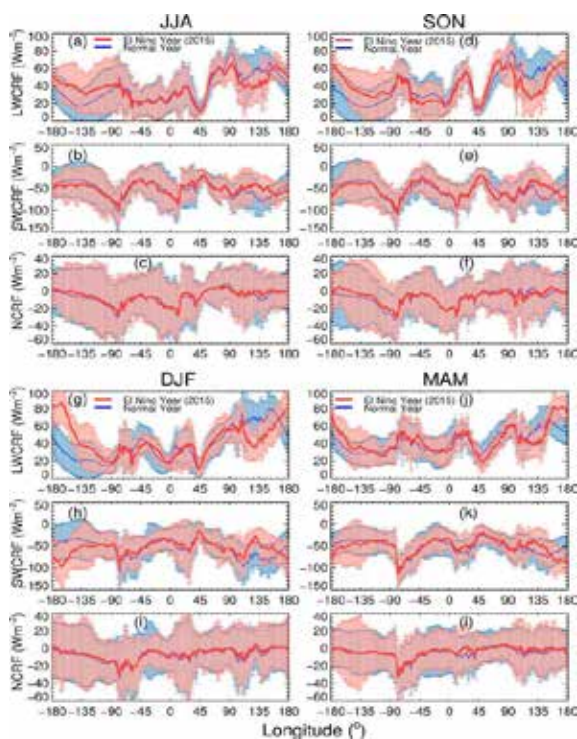


Figure 12: Zonal variations of the seasonal mean diurnally averaged LWCRF, SWCRF and NCRF averaged over the equatorial region (10°S to 10°N) during NH summer, autumn, winter and spring for the normal (July 2012 - October 2014) and El Niño periods (November 2014-February 2016). The vertical bars indicate the standard deviations [Gupta et al., Climate Dynamics, 2020]

are similar during all seasons. This remarkable feature occurs because the change in the diurnal mean LWCRF is compensated by an almost equal but opposite change in the diurnal mean SWCRF.

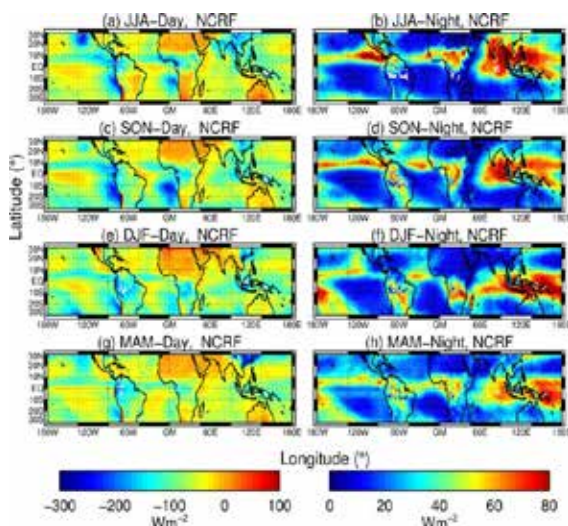


Figure 13: Seasonal mean net cloud radiative forcing (NCRF) averaged during the daytime (0800-1700 LT) (left panel) and nighttime (2000 - 0500 LT) (right panel) during the four seasons (averaged for 2012-2016).[Gupta et al., Climate Dynamics, 2020].

Day-night Variations of Net Cloud Radiative Forcing

The NCRF averaged during the daytime (0800-1700 LT) and nighttime (2000 - 0500 LT) during the four seasons (averaged for 2012-2016) are shown in Fig.13. The major features observed are: (i) NCRF is negative during the daytime over the entire tropics during all seasons. This causes a net cooling of the earth-atmosphere system during the daytime. (ii) The magnitude of the daytime NCRF cooling is largest over the sub-tropical oceanic regions in the southeast and the northeast Pacific and the southeast Atlantic which have prominent stratocumulus cloud occurrence where the NCRF cooling is $< -200 \text{ Wm}^{-2}$ over a vast region which is more than 30% of the total incoming solar radiation during the daytime. (iii) NCRF shows considerable daytime cooling ($< -150 \text{ Wm}^{-2}$) over the continental deep convective regions. (iv) Significant warming is observed at all the deep convective regions during the night, with the largest warming ($> 65 \text{ Wm}^{-2}$) observed over the oceanic regions

Dependence of SCATSAT-1 Backscattering Coefficient on Soil Moisture

Potential of the backscattering coefficient observed using SCATSAT-1 over the continents for deriving soil moisture was evaluated over different land surface types. SCATSAT-1 is a Ku-band wind scatterometer, which provides backscattering coefficient measurements over the globe in the horizontal and vertical polarizations at fixed incidence angles. Variabilities in the backscatter coefficients over different land surfaces over four different climate zones of India are investigated based on 3 years of SCATSAT-1 observations in conjunction with other collocated measurements. The variabilities in soil moisture and vegetation in these regions are compared and applicability of change detection method for estimating the soil moisture over these regions has been analysed. Based on regression analysis on SMOS-measured soil moisture and SCATSAT-1 measured backscattering coefficient, a relationship has been established for the soil moisture estimation from the SCATSAT-1 backscattering coefficient, as shown in Fig. 14. This shows good correlation between these two parameters and their time variations. The relationships (slop and intercept) are indicated in Fig. 14.

Payload Development

Chandra's Surface Thermophysical Experiment (ChaSTE)

Chandra's Surface Thermophysical Experiment (ChaSTE) payload is intended to investigate the thermophysical properties of lunar regolith over the polar region and is currently being developed for the Chandrayaan-3 lander, jointly by SPL in collaboration with Physical Research Laboratory (PRL) and other entities of VSSC (PCM, MVIT, AVN, SR, STR, AERO, SPRE, MME). This payload is similar to the one flown on Chandrayaan-2. The objective of ChaSTE is to make insitu measurements of temperature and thermal conductivity of the lunar regolith up to 100 mm

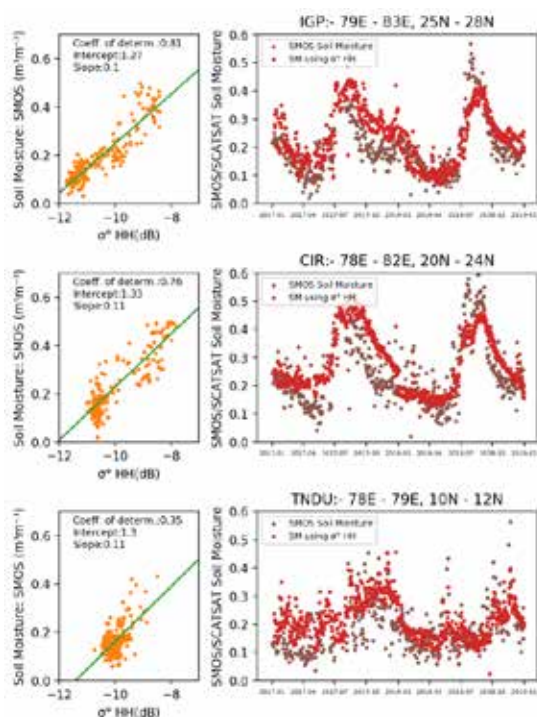


Figure 14: Estimation of soil moisture using regression analysis of SMOS soil moisture and SCATSAT backscattering coefficient over Indo-Gangetic Plain (IGP: top panel), central India (CIR: middle panel), and Tamil Nadu (TNDU: lower panel). Each panel contains two sub-panels. The left-sub panel is the regression of the backscattering coefficient (HH) vs SMOS soil moisture. Right sub-panel is the time series of soil moisture estimated using SCATSAT-1 σ^0 (HH) and SMOS measured soil moisture [Mishra et al., 2021].

Future Projections

- Development of UHF wind profiler (Progressing through RDA-ISTRAC)
- Studies on lunar regolith thermal characteristics using ChaSTE/Chandrayaan-3 lander.
- Characterization of boundary layer over distinct geographical zones.
- Genesis and radiative forcing of deep convective clouds using Megha-Tropiques SAPHIR and ScaRaB data.
- Three-dimensional distribution and variations in tropical clouds and precipitation and their impact on atmospheric energetics
- Estimation of soil moisture from spaceborne microwave observations

Publications in Peer-Reviewed Journals:

1. Gupta, Ashok Kumar, K. Rajeev, Edwin V Davis, Manoj Kumar Mishra, Anish Kumar M Nair, "Direct observations of the multi-year seasonal mean diurnal variations of TOA cloud radiative forcing over tropics using Megha-Tropiques-ScaRaB/3", *Climate Dynamics*, 55(11), 3289-3306, <https://doi.org/10.1007/s00382-020-05441-w>, 2020.
2. Samuel, Sisma, Nizy Mathew, Manoj Kumar Mishra and R. Renju, "Spatial and temporal variability of deep convective clouds over the tropics using multi-year Megha - Tropiques - Sondeur Atmosphérique du Profil d'Humidité Intertropicale par Radiométrie (SAPHIR) observations", *International Journal of Remote Sensing*, 42:13, 5176-5193, <https://doi.org/10.1080/01431161.2021.1910368>, 2021.
3. Renju, R., C. Suresh Raju, Manoj Kumar Mishra, N. V. P. Kiran Kumar, Nizy Mathew, "Attenuation characteristics of GSAT-14/Ka-band signals over the tropical coastal region", *IEEE transactions on Antennas and Propagation*, <https://doi.org/10.1109/TAP.2021.3076506>, 2021.
4. Mishra, Manoj Kumar, Nizy Mathew, R Renju, "SCATSAT-1 backscattering coefficient over distinct land surfaces and its dependence on soil moisture and vegetation dynamics", *International Journal of Remote Sensing*, 42:17, 6481-6501, <https://doi.org/10.1080/01431161.2021.1939909>, 2021.

depth. The payload is basically a thermal probe, which will be inserted into the lunar regolith in a controlled manner based on the tele-commands from the Earth station. The payload consists of three major modules i.e. thermal probe, electronic module and deployment mechanism. The cylindrical shaped thermal probe is made of composite with sharp Ti-alloy nose-tip to facilitate the insertion. The probe is embedded with 10 Pt-1000 PRT sensors and 1 foil heater. The electronic module will do the signal conditioning and data acquisition, telemetry and control. The deployment mechanism is driven by a BLDC motor to insert the probe into the lunar regolith. The flight model of ChaSTE is under development.

Ongoing Activities

The dependence of the convective atmospheric boundary layer (CABL) height on the coupled variations of the shortwave radiative flux, near-surface air temperature (T_{air}), soil skin temperature, soil moisture content, lower tropospheric thermal structure, and virtual potential temperature lapse rate (VPLR) during onshore and offshore-flows are investigated based on multi-year (2012-2017) observations carried out using a microwave radiometer profiler and in situ probes at Thumba (8.5°N, 77°E). The maximum CABL height increases linearly with the VPLR at the rate of 140 to 200 m per °C km⁻¹ (correlation coefficient of 0.82 to 0.92) during different seasons. When offshore-flow prevails, the CABL develops like the continental CABL, with a peak CABL height greater than that during onshore-flow by about 300 m.

5. Lavanya S., Kiran Kumar NVP, “Classification of tropical coastal precipitating cloud systems using disdrometer observations over Thumba, India”, *Atmospheric Research*, 253, 2021. <https://doi.org/10.1016/j.atmosres.2021.105477>, 2021.
6. Sivakumar Reddy N, N.V.P. KiranKumar, K. Rama Gopal, G. Balakrishnaiah, and K. Rajaobul Reddy, “Characteristics of atmospheric surface layer during winter season over Anantapur (14.62° N, 77.65° E), a semi-arid location in peninsular India”, *Journal of Atmospheric and Solar-Terrestrial Physics*, 216, <https://doi.org/10.1016/j.jastp.2021.105554>, 2021.
7. Barman, Nilamoni, Arup Borgohain, Shyam S. Kundu, N. V. P. Kiran Kumar, “Seasonal variation of mountain-valley wind circulation and surface layer parameters over the mountainous terrain of the north-eastern region of India”, *Theoretical and Applied Climatology*, <https://doi.org/10.1007/s00704-020-03491-y>, 2021.
8. Chakravarty, Kaustav, S. Khandare, N.V.P. Kiran Kumar, A. Maitra, “Unravelling the features of precipitation microphysics over two tropical stations of India that experiences different characteristics of Indian summer monsoon”, *Journal of Atmospheric and Solar Terrestrial Physics*, <https://doi.org/10.1016/j.jastp.2021.105710>, 2021.
9. Singh, Jaydeep, Narendra Singh, Narendra Ojha, Amit Sharma, Andrea Pozzer, N.V.P. Kiran Kumar, K. Rajeev, S.S. Gunthe, V. Rao Kotamarthi, “Effects of spatial resolution on WRF v3.8.1 simulated meteorology over the central Himalaya”, *Geoscientific-Model-Development*, 14, 1427-1443, <https://doi.org/10.5194/gmd-14-1427-2021>, 2021.
10. Reddy, T. Lokeswara, Balakrishnaiah G, Raja Obul Reddy K, Siva Kumar Reddy N, Chakradhar Rao T, Rama Gopal K and Bhavyasree A, “Perturbations of atmospheric surface layer characteristics during the annular solar eclipse on 26 December 2019 over a semi-arid region Anantapur in southern India”, *Journal of Atmospheric and Solar-Terrestrial Physics*, 211, 105467, <https://doi.org/10.1016/j.jastp.2020.105467>, 2020.

Presentations in Symposia/Workshop

1. Nizy Mathew and Sisma Samuel, ‘Temporal Variation of Deep Convective Clouds over the Tropics’, COSPAR-2021 (Hybrid Symposium), Sydney, Australia, 28 January - 4 February, 2021,.
2. Sisma Samuel and Nizy Mathew, ‘Seasonal Variation of Deep Convective Clouds over the Tropics using SAPHIR/Megha-Tropiques Observations’, 33rd Kerala Science Congress, 25-30 January, 2021.
3. R. Renju, Nizy Mathew and C. Suresh Raju, ‘Millimeter/Sub-millimeter Wave Radiometry for studying Planetary Atmospheres’, 33rd Kerala Science Congress (KSC) January 25-30, 2021.
4. Nizy Mathew and Sisma Samuel, ‘Deep Convective Cloud Cores: Radiative Flux, Upper Tropospheric Humidity and Latent Heat’, TROMET-2020, National Symposium on Weather and Climate Services over Mountainous Regions, Shillong, Meghalaya, 14-17 December, 2020.
5. Sisma Samuel and Nizy Mathew, ‘Spatial and Interannual Variability of Deep Convective Clouds over the Tropics using Multi-year Megha-Tropiques-SAPHIR Observations’, TROMET-2020, National Symposium on Weather and Climate Services over Mountainous Regions, Umiam, Shillong, Meghalaya, 14-17 December, 2020.

Invited Lectures

K. Rajeev

1. “Atmospheric Boundary Layers at Distinct Environments”, TROMET-2020, Umiam, Shillong, 14-17 December, 2020.
2. “Tropical Clouds”, Indian Institute of Space Science and Technology, 15 January 2021
3. “Understanding Tropical Clouds”, Recent Advances in Atmospheric Sciences, National Centre for Earth Science Studies (NCESS), Trivandrum, 30 April 2021.

Public Outreach

K. Rajeev

1. “Aerosols, Clouds, Ozone and Climate Change”, Sri Sathya Sai College of Arts & Science, Trivandrum, 16 September, 2020
2. “Earth’s Environment and Its Diagnosis from Space”, UL Space Club Webinar, 03 October 2020.
3. “Possibilities and Applications of Remote Sensing”, Samoohyapaddam (Malayalam), Doordarshan, 09 October 2020
4. “Atmospheric and Space Research - Science & Societal Benefits”, IEEE Computer Science Society, College of Engineering, Barton Hill, 26 October 2020
5. “Atmospheric and Space Science”, India International Science Festival (IISF) Pre-Event Lecture, Vikram Sarabhai Space Centre (through VSSC YouTube Channel), 12 December 2020.

ऐरोसॉल, ट्रेस गैस तथा रेडिएटिव फोर्सिंग AEROSOLS TRACE GASES AND RADIATIVE FORCING



एसपीएल की ऐरोसॉल ट्रेस गैस एवं रेडिएटिव फोर्सिंग (एटीआरएफ) शाखा ऐरोसॉलों और ट्रेस गैसों के भौतिक/रासायनिक गुणधर्मों के वैज्ञानिक समझ को लक्ष्य करती है, जिनमें वे प्रक्रियाएं शामिल हैं जो त्रिविमीय वायुमंडलीय वितरण एवं विकिरण से अन्योन्यक्रिया है जिसके कारण जलवायु में परिवर्तन हो जाते हैं। इस शाखा के मुख्य लक्ष्य हैं (i) अंतरिक्ष-वाहित तथा भू-आधारित प्रेक्षणों को मिलाते हुए भारतीय उपमहाद्वीप, साथ में लगे हुए महासागरों एवं हिमालयी व घुव्रीय पर्यावरणों के ऊपर दिगीय और सामयिक रूप से निश्चित ऐरोसॉल व ट्रेस गैस डेटाबेस का विकास, (ii) ऐरोसॉलों व ट्रेस गैसों के जलवायु प्रभाव के लिए प्रासंगिक विशेष समस्याओं का हल निकालते हुए विषयगत बहु-मंचीय (जहाज़, वायुयान व उच्च तुंगता गुब्बारा) क्षेत्रीय प्रयोगों का आयोजन, (iii) संभाव्य जलवायु प्रभाव के निर्धारण हेतु क्षेत्रीय जलवायु नमूनों के साथ ऐरोसॉल व ट्रेस गैस आंकड़ों को आत्मसात करना।

Aerosols Trace gases and Radiative Forcing (ATRF) Branch of SPL aims at scientific understanding of the physical/chemical properties of aerosols and trace gases, involving processes that control their three-dimensional atmospheric distribution and interaction with radiation leading to climate changes. The primary objectives are (i) development of spatially and temporally resolved aerosol and trace gas database over the Indian subcontinent, adjoining oceans as well as the Himalayan and Polar environments by combining the space borne and ground-based observations, (ii) conducting thematic multi-platform (ship, aircraft, and high altitude balloon) field experiments addressing specific problems pertinent to the climate impact of aerosols and trace gases, (iii) assimilation of the aerosol and trace gas data with regional climate models for the assessment of potential climate impact.

वैज्ञानिक टीम / Science Team

सुरेश बाबू एस / Suresh Babu S.
विजयकुमार एस नायर / Vijayakumar S. Nair
प्रशांत हेग्डे / Prashant Hegde
मुकुन्दा एम गोगोई / Mukunda M. Gogoi
शोभन कुमार कौपल्ली / Sobhan Kumar Kompalli
गिराच इम्रान असतार / Girach Imran Asatar
रेवती एस अजयकुमार / Revathy S. Ajayakumar

तकनीकी टीम / Technical Team

अजीषकुमार पी एस / Ajeeshkumar P. S.
संतोष केआर पाण्डे / Santosh K.R. Pandey

अनुसंधान सहयोगी और एनपीडीएफ / Research Associates & NPDRF

सुरेश कुमार रेड्डी बी / Suresh Kumar Reddy B.
अश्वनी ए आर / Aswini A. R.
सुबिन जोस / Subin Jose
सौम्याज्योती जाना / Soumyajyoti Jana*
लक्ष्मी एन बी / Lakshmi N. B.#

अनुसंधान अध्येता / Research Fellows

अजित टी सी / Ajith T. C.
अरुण बी एस / Arun B. S.
उषा के एच / Usha K. H.

*Joined in January 2021

Relieved in February 2021

Satellite Remote Sensing of Aerosols and its Radiative Effects

Aerosol Indirect Effect over the Northern Indian Ocean from Multi-Satellite Observations

Atmospheric aerosols play an important role in the formation of warm clouds by acting as efficient cloud condensation nuclei (CCN) and their interactions are believed to cool the Earth-Atmosphere system in a highly uncertain manner compared to the other forcing agents. In case of warm clouds having a fixed liquid water path, an increase in aerosol concentrations leads to a decrease in cloud effective radius (CER) and an enhancement in cloud albedo, known as “first indirect effect” or “Twomey effect”. Theoretical and observational studies revealed that aerosol-induced changes in macro and microphysical properties of warm clouds are determined by the competition between moistening of cloud layers by precipitation suppression and drying by enhanced entrainment of overlying air. Cloud brightening is prominent if the overlying air is moist and a reverse effect can occur in case of mixing with dry free tropospheric air.

Aerosol Cloud Interaction (ACI) on marine warm clouds for different cloud liquid water paths over south-eastern

Arabian Sea (SA1) and northern Bay of Bengal (SA2) is estimated and depicted in Fig. 1. The mean spatial distribution of long-term (2003-2017) aerosol optical depth at 550 nm (AOD_{550}) retrieved from Aqua-MODIS satellite indicates high aerosol loading ($AOD > 0.3$) over the continental outflow regions of northern Indian Ocean during winter months. Anthropogenic sources contribute ~60-70% to this high aerosol loading. The long-term satellite-based trend in AOD_{550} showed a significant increase (~ 2.2 - 2.3% year⁻¹) over the northern Indian Ocean.

Decrease in CER with aerosol loading (Twomey effect) is observed for clouds with liquid water path greater than 75 g m^{-2} (hereafter high LWP regime); while a statistically significant increase in CER with the increase in aerosol loading (anti-Twomey effect) is found for clouds having low LWP ($LWP < 75 \text{ g m}^{-2}$). Thus, it is demonstrated that the enhanced aerosol loading (due to anthropogenic emissions) can reverse the first indirect effect significantly.

In contrast to Twomey effect, a statistically significant increase in CER is observed with respect to an increase in aerosol loading for clouds having low liquid water path ($LWP < 75 \text{ g m}^{-2}$) and drier cloud tops. Probable physical mechanisms for this effect are the intense competition for available water vapour due to higher concentrations

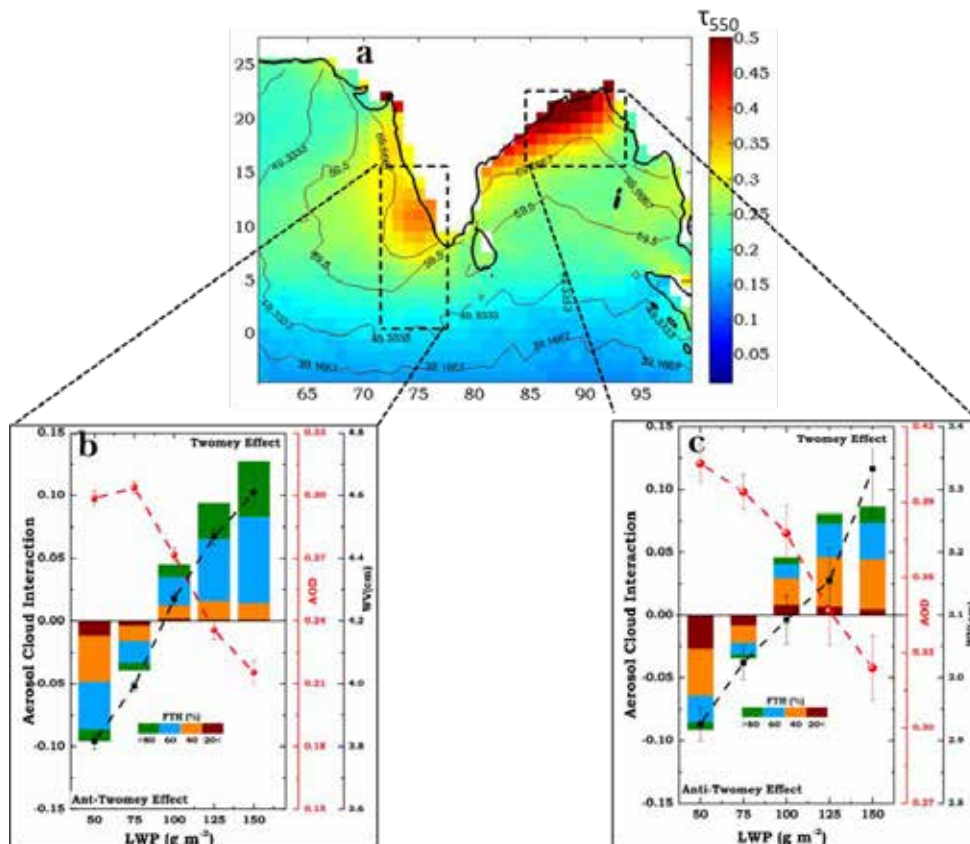


Figure 1: (a) Long-term (2003-2017) aerosol loading (AOD_{550}) over South Asia derived from MODIS sensor onboard Aqua satellite. Contour indicates the anthropogenic fraction to total $AOD(\%)$. Rectangular boxes represent the study area SA1 and SA2 respectively. (b and c) Aerosol cloud interaction over SA1 and SA2 respectively for different cloud liquid water path (LWP) bins. Red and black curves represent AOD_{550} and precipitable water vapour (PWV, cm) corresponding to respective cloud LWP bin used in the estimation of ACI. Colorbars represent the percentage occurrence of free tropospheric humidity (FTH) at 700 hPa [Jose et al., Sci. Rep 2020].

of anthropogenic aerosols and entrainment of dry air on cloud tops. For such clouds, cloud water content showed a negative response to cloud droplet number concentrations and the estimated intrinsic radiative effect suggest a warming effect. Although uncertainties exist in quantifying ACI using satellite observations, present study indicates the physical existence of anti-Twomey effect over the northern Indian Ocean during south Asian outflow.

Assessment of the Vertical Distribution of Speciated Aerosol Absorption using Space-borne LIDAR

Absorbing aerosols (dust and carbonaceous aerosols) diabatically warm the atmosphere by absorbing the solar radiation and cool the surface by reducing the surface reaching radiation. The warming effect of aerosols has a strong dependence on their vertical distribution. Vertically resolved, species-wise characterization of aerosols is essential for the validation of models and better estimation of aerosol radiative effects. Direct measurements of species resolved vertical profiles of absorbing aerosols are very limited over the Indian region.

The vertical distribution of the species-wise shortwave radiative effects of absorbing aerosols (dust and carbonaceous aerosols) over the Indian landmass were carried out for the first time using a synergy of space-borne and ground-based observations. Vertical profiles of dust and total aerosols are estimated using the multi-year (2006–2017) observations from CALIOP (Cloud Aerosol Lidar with Orthogonal Polarization) over the Indian region.

Aerosols are mostly confined within the boundary layer during the winter (December–February) season, and they extend vertically up to 6 km altitude during the pre-monsoon (March–May) season with a reduction in aerosol loading within the planetary boundary layer, while AOD remains comparable during both the seasons. It is attributed to high convective activities prevailing during the pre-monsoon season, which transport aerosols to higher altitudes causing a depletion of aerosols within the boundary layer. Pre-monsoon enhancement in aerosol loading over the Indian region is significantly contributed (~56%) by the transported mineral dust at free tropospheric altitudes. Based on the analysis of the depolarization ratio, it is observed that natural dust dominates dust loading during pre-monsoon, while dust loading during the winter season is mostly contributed by anthropogenic dust sources.

The present study assumes that the total aerosol absorption is purely constituted by mineral dust and carbonaceous aerosols and estimates the absorption optical depth of carbonaceous aerosols as the residual of total absorption optical depth measured using the ground-based radiometer and dust absorption optical depth estimated from CALIPSO measurements. The optical depth of the carbonaceous aerosols shows enhancement during winter and pre-monsoon seasons and decrease during the

summer monsoon season (June–September). Over the Indo Gangetic Plain (IGP), though black carbon at surface shows a significant decrease (60%) from winter to pre-monsoon, average optical depth of carbonaceous aerosols remains almost invariant (~9% enhancement from winter to pre-monsoon season) indicating the presence of elevated layers of carbonaceous aerosols over the IGP.

Radiative effects of mineral dust aerosol are estimated based on the satellite observations of dust optical depth and aircraft-based measurements of single scattering albedo carried out during the Regional Aerosol Warming Experiment (RAWEX). Though, shortwave radiative absorption due to dust in the atmosphere increases about three times from winter to pre-monsoon, dust causes cooling at the top of the atmosphere. Vertical profile of heating rate due to total aerosols is estimated over the study region by coupling ground-based columnar observations of AOD with space-borne observations of aerosol vertical distribution. The heating rate due to carbonaceous aerosols is obtained as a residual of aerosol heating rate and dust heating rate. Aerosol induced heating rate is high over the IGP during winter ($\sim 2 \text{ K day}^{-1}$), and $\sim 85\%$ of this heating is caused by carbonaceous aerosols (Fig. 2). Carbonaceous aerosols produce anomalous heating in the free troposphere over the eastern region at a rate of $\sim 1 \text{ K day}^{-1}$ within 0.5 km to 3.5 km altitude during pre-monsoon season. High aerosol-induced heating rates are observed within the planetary boundary layer which can affect boundary layer dynamics and convection over the study region. Enhanced aerosol heating at higher altitudes during pre-monsoon months over the Indian region is important. It can alter the meridional temperature and pressure gradients over south Asia and modify monsoon onset and associated rainfall.

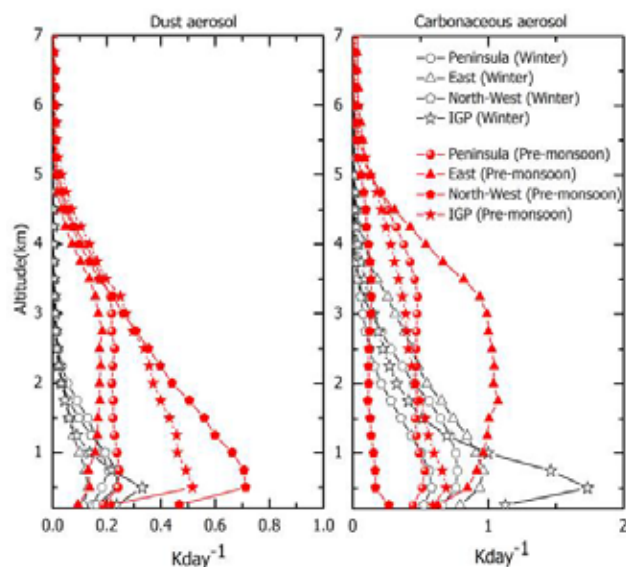


Figure 2: Vertical profile of heating rate due to dust and carbonaceous aerosols over Indo Gangetic Plain, Peninsular India, East India and North-west India during winter (black curves with open symbols) and pre-monsoon (red curves with solid symbols) [Lakshmi et al., *Remote Sens. Environ.*, 2020].

Modelling Studies on Aerosol-Climate Interactions

Effect of Aerosol-Induced Snow Darkening on the Direct Radiative Effect of Aerosols over the Himalayas

Deposition of absorbing aerosols like dust and black carbon (BC) decreases the snow albedo (snow darkening or SAE) and thereby traps more solar energy within snowpack over the Himalayas. This forcing mechanism plays a major role in the radiative forcing, regional temperature, snow runoff and hydrological cycle over the Himalayan–Tibetan region. The seasonal snow and glacier melt support major rivers of Asia, which are the source of fresh water for the diverse ecosystem and billions of people inhabited in this region. In contrast, the direct interaction of atmospheric aerosols with radiation through scattering and absorption (aerosol direct effect or DRE) leads to surface cooling and atmospheric warming, which enhances the snow over the region. Since the magnitude and sign of DRE depend on the surface albedo, the effect of SAE on DRE was investigated using a regional climate model coupled with the community land model having snow, ice and aerosol radiation module.

Western Himalayas experiences a large reduction in the snow albedo (0.037) despite having lower BC mass concentration compared to central (0.014) and eastern (0.005) Himalayas. This implies that snow albedo reduction not only depends on the amount of aerosols deposited but also on the snow microphysics and snow thickness. The inclusion of aerosol-induced snow darkening in to the model reduces its bias with respect to the satellite derived surface albedo by 59%, 53% and 35% over western, central and eastern Himalayas, respectively, during the spring season. It is interesting to note that, the model

simulations are closer to the observations only when the SAE is included, which confirms that the inclusion of the aerosol-induced snow darkening in the climate models is very crucial for the proper representation of the radiation balance over the Himalayas.

The implications of aerosols-induced snow-darkening on the DRE of aerosols over the Himalayan-Tibetan region is estimated using simulation with and without SAE. The forcing due to aerosols at TOA is overestimated by 3.8, 2.4 and 1 Wm⁻² over western, central and eastern Himalayas, respectively, when SAE is not considered (Fig. 3). Hence, the aerosol-induced decrease in snow albedo causes an early reversal in the sign of aerosol DRE at the top of the atmosphere from warming to cooling over the western and central Himalayas, which can have implications in the radiation balance and water security over the region. This SAE induced increase in surface cooling due to DRE partly compensate for the warming of the SAE. The western and central Himalayas are more vulnerable to SAE, whereas the eastern Himalayas is mostly dominated by the DRE of aerosols.

Amplification of South Asian Haze by Water Vapour–Aerosol Interactions

South Asia experiences severe air pollution events during the winter season. Air pollution and winter time fog over South Asia is a major concern due to its significant implications for air quality, visibility and health. Using a regional climate model coupled with chemistry, the contribution of the hygroscopic growth of aerosols (ambient-dry) to the total aerosol optical depth and its feedbacks on the regional meteorology, visibility and low-air-quality conditions over the region was investigated.

The aerosol hygroscopic growth can contribute up to 40% of the total AOD (Fig. 4) and that feedback processes

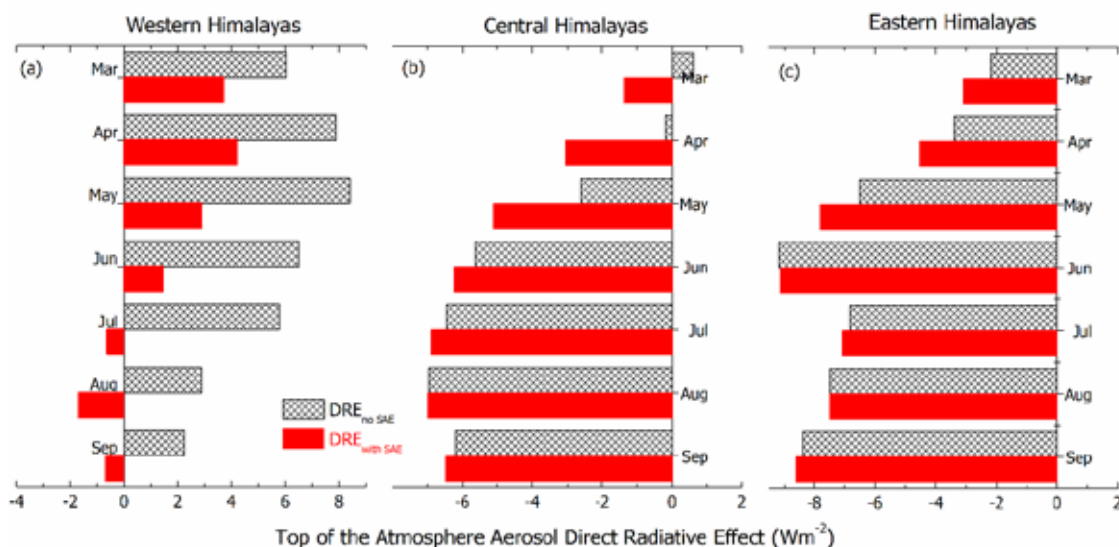


Figure 3: Aerosol direct radiative effects (DRE) at the top of the atmosphere estimated with and without aerosol snow albedo effect (SAE) ($DRE_{with SAE}$ and $DRE_{no SAE}$) for (a) western (b) central and (c) eastern Himalayas [Usha et al., Environ. Res. Lett., 2021].

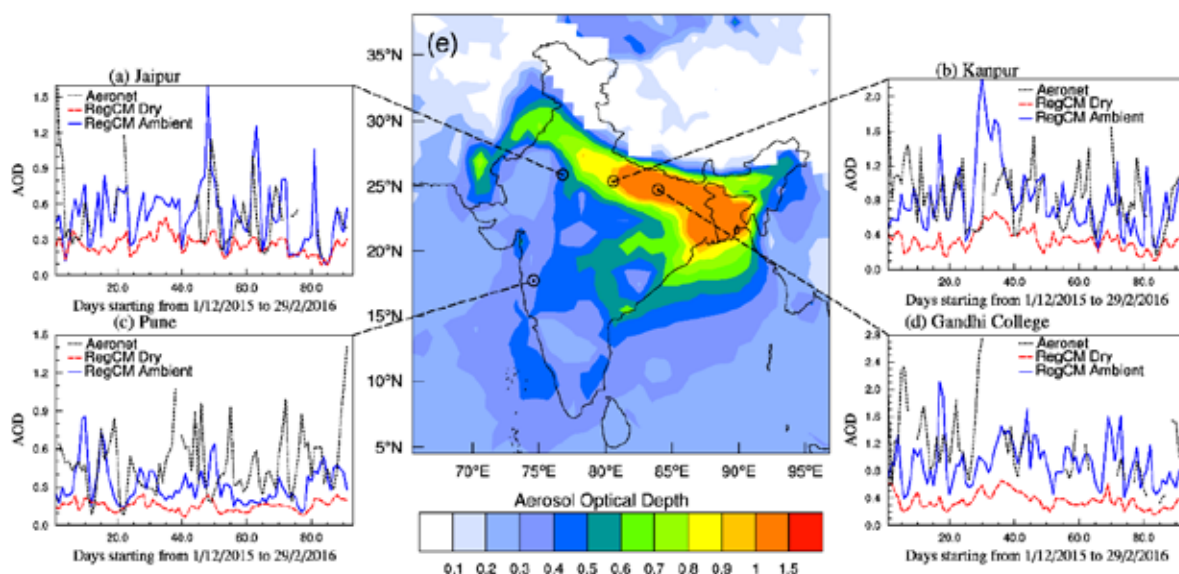


Figure 4: Wintertime AOD measured using AERONET radiometers and simulated with RegCM4 for ambient and dry humidity conditions with meteorological feedback at (a) Jaipur, (b) Kanpur, (c) Pune and (d) Gandhi College. Stations (b) and (d) are located in the IGP, while (a) and (c) are located outside the IGP. (e) Spatial distribution of satellite-retrieved (MODIS) aerosol optical depth at 550 nm [Nair et al., Atmos. Chem. Phys. 2020].

significantly increase near-surface relative humidity and decrease lower-free-troposphere humidity. This positive feedback mechanism along with aerosol-boundary layer interactions plays an important role in the confinement of pollutants within in the boundary layer and prevalence of wintertime fog and poor air quality conditions over South Asia. The moisture content in the atmosphere increases the AOD directly by its hygroscopic effect and indirectly through its radiative and meteorological feedbacks. The inclusion of the meteorological feedback due to the hygroscopic growth of aerosols produces an increase in AOD along the IGP, especially over the central IGP regions. The aerosol-boundary layer interactions lead to moistening of the boundary layer and drying of the free troposphere, which amplifies the long-term trend in relative humidity over the IGP during winter.

This study clearly demonstrates that the aerosol-moisture interaction is the most significant contributor favouring and strengthening the high-aerosol conditions (poor air quality) prevailing over the IGP during winter, which needs to be considered for planning mitigation strategies.

Microphysical and Morphological Characteristics of Aerosols

Mixing State of Refractory Black Carbon Aerosol in the South Asian Outflow over the Northern Indian Ocean during Winter

Regional climatic implications of aerosol black carbon (BC) are well recognized over South Asia, which has a wide variety of anthropogenic sources. Significant uncertainties remain in its quantification due to lack of sufficient information on the microphysical properties (its

concentration, size, and mixing state with other aerosol/gaseous components during its ‘aging’), which determine the absorption potential of BC. In this regard, first-ever observations of the size distribution and mixing state of individual refractory black carbon particles in the South Asian outflow to South-eastern Arabian Sea (SEAS), northern (NIO) and equatorial Indian Ocean (EIO) regions were carried out using a single particle soot photometer (SP2) on-board the ship cruise of the Integrated Campaign for Aerosols, gases, and Radiation Budget (ICARB-2018) during winter-2018 (16 January to 13 February).

The spatial variation of BC mass concentrations (Fig.5a) showed high values over the SEAS (mean $\sim 938 \pm 293$ ng m^{-3}), which received direct outflow from the western coast/peninsular India. The concentrations decreased gradually away from the land towards the eastern leg of NIO (NIO-E). The lowest concentrations (4-5-fold lower than the SEAS) were seen over the EIO due to cleaner oceanic air masses. As the outflow changed to continental, the concentrations increased again over the western leg of the NIO (NIO-W). Despite widely varying BC mass concentrations, the mass median diameters (Fig.5b) were in a narrow range (0.18-0.21 μm) in all the regions. The MMD values indicated BC from a combination of sources and aged (temporally and/or chemically) continental outflow. Importantly, the South Asian outflow to the adjacent oceans is characterized by thickly coated BC particles (Fig.5c), highlighting the physicochemical changes in the BC characteristics during its atmospheric aging. The BC particles over the SEAS depicted the highest coating (ACT ~ 109 nm) due to strength of substantial condensable vapours. The ACT values showed an east-west contrast over the northern Indian Ocean with higher coatings over NIO-E (ACT ~ 104

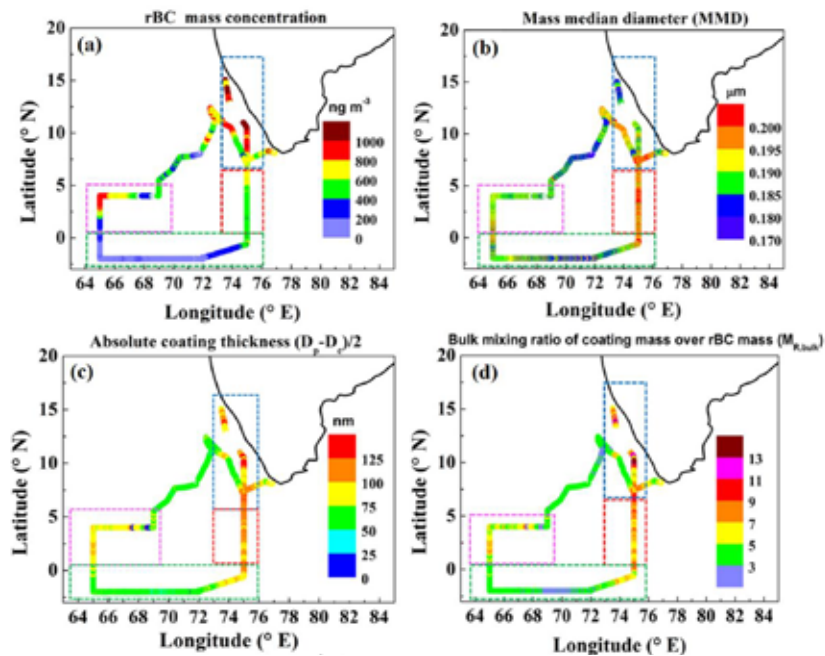


Figure 5: Spatial distribution of (a) refractory black carbon (rBC) mass concentration, (b) mass median diameter (MMD) of rBC core size distributions (c) absolute coating thickness and (d) bulk mixing ratio of coating mass to rBC mass ($M_{R,bulk}$) during the ICARB-2018. Rectangles with dashed borders highlight different sub-regions [Kompalli et al., Atmos. Chem. Phys., 2021].

nm) than the NIO-W (ACT~86 nm). Further, high values (2.5-15) of the bulk mixing ratio of coating mass to BC mass were noticed in the outflow reflecting the thick coatings on BC (Fig.5d).

Concurrent measurements of sub-micron (NR-PM1.0) aerosol chemical composition was used to identify the possible coating material. The association between ACT and mass concentrations of organics and sulfate aerosols for low (< 50 % of MMD) ACT values revealed that sulfate tend to be the dominant coating material.

New Particle Formation Events over the Northern Indian Ocean during the South Asian Outflow

Nucleation mode (size <25 nm) particles form through gas to particle conversion and subsequent growth of these particles to larger sizes can potentially influence aerosol climate forcing. The information of particle number size distributions (PNSDs) and new particle formation (NPF) over pristine marine regions are limited due to observational constraints. In this regard, the characteristics

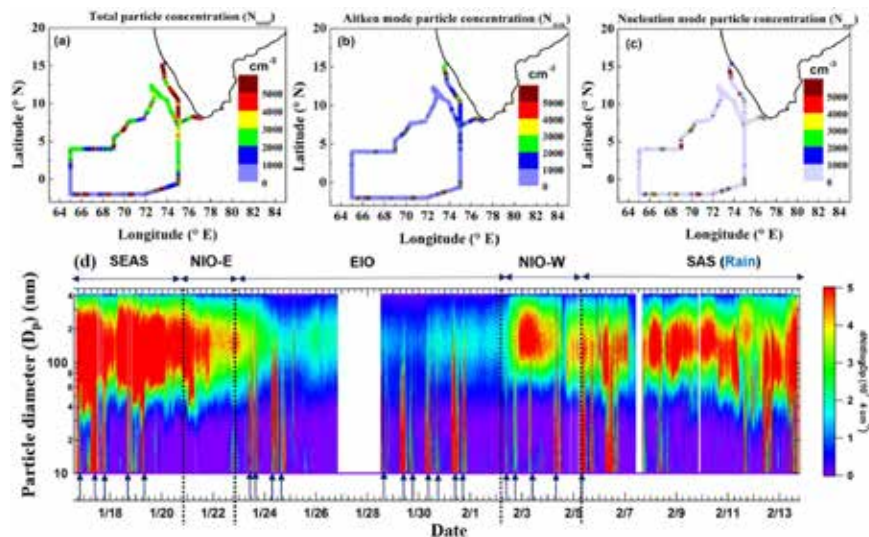


Figure 6: (a-c) Spatial distribution of total (N_{total}), Aitken (N_{Aitk}), and nucleation (N_{nuc}) mode particle number concentrations; (d) Time series of particle number size distributions ($dN/dlnD_p$) (color scale) during the ICARB-2018; the NPF events with a large influx of nucleation mode particles are identified with arrow symbols. Black vertical lines delineate different regions covered [Kompalli et al., Atmos. Environ. 2020].

of ultrafine and fine particle concentrations (10-414 nm) over the South-eastern Arabian Sea, northern and equatorial Indian Ocean during winter, when these regions experienced continental outflow, were explored as a part of the ICARB-2018.

As seen in Fig.6a-c, the total (N_{total}) and ultrafine particle (N_{UFP} , $D_p < 100$ nm) number concentrations were highest (>5000 cm^{-3}) over the SEAS, which is proximate to the west coast of India. The values gradually dropped away from the continent to reach the lowest values (<1000 cm^{-3}) over the EIO (where marine air masses were predominant), but recovered again over the NIO-W (Northern Indian Ocean – west). The concentrations of Aitken (N_{Aitk}) and nucleation (N_{nuc}) mode particles also followed a similar pattern. (Figs.6b and 6c). Temporal variation of particle number size distributions (Fig.6d) reflected the NPF events with enhanced particle concentrations. NPF occurred more frequently (30% of the observations) over the remote oceanic EIO, but more intensely over the regions in the continental proximity, thus demonstrating the varying precursor vapor source strengths.

To investigate the NPF pathways, concurrent measurements of particle concentrations, submicron aerosol chemical composition and meteorological variables (dew point temperatures $-T_d$) were examined in Fig.7, which confirms that the nucleation events possibly occurred due to the entrainment of the FT air masses to the marine atmospheric boundary layer (MABL). Such mixing of contrasting air masses caused a dilution of condensation sink as well as altered thermodynamic variables in the vertical column to provide conducive conditions for NPF. Temporal evolution of mass loadings of sulfate and organics suggested possible

multi-component nucleation involving volatile organic products, and/or particle growth due to the uptake of organic vapours by newly formed particles. To identify the nature of organics, the relative association between fractional signals at $m/z44$ (i.e., CO_2^+ , which indicates secondary organics formed due to photochemistry or oxidation reactions in the atmosphere, mainly the carboxylic acids) and $m/z 43$ (comes from both oxygenated organics and saturated hydrocarbon compounds) were used. The variation of relative intensities f_{44} and f_{43} suggested that the organics were likely semi and low volatile oxygenated organic aerosols, predominantly anthropogenic origin, over the SEAS. Further, over the EIO, apart from f_{44} and f_{43} , spatial variation of organics f_{79} and sulfate f_{81} signals (which are indicators for marine biogenic organics) were used to identify possible sources. This analysis, and air mass back trajectories, confirmed that organics emanated from marine biogeochemistry contributed to nucleation events over the EIO.

Vertical Distributions of Aerosol Morphology and Elemental Composition over India

Particle morphology and elemental compositions are important parameters for the accurate estimation of optical properties of aerosols and are poorly characterised due to sparse in-situ measurements and are poorly characterised worldwide due to technical challenges. Present study classifies and quantifies the vertical distributions of the morphological characteristics and elemental composition of aerosols based on single particle as well as bulk chemical analysis over seven geographically diverse regions of northern and central parts of India during spring, carried out as a part of

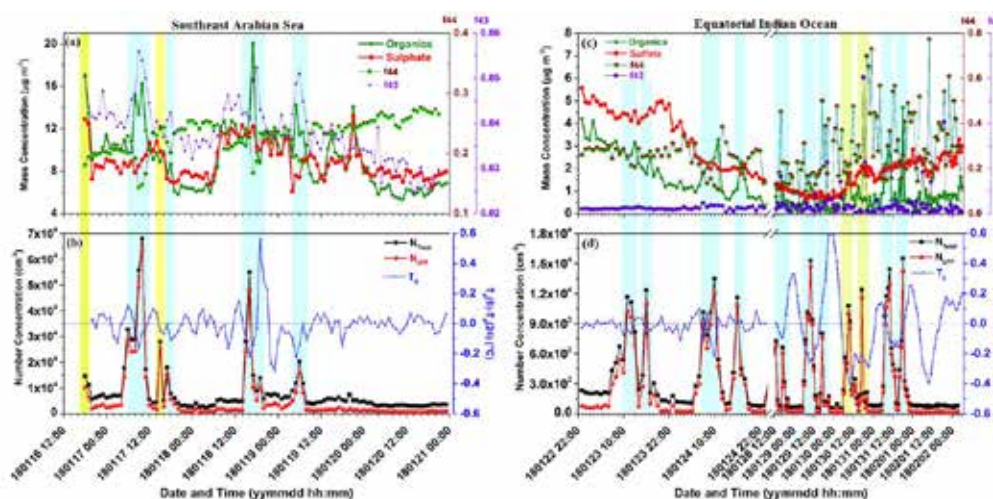


Figure 7: Temporal variation of the hourly mean (a) mass concentrations of organics and sulfate ($\mu g m^{-3}$); fractions f_{44} , f_{43} (i.e., the ratio between the mass-to-charge ratios (m/z) 44/43 and the total organics signal in the component mass spectrum) (right axis), (b) particle number concentrations of total (N_{total}), UFP (N_{UFP}) (cm^{-3}) along with $T_d(6)-T_d(24)$ (the difference between the 6-hour and 24-hour running means of dew point temperatures in $^{\circ}C$) over the SEAS region while c-d show the same for EIO region during the ICARB-2018. Cyan shaded portions indicate the periods of NPF events with an enhancement in the organics mass loading. Yellow shaded portion to highlight the events with a notable increase in the mass concentration of sulfate, with or without an increase in organics [Kompalli et al., Atmos. Environ. 2020].

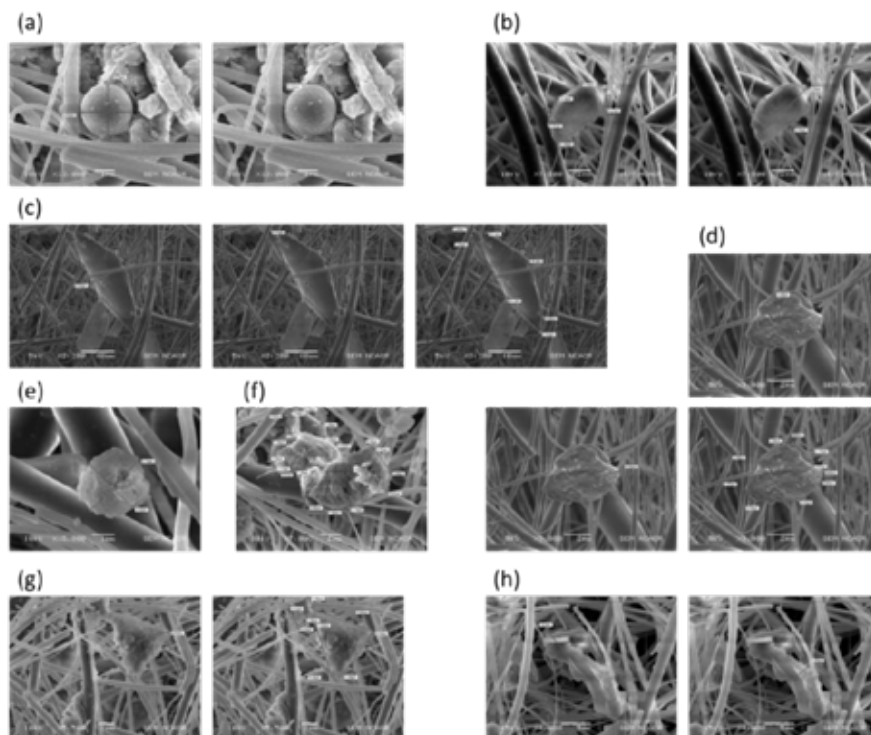


Figure 8: Typical morphological structures of aerosol particles seen over the Indian region during spring-2013, which include (a) spherical smooth, (b) irregular smooth, (c) rectangular smooth, (d) irregular rough, (e) spherical rough, (f) granular chain like, (g) triangular rough, and (h) irregular aggregated. The shape parameters, such as length, thickness and perimeter of the particles are also shown [Gogoi et al., *J. Atmos. Chem.* 2020].

Regional Aerosol Warming Experiment (RAWEX). Significant regional distinctiveness in shapes (non-sphericity), sizes and elemental compositions of the airborne particles were conspicuous over the north Indian sites (Fig. 8). Irregular rough (IR) particles are found to dominate over all the sites irrespective of the sampling height, while that of highly irregular granular aggregates formed the second most abundant shape over the north Indian sites (Fig. 9). The non-spherical coarse mode particles dominated the lower free tropospheric regions (>2 km) of the Indo-Gangetic Plains (IGP). These particles could be responsible for enhanced spring time aerosol absorption in the elevated region of the atmosphere.

Elemental compositions of the single particle analysis indicate that the free tropospheric layer over the IGP and central India is enriched with Na and Ca compounds mixed with Fe or Al (soil particles), indicating long-range transport of crustal aerosols. This finding is very well supported by the bulk particle analysis indicating abundance of Ca^{2+} in the free troposphere with low contribution of sea-salt Na^+ . Particles with irregular rough surfaces having dominance of SiO_2 were observed over all the study sites. The percentage share of spherical particles to the total number of particles having various morphological properties was found to be highly subdued. The present study thus critically assesses the relevant knowledge pertaining to the morphological features of aerosols over the IGP during spring for the accurate estimation of aerosol radiative properties.

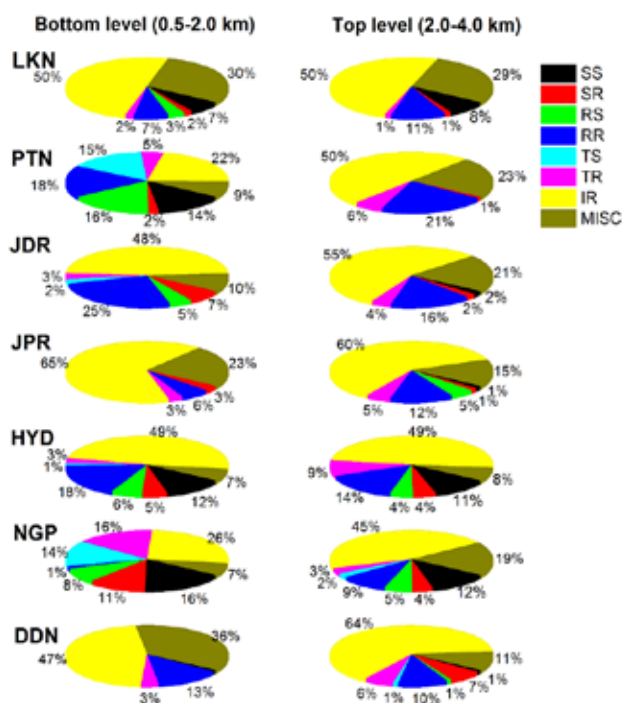


Figure 9: Vertical distribution of the morphological structures of particles at two distinct altitudes of the atmosphere at different geographic locations of India (Lucknow (LKN) and Patna (PTN) in the IGP, Jodhpur (JDR) and Jaipur (JPR) in the western part of India, Dehradun (DDN) in the foothill region of Himalayas and Nagpur (NGP) and Hyderabad (HYD) in the central and peninsular India) during spring-2013 [Gogoi et al., *J. Atmos. Chem.* 2020].

Aerosol Chemistry

Size-Resolved Chemical Characteristics of Coastal Urban Aerosols from West Coast of India

Knowledge of size-resolved chemical composition of aerosols is important in modelling the climate and environmental effects of aerosols. The present study reports major water-soluble ionic species (MS^- , Cl^- , SO_4^{2-} , NO_3^- , PO_4^{3-} , $\text{C}_2\text{O}_4^{2-}$, Na^+ , NH_4^+ , K^+ , Ca^{2+} , and Mg^{2+}), carbonaceous species, water-soluble organic carbon and water-soluble total nitrogen (WSOC and WSTN) in size-resolved aerosols collected under different polluted air masses over a coastal urban location (Cochin, 10.05°N, 76.33°E) of tropical India. Aerosol samples were collected on quartz filters using a multi-stage (i.e., with 5 size bins: <1.1, 1.1–2.0, 2.0–3.3, 3.3–7.0, and >7.0 μm) high-volume sampler.

Results show that the high abundance of carbonaceous, non-sea-salt (nss)- SO_4^{2-} , nss- K^+ , and NH_4^+ in fine mode (<2 μm) over the observational site was associated with north-easterly air masses, whereas sea-salts (Na^+ and Cl^-), NO_3^- , and nss- Ca^{2+} were higher in coarse mode (>2.0 μm) aligned with north-westerly and southwest air masses (Fig. 10). Organic carbon (OC) was characterized by a unimodal size distribution with a peak in fine mode during north-easterly and north-westerly air masses, whereas the peak was shifted to the coarse mode during southwest air masses. Elemental carbon (EC) showed unimodal size distribution during southwest air masses while bimodal distribution under north-easterly and north-westerly air masses with a prominent peak in fine mode was observed. The NH_4^+ , nss- SO_4^{2-} , nss- K^+ and WSOC showed unimodal size distributions with a peak in fine mode, whereas NO_3^- , sea-salts, and dust particles showed unimodal size distributions with a peak in the coarse mode. On the basis of these results together with correlation analysis and specific mass ratios, this study emphasizes that north-easterly air

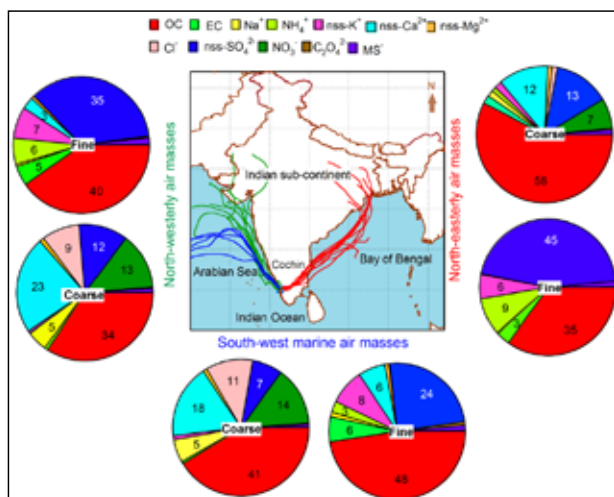


Figure 10: Chemical composition of different air masses at Cochin for fine (<2.0 μm) and the coarse mode (>2.0 μm) aerosols [Boreddy et al., *Earth Space Chem.* 2021].

masses are highly enriched with secondary anthropogenic aerosols whereas primary coarse mode aerosols come from various sources such as sea-salts, dust, and NO_x emissions linked with north-westerly and southwest air masses. The estimated aerosol-liquid-water (ALW) revealed that sea-salts, nitrate, and dust aerosols contribute to ALW in the coarse mode, whereas NH_4^+ , SO_4^{2-} , and water-soluble organics are significantly important in fine mode aerosols.

Geochemical Characteristics of Size-Resolved Trace Metals from West-Coast of India

Trace elements in atmospheric particulate matter play a significant role in air quality, health and biogeochemical cycles. The identification and quantification of metals (Li, Al, P, Ti, V, Cr, Mn, Fe, Co, Ni, Cu, Zn, As, Sr, Cd, Sn, Sb, Ba, and Pb) at a coastal urban location (Cochin) in the west coast of India were carried out using the inductively coupled plasma-mass spectrometry (ICP-MS). The temporal variation of size-resolved trace metals in aerosols were found to be associated with different air masses from the west-coast of tropical India, as shown in Fig. 11.

It is obvious that Al and Fe are the most abundant trace metals in all sizes and it is consistent for all the air masses. However, there was a noteworthy difference in the elemental distribution of fine and coarse sized particles, with $\text{Fe} > \text{Al}$ for size <1.1 μm under the influence of north-easterly and southwest air masses but not for the north-westerly air masses. This inference suggests an additional source of fine-sized Fe during north-easterly and southwest air masses that may be associated with sources other than crustal emissions. Higher contribution of Al was observed in north-westerly air masses indicating abundant dust loading, irrespective of the size of the particle. Zn is the third most abundant metal, which is enriched in the fine-sized (<2.0 μm) particles. A significant contribution (~5%) of Pb was observed in fine mode aerosols associated with north-easterly air masses (Fig. 11), indicating the long-range transport of combustion-derived metals from the northern India (IGP region). The transport of coal combustion-derived Pb in fine mode from IGP may be reasonable during this period at Cochin. The Ni (by product of the oil combustion) was apparent in <1.1 μm size during the northwest air masses, suggesting the significant transport of combustion related emissions during north-westerly air masses over the westcoast of India.

Most of the crustal metals (Al, Fe, Ti, P, Ba, Co) showed higher concentrations under the influence of north-westerly air masses and observed unimodal size distribution with a peak in coarse mode (>2.0 μm). On the other hand, combustion-derived metals (Cu, Zn, Cd, Sb, and Pb) showed higher concentrations associated with north-easterly air masses and characterized by the unimodal size distribution with a peak in fine mode (<2.0 μm). These results suggest that different sources associated with different air masses are probably responsible for these peaks in fine and coarse

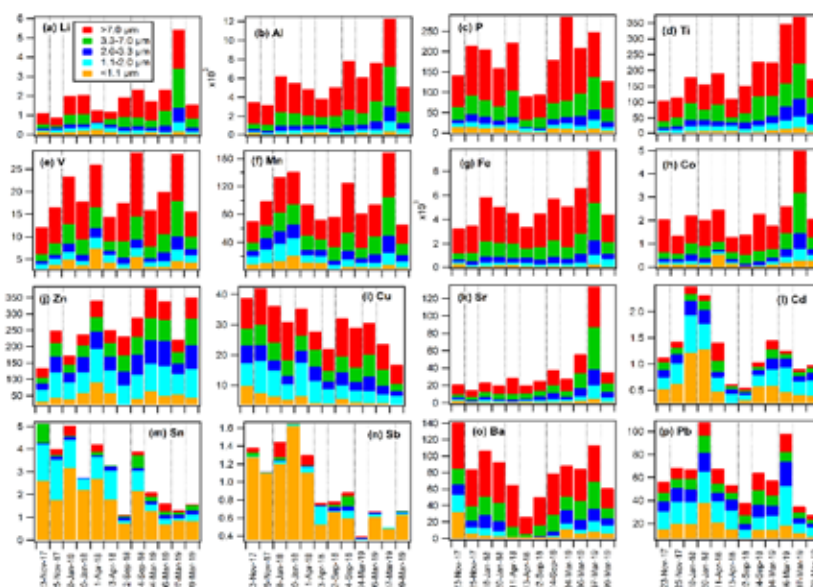


Figure 11: Temporal variations of each trace metal (ng m^{-3}) identified in size-resolved aerosols under different air masses at Cochin from the west-coast of tropical India [Boreddy et al., *Sci. Tot. Environ.* 2021].

mode particles. The estimated fine-to-course (F/C) mode ratios were found to be greater than unity for Cu, Zn, Sb, Cd, and Pb metals and lower (<0.05) for Al, Fe, Ti, P, Ba, and Co metals. The enrichment factors (EFs) >100 for Cd, Sb, Zn, Pb, Sn metals whereas its values were less than 10 for Al, Fe, Ti, P, Mn, Co, Sr, and Ba in fine mode particles. However, the combustion derived metals such as V, Cr, Ni, As in fine mode showed EFs in the range between 10 and 100. In the coarse mode, most of the metals showed EFs less than 10, however, Cr, Zn, Cd, As, and Pb EFs ranged between 10 and 100. The Positive Matrix Factorization (PMF) analysis revealed that crustal source (52–90%) was most abundant for the $>7.0 \mu\text{m}$ sized particles, whereas vehicular and traffic-related sources were predominant

for particles sized $<1.1 \mu\text{m}$ depending on the prevailed air masses.

Since trace metals, particularly transition metals (for example, Fe), serve as catalysts, affect the formation of secondary inorganic and organic aerosols in the atmosphere, thus having significant implications towards the Earth's radiative forcing.

Chemical Composition of Urban Aerosols over East-Coast of Tropical India

Tropical coastal urban aerosols were collected on day and night basis at Chennai during 2017-2018. Aerosol samples were analysed for carbonaceous and water-soluble ionic compounds. EC, OC, WSOC showed clear seasonal

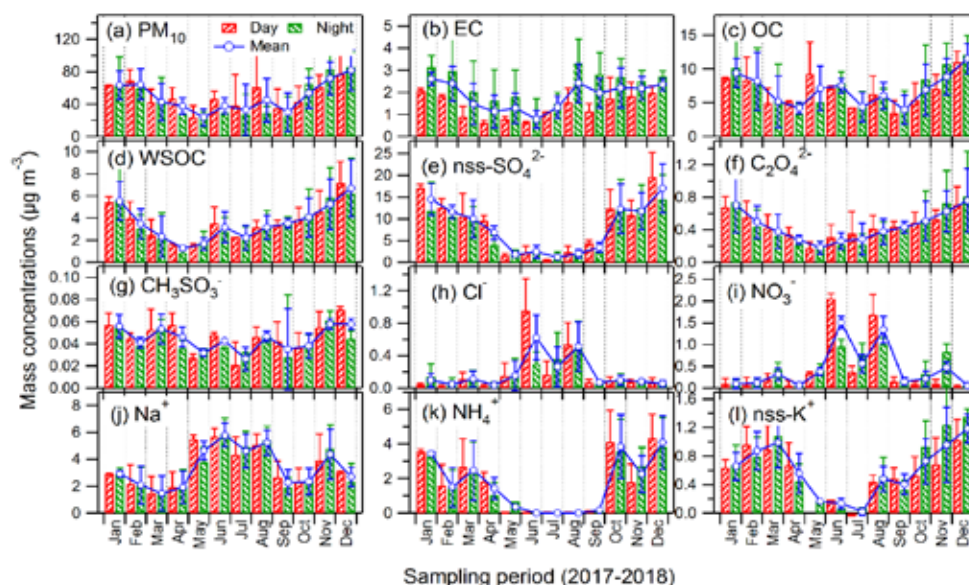


Figure 12: Monthly variation of different chemical species in PM_{10} aerosols at Chennai in the east-coast of tropical India [Boreddy et al., *Environ. Chem.* 2021].

variations with higher concentrations during winter and lower in summer (Fig. 12). OC-to-EC ratios were maximized in summer and monsoon while WSOC-to-OC ratios were consistently high in all seasons (>0.5) except for summer. The nss-SO₄²⁻ was found to be the predominant component among all measured chemical species showing higher values in winter and lower in monsoon. Likely, nss-K⁺ and NH₄⁺ were higher in winter and lower in monsoon. Oxalate (C₂O₄²⁻) showed higher values in winter and post monsoon and lower concentrations in summer and monsoon (Fig. 12f). Methane sulfonate (CH₃SO₃⁻) was higher in winter as well as summer and lower in monsoon (Fig.12g). In contrast, nss-Ca²⁺ and NO₃⁻ concentrations were maximized in monsoon.

Further, a clear sea-breeze (day) and land-breeze (night) variability was noticed in the measured chemical species over the sampling site because of its close proximity to the Bay of Bengal. EC showed a significant difference during sea-breeze and land-breeze periods. The abundance of EC was 2 to 3 times higher during land-breeze than sea-breeze except in July. WIOC was largely contributed during land-breeze phase of winter and post-monsoon while sea-breeze contributions were abundant during monsoon, implying a clear difference in their sources, which were associated with continental and marine biogenic emissions, respectively. Contributions of SO₄²⁻ were higher during sea-breeze in winter and post-monsoon however, NH₄⁺ showed no significant difference during the sea- and land-breeze although it was apparent in winter and post-monsoon. Likewise, Mg²⁺ and Na⁺ did not show any significant difference (p>0.05) during sea-breeze and land-breeze periods, however, it was found to have significant contribution in monsoon, suggesting the predominance of oceanic influence. Further, high concentration of Ca²⁺ and NO₃⁻ were found during monsoon and it was higher during daytime indicating windblown dust and local traffic emissions are significant in addition to marine emissions.

All these inferences together with seasonal variation of mass ratios and regression analysis, the organic carbon aerosols over the coastal urban location of tropical India are largely of aged secondary organic aerosols associated with anthropogenic sources and combustion derived sources in winter and post-monsoon. In contrast, marine emissions mixed with local sources (dust and vehicular emissions) are major sources of organic aerosols in monsoon.

These results provide crucial information to understand the nature of origin and formation processes of organic aerosols, consequently alter the CCN activity of inorganic matter by mixing processes in the ambient atmosphere, thus posing significant implications towards indirect effect.

Size-Resolved Chemical Composition of Coastal Aerosols from West-coast of India

Study on size-segregated chemical composition of aerosols present in the atmosphere gives valuable insights into their

origin (source), formation processes, state of mixing, chemical processes and physical modifications that they undergo during their residence time in the atmosphere. Aerosols present over coastal atmospheres are often a complex mixture of continental and marine aerosols, with their properties highly dependent on air mass history. Present study carried out from a coastal location (Thumba in Thiruvananthapuram) in the southern tip of peninsular India during the period 2017–19. The characteristics in chemical composition of aerosols in different size-ranges including carbonaceous [Organic Carbon (OC), Elemental Carbon (EC), Water-soluble OC (WSOC), Water insoluble OC (WIOC)], water-soluble ions [Na⁺, NH₄⁺, K⁺, Ca²⁺, Mg²⁺, methane sulfonic acid (MSA⁻), Cl⁻, NO₃⁻, SO₄²⁻, oxalate (C₂O₄²⁻)] and metallic species (Al, Fe, Ti, V, Mn, Co, Zn, As, Sr, Cd, Sn, Sb, Tl, Pb) were evaluated.

During winter (Dec-Feb) and post-monsoon (Oct-Nov), <1.1 μm size bin shows the highest concentration. The chemical analysis of aerosols shows that the annual mean concentration of the species Na⁺, Ca²⁺, Mg²⁺, Cl⁻, NO₃⁻, Al, Fe exhibited dominance in coarse mode (> 2 μm); while NH₄⁺, K⁺, SO₄²⁻, MSA⁻, oxalate, OC, and EC exhibited enhancement in fine mode (< 2 μm). The seasonal nature of size segregated mass concentration of carbonaceous aerosols is shown in Fig.13. It can be seen that fine mode OC (< 2 μm) dominating during post-monsoon and winter (62% and 61% of total OC, respectively) and coarse mode (> 2 μm) OC peaking during pre-monsoon and monsoon (54% and 52% of total OC, respectively). This indicates that OC had multiple sources and formation pathways over this coastal atmosphere.

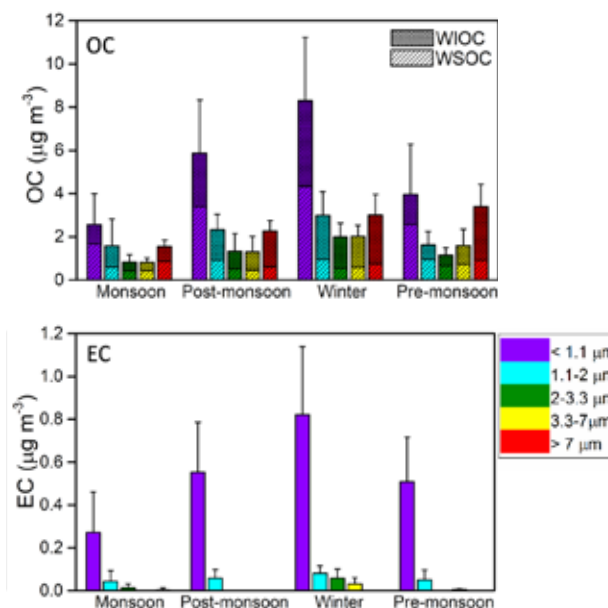


Figure 13: Seasonal average concentrations of carbonaceous species in different size-bins during 2017-19 [Aswini and Hegde, Atmos. Res. 2020].

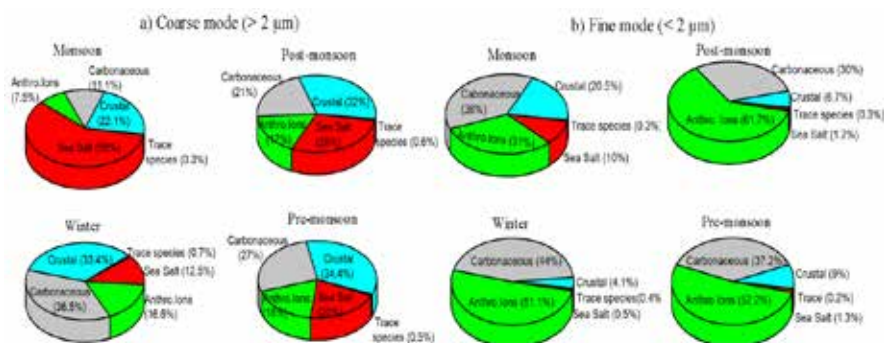


Figure 14: Percentage contribution of species in analysed mass for a) coarse mode (> 2 μm) and b) fine mode (< 2 μm) [Aswini and Hegde, Atmos. Res. 2020].

WSOC predominantly contributed to fine mode and was modulated by changing synoptic air-mass. The WIOC fraction was found to be modulated by sea-land breeze activities and exhibited coarse mode nature. WSOC and WIOC in coarse mode have distinct sources and formation pathways. Heterogeneous condensation of organics on coarse mode particles has been considered as an important pathway for coarse mode WSOC. Coarse mode WIOC has been identified to be from local production, since they have not undergone chemical ageing in the atmosphere and showed significant variation with land-sea breeze circulation.

The relative seasonal contribution of aerosol species in total analysed mass in coarse and fine mode is shown in Fig.14, it can be seen that sea-salt fraction peaked in coarse mode during monsoon (59%), anthropogenic ions in fine mode during post-monsoon (62%), crustal species (Al, Fe, Ti, nss-Ca²⁺, nss-Mg²⁺) in coarse mode during pre-monsoon (34%) and carbonaceous species (OC, EC) in fine mode during winter (44%).

Characteristics of Near-Surface Aerosols at a Tropical site: Concurrent Measurements of their Physico-Chemical Properties

Pattern of aerosol mass loading, size distribution, physical and chemical composition over an urban coastal station at the tropical coastal site, Thumba near to Thiruvananthapuram was investigated. Based on the seasonality in chemical composition, size information and source characteristics, the following five major components were identified; (1) sea-salt (SS), (2) water-soluble non-sea-salt components (WSN), (3) mineral dust (MD), (4) particulate organic matter (POM), and (5) black carbon (BC). The aerosol chemical composition over the study region for different seasons is shown in Fig.15. The component SS shows higher contribution (40%) for the monsoon season and least in winter (6%) and remained 20% and 25% in pre-monsoon and post-monsoon seasons. WSN consisting of SO₄²⁻, NO₃⁻, etc. (mostly of anthropogenic origin) contributes 20-22% in pre-monsoon, post-monsoon and winter with minimum in monsoon (13%). MD peaks in pre-monsoon (29%) and least for winter (10%) even though the winds are north-

easterlies from the land. BC and POM were highest in winter (~5% and 34%, respectively). POM remained more or less same (~23-24%) in all other seasons indicating the same type of sources. On the other hand, BC attained its minimum in monsoon (2%) and remained 3-5% in pre-monsoon and post-monsoon. The principal component analysis (PCA) indicated the dominance of sea salt species like Na⁺, Cl⁻, etc., in monsoon and mixed sources during post-monsoon and winter. Strong mixing of aerosols from various sources is also observed in different seasons, in particular during the winter season.

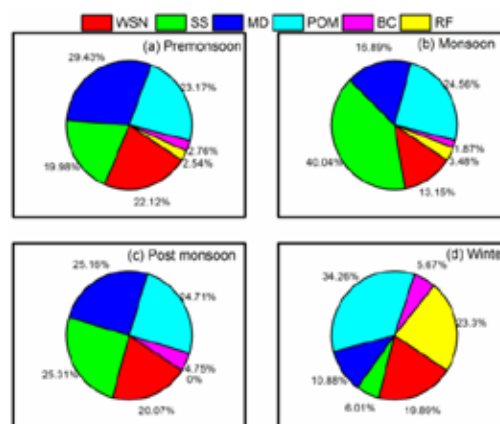


Figure 15: First-cut model for aerosol chemical composition at Thiruvananthapuram for different seasons [Aryasree et al., J. Earth Syst. Sci. 2020].

Aerosols over the Himalayas and Polar Regions

Multi-layer distribution of Black Carbon and Inorganic Ions in the Snow-packs of Western Himalayas and Snow Albedo Forcing

The characteristics of multi-layer distribution and effects of Black Carbon and inorganic ions (such as Na⁺, K⁺, Mg²⁺, Ca²⁺, SO₄²⁻, NO₃⁻, Cl⁻, K⁺) in the snow packs of (i) Khardung Glacier (KG) and (ii) Phuche Glacier (PG), located (> 5 km a.s.l.) in the Ladakh region of Indian Western Himalayas is investigated. The measured BC mass concentrations at the different vertical levels of the snowpits at PG, KG1, and KG2 (as shown in Fig.16) depict highly variable

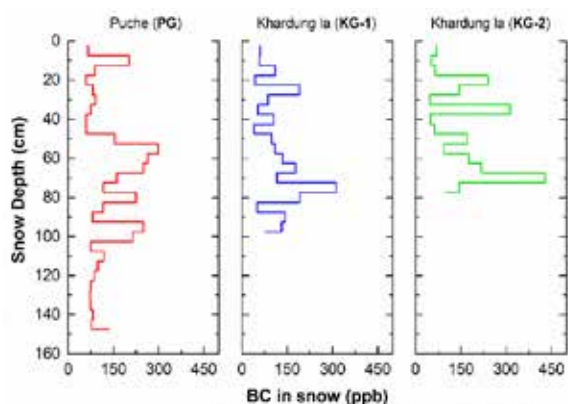


Figure 16: BC mass concentrations at different snow depths at Puche Glacier (PG, 5613 masl) and Khardung Glacier (KG1, 5340 masl and KG2, 5439 masl) [Thakur et al., Atmos. Environ. 2021].

distributions from surface to the bottom of the pits. The BC mass concentrations in the fresh snow layers of the snowpits are lower than the values in the bottom (aged) snow layers of the pit. The maximum concentrations of BC are observed at the depth of 50-55 cm (winter snow) in PG, whereas, it is observed to be at 65-75 cm (aged snow) in the KG1 and KG2. The observed heterogeneity in the vertical distribution of BC in the snowpacks could be attributed to the seasonal changes in the deposition as well as the post-depositional processes of light absorbing aerosols within the snowpit. During snow melt, the downward percolation of melt water redistributes BC in the snowpack.

The chemical analysis revealed that the relative dominance of nss-Ca²⁺ is found to be very significant (51%-80%) in all the three snow-pits, both in the fresh (seasonal) and aged snow layers. The vertical distribution of nss-Ca²⁺ in the aged snow of KG1 is also highly variable. These observations are indicative of the strong crustal influence on the vertical distribution of ions in the snow-packs of the

Himalayan glaciers. The nss-SO₄²⁻, which is an indicator of anthropogenic influence, is also not significant (<3%) either in the fresh or in the aged snow layers of all the pits. Another ion, NH₄⁺ generally sourced from biomass burning sources, showed high variability in the snow layers. All of these observations depict that even the clean glaciers at such high altitudes are impacted by dust and some anthropogenic local activities. In Fig.17, higher concentrations of nss-SO₄²⁻ and NO₃⁻ are noticeable in the uppermost layers (0-10 cm), indicating the influence of anthropogenic sources on the surface snow. Subsequently, the concentrations are higher beyond 80 cm. This type of vertical distribution reflects the elution of ions within the snowpack, preferentially during melt. Thus the process of deposition, followed by percolation and elution and then refreezing in the bottom layers (where the spike in concentration is observed) leads to vertical heterogeneity in the ionic concentrations.

The computation of the effective snow albedo using the offline version of the SNow-ICe-Aerosol Radiative (SNICAR) model for different cases of the snow pack (e.g., single layer, dual layer, multi-layer) indicated that the consideration of multi-layer model (that accounts for BC in the surface and bottom layers) is suitable for the accurate estimation of albedo reduction. Considering multilayer model, the snow albedo forcing (SAF) is estimated using the differences (i.e., albedo reduction) between clean and contaminated (due to deposition of LAA) snow spectrum and the spectral direct shortwave spectral irradiance (I) reaching the surface. The values of SAF are found to vary between 20.8 and 42.4 Wm⁻² at KG and between 36.7 and 66.4 Wm⁻² at PG. As snow grain size is a crucial parameter in changing the snow albedo properties, the large variability observed is mainly due to the wide range of snow grain size considered in the simulations.

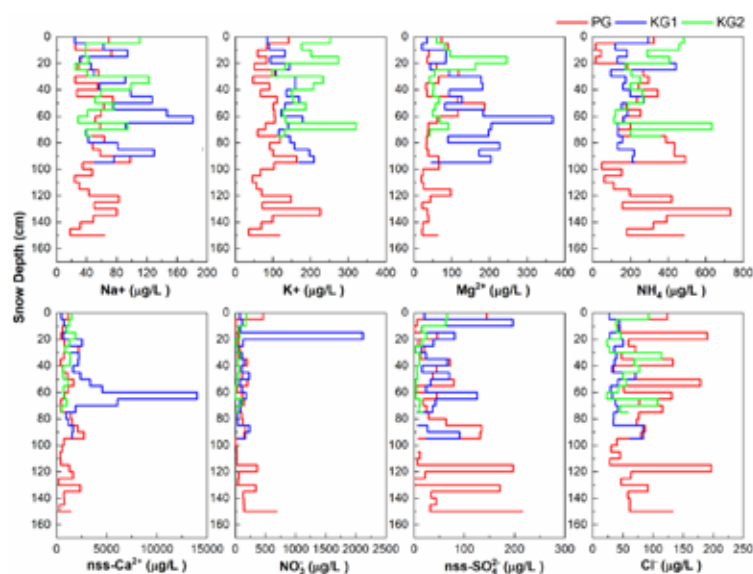


Figure 17: Vertical profiles of major inorganic ion concentrations in fresh snow (FS) and aged snow (AS) layers of the Himalayan glaciers [Thakur et al., Atmos. Environ. 2021].

Long-Term Changes in Aerosol Radiative Properties over Ny-Ålesund: Results from Indian Scientific Expeditions to the Arctic

The long-term monitoring of Black Carbon mass concentrations and aerosol scattering coefficient (σ_{SCA}), supplemented by number size distribution and chemical composition, are utilized to understand the temporal changes in the aerosol properties, associated source processes and radiative effects at Ny-Ålesund (79° N) in the Svalbard Archipelago. The long-term (2010-2019) observations of BC mass concentrations (Fig. 18a) at Ny-Ålesund revealed, in general, a decreasing trend of $-24.7 \text{ ng m}^{-3} \text{ decade}^{-1}$, however the observed trend is statistically significant ($p \sim 0.048$; $\alpha \sim 0.05$) only during spring season. The decreasing trend of BC during spring could be attributed to the enhanced wet scavenging of aerosols associated with the increasing warmer climate and resulting increased precipitation at higher latitudes. Since the concentrations of BC at Arctic mainly peak during the spring season, the decreasing-trend of BC during spring mainly controls the annual trend.

In contrast to BC, aerosol scattering coefficients showed a statistically significant increasing trend (Fig. 18b) with values (at 550 nm) increasing at a rate of $+5.2 \text{ Mm}^{-1} \text{ decade}^{-1}$. Despite the contrasting trend, the seasonal values of BC and σ_{SCA} were higher in winter/ spring and lowest in summer. Aerosol single scattering albedo (SSA) showed a clear seasonal transformation with highest SSA in May (~ 0.95) and lowest in September (~ 0.87). In contrast, higher values of aerosol backscatter fraction (~ 0.2) and lowest values of aerosol asymmetry parameter in summer are indicative of the contribution of natural sea-salt aerosols. The aerosol number size distribution depicted dominant contribution of coarse mode particles in summer. The percentage share of PM10 to total aerosol mass is $>20\%$, having highest PM10 fraction in summer ($\sim 21.4\%$). BC mass fraction (F_{BC}) is higher in winter (~ 2.43) and summer (~ 2.15) and lowest in spring (~ 1.3). The chemical properties of aerosols revealed considerably higher influence of sea spray (ssNa⁺, K⁺, Mg²⁺ and Cl⁻), crustal (nssCa²⁺) and anthropogenic (nssSO₄²⁻ and NO₃⁻) sources in July (summer) as compared to October (autumn). The locally emitted coarse mode aerosols (basically from sea spray and crustal sources) play an important role during Arctic summer as it can alter the ionic budget, more specifically for Na⁺ and SO₄²⁻. Investigation of the carbonaceous components (elemental carbon - EC) and organic carbon-OC) in total carbon revealed a significantly higher amount of OC ($344.1 \pm 91.8 \text{ ng m}^{-3}$) and EC ($55.2 \pm 14.9 \text{ ng m}^{-3}$) concentrations during spring.

Multi-year measurements of columnar aerosol optical depth (AOD) at 500 nm varied from a low value of ~ 0.01 (in July 2014) to as high as ~ 0.20 (in April 2017). The mean AOD for the entire period of study is $\sim 0.09 \pm 0.03$ (at 500 nm). The estimation of aerosol direct radiative forcing yield surface cooling in the range of -1.2 to -2.1 Wm^{-2} , with a corresponding forcing at the top of the atmosphere of 0.15

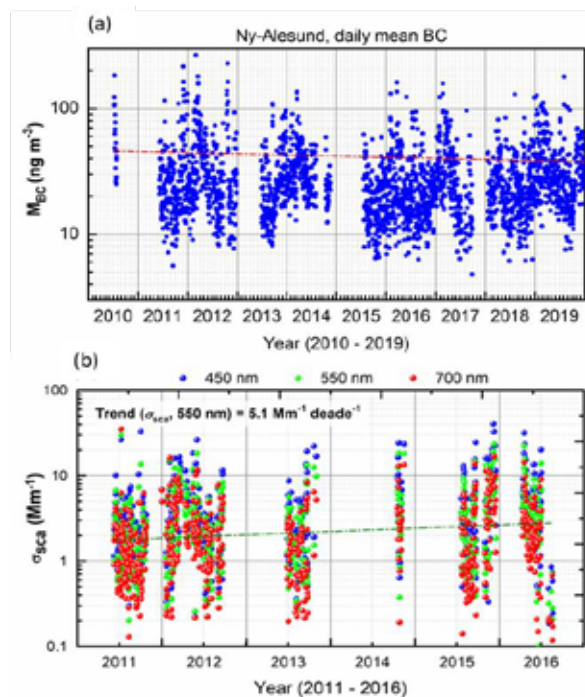


Figure 18: (a) Time series of the daily mean values of BC mass concentrations during 2010-2019; (b) Daily mean aerosol scattering coefficients (σ_{sca}) at 450, 550, and 700 nm [Gogoi et al., Polar Science, 2021].

-2.69 Wm^{-2} during April. Potential source contribution function revealed that 65% of the trajectories during winter are either from Europe or Russia. North Europe is the dominant source region during summer, with $\sim 27\%$ of trajectories passing over it.

ARFINET Observations

Multi-year Characterization of Aerosol Black Carbon Concentrations over a Semi-arid Tropical Site, Udaipur

As part of the ARFI project of ISRO-GBP, several region-specific features of BC from the southern, central, eastern and northern part of India have been reported by various researchers. However, measurements of BC over the north-western part of India are very limited. In this regard, multi-year data collected during the period from July 2008 to December 2012 have been analysed for characterization of BC, at Udaipur (UDP, 24.6°N, 74°E, 580 m above mean sea level), a semi-arid and urban site located to the south eastern foothill region of Aravalli Mountain range, with proximity to the Great Indian Desert in north west India.

The annual average BC is $4.5 \pm 2.6 \mu\text{g m}^{-3}$; highest in winter ($7.4 \pm 3.3 \mu\text{g m}^{-3}$), followed by post-monsoon ($6.6 \pm 3.4 \mu\text{g m}^{-3}$) and pre-monsoon ($2.8 \pm 1.6 \mu\text{g m}^{-3}$) and lowest in monsoon ($2.5 \pm 2.2 \mu\text{g m}^{-3}$) seasons (Fig.19). The share of BC to PM_{2.5} attained peak values of $9.1 \pm 0.05\%$ in winter, followed by $7.1 \pm 0.06\%$ in post-monsoon and $6.8 \pm 0.04\%$ in summer and the dip of $2.6 \pm 0.01\%$ in the monsoon. Investigation of the spectral signature of

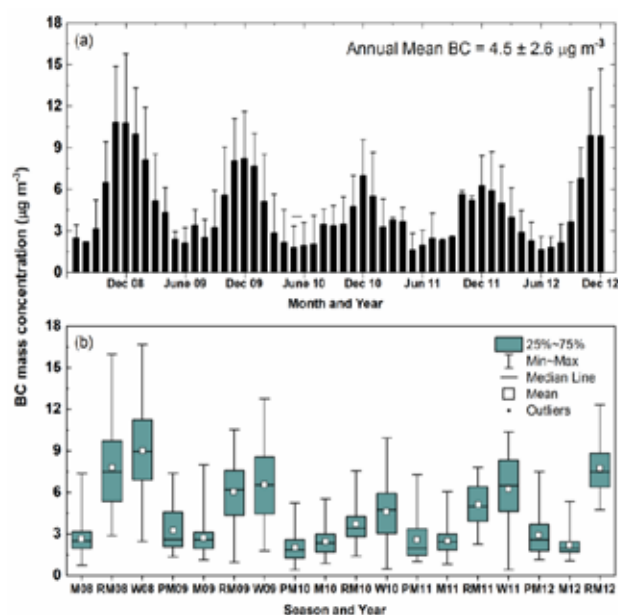


Figure 19: (a) Annual variation of BC for the period from July-2008 to December-2012, (b) Box and whisker plots of the seasonal mean values of BC during the entire period of study [Vyas et al., Env. Sc. And Poll. Res., 2021].

BC indicated fossil fuel combustion emission as most predominant source of light absorbing aerosols over UDP. Apart from local anthropogenic sources, influence of long-range transport of aerosols is found to be significant during winter, with dominant transport from IGP. On the other hand, the pre-monsoon period is dominated by trajectories from the north-western and western Indian region. The region is influenced by marine air masses during monsoon and post-monsoon seasons. Diurnal variation of BC revealed an enhancement value during morning and late evening hours and then depleted during the early morning hours which eventually attains minimum in the afternoon

hours. The diurnal pattern of BC mass concentration is seen to be altered in opposite phase with the diurnal pattern of planetary boundary layer, air temperature and ventilation coefficient at different months, suggesting that prevailing meteorology has a significant role in BC variation over Udaipur.

Effect of Nation-wide COVID-19 Lockdown on Aerosols and Trace Gases

Response of Ambient BC Concentration across the Indian Region to the Nation-wide Lockdown: Results from the ARFINET Measurements of ISRO-GBP

It is well accepted that the short-lived climate forcing agents, such as atmospheric aerosols, cause significant regional and global climatic impact, in which the role of Black Carbon aerosols and its impact on radiation, cloud, and cryosphere is unique due to a variety of reasons. In this study, an assessment is made on the response of ambient BC mass concentrations and spectral absorption properties across Indian mainland during the nation-wide lockdown (LD) in connection with the Corona virus Disease 19 (COVID-19) pandemic. The LD had brought near to total cut-off of emissions from industrial, traffic (road, railways, marine and air) and energy sectors, though the domestic emissions remained fairly unaltered. This provided a unique opportunity to delineate the impact of fossil fuel combustion sources on atmospheric BC characteristics.

In this context, the BC measured at the national network of aerosol observatories (ARFINET) under ISRO-GBP are examined to assess the response to the seizure of emissions over distinct geographic parts of the country (Fig. 20). Results indicate that average BC concentrations over the Indian mainland are curbed down significantly

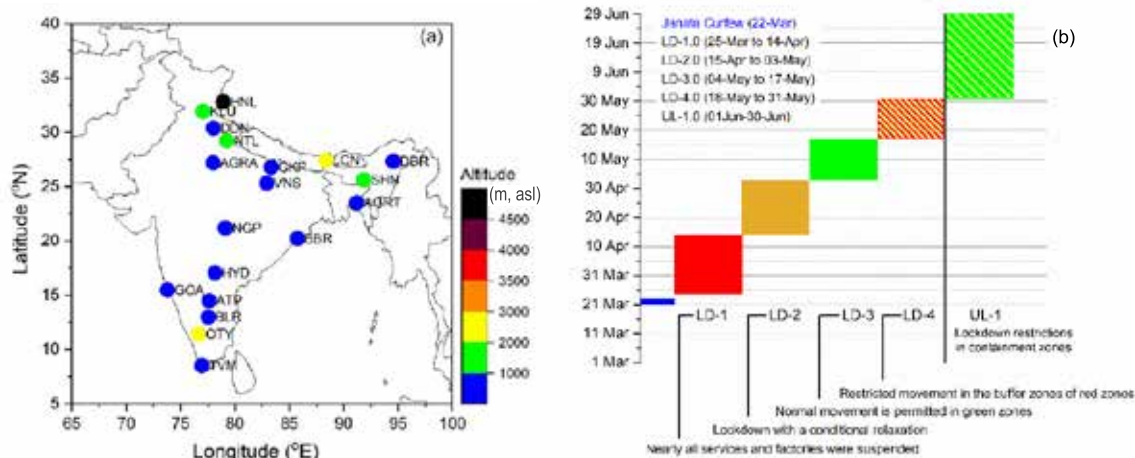


Figure 20: (a) Geographic positions of the ARFINET stations over India, the primary BC data from which are used in the present study. The stations include: TVM-Trivandrum, OTY-Ooty, BLR-Bangalore, ATP-Anantapur, Goa-Goa, HYD-Hyderabad, NGP-Nagpur, BBR-Bhubaneswar, AGRT-Agartala, SHN-Shillong, DBR-Dibrugarh, LCN-Lachung, VNS-Varanasi, GKP-Gorakhpur, AGRA-Agra, NTL-Nainital, DDN-Dehradun, KLU-Kullu, HNL-Hanle. The colour scale indicates the altitude of the stations. (b) Temporal scales of the lockdown (LD) periods (during 2020) imposed by the Government of India to contain the spread of COVID-19 pandemic. The magnitude of social and travel restrictions varied with the progression of LD from 1 to 4 [Gogoi et al., Current Science, 2021].

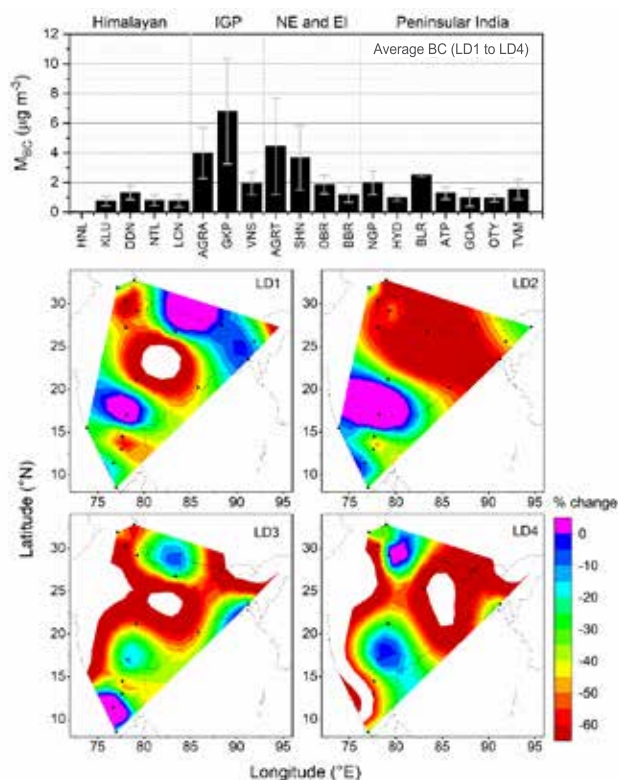


Figure 21: Change (in percentage) in the magnitude of BC concentrations during the lockdown periods (LD1, LD2, LD3 and LD4) in comparison to the average values of the corresponding period of the year 2015-2019. The top panel shows average values of BC during the entire period of lockdown (i.e., LD1 to LD4) [Gogoi et al., Current Science, 2021].

(10–40%) from pre-lockdown observations during the first and most intense phase of lockdown (Fig. 21). This decline is significant with respect to the long-term (2015–2019) averaged (climatological mean) values. The drop in BC is most pronounced over the Indo-Gangetic Plain (> 60 %) and north-eastern India (> 30 %) during the second phase

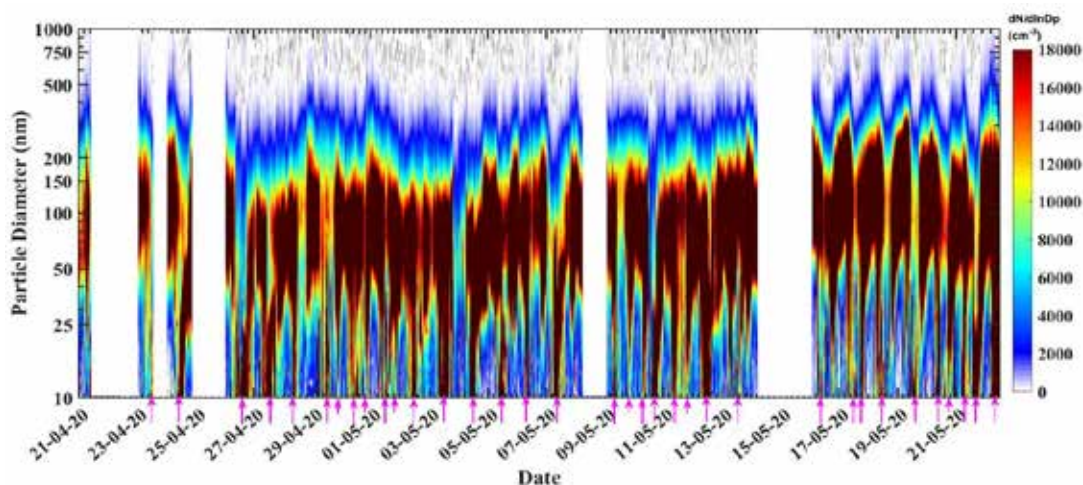


Figure 22: Temporal variation of particle number size distribution (PNSD). The arrows on the bottom indicate the new particle formation events. The colorbar indicates number concentrations, and the white portion indicates the data gap [Yadav et al., Atmos. Environ. 2021].

of lockdown, while significant reduction is seen during LD1 (16 – 60 %) over central and peninsular Indian as well as Himalayan and sub-Himalayan regions. Despite such a large reduction, the absolute magnitude of BC remained higher over the IGP and north-eastern sites compared to other parts of India. Notably, the spectral absorption index of aerosols changed very little over most of the locations, indicating the still persisting contribution of fossil-fuel emissions over most of the locations.

New Particle Formation Events over a Megacity -New Delhi during the COVID-19 Lockdown

Urban new particle formation (NPF) events are highly localized in nature and occur during conducive conditions (e.g., photochemistry and local meteorological features), and these events significantly contribute to the $PM_{2.5}$, thereby degradation of air quality. Using the unique opportunity provided by the lockdown imposed by the Government of India to tackle the spread of Corona virus Disease 19 pandemic leading to a near-complete cut-off of the primary sources, particle number concentrations in the ultrafine and fine-sized (10.2 to 1090 nm) regimes over a polluted megacity, New Delhi (28.75° N, 77.12° E) were investigated. The impact of varying urban emissions during the different phases of the lockdown during April-May 2020 reflected in particle concentrations and particle number size distributions (PNSDs). The mean total number concentrations were in the range of $\sim (2 \text{ to } 3.5) \times 10^4 \text{ cm}^{-3}$ and depicted a gradual increase ($\sim 26\%$) with progressive unlock of the anthropogenic activities. At the same time, accumulation particle concentrations were doubled with gradual unlock from stringent lockdown period, highlighting the effect of intensified anthropogenic activities on particle number concentrations. However, ultrafine particles (diameter < 100 nm) dominated (50-88%) the total number concentrations during most of the days during the study period. As seen in Fig.22, the temporal variation of PNSDs

revealed several NPF events (marked with arrows) with a clear appearance of significant amounts (2-5 times increase from values before the event) of nucleation mode particles.

Compared to the non-event days, N_{nuc} was ~ 1.5 -2 times higher on the event days. Subsequently, the particles grew to larger sizes with rates 3.31 - 8.37 nm hr^{-1} , and therefore many of the events depicted a clear ‘banana’ pattern. The NPF events occurred during the daytime, and during the events, a clear enhancement in the concentrations of $[H_2SO_4]$ proxy (2 to 3.5×10^7 molecules cm^{-3} ; 2-3 orders higher than the non-event values) suggesting the role of strong gas-phase photochemistry. The frequency of the NPF events decreased from 21% to 3% as the lockdown progressed. As the frequency, intensity, and shape of the NPF events reflected, higher condensation sink in the urban region with a gradual increase in traffic ensures that gaseous precursors, molecular clusters, and newly formed particles experienced a high loss rate. This study highlighted that urban pollution mitigation policies need to consider ultrafine particles emanating from the secondary aerosol formation process from traffic emissions.

Contrasting Impact of COVID-19 Lockdown on Surface Ozone over Coastal and Urban Locations

Weeklong observations of trace gases were carried out at Thumba, Thiruvananthapuram (8.5° N, 76.9° E, ~ 3 m asl) during COVID-19 lockdown. Fig.23a shows daytime mean O_3 (12–17 h) during lockdown period (yellow shaded region) and the same period of previous years. Daytime O_3 showed significant reduction by 15 ppbv (36%). Since emission of NO_2 (mainly from vehicular and industrial sources) came to a halt under the lockdown, $\sim 40\%$ of NO_2 reduction is observed. Consequently, this led to reduction in O_3 as NO_2 is a major precursor for O_3 formation. Fig.23b shows the mean diurnal variations of O_3 where suppression in O_3 production is evident during lockdown period. O_3 production rate which was 9.8 ppbv h^{-1} during previous years is found to be reduced to 3.3 ppbv h^{-1} . The effective suppression of fumigation peak in NO_2 during morning hours, besides lower NO_2 values during daytime is responsible for the reduction of O_3 production rate during morning hours.

Interestingly, a hump of 5–10 ppbv around the land breeze (LB) onset is observed over three days. In order to explain the O_3 -hump, simulations were carried out using a photochemical box model. Fig.23c shows the diurnal variation of observed and simulated O_3 on 26 March 2020 when O_3 hump was prominent. The model reproduced the observed diurnal feature of O_3 , including the O_3 -hump around onset of LB. Diurnal variation of O_3 simulated for the airmass over land showed higher levels of O_3 during daytime, which is in agreement with the observations at an inland station, Kariavattom (8.56° N, 76.89° , ~ 4 km from the coast). Significant O_3 level sustained in the evening

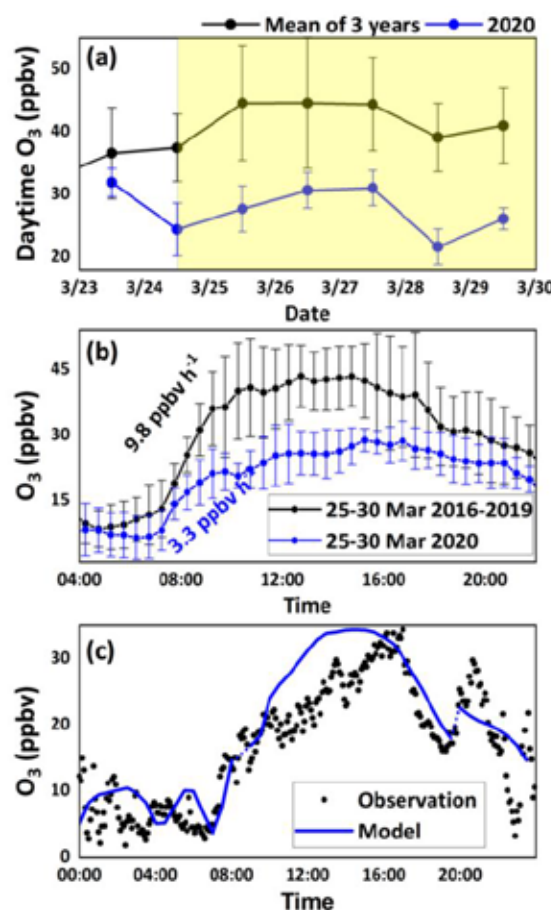


Figure 23: (a) Mean daytime O_3 and (b) diurnal variation of O_3 during lockdown period of 2020 and during the same period of previous 3 years over Thumba, Thiruvananthapuram. (c) Observed and model simulated diurnal variation of surface O_3 on 26 March 2020. Blue dots connect O_3 simulated for airmasses over land and sea. [Girach et al., *Journal of Earth System Science*, 2021].

hours due to lower NO caused by reduced emission under lockdown. This slow loss of O_3 after sunset, results in significant O_3 even in evening hours. Thus, in nutshell, this feature of O_3 -hump is attributed to the weaker O_3 titration with NO over land during lockdown. This allowed a significant amount of O_3 to sustain over land and get transported to the observational site with the onset of LB.

In contrast to the observations over Thumba, urban location (Ahmedabad; 23° N, 72.6° E) showed an increase in daytime surface O_3 during lockdown period (24 March-10 May 2020) as compared to pre-lockdown conditions (1-21 March 2020). While primary pollutant and O_3 precursors showed reduction, daytime O_3 is enhanced during the lockdown by $\sim 39\%$ (~ 17 ppbv). Box model simulations were carried out based on changes in precursors and meteorological conditions during pre-lockdown and lockdown. Simulations showed that the meteorological changes enhanced O_3 by $\sim 16\%$ whereas additional 25% enhancement was due to chemistry. Percentage reduction in NO , which titrates O_3 , was higher than the NO_2 which

contributed for the O₃ enhancement observed over the urban location in contrast to the observations over Thumba. The changes in volatile organic compounds (VOCs) also would have played a significant role in the non-linear O₃ chemistry for the contrasting changes presented here.

Simulation of CO₂ using an Artificial intelligence/Machine learning model

Under the ISRO's new initiative of Artificial intelligence/ Machine learning (AI/ML) programme, CO₂ mixing ratio was simulated successfully based on inputs of meteorological parameters for a background site. It was also shown that CO₂ can be predicted well for the near future. This demonstrates the potential of AI/ML in the area of atmospheric science. The developed AI model fetch the necessary data from Internet (or use existing file), validate the model result for recent two years and make prediction of CO₂ for next two years for a background site.

Technical activities

SPL is operating a national network of aerosol observatories (ARFINET) over Indian region under the ARFI Project of ISRO GBP. In addition, state of the art aerosol and trace gas observatory is operational at Thumba. For the smooth operation and maintenance of these observatories, several sub-systems and software are developed. The technical activities are

- Development of Data Acquisition Software for Automatic Weather Station (AWS).
- Development of RS422 to USB and Serial converters

Future Projections

- Modelling studies on the effects of aerosol-induced snow albedo forcing and its feedback on the seasonal snowmelt and run-off over the Himalayan region.
- Investigations on the (i) molecular level analysis of organic aerosols and their light absorbing properties (BrC measurements) and (ii) atmospheric chemistry of organic nitrogen aerosols, their sources and formation processes over Indian region.
- Development of an experimental setup for the real-time measurements of volatility and hygroscopicity of organic aerosols.
- Role of aerosols on surface temperature trend over India using Climate modelling.
- Development of aerosol climatology over the Oceanic regions around India from OceanSat-3 (EOS-6).
- Development of high-altitude balloon payload for the *in-situ* measurements of aerosol characteristics in the UTLS region.

Publications in peer reviewed scientific journals

1. Boreddy, S. K. R., Hegde, P., and Aswini, A. R., "Geochemical characteristics of trace elements in size-resolved coastal urban aerosols associated with distinct air masses over tropical peninsular India: Size distributions and source apportionment", *Science of the Total Environment*, 763, 142967, <https://doi.org/10.1016/j.scitotenv.2020.142967>, 2021
2. Boreddy, S. K. R., Hegde, P., and Aswini, A. R., "Chemical Characteristics, Size Distributions, and Aerosol Liquid Water in Size-Resolved Coastal Urban Aerosols Allied with Distinct Air Masses over Tropical Peninsular India" *ACS Earth and Space Chemistry*, 5, 3, 457–473, <https://doi.org/10.1021/acsearthspacechem.0c00282>, 2021.



Figure 24: RS422 Converters

for data transmission over long/medium distance (Fig.24).

- Refurbishment of MWR at ARFINET stations at TNAU, Ooty; Dibrugarh University, Dibrugarh; ARIES, Nainital and ISTRAC, Port Blair.
- Refurbishment of instruments at ARFI lab, TERLS.
- Installation and testing of Sky Radiometers.

Development of Standalone Sun Tracking Radiometer (SSTR) – TDP

As part of the SSTR realisation, the development of the subsystems and procurement of components are in progress. Development of the Microcontroller codes for Solar Position Estimation Algorithm and Quadrant Detector based sun alignment algorithm are completed.

3. Boreddy, S. K. R., Hegde, P., Aswini, A. R., Williams, M. A., Elavarasi, R., and Kumar T. V. L. “Seasonal variations in characteristics, sources and diurnal patterns of carbonaceous and water-soluble constituents in urban aerosols from the east coast of tropical India”, *Environmental Chemistry*, 18(2), 45-60, <https://doi.org/10.1071/EN21017>, 2021.
4. Girach, I. A., Ojha, N., Babu, S. S., “Ozone chemistry and dynamics at a tropical coastal site impacted by the COVID-19 lockdown”, *Journal of Earth System Science*, 130, 158, <https://doi.org/10.1007/s12040-021-01666-3>, 2021.
5. Gogoi, M. M., Babu, S. S., Arun, B. S., Moorthy, K. K., Ajay, A., Ajay, P., Suryavanshi, A., Borgohain, A., Guha, A., Shaikh, A., Pathak, B., Gharai, B., Ramaswamy, B., Menon, H. B., Kuniyal, J. C., Krishnan, J., Rama Gopal, K., Maheswari, M., Naja, M., Kaur, P., Bhuyan, P. K., Gupta, P., Singh, P., Srivastava, P., Singh, R. S., Kumar, R., Rastogi, S., Kundu, S. S., Kompalli, S. K., Panda, S., Das, T., Kant, Y., “Response of ambient BC concentration across the Indian region to the nation-wide lockdown: Results from the ARFINET measurements of ISRO-GBP”, *Current Science*, 120, 2, 341-351, <https://doi.org/10.18520/cs/v120/i2/341-351>, 2021.
6. Gogoi, M. M., Santosh K Pandey, Arun, B. S., Nair, V. S., Thakur, R. C., Chaubey, J. P., Tiwari, A., Manoj, M. R., Kompalli, S. K., Vaishya, A., Prijith, S. S., Hegde, P., and Babu, S. S., “Long-term changes in aerosol radiative properties over Ny-Ålesund: Results from Indian scientific expeditions to the Arctic”, *Polar Science*, <https://doi.org/10.1016/j.polar.2021.100700>, 2021.
7. Kompalli, S. K., Babu, S. S., Moorthy, K. K., Satheesh, S. K., Gogoi, M. M., Nair, V. S., Jayachandran, V., Liu, D., Flynn, M. J., Coe, H., “Mixing state of refractory black carbon aerosol in the South Asian outflow over the northern Indian Ocean during winter”, *Atmospheric Chemistry and Physics*, 21, 9173–9199, <https://doi.org/10.5194/acp-21-9173-2021>, 2021.
8. Soni, M., Ojha, N., Girach, I., “Impact of COVID-19 lockdown on surface ozone build-up at an urban site in western India based on photochemical box modelling”, *Current Science*, 120, 2, <https://doi.org/10.18520/cs/v120/i2/376-381>, 2021.
9. Srivastava, P., Naja, M., Seshadri, T. R., Joshi, H., Dumka, U. C., Gogoi, M. M., and Babu S. S., “Implications of Site-specific Mass Absorption Cross-section (MAC) to Black Carbon Observations at a High-altitude Site in the Central Himalaya”, *Asia-Pacific Journal of Atmospheric Sciences*, 168 (98), <https://doi.org/10.1007/s13143-021-00241-6>, 2021.
10. Thakur, R. C., Arun, B. S., Gogoi, M. M., Thamban, M., Thayyen, R. J., Redkar, B. L., Babu S. S., “Multi-layer distribution of Black Carbon and inorganic ions in the snowpacks of western Himalayas and snow albedo forcing”, *Atmospheric Environment*, 261, <https://doi.org/10.1016/j.atmosenv.2021.118564>, 2021.
11. Usha, K. H., Nair, V. S., Babu, S. S., “Effect of aerosol-induced snow darkening on the direct radiative effect of aerosols over the Himalayan region”, *Environmental Research Letters*, 16(6), <https://doi.org/10.1088/1748-9326/abf190>, 2021.
12. Vyas, B. M., Gogoi, M. M., and Subin Jose. “Multi-year characterization of Aerosol Black Carbon concentrations over a semiarid tropical site Udaipur”, *Environmental Science and Pollution Research*, 28, 22864–22877, <https://doi.org/10.1007/s11356-020-12300-y>, 2021.
13. Yadav, S. K., Kompalli, S. K., Gurjar, B. R., Mishra, R. K., “Aerosol number concentrations and new particle formation events over a polluted megacity during the COVID-19 lockdown”, *Atmospheric Environment*, 259, 118526, <https://doi.org/10.1016/j.atmosenv.2021.118526>, 2021.
14. Yumin, Li., Tzung-May Fu, Jian Zhen Yu, Xu Feng, Lijuan Zhang, Jing Chen, Suresh Kumar Reddy Boreddy, Kimitaka Kawamura, Pingqing Fu, Xin Yang, Lei Zhu, Zhenzhong Zeng, “Impact of Chemical Degradation on the Global Budget of Atmospheric Levoglucosan and its Use As a Biomass Burning Tracer”, *Environmental Science & Technology*, 55, 5525-5536, <http://doi.org/10.1021/acs.est.0c07313>, 2021.
15. Aryasree, S., Nair, P. R. and Hegde, P., “Radiative characteristics of near-surface aerosols at a tropical site: An estimation based on concurrent measurements of their physico-chemical characteristics”. *Journal of Earth System Science*, 129, 185, <https://doi.org/10.1007/s12040-020-01444-7>, 2020.
16. Aswini, A. R., Hegde, P., “Impact assessment of continental and marine air-mass on size-resolved aerosol chemical composition over coastal atmosphere: Significant organic contribution in coarse mode fraction”, *Atmospheric Research*, 248, 105216, <https://doi.org/10.1016/j.atmosres.2020.105216>, 2020.
17. Gogoi, M. M., Thakur, R. C., Gazi, S., Nair, V. S., Mohan, R., Babu, S. S., “Vertical distributions of the microscopic morphological characteristics and elemental composition of aerosols over India”. *Journal of Atmospheric Chemistry*, 77, 117–140, <https://doi.org/10.1007/s10874-020-09406-5>, 2020.

-
18. Jose, S., Nair, V.S., Babu S. S., “Anthropogenic emissions from South Asia reverses the aerosol indirect effect over the northern Indian Ocean”, *Scientific Reports*, 10, 18360, <https://doi.org/10.1038/s41598-020-74897-x>, 2020.
 19. Kompalli, S. K., Nair, V. S., Jayachandran, V., Gogoi, M. M., and Babu, S. S., “Particle number size distributions and new particle formation events over the northern Indian Ocean during continental outflow”, *Atmospheric Environment*, 238,117719, <https://doi.org/10.1016/j.atmosenv.2020.117719>, 2020.
 20. Lakshmi, N. B., Nair, V. S., Babu, S.S., “Assessment of the vertical distribution of speciated aerosol absorption over South Asia using spaceborne LIDAR and ground-based observations”. *Remote Sensing of Environment*, 112164. <https://doi.org/10.1016/j.rse.2020.112164>, 2020.
 21. Nair P. and Kavitha M., “Stratospheric distribution of methane over a tropical region as observed by MIPAS on board ENVISAT”, *International Journal of Remote Sensing*, <https://doi.org/10.1080/01431161.2020.1779376>, 2020.
 22. Nair, V. S., Giorgi, F., Usha, K. H., “Amplification of South Asian haze by water vapour-aerosol interactions”, *Atmospheric Chemistry and Physics*, 20, 14457–14471, <https://doi.org/10.5194/acp-20-14457-2020>, 2020.

Book Chapter

- Ojha, N., Girach, I., Soni, M., Singh, N., “Distribution of reactive trace gases over south Asia: Observations and modelling” in the book titled “Asian Atmospheric Pollution”, Elsevier, <https://doi.org/10.1016/B978-0-12-816693-2.00022-6>, 2021.

Publications in Proceedings

- Chutia, L., Ojha, N., Girach, I. A., Pathak, B., Sahu, L. K., and Bhuyan, P.K., “Seasonal Evolution of Sulfur Dioxide Over the Indian Subcontinent”, *URSI Radio Science Letters*, <https://doi.org/10.46620/20-0046>, 2, 2020.

Scientific/Technical Reports

1. Ajeeshkumar P.S. and Girach I. A., “Development of a Data Acquisition Software for Automatic Weather Station”, SPL-TR-05-2020/ISRO-VSSC-TR-0384-0-20, 2020.
2. Arun, G. S. and Mukunda M Gogoi, “Multi-station MWR data processing code for cloud-screening, QC and generation of AOD map over India”, ISRO-VSSC-TR-0081-0-21, 2020.
3. Lakshmi, N. B., Arun G. S. and Mukunda M Gogoi, “Multi-station ARFINET data software for generating BC map over India”, ISRO-VSSC-TR-0079-0-21, 2020.
4. Ajeeshkumar P. S., Vijayakumar S Nair and Mukunda M Gogoi, “Standalone suntracking radiometer”, ISRO-VSSC-TR-0087-0-21, 2020.

Presentation in Symposium/Conferences/Workshops

International

1. Nair, V. S., Usha, K. H. and Babu, S. S., “Implications of aerosol-induced snow darkening on regional hydroclimate over the Himalayas”, EGU General Assembly, Session AS2.10 - ‘Atmosphere-Cryosphere interaction with focus on transport, deposition and effects of dust, black carbon, and other aerosols’, 26 April 2021.
2. Chutia, L., Ojha, N., Girach, I. A., Pathak, B., Sahu, L. K., and Bhuyan, P. K., “Distribution of sulfur dioxide over Indian subcontinent: Remote sensing observations and model reanalysis”, General Assembly and Scientific Symposium (GASS) of the International Union of Radio Science (Union Radio ScientifiqueInternationale-URSI), Rome, Italy, 29 August - 05 September, 2020.
3. Arun, B. S., Gogoi, M. M., Hegde, P., and Babu, S. S., “Contrasting signatures of the sources and types of aerosols in the western and eastern Himalayas: Radiative implications”, EGU General Assembly, Session AS3.1 – Aerosol Chemistry and Physics (General Session), 26 April 2021.
4. Srivastava, P., Manish Naja, Hema Joshi, Mukunda M. Gogoi, and Babu S.S., “Characterization of aerosols and trace gases at the Central Himalayas using long-term ground and satellite observations”, EGU General Assembly, Session AS3.5 – Atmospheric composition variability and trends, 27 April 2021.

National

1. Soni, M., Girach, I., Ojha, N., “Chemistry and dynamics of reactive trace gases over India”, Aerosol Air Quality, Climate Change and Impact on Water Resources and Livelihoods in the Greater Himalayas, ARIES, Nainital, India, 14-16 September 2020.

2. Sharma, K., Girach, I., Sharma, N., Singh, N., Ojha, N., “Ozone variations in a central Himalayan valley: Seasonal changes and impact of biomass-burning”, Aerosol Air Quality, Climate Change and Impact on Water Resources and Livelihoods in the Greater Himalayas, ARIES, Nainital, India, 14-16 September 2020.
3. Arun, B. S., Mukunda M. Gogoi, A Borgohain, S. S.Kundu and S. Suresh Babu, “Optical properties and radiative effects of aerosols in the eastern Himalayas”, Tropmet-2020, 14-17 December, 2020.

Invited Talks

S Suresh Babu

1. “Aerosol – Cloud Interaction in South Asian outflow” in Tropmet 2020, National Symposium on “Weather And Climate Services Over Mountainous Regions”, NESAC, Shillong, 14-17 December, 2020.
2. “COVID 19: A window of opportunity to assess the impact of Anthropogenic Emissions” on the occasion of CSIR Foundation Day at CSIR-National Environmental Engineering Research Institute (CSIR-NEERI), Nagpur, 26 September 2020.
3. “Physics of Atmosphere and Climate” in the UGC refresher course in Physical Sciences to the University/College Teachers, 10 October 2020.
4. “Aerosols and Climate” in the webinar series on “Impact of Climate Change” at V.T.M.N.S.S. College Dhanuvachapuram, 28 September 2020.
5. “Aerosols and Climate” in the conference on recent trend in Theoretical and Applied Physics at S N College, Kollam on 14 December 2020.
6. “Satellite and Ground based Aerosol Observations” AICTE ATAL Sponsored Faculty Development Programme on Atmospheric Remote Sensing: Methods and Advances. Indian Institute of Space Science and Technology, 30 January 2021.
7. “Aerosol Radiative Forcing over India and Regional Climate” in the session on ‘Sustainable Earth’ in the 11th Indo – German Frontiers of Engineering Conference (INDOGFOE 2021), 25 February 2021.
8. “Aerosol Radiative Forcing” in the 6th Graduate Seminar on Natural Resource Management (Online Mode), Institute of Environment and Sustainable Development, Banaras Hindu University, Varanasi, India, 17 March 2021.
9. “Aerosols over the Indian Ocean: An ICARB Experience” in the webinar conducted as part of WMO day celebration at Amity University, Gurgaon, on 23 March 2021.
10. “Recent Advances in Aerosol Research” in the webinar organised by NCESS, Thiruvananthapuram, 30 April 2021.
11. “Aerosol Radiative Forcing and Regional Climate”, 32nd mid-year meeting of Indian Academy of Science, 25 June 2021.

Vijayakumar S Nair

1. “Aerosol Cryosphere interactions over the Himalayas”, International workshop on ICTP Regional climate model: Applications over South Asia CORDEX domain, Dibrugarh University, Assam, 22-28 February, 2021.
2. “Climate Change and Earth Sciences: Challenges and opportunities”, Training programme on “Exploring DST funding schemes” jointly organized by training section, DTE Kerala and SPFU Kerala for faculty members from Government Engineering Colleges in Kerala, 27 January-2 February, 2021.
3. “Climate change over the Third Pole: Role of aerosols”, Faculty Development Programme on Climate Change Challenges – Mitigation and Adaptation, College of Engineering, Trivandrum, 15-20 March 2021.

Girach Imran Asatar

1. “Climate Change and its Impact” at International webinar on World Environment day, J.D. Birla Institute, Kolkata, 05 June 2021.
2. “Tropospheric carbon monoxide over India and surrounding oceanic region” at Physical Research Laboratory, Ahmedabad, 05 April 2021.
3. “Atmospheric trace gases – An overview” at webinar series on Energy and Environment, Indian Institute of Technology Jodhpur, 20 February 2021.

-
4. “Climate Change” at International Webinar on Advances in Nonlinear Optics and Space Science, Providence Women’s College, Kozhikode, Kerala, 19 September 2020.
 5. “Climate Change” at KKTM Government College, Pullut, Kerala, 03 October 2020.

Sobhan Kumar Kompalli

- “Aerosol microphysical properties: scientific perspective and experimental challenges” at virtual skill development workshop organized by CSIR-Institute of Minerals and Materials Technology, Bhubaneswar, 12 January 2021.

Mukunda M. Gogoi

- “Tackling the big impact of short-lived toxic aerosols on earth’s climate along the spiral of Geologic Time Scale: rhetoric or reality?”, Department of Physics, Nowgong College, Assam.

Session Chairman/Convener in Conference/Symposium/Workshops

S. Suresh Babu

- Chaired the technical session on “Aerosol-cloud-precipitation interactions” in the Tropmet-2020, the virtual National Symposium on “Weather and Climate Services over Mountainous Regions”, NESAC, Shillong, 14-17 December, 2020.

Mukunda M. Gogoi

- Co-chaired the technical session on “Aerosol-cloud-precipitation interactions” in the Tropmet-2020, the virtual National Symposium on “Weather and Climate Services over Mountainous Regions”, NESAC, Shillong, 14-17 December, 2020.

Training Programme

Hegde, P.

1. Introduction to GC-MS: Principles, Instrumentation and Applications, online training conducted by Chromatographic Society of India, 12 December 2020.
2. Chemistry and its influence on Global Warming and Climate, online training conducted by IIT Madras, 05 June 2020.

Boreddy, S. K. R.

- SMART online training on “Basics of Satellite Meteorology” organized by Space Application Centre (SAC), Indian Space Research Organisation, Ahmedabad, 21-23 December 2020.

Vijayakumar S. Nair

- One day Training Programme on “Labour Laws”, HRDD, VSSC, Thiruvananthapuram, 25 May 2021.

Girach Imran Asatar

- Attended the phase-3 and phase-4 of the Artificial Intelligence (AI) training programme organized by Directorate of Technology Development and Innovation (DTDI), ISRO Head Quarters, Bangalore, 04–13 October 2020, and 04–08 December 2020.

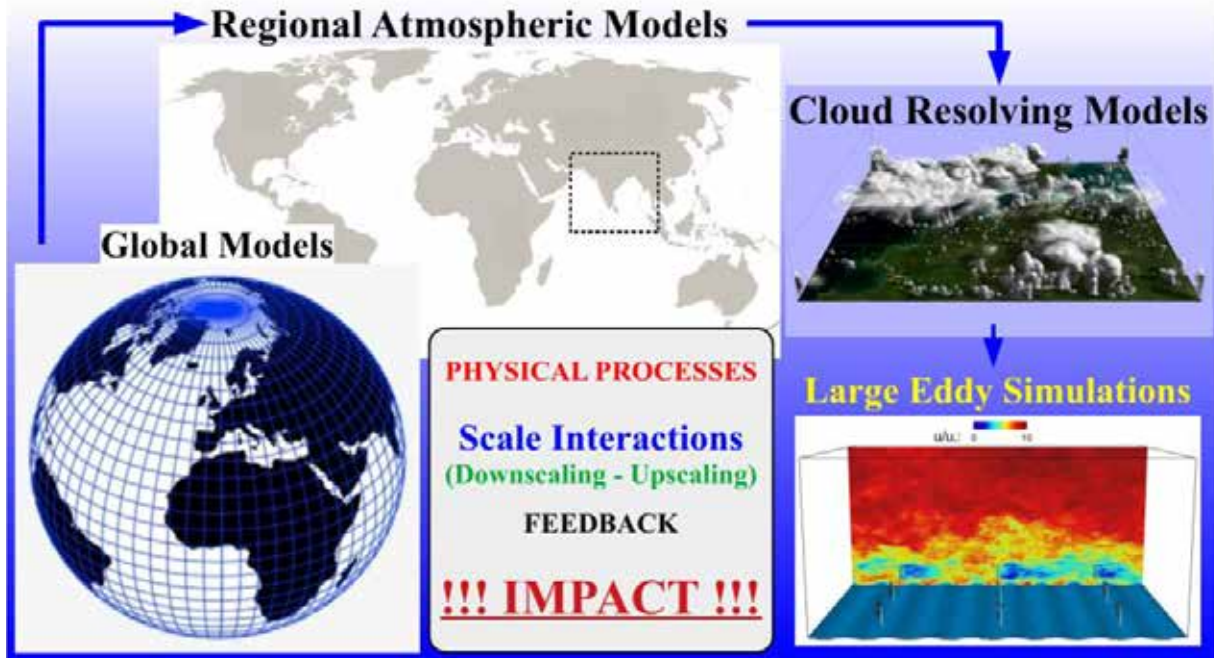
Sobhan Kumar Kompalli

- Four day “Virtual AMS/ACSM users meeting”, 19-22 January 2021.

Mukunda M Gogoi

- Online Orientation Workshop on “Geoportals of ISRO”, 27-28 May 2020.

संख्यात्मक वायुमंडल प्रतिरूपण NUMERICAL ATMOSPHERE MODELLING



संख्यात्मक वायुमंडल प्रतिरूपण शाखा, सामान्य परिचालन नमूनों, क्षेत्रीय संख्यात्मक मौसम पूर्वानुमान व जलवायु नमूनों, वायुमंडलीय परिवहन नमूनों और बड़े भंवर अनुकरणों सहित वायुमंडलीय नमूनों के एक रेंज के माध्यम से मौसम एवं जलवायु प्रणाली के पूर्वानुमान और विश्लेषण से संबंधित वैज्ञानिक पहलुओं पर ध्यान केंद्रित करती है। यह शाखा प्रेक्षित वायुमंडलीय विचलनों के आधार पर, प्रेक्षित विविध विशेषताओं के लिए उत्तरदायी क्रियाविधियों एवं भौतिक प्रक्रियाओं को समझते हुए और प्रतिलोम प्रतिरूपण का उपयोग करते हुए भारतीय क्षेत्र के ऊपर ग्रीनहाउस गैस अभिवाहों का आकलन करते हुए नमूने संबंधी पूर्वानुमानों में सुधार लाने का लक्ष्य करती है। श्रीहरिकोटा से उड़ान भरनेवाले इसरो के प्रमोचन यान अभियानों का लघु-परास मौसम पूर्वानुमान करने के लिए भी यह शाखा सहयोग प्रदान करती है।

The Numerical Atmosphere Modelling branch focuses on the scientific aspects dealing with the prediction and analysis of the weather and climate system through a range of atmospheric models including the general circulation models, regional numerical weather prediction and climate models, atmospheric transport models, and large eddy simulations. It aims at improving the model predictions based on the observed atmospheric variations, understanding the mechanisms and physical processes responsible for various observed features, and optimizing the estimation of greenhouse gas fluxes over the Indian region using inverse modeling. This branch also supports the short-range weather predictions for ISRO's launch vehicle missions from Shriharikota.

वैज्ञानिक टीम / Science Team

राधिका रामचन्द्रन / Radhika Ramachandran[#]
बाला सुब्रहमण्यम डी / Bala Subrahmanyam D.
सिजिकुमार एस / Sijikumar S.
उमा के एन / Uma K. N.

अनुसंधान अध्येता / Research Fellows

अंजुमोल राजू / Anjumol Raju
बूक्या सामा / Bukya Sama

[#] Relieved in January 2021

Numerical Simulation of Tropical Cyclones

Prediction of Tropical Cyclone Trajectories using COSMO Model

The performance of COSMO (Consortium for Small-scale Modelling) model for the prediction of tropical cyclone (TC) trajectories for varying intensities of the storm has been investigated. A total of 8 TCs over the Northern Indian Ocean from 2017 to 2019 are chosen for the evaluation (Fig.1). The initial and lateral boundary conditions (LBCs) for the COSMO model simulations are derived from the analysis and forecast fields of the ICON global model, respectively. This study addresses two important aspects: (i) the COSMO model simulations are assessed for the identification of a TC, and the behaviour of model-simulated cyclone trajectories are investigated in relation with the forecasting lead time; (ii) the predictability of a TC for various intensities of a storm is explored in terms of the pressure drop (ΔP), the maximum sustained wind speed (MSW), and errors in the simulated trajectories of cyclones. For incorporating all the 8 TCs within a uniform time-scale, the calendar day numbers associated with each of these cyclones are indexed as cyclone day numbers spanning from 1 to 49. A composite picture on the mean variations in the model-simulated trajectory as a function of forecasting lead time is shown in Fig. 2. This shows a mean track error of about 50 km for the initial position of the storm, which increases to 95 km for a lead time of 24 h and to about 140 km for a lead time of 48 h.

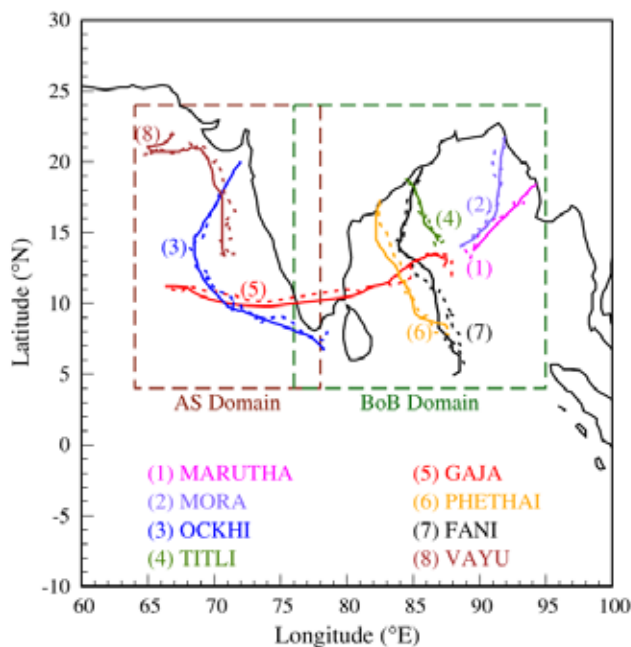


Figure 1: Geographical model domain of the COSMO for the Arabian Sea (AS) and the Bay of Bengal (BoB) is depicted through two rectangular boxes. Also shown are the observed (continuous lines) and predicted (dashed lines) trajectories of the 8 TCs, namely (1) Marutha, (2) Mora, (3) Ockhi, (4) Fani, (5) Titli, (6) Gaja, (7) Phethai, and (8) Vayu [Paul and Subrahmanyam, Meteorol. Atmos. Phys., 2021].

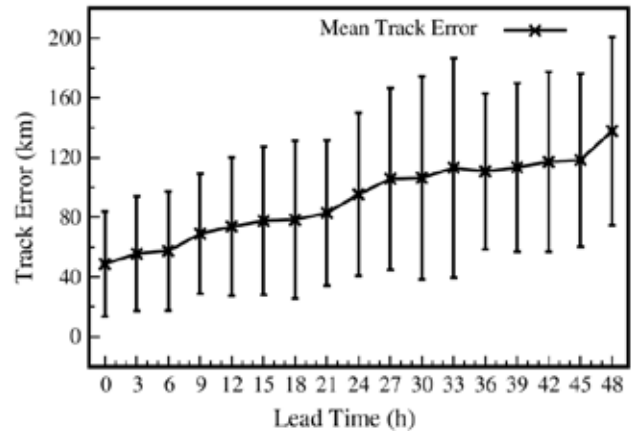


Figure 2: Mean track error in the COSMO model-simulated cyclone trajectories as a function of forecasting lead time. Vertical bars indicate standard deviations (Paul and Subrahmanyam, Meteorol. Atmos. Phys., 2021).

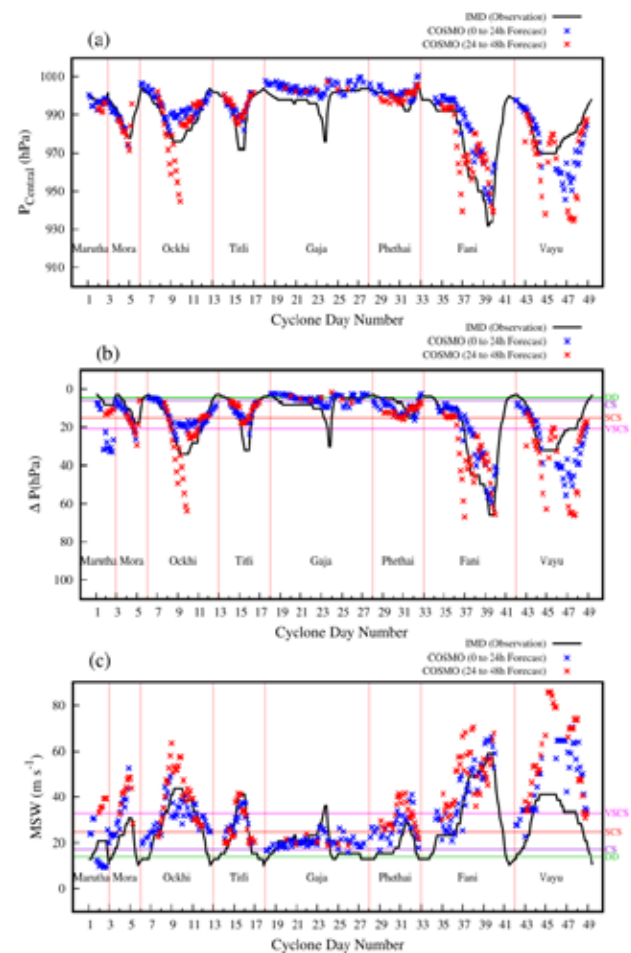


Figure 3: COSMO model simulations together with the IMD observations of (a) estimated central pressure ($P_{Central}$ in hPa); (b) pressure drop (ΔP , in hPa); and (c) maximum sustained surface wind speed (MSW, in $m s^{-1}$) as a function of the cyclone day number. Standard thresholds of the ΔP and MSW for classification of the TC as a Deep Depression (DD), Cyclonic Storm (CS), Severe Cyclonic Storm (SCS), and Very Severe Cyclonic Storm (VSCS) are marked as the horizontal lines in panel b and c [Paul and Subrahmanyam, Meteorol. Atmos. Phys., 2021].

The simulated and observed magnitudes of estimated central pressure (P_{central}), ΔP , and MSW are plotted as a function of the cyclone day numbers in Fig. 3. Qualitatively, there is a fair agreement between the model simulations and observations in terms of P_{central} for a lead time of 0 to 24 h; however, there are large errors in the magnitude of P_{central} with a lead time of 24 - 48 h (Fig. 3a). The gross features in the temporal variation of P_{central} as well as ΔP observed by IMD are well reflected in the model simulations, but the differences between the model and observation tends to increase for the most intense phase of a TC (Fig. 3 a-b). To investigate whether the COSMO model simulations behave differently for different stages of a storm, the database is classified into four categories namely, the DD, CS, SCS, and VSCS, as marked in Fig.3. COSMO model simulations with a lead time of 0 – 24 h yield better agreement with the concurrent observations as against those with a lead time of 24 h – 48 h. During the initial stage of a cyclone, when its intensity is equal to that of a DD, COSMO overestimates ΔP irrespective of the forecasting lead time; however, the magnitudes of MSW are found to be close to the observations for the first 24 h. Beyond a lead time of 24 h, the MSW is roughly overestimated by 5 m s^{-1} . In conjunction with the errors in ΔP and MSW, the exact location of the storm also remains uncertain during the DD stage of a cyclone.

Large variations in the track error (15–140 km) are observed during the initial stage of a TC, when the storm is categorized as a DD. As the intensity of the storm increases from a DD to CS, SCS, VSCS, and ESCS, the track

error decreases with increasing magnitudes of ΔP . Such a decline in the track errors with increasing intensity of the storm indicates improved accuracy in the identification of the storm's position when it is well established. Thus, the predictability of the cyclone tracks for the VSCS stage is better than the remaining stages of the storm; however, the magnitudes of pressure drop and MSW are underestimated in this stage. This implies that the COSMO can capture the location of a storm with better accuracy after it attains severe intensity. As the forecasting lead time goes beyond 24 h, the track prediction for the VSCS stage is still better than the other stages of a storm, but the intensity of the storm is overestimated.

Assessment of Convection / ABL Processes during Ockhi Cyclone

Ockhi was one of the rarest cyclonic storms in terms of its genesis location and rapid intensification. A well-marked low-pressure system was observed over the Comorin Sea in the early morning hours at 0530 IST on 29 November 2017. This became a depression by 0830 IST on 29 November 2017 and crossed Sri Lankan coast and moved northwestward. On the same day, P_{central} of this system dropped by more than 4.5 hPa and became a deep depression. Within 6 hours after becoming deep depression, it turned into a cyclonic storm; this rapid intensification was unusual compared to normal storms. Due to its long life span and associated intense rainfall over the central Arabian Sea, this cyclonic event is an ideal case for investigation on the treatment of convection and ABL processes in the COSMO model.

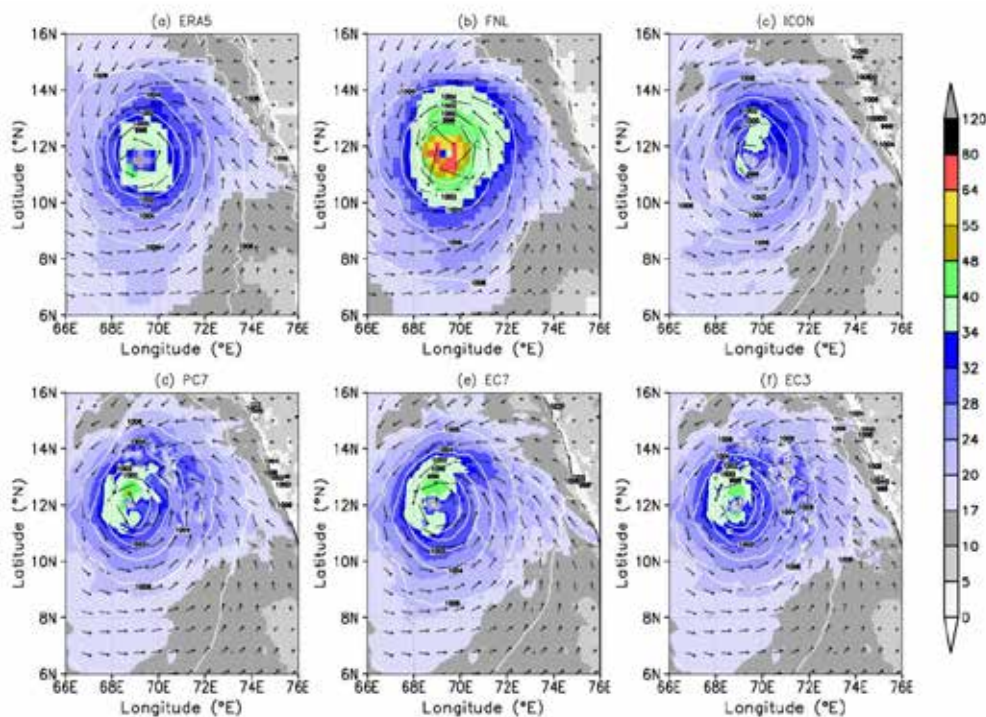


Figure 4: Sea level pressure (in hPa) and maximum sustained surface wind speed (in m/s) corresponding to 00 UTC of 3 December 2017 in (a) ERA5 reanalysis, (b) FNL reanalysis; and (c) ICON analysis fields. (d)–(f) a time-lagged ensemble mean forecast of different lead times obtained from COSMO for PC7, EC7 and EC3 simulations [Roshny et al., SN App. Sci., 2020].

Impact Analysis of Dynamical Downscaling on the Treatment of Convection

This study provides an impact analysis of the implicit and explicit treatment of convection in COSMO for an intense convective episode associated with the passage of Ockhi cyclone. The main objectives of this investigation are: (1) to study impact of downscaling on different atmospheric fields; (2) to assess the relevance of implicit treatment of convection at very fine grid resolutions. A time-lagged ensemble of model simulations with different lead times of +48 h, +36 h, +24 h, and +12 h is considered for addressing the above-mentioned objectives and configured three distinct numerical experiments with the COSMO model.

In the first set of simulations (parameterized convection at ~ 7 km resolution, hereafter referred to as the PC7 simulations), COSMO model is configured for a spatial grid resolution of 0.0625° (~ 7 km), and the necessary constant and varying surface/atmospheric variables are downscaled from coarse grid ($\sim 0.13^\circ$) fields of ICON to a fine grid (0.0625°) of COSMO for the generation of initial and lateral boundary conditions. For PC7 simulations, convective processes are parameterized using the Tiedtke scheme. In the second set of simulations (explicit treatment of convection at ~ 7 km resolution, hereafter referred to as the EC7 simulations), the grid resolution of the model is kept as same as the PC7 simulations, but the convective processes are explicitly simulated, and the provision for parameterization of convection is switched off. The last set of simulations (explicit treatment of convection at ~ 3 km resolution, hereafter referred to as the EC3 simulations) are similar to the EC7 simulations, except for the reduced horizontal grid resolution of 0.025° .

Figure 4 compares the spatial maps of sea level pressure and 10 m horizontal wind fields simulated by COSMO, with the global datasets. Spatial maps of sea level pressure inferred from the ERA5 and FNL reanalysis as well as the ICON analysis clearly showed the presence of a prominent low-pressure region with a pressure drop of more than 15 hPa over the central Arabian Sea. The location of the low-pressure region simulated by three global models is within a range of about 50 km from the actual location reported by the IMD. All three configurations of COSMO model simulations could also capture the presence of an intense low-pressure system. Interestingly, COSMO model simulations with three distinct configurations do not show significant differences among themselves in terms of the intensity and location of the low-pressure region. This indicates that simulation of large-scale feature is more important in such cases rather than representation of fine-scale features. The ERA5, FNL, and ICON global models showed identical large-scale features, but differed from each other in terms of the magnitudes of associated wind speed which ranged from 32 to 80 knots. In contrast, the differences in the magnitudes of the wind speed simulated by three distinct configurations of COSMO were very minimal.

Figure 5 depicts a time-series of the P_{Central} and maximum sustained wind speed obtained from ICON, COSMO and IMD. As Ockhi turned into a VSCS at 12 UTC of 1 December, P_{Central} over the eye of the cyclonic storm further dipped from 986 to 976 hPa at 6 UTC of 2 December 2017. In the case of ICON forecasted fields, the simulated core pressure was in the range of 989–991 hPa. However, the COSMO model with three configurations yields core pressure to a minimum of about 984 hPa, which is better than the ICON fields. Nonetheless, it has to be noted that the estimated core pressure from COSMO was still higher than the observed central pressure. The magnitudes of maximum sustained winds simulated by ICON were relatively lower than the concurrent values obtained from three distinct configurations of COSMO (Fig.6b). These differences can be attributed to the wind-pressure relationship, as the magnitudes of P_{Central} in ICON simulations were higher than that of the COSMO. During the first 24 h of simulations, PC7 and EC7 configurations of COSMO yield almost similar magnitudes of wind speed, whereas the EC3 configuration allows the system to become more intense. Though the observed wind speeds were not as intense as that seen in the EC3 configuration, it is interesting to note that the finer resolution allows the tropical storm to become more intense, which is likely to be a systematic impact of the finer resolution.

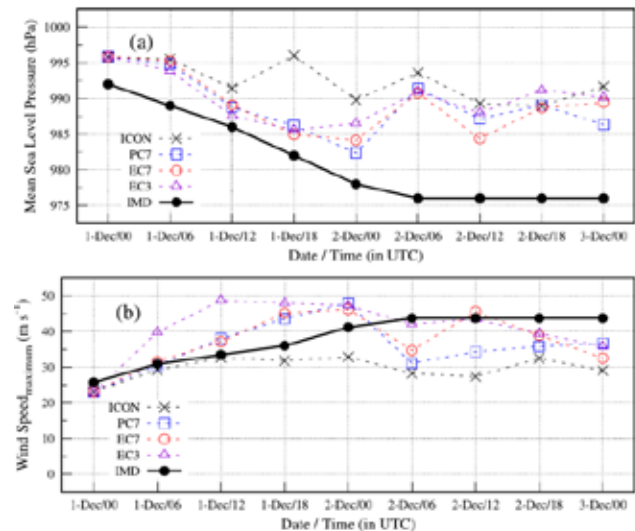


Figure 5: (a) Time-series plot of minimum central pressure (in hPa) observed over the core of cyclonic storm through ICON fields and COSMO simulations, together with the estimated central pressure by IMD. (b) Same as (a), but for the maximum sustained surface winds (in m/s) [Roshny et al., SN App. Sci., 2020].

As shown in Fig.6, the parameterized convective simulation PC7-24 yield fairly widespread rainfall over the central Arabian Sea similar to that seen in the IMERG data (which is satellite-based rainfall estimate). The EC7 and EC3 configurations of the COSMO result in a lack of rainfall for a broader region of the model domain. In general, the area with heavy precipitation is confined to a very small region across the track of Ockhi in EC7 and EC3 simulations. One

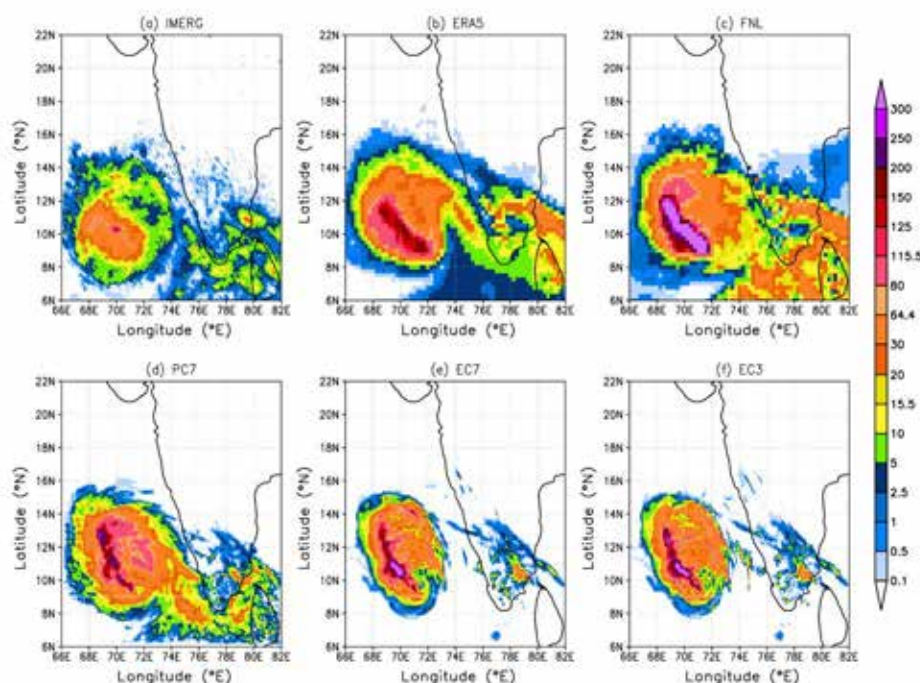


Figure 6: 24 h accumulated rainfall (in mm), from 00 UTC of 2 December 2017 to 00 UTC of 3 December 2017 extracted from (a) satellite-based IMERG data, (b) ERA5 reanalysis, (c) FNL reanalysis; bottom row: (d)–(f) concurrent + 24 h predictions based on PC7, EC7 and EC3 simulations, respectively [Roshny et al., *SN App. Sci.*, 2020].

of the important conclusions from this comparison is that the difference between in the estimated rainfall between EC7 and EC3 is much smaller than the difference between EC7 and PC7. This indicates that the impact of representation of convection is more important than the spatial resolution of the model.

Impact of Ockhi on the Vertical Structure of Marine ABL (MABL)

The impact of Ockhi cyclone on the MABL parameters over the Arabian Sea is investigated by comparing the characteristics of MABL parameters during the normal days with the cyclone-affected disturbed days using COSMO model simulations. Synoptic charts of sea-level pressure corresponding to 1200 UTC (i.e. 1730 IST) are used for the identification of the eye of the storm. To distinguish the impact of the Ockhi on the MABL parameters from day-to-day variations, the time-series data over the six locations of the cyclone during the passage through the Arabian Sea from 30 November to 05 December 2017 (hereafter referred to as days 30N, 01D, 02D, 03D, 04D and 05D) is classified into two categories: (i) the control days and (ii) the disturbed days. The temporal evolution of different MABL parameters over the six locations is examined during the passage of the storm. At each location, the data is classified for a time duration of 24 h centred at 1200 UTC (i.e. 12 h before the arrival and 12 h after the departure of the storm). Similarly, the impact of the storm on the control days is avoided by selecting the data only if the eye of the storm was at least 36 h away from the current location. On average, the eye of the storm was moving with a mean

velocity of 14.3 km/h, and crossed the six locations at 1200 UTC on subsequent days from 30 November to 5 December 2017. The mean diameter of the eye was about 25 to 45 km; therefore, the time-series data between 1000 UTC and 1400 UTC for the disturbed days can be taken to represent the characteristics of the eye.

During the control days, the maximum incoming solar radiation ranged between 132 and 864 W m^{-2} with a mean of about 650 W m^{-2} (Fig. 7a). For the disturbed days, the incoming solar radiation at the surface was absent during 0100 UTC to 0700 UTC, and the magnitudes of S_{in} ranged between 0 and 12 W m^{-2} (Fig. 7a). Due to the prevailing cloudy conditions, the peak magnitude of S_{in} (82 W m^{-2}) for the disturbed days was significantly lower than that on the control days. The mean diurnal variations of the surface-layer parameters shown in Fig. 7a-e indicate significant differences between the control and the disturbed days. During the control days, the mean magnitude of SHF was about 10 W m^{-2} , whereas the LHF was about 125 W m^{-2} . In contrast, the mean SHF on the disturbed days was approximately four times of its mean value on the control days. The LHF values on the disturbed days were approximately two times the mean magnitude of the control days. A gradual decay in the magnitudes of SHF and LHF during the first half followed by a gradual rise in their magnitudes from 1200 UTC in the second half of the day is discernible (Figs. 7c–d). At 1200 UTC on the subsequent days, the eye of the storm was positioned over these six locations, resulting in weak winds, which led to low values of fluxes at 1200 UTC. Mean magnitude of P_s for the

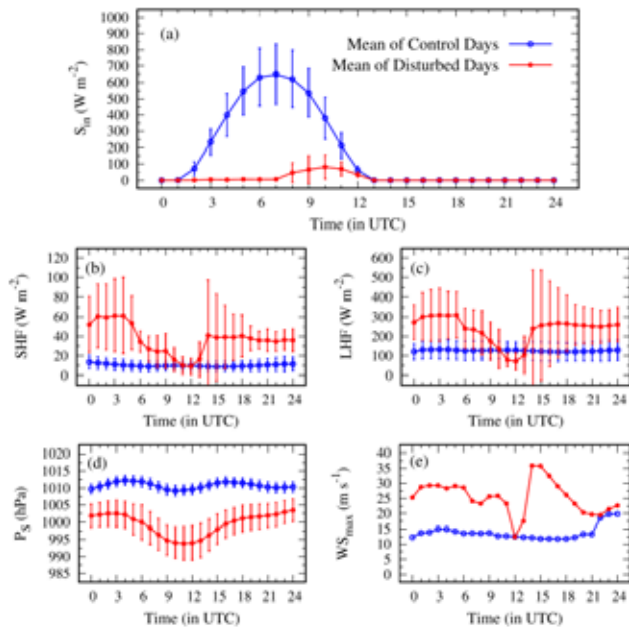


Figure 7: Mean diurnal variations in (a) incoming solar radiation at surface (S_{in}) in $W m^{-2}$, (b) sensible heat flux (SHF) in $W m^{-2}$, (c) latent heat flux (LHF) in $W m^{-2}$, (d) surface pressure (P_s) in hPa and (e) maximum sustained surface wind speed (WS_{max}) in $m s^{-1}$ simulated by COSMO for the control and disturbed days. Vertical bars indicate the standard deviation of the concerned parameter for that particular time. WS_{max} is a single peak value; hence, there are no vertical bars associated with it [Subrahmanyam et al., Bull. Atmos. Sci. Tech., 2020].

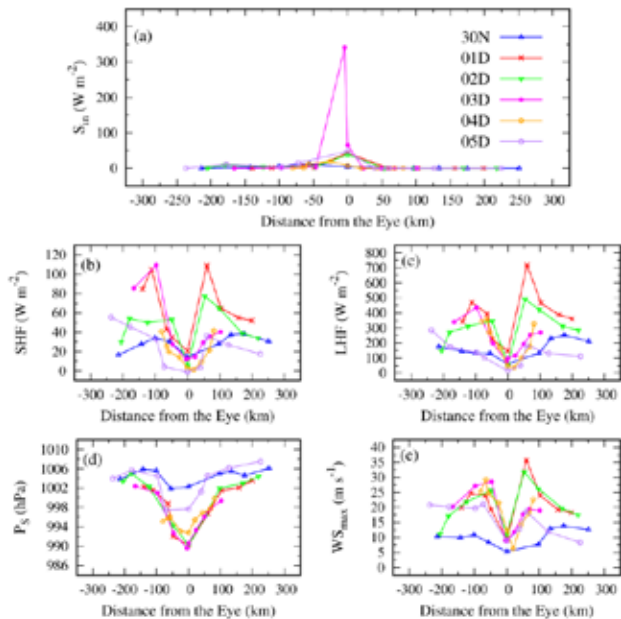


Figure 8: Spatio-temporal variation in (a) incoming solar radiation at surface (S_{in}) in $W m^{-2}$, (b) sensible heat flux (SHF) in $W m^{-2}$, (c) latent heat flux (LHF) in $W m^{-2}$, (d) surface pressure (P_s) in hPa and (e) maximum sustained surface wind speed (WS_{max}) in $m s^{-1}$ simulated by COSMO over six time-series locations, namely, 30N to 05D for the disturbed days (i.e. 30 November to 5 December 2017). The variations are plotted as a function of the horizontal distance between the eye of the storm and respective location [Subrahmanyam et al., Bull. Atmos. Sci. Tech., 2020].

control days was about 1011 hPa while it was about 999 hPa for the disturbed days (Fig. 7d), indicating lowering of P_s by about 12 hPa on the disturbed days. Similarly, the mean magnitude of WS_{max} for the disturbed days ($= 17.7 m s^{-1}$) was about three times larger than that of the control days ($= 6.3 m s^{-1}$) as shown in Fig. 7e.

The variations in S_{in} , SHF, LHF, P_s and WS_{max} are shown as a function of the distance between the eye and six respective locations for the disturbed days in Fig. 8a–e. The line plots in Fig.8 correspond to a duration of 24 h each during which the storm crossed the respective location. The distance between the eye and the time-series location (30N to 05D) corresponding to the first half (second half) of the day is indicated as negative (positive) when the storm was approaching (moving away from) these locations. The zero distance in X-axis corresponds to 1200 UTC when the eye of the storm was over the respective location. The eye of the storm was characterized by low values of SHF, LHF, P_s and WS_{max} over the six locations at 1200 UTC, which is indicative of the calm conditions over the eye (Figs.8b–e). In contrast, the eye-wall region spreading radially outward between 50 and 200 km from the centre of the storm experienced large values of SHF and LHF (Figs.8b–c). The eye-wall region is subjected to a large pressure gradient force, yielding large values of WS_{max} . High values of LHF over the eye-wall region are due to the large winds and vertical flux of moisture from the sea surface.

Based on the equivalent day analysis of surface-layer parameters in association with the altitude profiles of thermodynamic parameters for the control days, the convective mixed layer was seen to extend up to 800 m, which was capped with a thin stable layer. On most of the control days, the mixed layer was capped with stratus and stratocumulus clouds which extend up to an altitude of about 3000 m and a prominent trade-wind inversion was observed on top of it. On the disturbed days, the entire MABL was highly moist and convective clouds with vertical development were observed along the eye-wall regions of the storm. In extreme cases, the cloud base on the disturbed days was as low as 100 m, and the convective mixed layer was very shallow. The top of the mixed layer was marked at the cloud base itself, which was comparatively at lower heights than those seen during the fair-weather conditions.

During the control days, the the conserved variable analysis (CVA) shows a conventional ABL mixing line within the MABL, wherein the magnitudes of θ_e and q decrease gradually with increasing altitudes (Fig.9). Close to the marine surface, a large amount of moisture and warm air temperatures yield high values of θ_e . During typical daytime conditions, the rising air parcel experiences vertical convective mixing and travels along the ABL mixing line until it reaches the top of the MABL. Above the MABL, the air parcel undergoes radiative cooling during which the amount of moisture q remains constant. The CVA during the control days shows a fair representation of the

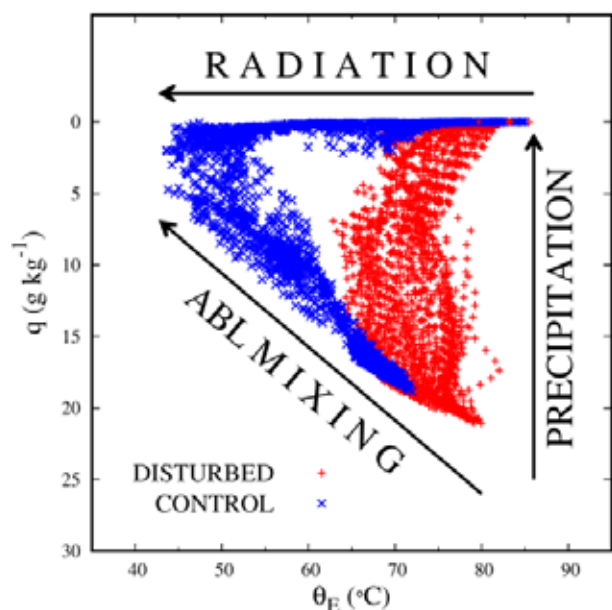


Figure 9: Conserved variable analysis plots between the equivalent potential temperature (θ_e) shown along the X-axis in deg.C and specific humidity (q) along the Y-axis in $g\ kg^{-1}$ for the control (symbol 'x') and the disturbed days (symbol '+'). Y-axis labels are intentionally reversed so as to resemble a altitude profile of q . Three important thermodynamic processes of the atmospheric boundary layer (ABL) mixing, radiation and convective precipitation are schematically represented through arrows [Subrahamanyam et al., Bull. Atmos. Sci. Tech., 2020].

ABL mixing within until the top of the MABL, which is capped by the radiative cooling processes. In contrast, the disturbed days tends to follow a typical precipitation line. During the disturbed days, the ascending deep convective cell of the storm moves the air parcel from the sub-cloud layer to the free troposphere above without distinct changes in the magnitude of θ_e . A consistent latent heat release from the precipitating clouds heats the surrounding environment,

and the air parcel follows the precipitation line, wherein the magnitude of θ_e remains almost constant. At the same time, q gradually decreases with increasing altitudes.

Assessment of Reanalysis Data

Assessment of Vertical Air Motion in Reanalyses Data Using Radar Measurements over Two Tropical Stations

Vertical wind (w) in any region of the Earth's atmosphere reflects the structure and dynamical features of that region. It controls the intensity of convection and vertical transport of mass, energy, moisture and trace gases, which play a crucial role in the vertical coupling of the atmosphere. Different scales of variability exist in w ranging from microscale to synoptic scale. Reanalysis data of w is widely used for assessing convection, vertical transport and diabatic heating. For the first time, the present study assesses the reanalysis data on vertical wind (NCEP-2, MERRA-2, ERA-Interim, ERA-5, and JRA-55) by comparing them with 20 years of radar data from Gadanki and Kototabang, two convectively active tropical regions.

Figure 10 shows the climatological monthly mean altitude profiles of w observed using Indian MST radar (IMSTR) and those obtained from ERAi, ERA5, MERRA-2, NCEP/DOE-2 and JRA-55 reanalysis data over Gadanki. Significant differences are seen between the observations and reanalysis data on w . Part of these differences is due to the spatial averaging implicit in the reanalyses products, whereas the radar measurements are for a single point. Hence, only the tendency of w is evaluated here. The IMSTR observations show updrafts between 8 and 20 km from December to April, with the largest values in the tropical tropopause layer (TTL, about 12-16 km). These features are not reproduced by any of the reanalyses, all of which show downdrafts from December to April between 1 km

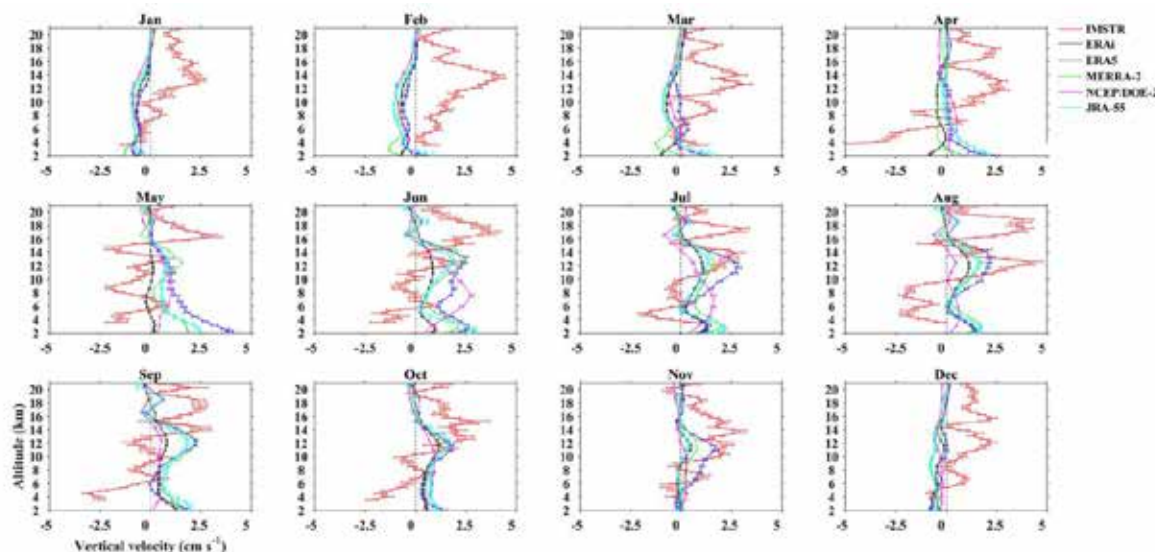


Figure 10. Climatological monthly mean altitude profile of w obtained from Indian MST Radar (IMSTR) and 5-reanalysis over Gadanki from 1995-2015. Horizontal lines indicate the standard error [Uma et al., Atmos. Chem. Phys., 2021].

and the tropopause level (mean tropopause is ~ 16.5 km). The vertical velocity in ERAi differs in both magnitude and direction from other reanalyses, especially in the lower troposphere from March to June. The magnitude of vertical velocity in ERA5 is a little larger than that in the other reanalyses from May to June. Updrafts are observed in the TTL by the IMSTR during June, when all reanalyses show similar features but only located below the TTL. During July and August, the radar observations and the reanalyses data show updrafts in the vicinity of the TTL. Updrafts are observed in the TTL from September to November but the peak in the updrafts in the reanalyses data is shifted lower than that observed by the IMSTR. Below 8 km, the IMSTR shows downdrafts from April to October. The reanalyses data are unable to reproduce downdrafts above 2 km.

Vertical velocity from the EAR (Equatorial Atmospheric Radar) at Kototabang is also analyzed where the observations are available for the full diurnal cycle. All reanalyses data over Kototabang are averaged for the full diurnal cycle. The updrafts observed by the radar in the TTL are well reproduced by all five reanalyses although the magnitude and vertical location of the maximum in w remain lower than observed. However none of the reanalyses reproduces the downdrafts. A distinct bimodal distribution in w from May to September (two peaks between 8-10 km and 14-17 km) with a local minimum between 12 and 13 km is observed in the EAR measurements which are not observed in the reanalysis. The magnitudes of both updrafts and downdrafts are larger than those observed over Gadanki. JRA-55 produces the largest w among the reanalyses. The monthly means show significant differences in the direction of w between the observations and the reanalyses below 6 km.

The directional tendencies of reanalysis data relative to the radar measurements are shown in Fig.11. The directional tendencies would be 100% when all radar measurements at certain height range are reproduced by a reanalysis in terms of vertical wind direction. The tendency is calculated separately for updrafts and downdrafts. The directional tendency is calculated at each height for every month when the radar or reanalysis data exceed 0.1 cm s^{-1} in either directions and aggregated into seasons. Over Gadanki during December-February (DJF), all reanalyses produce updrafts only for less than 10% of the time throughout the profile. During March-May (MAM), it increases to around 15%, with NCEP/DOE-2 reproducing updrafts about 25% of the time. During June-August (JJA) and September-November (SON), the percentage occurrence increases with the height from 25% to a maximum of 50% between 12 and 14 km. The percentage occurrence of updraft then decreases from 14 to 20 km. This trend is similar for all reanalyses. The maximum ratio of updrafts over Gadanki is located between 12 and 15 km altitude. The percentage occurrence of downdrafts over Gadanki is also less than 50% at all levels. During DJF and MAM the reanalyses reproduce downdrafts 40 to 50% of the time, a much higher frequency than that for updrafts ($<10\%$). This fraction decreases above 10 km. By contrast, the percentage of downdrafts reproduced during JJA and SON is less than that of updrafts, with frequencies less than 25% at all levels during these seasons. Over Kototabang the percentage occurrence of updrafts increases with height in all seasons reaching a maximum of 75- 90% between 10 and 14 km. Above 14 km the percentage decreases to a minimum of 5% at 19 km. Updrafts are rarely reproduced by the reanalyses at altitudes less than 4 km. It is important to note that none of the reanalyses reproduce daily mean downdrafts exceeding 1 cm s^{-1} except ERAi and ERA5

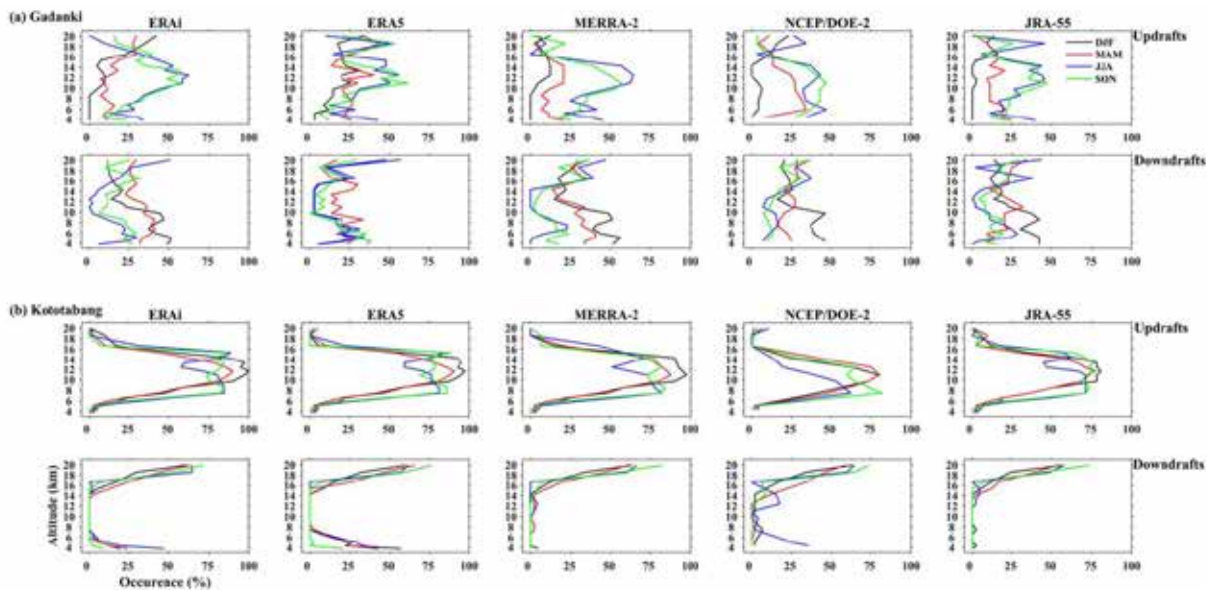


Figure 11. Comparison of directional tendency of w between the radars and various reanalysis data sets for (a) Gadanki (1995-2015) and (b) Kototabang (2001-2015). Updrafts are shown in top and third panels and downdrafts are shown in middle and bottom panels [Uma et al., Atmos. Chem. Phys., 2021].

which reproduced downdrafts below 6 km. The percentage of downdrafts increases above 17 km where it reaches a maximum and show occurrence frequencies around 65 to 75% above 18 km.

Ongoing Studies

Role of Deep Convection in Regulating the Indian Summer Monsoon Dynamics

The deep convection and associated moist processes have a major role in regulating circulation and precipitation characteristics of the Indian summer monsoon. This aspect was examined using sensitivity experiments with the Weather Research and Forecast model. Three active monsoon cases during the periods 16-25 June 2015, 20-29 July 2010 and 1-9 August 2007 were selected for the study. Control simulations with reanalysis data revealed that the model could capture general features of the mean precipitation and circulation pattern during those active monsoon periods. In sensitivity experiments, latent heating process in the model was switched off and all other conditions were kept same as that of control simulations. The removal of latent heat release in the model suppressed deep convection over the monsoon domain and causes substantial reduction in precipitation. A large scale descending motion appears in the mid-troposphere, hampering the vertical growth of clouds. As a result, thick cloud bands form in the lower atmosphere

that reduce the incoming short wave radiation reaching the surface causing land surface temperature reduction over the Indian region. The present study unambiguously established the fact that the organized deep convection and concomitant vertical heating over the monsoon domain has a prominent role in regulating the monsoon dynamics.

Atmospheric Inverse Modelling for assessing Carbon Fluxes over the Indian Region

Atmospheric inverse modelling is used to estimate biospheric and fossil fluxes over India using prior inventory fluxes, backward simulations of Lagrangian particle dispersion model FLEXPART and CO₂ observations from the stations Thumba and Sinhagad. Preliminary analysis of the data showed noticeable modifications in the annual mean posterior fluxes over the regions near to stations Sinhagad and Thumba. Mostly the posterior flux values are higher than that of the prior fluxes. On a seasonal scale, post monsoon season showed maximum changes covering the entire peninsular and central India. During winter and pre-monsoon seasons, noticeable enhancement in fluxes was observed over the southern peninsular India. The monsoon season showed increase in fluxes over the west coast of peninsular India. The study pointed out that even with two observations from the Indian region, noticeable changes in posterior fluxes are found over most part of India.

Future Projections

- Quantification of CO₂ and CH₄ fluxes over the Indian region through Bayesian inverse modelling by incorporating ground and space based observations.
- Investigating the role equatorial waves in the rainfall characteristics over the southern peninsular India.
- Investigation of the diurnal variability in the atmospheric boundary layer parameters with the aid of Parallelized Large Eddy Simulation (PALM) model
- Analysis of the surface-layer turbulent fluxes during a clear-sky and a cloudy day through PALM model
- Treatment of ABL and Convective Processes in Large Eddy Simulation (LES) model

Publications in Peer-Reviewed Journals

1. Subrahmanyam, D. Bala, Roshny S., Freddy P. Paul, Anurose T. J., and Radhika Ramachandran, "Impact of a very severe cyclonic storm 'OCKHI' on the vertical structure of marine atmospheric boundary layer over the Arabian Sea", *Bulletin of Atmospheric Science and Technology*, 1, 407 – 431, <https://doi.org/10.1007/s42865-020-00020-7>, 2020.
2. Uma, K. N., S. S. Das, M. V. Ratnam, and K. V. Suneeth, "Assessment of vertical air motion among reanalyses and qualitative comparison with direct VHF radar measurements over the two tropical stations", *Atmospheric Chemistry and Physics*, 21, 2083 – 2103, <https://doi.org/10.5194/acp-21-2083-2021>, 2021.
3. Freddy, P. Paul, and D. Bala Subrahmanyam, "Prediction of tropical cyclone trajectories over the Northern Indian Ocean using COSMO", *Meteorology and Atmospheric Physics*, 133, 789 – 802, <https://doi.org/10.1007/s00703-021-00782-5>, 2021.
4. Roshny, S., D. Bala Subrahmanyam, Anurose T. J., and Radhika Ramachandran, "An assessment of a very severe cyclonic storm in the Arabian sea using the COSMO model", *SN Applied Sciences*, 2, 1869, <https://doi.org/10.1007/s42452-020-03645-7>, 2020.
5. Santanu Halder, Yogesh K. Tiwari, Vinu Valsala, M. G. Sreeush, S. Sijikumar, Rajesh Janardanan, Shamil Maksyutov, "Quantification of Enhancement in atmospheric CO₂ background due to Indian biospheric fluxes and fossil fuel emissions", *Journal of Geophysical Research (Atmosphere)*, <https://doi.org/10.1029/2021JD034545>, 2021.

-
6. Valsala, Vinu, Sreeush M. G, Anju M, Sreenivas Pentakota, Tiwari Yogesh K, Chakraborty Kunal, S. Sijikumar, “An observing system simulation experiment for Indian Ocean surface pCO₂ measurements” *Progress in Oceanography*, 194, 102570, <https://doi.org/10.1016/j.pocean.2021.102570>, 2021.
 7. Das, S. K., Tanaya Thatte, K. N. Uma, U. V. Murali Krishna, and Sanjoy Kumar Saha, “Characteristics of temperature inversion from radiosonde measurements in the Western Ghats region”, *Atmospheric Research*, 250, 105391, <https://doi.org/10.1016/j.atmosres.2020.105391>, 2021.

Invited Talks

Bala Subrahmanyam D.

1. “Historical Evolution of the Atmospheric Boundary Layer: Past, Present and Future”, ARIES Online Remote Colloquium, Aryabhata Research Institute for Observational Sciences (ARIES), Nainital, Colloquium No. 454, 16 Jul 2020.
2. “Role of Atmospheric Boundary Layer in Air-Sea Interaction Processes”, OSI Webinar Series, Ocean Society of India, 23 January 2021.

Uma K. N.

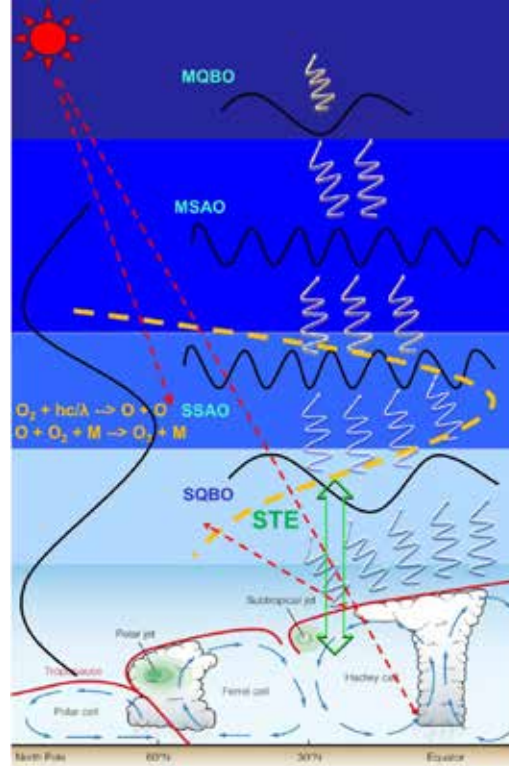
1. “Monsoon Convection – A Radar and Satellite Perspective” as a part of National Webinar “Recent developments and challenges in weather and climate-Indian perspective”, Andhra University, Visakhapatnam, 25 August 2020.
2. “Indian Space Programme” at Ebenezer International School and Kuraikose Elias English medium school, Kottayam and Sree Narayana Public School as a part of World Space Week celebrations held during 04 - 10 October 2020.
3. “Indian Space Programme” organized by Navodya Schools around South India, 17 October 2020.

Training Programme

Uma K. N.

1. Program on Integrated Scientific Project Management for Women Scientists/Technologists organised by Centre for Organisation development (COD), Hyderabad during 18-22 January 2021.
2. Attended Stress Management Programme conducted by HRDD, VSSC, Trivandrum, 19 - 21 October 2020.

वायुमंडलीय गतिकी शाखा ATMOSPHERIC DYNAMICS BRANCH



क्षोभमंडल से निम्न तापमंडल तक ऊर्ध्वाधर युग्मन सहित पृथ्वी के वायुमंडल की गति को बदलने के लिए उत्तरदायी वायुमंडलीय प्रक्रमणों पर वायुमंडलीयगतिकी शाखा(एडीबी) अग्रणी अनुसंधान का कार्य कर रही है। इस स्थूल उद्देश्य के साथ अनुसंधान गतिविधियों का लक्ष्य भू तथा अंतरिक्ष आधारित प्रेक्षणों का उपयोग करते हुए गुरुत्वीय तरंगों से सौर चक्र तक वायुमंडलीय तरंगों तथा परिवर्तनीयों के स्पेक्ट्रम का मात्रिकरण करना है। वायुमंडलीय तरंगों का अभिलक्षणन, उनके स्रोत व क्रियाविधि, संचरण अभिलक्षणन, वायुमंडल युग्मन की भूमिका, अल्प व दीर्घकालीन परिवर्तनशीलता तथा वैश्विक नमूनों में प्रतिनिधित्व के आधार पर किया जाता है। यह शाखा बहु मंचीय मापों के ज़रिए समताप मंडल-क्षोभ मंडल विनिमय प्रक्रियाओं पर भी अपना ध्यान केंद्रित कर रही है। व्यापक परिसंचरण तथा मौसम व जलवायु पर उसके प्रभाव भी शाखा के एक मुख्य कार्य के रूप में उभर कर सामने आ रहे हैं।

Atmospheric Dynamics Branch (ADB) is carrying out front line research on atmospheric processes responsible for altering the motion of the Earth's atmosphere including the vertical coupling from troposphere to lower thermosphere. With this broad objective, the research activities are aimed at quantifying the spectrum of atmospheric waves and variabilities from gravity waves to solar cycle using ground and space based observations. The atmospheric waves are characterized in terms of their source mechanism, propagation characteristics, role in atmosphere coupling, short and long-term variability and their representation in global models. The branch also focuses on stratosphere-troposphere exchange processes by employing multi-platform measurements. The large scale circulations and their impact on weather and climate are also emerging as prime research areas.

वैज्ञानिक टीम / Science Team

किशोर कुमार के / Kishore Kumar K.
सिद्धार्थ शंकर दास / Siddarth Shankar Das
सुनिलकुमार एस वी / Sunilkumar S.V.
वेन्कटा सुब्रमण्यम के / Venkata Subrahmanyam K.
जयदेव प्रदीप / Jayadev Pradeep

तकनीकी टीम / Technical Team

मणिकंठन नायर एन / Manikantan Nair N.
मोहम्मद नज़ीर एम / Mohammad Nazeer M.

अनुसंधान सहयोगी / Research Associates

विष्णू आर / Vishnu R.*
प्रमिता एम / Pramitha M.
मरिया इममानुवेल / Maria Emmanuel
कौशिक एन / Koushik N.
स्नेहा सुसन मात्थ्यू / Sneha Susan Mathew

अनुसंधान अध्येता / Research Fellows

सतीष चन्द्रन पी आर / Satheesh Chandran P.R.
अंजना यू / Anjana U.
वीनस वी / Veenus V.

* Relieved in March 2021

Middle Atmospheric Dynamics

Long-Term Observations of Mesospheric Quasi-Biennial Oscillation

Interannual variability of the equatorial middle atmosphere is dominated by the quasi-biennial oscillation (QBO), whose time period ranges from 22 to 34 months with an average period around ~ 28 months. The stratospheric QBO (SQBO) in zonal winds maximizes in 27-30 km altitude region whereas the mesospheric QBO (MQBO) maximizes at around 85-90 km altitude. Owing to relatively frequent and long-term observations of the stratosphere, there are large number of studies on the SQBO as compared to the MQBO. There are some discrepancies in the reported amplitudes as well as period of the MQBO. In this regard, the time evolution of MQBO in the 82-98 km altitude region using long-term meteor radar observations over low and equatorial latitudes and TIMED Doppler Interferometer (TIDI) observations is investigated. The time-height sections of monthly mean zonal winds in the 82-98 km region over Serpog (1993-1998), Koto Tabang (2003-2012) and Thumba (2006-2015) are depicted in Figs. 1a, 1b and 1c, respectively.

A prominent signature of semi-annual oscillation (SAO) can be noticed in the zonal winds below 90 km altitude with the westward winds during equinoxes and the eastward winds during solstices. The second column of Fig.1 shows the wavelet spectra of zonal winds at 90 km

altitude over the three observational sites. The time series of zonal winds are not deseasonalized while computing these spectra depicted in the second column. From Fig.1d, it is evident that there are three prominent oscillations having periodicities of 6, 12 and 24 months corresponding to SAO, AO and QBO, respectively. The QBO is present throughout the observational period with amplitude of ~ 6 m/s at this altitude. This spectrum also shows a prominent QBO and as a result of deseasonalization, the signatures of SAO and AO are diminished.

The QBO signature can be noted from the figures 1e and 1h with peak amplitude of ~ 4 m/s and it is prominently observed during 2006-2012. This observation provides the first clue on the intermittency of the MQBO. In fig. 1f and 1i, the QBO amplitudes are in the range of 3-4 ms^{-1} and present throughout the observational period 2006-2015. From Fig. 1 it is evident that the upper mesospheric winds at 90 km altitude exhibit a robust QBO with relatively larger amplitudes over Serpog as compared to Koto Tabang and Thumba. However, intermittency is observed in the QBO, especially over Koto Tabang where the oscillations are not having significant amplitudes during 2003-2006. Fig.1 thus show that the MQBO amplitudes lie within the range of 3-6 ms^{-1} , which contradicts with the earlier reported values using High Resolution Doppler Imager (HRDI) measurements. The present analysis shows that the MQBO is transient rather than a permanent feature in the MLT region.

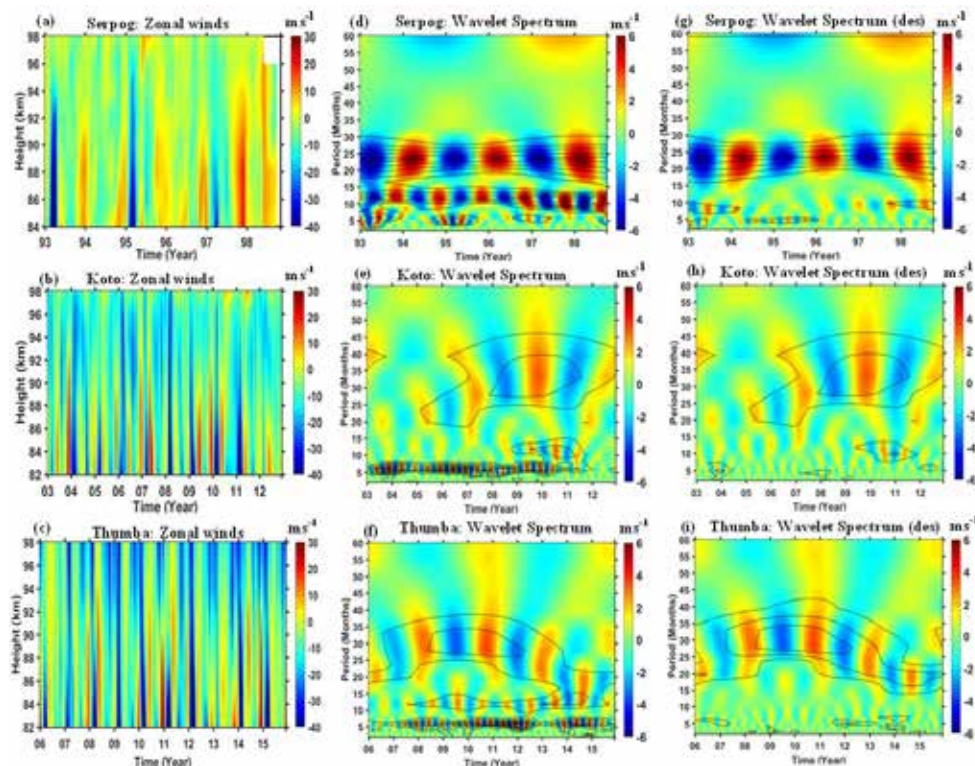


Figure 1: Time-height sections of monthly mean zonal winds over (a) Serpog, (b) Koto Tabang and (c) Thumba. Wavelet spectra of monthly mean zonal winds at 90 km altitude over (d) Serpog, (e) Koto Tabang and (f) Thumba. Wavelet spectra shown in (g), (h) and (i) are also same as (d), (e) and (f) but for deseasonalized zonal winds. Black contours in the wavelet spectra represent 95% confidence levels [Kumar, Geophys. Res. Lett., 2021].

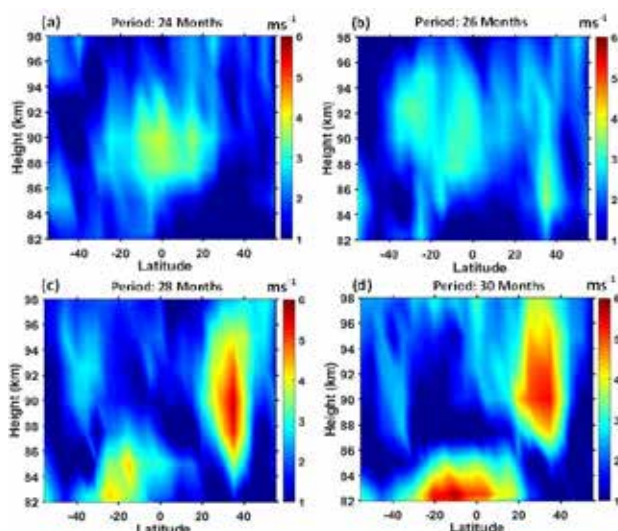


Figure 2: Latitude-height sections of MQBO amplitude for (a) 24, (b) 26, (c) 28 and (d) 30 month periodicities [Kumar, *Geophys. Res. Lett.*, 2021].

The amplitudes of the MQBO with 24-month period are found to be dominant in the 86-94 km altitude region over 20° N-15° S latitudes (Fig. 2a, 2b, 2c, and 2d). The 26-month period shows a broader peak in 0-30°S and a narrow peak around 35-40° N. On the other hand, the latitude-height sections of 28 and 30 month MQBO show similar features with two distinct peaks in the 84-86 km (spread over 20° N-30°S) and 86-92 km altitude regions (spread over 30° N -50° N). Though the generating mechanism for the equatorial MQBO is known, the same for the observed MQBO signature over the northern hemispheric midlatitudes is yet to be established, conclusively.

Stratospheric QBO Modulations of Migrating Diurnal tides in the Mesosphere and Lower Thermosphere over the Low and Equatorial Latitudes

Horizontal wind measurements using meteor radars located at Thumba (8.5°N, 77°E; 2006-2015) Koto Tabang (0.2°S, 100.3°E; 2002-2017) and Tirupati (13.63°N, 79.4°E; 2013-2017) in the mesosphere-lower thermosphere (MLT) and Specified Dynamics Whole Atmosphere Community Climate Model (SD-WACCM) simulations were employed for investigating the diurnal tide variability at quasi-biennial scales. The model simulations are evaluated using the meteor radar observations at three tropical locations. WACCM simulations could reproduce the seasonal evolution of diurnal tides very well over Thumba and Tirupati but there are small discrepancies over Koto Tabang. In order to investigate the modulation of the diurnal tide amplitudes in the MLT region by the SQBO, deseasonalized perturbations of diurnal tides and stratospheric winds are analyzed.

Figure 3 shows the time series of radar measured as well as WACCM simulated diurnal tide amplitudes at 88 km altitude and the SQBO winds at 20 hPa over three study locations. As the diurnal tides in the meridional winds have relatively large amplitudes as compared to those in zonal winds, only meridional diurnal tide perturbations are shown here. One can notice a very good correspondence between meridional diurnal tide perturbation amplitudes and the SQBO phase, which show positive tidal perturbations during the eastward phase of QBO and negative perturbations during the westward phase. The

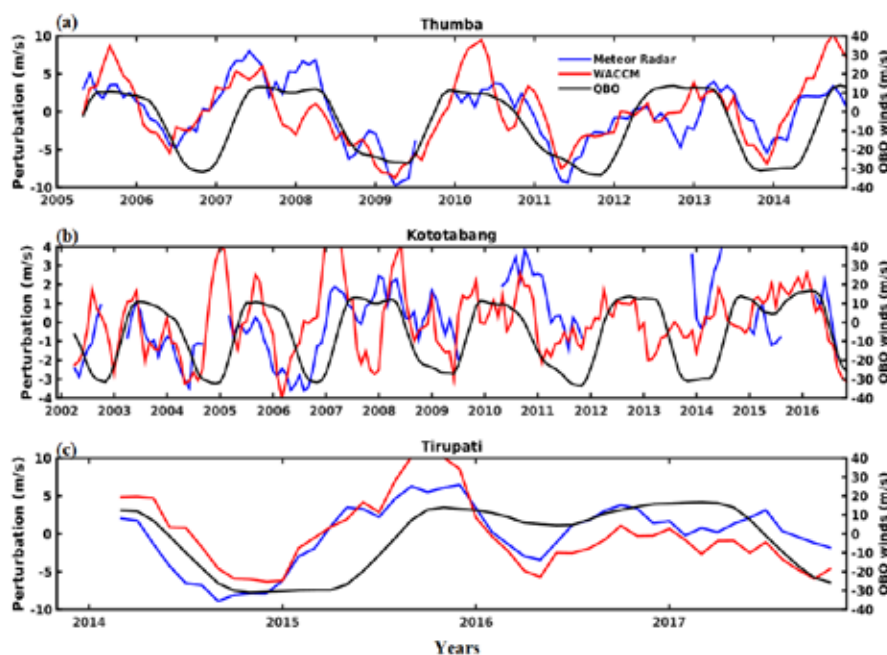


Figure 3: Interannual variability of deseasonalized diurnal tide perturbations in the meridional winds at 90 km altitude derived from meteor radar observations (blue) and WACCM simulations (red) along with SQBO winds (black) at 20 hPa level over (a) Thumba, (b) Koto Tabang and (c) Tirupati [Pramitha et al., *J. Geophys. Res.-Space Physics*, 2021].

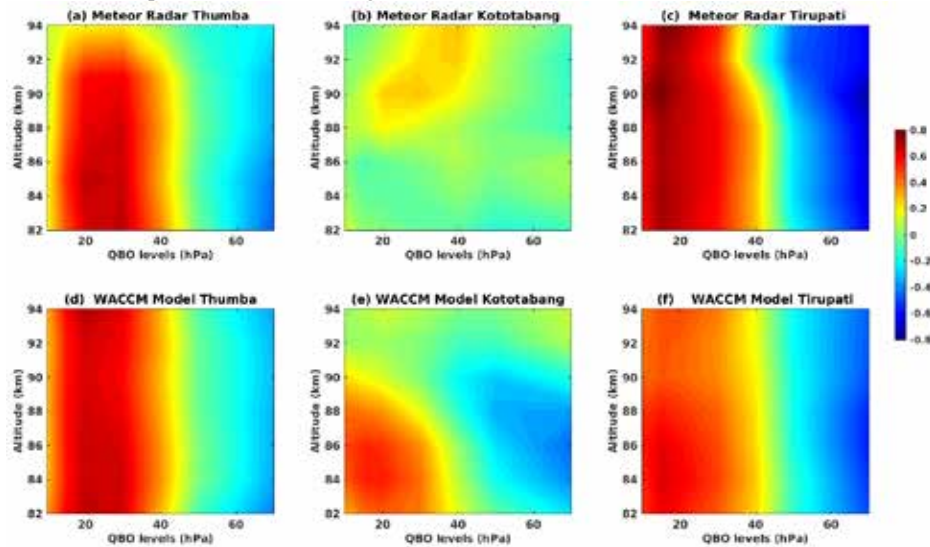


Figure 4: Correlation coefficients between monthly mean diurnal tide perturbations in meridional winds obtained from meteor radar in the 82-94 altitude region and SQBO winds in the 10-70 hPa levels over (a) Thumba, (b) Kototabang and (c) Tirupati. (d), (e), and (f) are same as (a), (b) and (c) but for WACCM simulations [Pramitha et al., *J. Geophys. Res.-Space Physics*, 2021].

observed correlation is relatively weak over Koto Tabang as compared to other two locations. This can be attributed to relatively weak diurnal tide amplitudes in winds over the equatorial region. The WACCM simulated diurnal tide perturbations also show good correspondence with the SQBO as observed by the radars. Though there are notable differences in radar measured and WACCM simulated diurnal tide amplitudes, the deseasonalized perturbations derived from radar and model are comparable as shown in Fig.3.

Further, these deseasonalized meridional diurnal tide perturbations in 82-94 km altitude region are correlated with the SQBO winds in the 10-70 hPa levels as shown in Fig.4. It is interesting to note a significant positive correlation between the diurnal tide perturbations at all the altitude levels and the SQBO winds in 10-40 hPa levels over Thumba and Tirupati. These correlation coefficients are found to be significant at 95% level. However, there is no significant correlation between these two quantities over Koto Tabang at any altitude as seen in Fig. 4b. As expected, a negative correlation is observed between diurnal tide amplitude perturbations and the SQBO winds in the 60-70 hPa, which is very significant over Tirupati as compared to Thumba. The QBO descends downwards at the rate of about 1 km per month. Therefore, the QBO at the 10 hPa level is roughly out of phase with that at the 70 hPa level. The WACCM simulations also show positive correlation of diurnal tide amplitudes with QBO winds in the 10-40 hPa levels and negative correlation with 50-70 hPa levels over Thumba and Tirupati and thus agreeing very well with the radar observations. Overall, the WACCM simulations are able to reproduce the radar observations very well over low latitudes and some discrepancies are observed over the equatorial region. The significance of present study lies in evaluating WACCM simulations at tropical locations using

meteor radar measurements and in investigating the SQBO modulations of diurnal tides.

Disrupted Stratospheric QBO Signatures in the Diurnal Tides over the Low-Latitude MLT Region

Meteor radar measurements of winds in the MLT region over Tirupati (13.63°N, 79.4°E; 2013-2020) and Microwave Limb Sounder (MLS) observations of ozone were used for investigating the effect of the disrupted SQBO during the year 2016 on the diurnal tides. This study reports the signatures of the disrupted SQBO in the diurnal tide variability in the MLT region using meteor radar observations over Tirupati.

Figure 5d depicts the zonal winds in the 50-10 hPa pressure levels during 2014-2019 over Singapore, which readily reveals the well-known pattern of the QBO with descending eastward and westward winds with a period ~28 months. During the year 2016, an abrupt disruption in the QBO structure can be noted and which is highlighted by a rectangular box. The westward winds appear at 40 hPa and block the descending westward winds above 20 hPa. From Fig.5c, the signature of the QBO can be noted in ozone variability, especially during 2014-2016. It is also clear that there is a pronounced negative ozone anomaly during the disrupted QBO period.

From figures 5a and 5b, it is clear that both observations and model simulations show similar variability in the tidal amplitudes, especially during 2014-2016. However, there are some discrepancies between the two during the year 2017. It is interesting to note that the observed variations in ozone and the diurnal tide amplitude perturbations are very similar, especially during 2014-2016 and there is an abrupt decrease in the diurnal tide amplitude in the 82-90 km

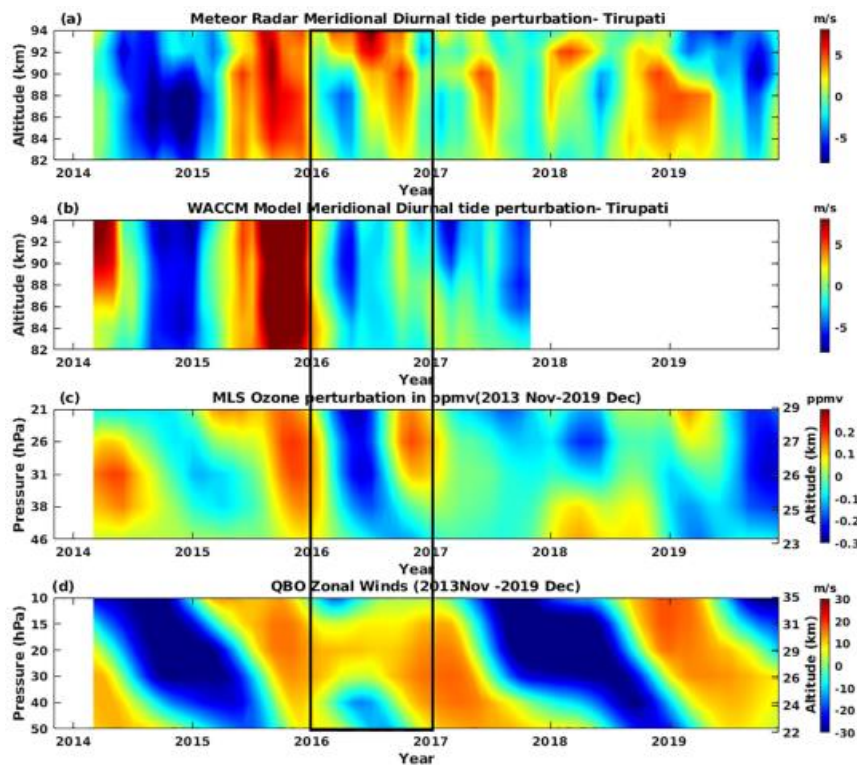


Figure 5: (a) Height (Pressure)-month sections of deseasonalized meridional diurnal tide amplitude perturbations over Tirupati obtained from SVU Meteor Radar. (b) Same as (a) but obtained from SD WACCM simulations (c) Pressure level-month section of deseasonalized ozone perturbations over Tirupati obtained from MLS observations and (d) The SQBO winds over Singapore in the range of 50-10 hPa levels during the period of November 2013 -December 2019. The right side axis of figures (c) and (d) provides approximate altitude. The rectangular box highlights the QBO disruption period [Pramitha et al., Geophys. Res. Lett., 2021].

altitude during the year 2016 following the disruption of the QBO. The observed decrease in the diurnal tide amplitudes associated with QBO disruption is also reproduced by the WACCM simulations. The disruption in the QBO winds resulted in decreased ozone, which is in turn reflected in the diurnal tide amplitudes in the MLT region. However, the role of stratospheric winds in modulating the tidal amplitudes cannot be ruled out completely. This figure thus provides evidence for the role of both winds and ozone in diminishing the diurnal tide amplitudes in the MLT region. Further, to examine the co-variability of stratospheric

ozone and tidal amplitudes in the MLT region, a correlation analysis is carried out between these two quantities at various pressure levels and altitudes over Thumba and Tirupati and is shown in Figs.6a and 6b, respectively. From Figure 6 (a), it can be noted that the ozone perturbations in the 20-40 hPa level show a positive correlation with tidal perturbations in the 80-90 km altitude. However, over Tirupati, the positive correlation between the two is limited to 20-30 hPa levels as shown in Fig.6b with a relatively smaller correlation coefficient as compared to that over Thumba. This implies that the SQBO in winds and ozone is correlated and thus can have similar relation

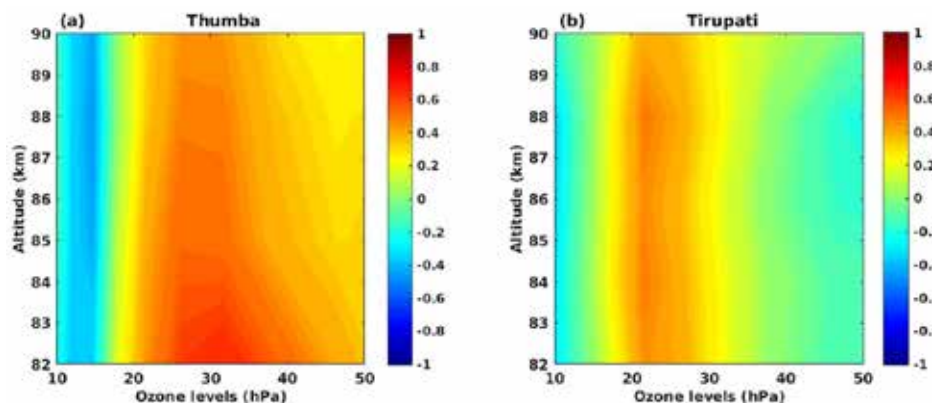


Figure 6: Correlation between deseasonalized ozone perturbations in the stratosphere and deseasonalized diurnal tide amplitude perturbations in the MLT over (a) Thumba and (b) Tirupati [Pramitha et al., Geophys. Res. Lett., 2021].

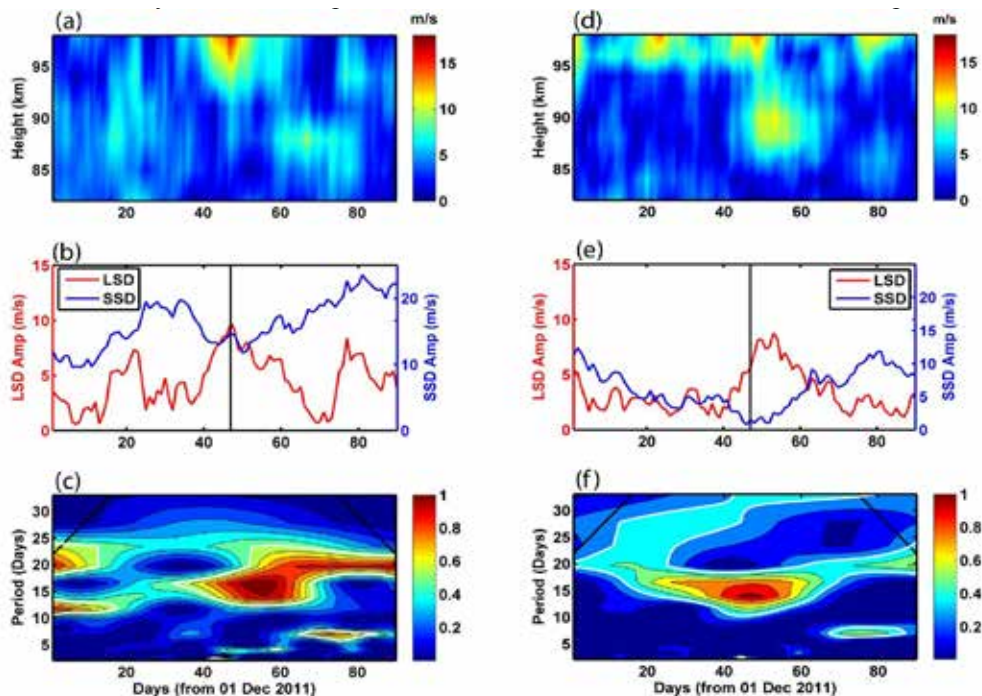


Figure 7: (a) Height-time section of zonal component of LSD, (b) amplitudes of LSD (red) and SSD (blue) at 94 km, and (c) normalized wavelet power spectrum of zonal winds at 94 km over Thumba during 01 Dec 2011 to 28 Feb 2012. (d-f) are same as (a)-(c) except for Koto Tabang at 92km. Vertical black lines in (b) and (e) denote PVW events. Black slanted lines in (c) and (f) represent the cone of influence and white contours represent the 95% confidence levels [Koushik et al., *J. Geophys. Res-Space Physics*, 2020].

with MLT tides. The present study using simultaneous observations of MLT tides, stratospheric winds and ozone suggests that the SQBO winds as well as ozone play a key role in inducing the QBO signals in the MLT diurnal tides. The relative roles played by stratosphere winds and ozone in modulating the diurnal tides, however, is still an open question to be addressed.

Observations of Lunar Semi Diurnal Tides during Sudden Stratospheric Warming Events

Meteor wind radar observations from the low latitude site Thumba (8.5°N, 76.9°E) and the equatorial site Koto Tabang (0.2°S, 100.3°E) were used to study the lunar semidiurnal oscillations in the MLT region and their response to Sudden Stratospheric Warming (SSW) events. Amplitudes and phases of lunar semidiurnal (LSD) and solar semidiurnal (SSD) oscillations were estimated by using least square fit method applied on a 16-day moving window. Using more than a decade of observations from both the sites, climatology of LSD amplitudes in the low and equatorial latitudes was constructed. The results were compared with the monthly mean LSD amplitudes from Vial and Forbes lunar tidal model outputs.

To quantify the strength of the warming event, the definition of Polar Vortex Weakening (PVW) is used, which is based on the strength of zonal mean zonal winds at 70°N, 48 km, and temperature over the North Pole at 40 km. From Figure 7, it can be noted that the LSD amplitudes enhance around the PVW period with maximum amplitudes one day before the PVW event on Day 49. At the same time,

SSD amplitudes undergo a reduction from days 35 to 60, concurrent with the enhancement of LSD. The wavelet spectrum in Fig.7c shows a very strong and statistically significant enhancement of quasi 16-day (Q16D) wave starting from day 35 lasting up to day 70. Over Koto Tabang also, a significant increase in LSD amplitudes is accompanied by an equally significant reduction in SSD amplitudes during the PVW event. Multiple PVW events showed simultaneous enhancement of LSD amplitudes, reduction in SSD amplitudes together with the presence of Q16D wave. In order to verify whether nonlinear interaction between the Q16D planetary wave and SSD exists in the equatorial and low-latitude MLT region during SSW events or not, bispectral analysis was employed. Bispectrum analysis emphatically demonstrated that nonlinear interaction between the Q16D wave and the SSD tides exists in the MLT region during PVW/SSW events and that the resulting secondary waves have periods around 12.4 hr.

Additionally, ground based magnetometer observations of geomagnetic field variations at Alibag (18.7°N, 73°E, 13°N dip angle) and the dip equatorial station Tirunelveli (8.7°N, 77°E, 0.23° dip angle) were used to study the LSD in the Equatorial Electrojet (EEJ). Hourly geomagnetic field values at Alibag (HABG) are subtracted from those at Tirunelveli (HTIR) to infer EEJ-induced magnetic field variations. On closer examination of Figs.8a-f, it is worth noting that there is an excellent correlation existing between the LSD amplitudes in zonal winds and the EEJ. This is also evident in the high coefficients of correlation

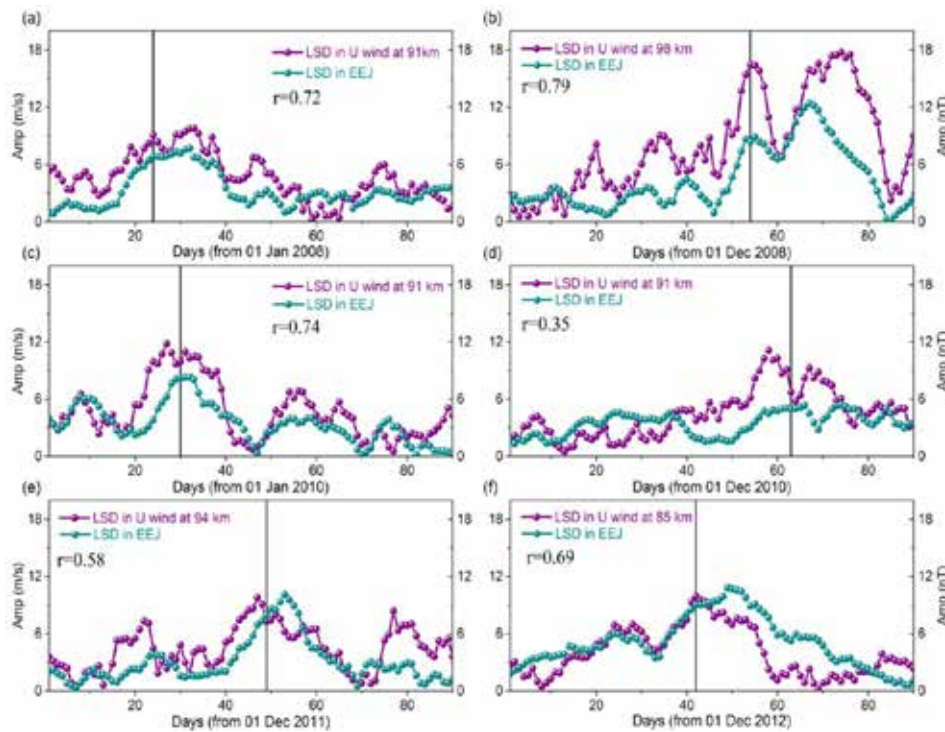


Figure 8: Amplitudes of lunar semidiurnal oscillations in the MLT zonal winds over Thumba (violet) and lunar semidiurnal oscillations in EEJ amplitudes (green) over Tirunelveli for (a) 1 January to 31 March 2008, (b) 1 December 2008 to 28 February 2009, (c) 1 January to 31 March 2010, (d) 1 December 2010 to 28 February 2011, (e) 1 December 2011 to 28 February 2012, and (f) 1 December 2012 to 28 February 2013. The correlation coefficients for the aforementioned quantities are also given in each panel [Koushik et al., *J. Geophys. Res.-Space Physics*, 2020].

obtained in the individual cases. It was observed that all the correlation coefficients were significant at 95% level. Thus it can be seen that there is an unprecedented resemblance between the LSD amplitudes in zonal winds in the MLT over Thumba and the LSD amplitudes in EEJ intensities observed from a nearby dip equatorial station Tirunelveli. This can be considered as one of the classical examples demonstrating the MLT-ionosphere coupling existing over low latitudes.

Gravity Wave Source Spectra Appropriation for Mesosphere Lower-Thermosphere Using Meteor Radar Observations and GROGRAT Model Simulations

Meteor radar observations of gravity wave momentum fluxes (GWMFs) in the 82-94 km altitude region are employed to identify the best fit gravity wave source spectrum using Gravity wave Regional or Global Ray Tracer (GROGRAT) model simulations over a low-latitude location, Tirupati (13.63°N, 79.4°E). Five spectral functions shown in Fig.9 are used as GW source spectra in the GROGRAT model simulations and which are not representative of any specific physical sources (except for B4, which represent transient mountain mechanism of the GW generation from convection) nor do they represent any particular event but these spectra represent climatological picture of mixed source and propagation information at a given altitude.

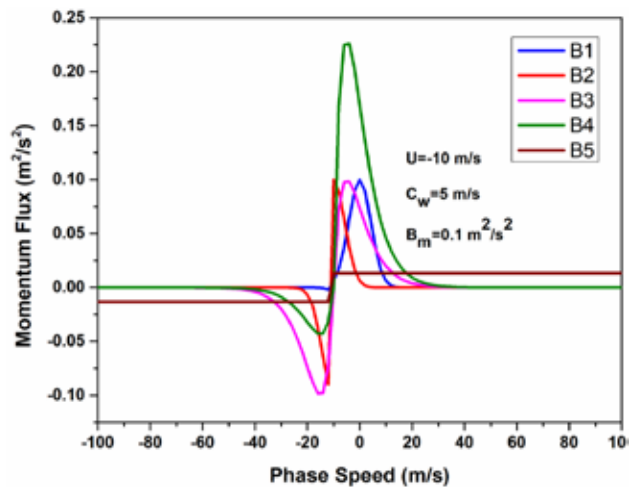


Figure 9: Source spectra B_1 , B_2 , B_3 , B_4 and B_5 employed in the GROGRAT simulations for a particular combination with $U=-10 \text{ ms}^{-1}$, $c_w=5 \text{ m/s}$ and $B_m=0.1 \text{ m}^2/\text{s}^2$ [Pramitha et al., *Geophys. Res. Lett.*, 2020].

As GROGRAT model requires the background wind and temperature information from troposphere to 100 km altitude, monthly mean winds right from troposphere to lower thermosphere during 2013-2017 are constructed from Whole Atmosphere Community Climate model (WACCM) simulations and temperature is obtained by combining GPS sonde (0-30 km) and SABER/TIMED (30-100 km) observations. B_1 - B_5 spectra are launched at an

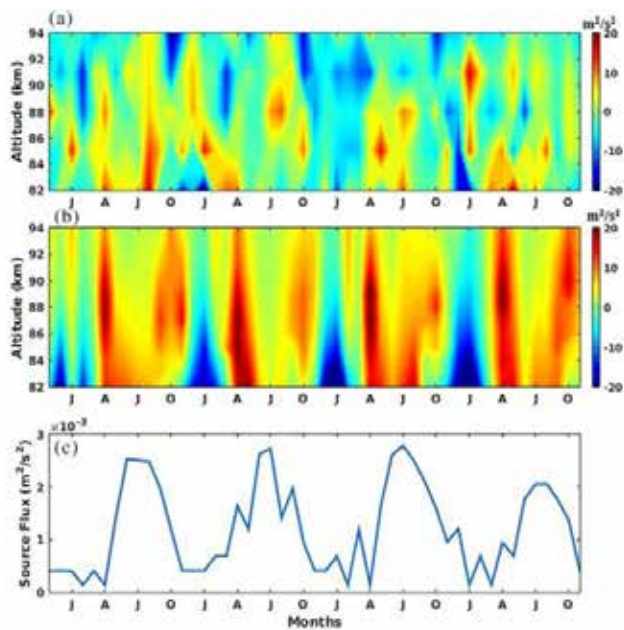


Figure 10: Height-month section of GWMF in the MLT region using (a) meteor radar measurements and (b) GROGRAT simulations. (c) Monthly mean source fluxes obtained using best fit spectrum at 18 km altitude [Pramitha et al., Geophys. Res. Lett., 2020].

altitude of 18 km for all the permutation combination of the parameters for phase speed ranging from -100 to 100 ms^{-1} with 2 ms^{-1} resolution using GROGRAT model.

In order to find the best fit spectra, the criteria used is that there should be a positive correlation (> 0.3) with slope ranging from 0.8 - 1.2 and relative intercept less than 0.4 between observed momentum fluxes and kinetic energy of GWs with that of the simulated using different source spectra. In this regard, the monthly mean kinetic energy and zonal momentum fluxes of GWs estimated from meteor radar observations during 2013-2017 are compared. A correlation coefficient of 0.4 is found, which is significant at 95% level. After comparing the simulated and observed MF for all possible combinations of parameters, a best fit spectrum is identified. Among all combinations, B_1 spectrum with horizontal wavelength of 300 km , spectral amplitude (B_m) of $0.01 \text{ m}^2/\text{s}^2$, spectral width (c_w) of 20 m/s and intermittency of 9 is relatively compared well with meteor radar observations of monthly mean MF. Using the best fit spectra B_1 with obtained appropriate parameters, height-month sections of GWMF are constructed from simulations as well as radar observations and are shown in Fig.10. From this figure, it is clear that the overall pattern of height-month sections of simulated and observed GWMF

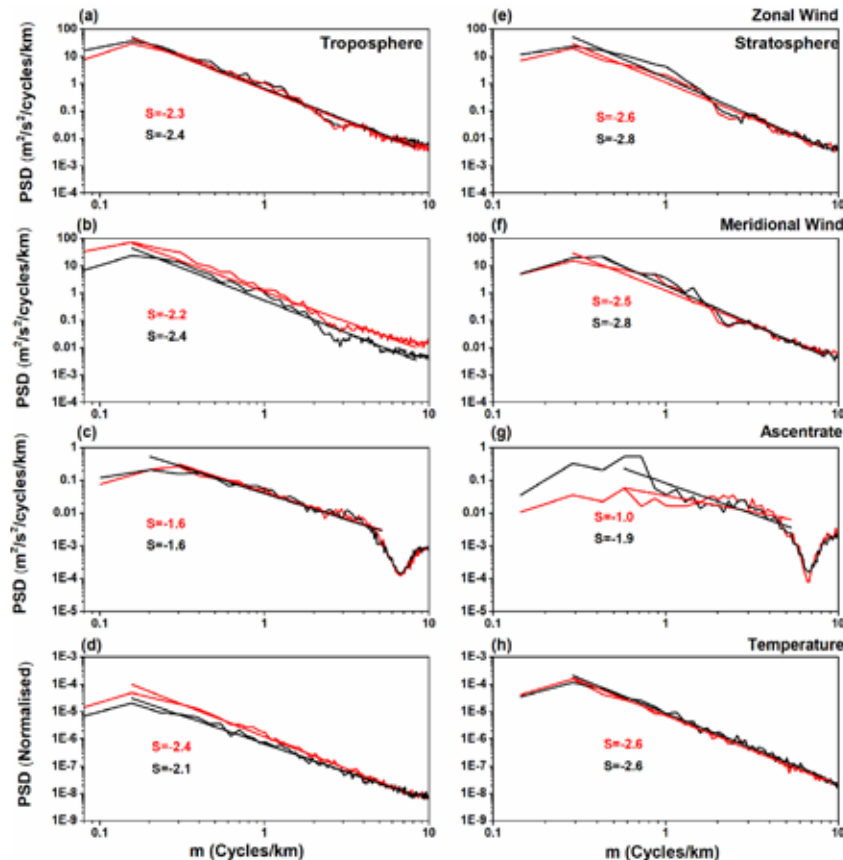


Figure 11: Monthly mean vertical wavenumber spectra of (a) zonal, (b) meridional, (c) vertical winds and (d) temperature in the troposphere for January (red) and July (black) months of 2011. Figures (e), (f), (g) and (h) are same as (a), (b), (c) and (d), respectively but for the stratosphere. The slanting lines represent linear fits and slopes of the spectra are given in corresponding colours [Pramitha et al., J. Atmos. Sol. Terres. Phys., 2021].

exhibit similar features with discrepancies in the observed magnitude. The seasonality of easterly and westerly momentum is very well captured by the model simulations especially in the lower heights below 90 km. A SAO in the GWMF with easterlies during winter and summer and westerlies during both equinoxes can be predominantly noted at 84-88 km altitude.

Further, the best fit spectrum B_1 identified in the present study with appropriate parameters are employed to estimate the source flux at the launching altitude 18 km and is shown in Fig.10c. The source fluxes show relatively large momentum during Indian monsoon season with a peak during the month of August. However, large westerly momentum is observed in the 82-94 km region during April and October months in the simulations thus emphasizing the role of background winds in shaping up the GW spectra. Thus in present study, radar measured and model simulated GWMFs in the MLT region are employed for the appropriation of gravity wave source spectra.

Observations and Model Predictions of Vertical Wavenumber Spectra of Gravity Waves in the Troposphere and Lower Stratosphere over a Tropical Station

Vertical wavenumber spectra of gravity wave (GW) perturbations of horizontal wind, temperature and ascent rate of the balloon obtained from 10 years (2007-2017) of high resolution radiosonde measurements in the troposphere and lower stratosphere over a tropical station, Gadanki (13.45°N, 79.2°E) are investigated. The vertical wavenumber spectrum of ascent rate perturbations obtained from radiosonde is compared with the vertical wavenumber spectrum of the vertical wind perturbations obtained from collocated VHF radar observations. The vertical wavenumber spectrum is characterized in terms of its slope and amplitude.

The tropospheric zonal wind spectra depicted in Fig.11a exhibit very similar characteristics in terms of slope and amplitude during summer and winter. The tropospheric meridional wind spectra depicted in Fig.11b exhibit same slope during winter and summer but relatively higher spectral amplitudes in winter. In the lower stratosphere, both zonal and meridional wind spectra depicted in Fig.11e and 11f, respectively show relatively less negative slopes during winter as compared to summer. Horizontal wind spectral slopes are more negative in the lower stratosphere as compared to the troposphere. The spectral slopes of zonal and meridional wind spectra in the lower stratosphere is -2.8 which is nearly equal to the canonical slope of the predicted universal spectrum (-3) during summer months. In Figs.11c and 11d, the slope of the vertical wind spectra is different from horizontal winds as well as temperature. The vertical wind spectra in the lower stratosphere are shallow as compared to all other spectra. This particular observation is very important as the slope of the vertical

winds provides some clue on the separability of frequency-wavenumber spectra.

In Figs.12a-d, the zonal wind spectral slopes show no seasonality in the tropospheric region whereas in the lower stratosphere relatively steeper slopes are noticed during summer. Mean slopes are very close to the canonical value in the lower stratosphere. The annual cycle of spectral slopes of meridional winds depicted in Fig.12b shows similar characteristics as zonal winds with steeper slopes in the lower stratosphere as compared to the troposphere. The seasonality of the slopes both in the troposphere and the lower stratosphere is less pronounced with former values very close to the canonical value. Fig. 12c shows the mean annual cycle of spectral slopes of temperature. The seasonal cycle is not very strong in the case of temperature, especially in the lower stratosphere. The deviation of spectral slope from canonical value is relatively large for temperature spectra as compared to horizontal wind spectra. Fig.12d shows the mean annual cycle of spectral slopes of vertical winds. Overall, the vertical wind spectral slopes are shallow as compared to both horizontal wind and temperature spectral slopes. Further, the spectral slopes and amplitudes are quantitatively compared with those predicted by the linear instability theory (LIT), saturated-cascade theory, and diffusive filtering theory. Observed spectra in the lower stratosphere are agreeing well with LIT and Saturated-Cascade theories. Quantitatively, LIT seems to be better in predicting the spectral amplitudes as compared to other theories.

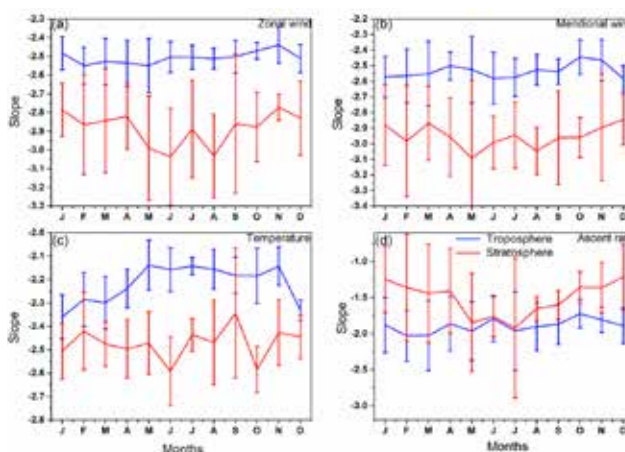


Figure 12: The mean annual cycle of spectral slopes of (a) zonal winds (b) meridional winds (c) temperature and (d) ascent rate in the troposphere (blue) and stratosphere (red). The vertical bars indicate the standard deviation representing interannual variability [Pramitha et al., *J. Atmos. Sol. Terres. Phys.*, 2021].

Stratosphere-Troposphere Exchange

Multi-Platform Observations of Stratosphere-Troposphere Exchange over Bharati (69.41°S, 76°E), Antarctica during ISEA-35

During the 34th (2014-2015), 35th (2015-2016) and 36th (2016-2017) Indian Scientific Expeditions to Antarctica

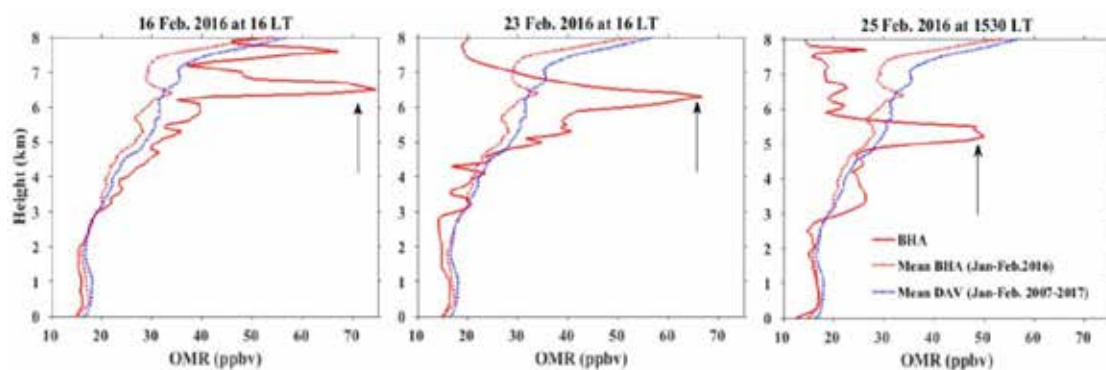


Figure 13: Height profile of ozone mixing ratio (OMR) on 16, 23 and 25 February 2016 over Bharati (BHA). Dashed lines indicate mean OMR (combination of BHA and DAV profiles) during ISEA-35 (27 Jan. to 2 Mar. 2016, 12 profiles) and the long-term mean of Jan.-Feb. (2007-2017) over the DAV. Vertical arrows indicate the enhancement of the upper tropospheric ozone [Das et al., *J. Atmos. Solar. Terr. Phys.*, 2020].

(ISEA), experimental campaigns were conducted by SPL at Bharati (69.41° S, 76.19° E), Antarctica. One of the objectives of this campaign was to study the stratosphere-troposphere exchange processes using balloon borne radiosonde/ozonesonde measurements. In addition to these measurements at Bharati, there were regular radiosonde and fortnightly ozonesonde measurements along with ground-based VHF radar measurements from Davis (68.6°S, 78°E), which is about 85 km from Bharati. These observations were supplemented with space based observations, i.e. Microwave Limb Sounder (MLS) and Indian National Satellite System (INSAT-3D) satellite measurements. The

present study deals with the observations of stratospheric ozone intruding into the troposphere over Bharati during a jet stream condition.

There were 12 ozonesonde launches during ISEA-35 between 27 January to 02 March 2016 and stratospheric intrusion was observed on 16, 23, 25 February 2016. In figure 13, enhanced OMR of about 75, 70 and 50 ppbv are observed at 6.5, 6, and 5 km on 16, 23 and 25 February 2016, respectively. The climatological mean O_3 observed in these height regions is between 25-30 ppbv. The present observations reveal that there is a possibility for downward

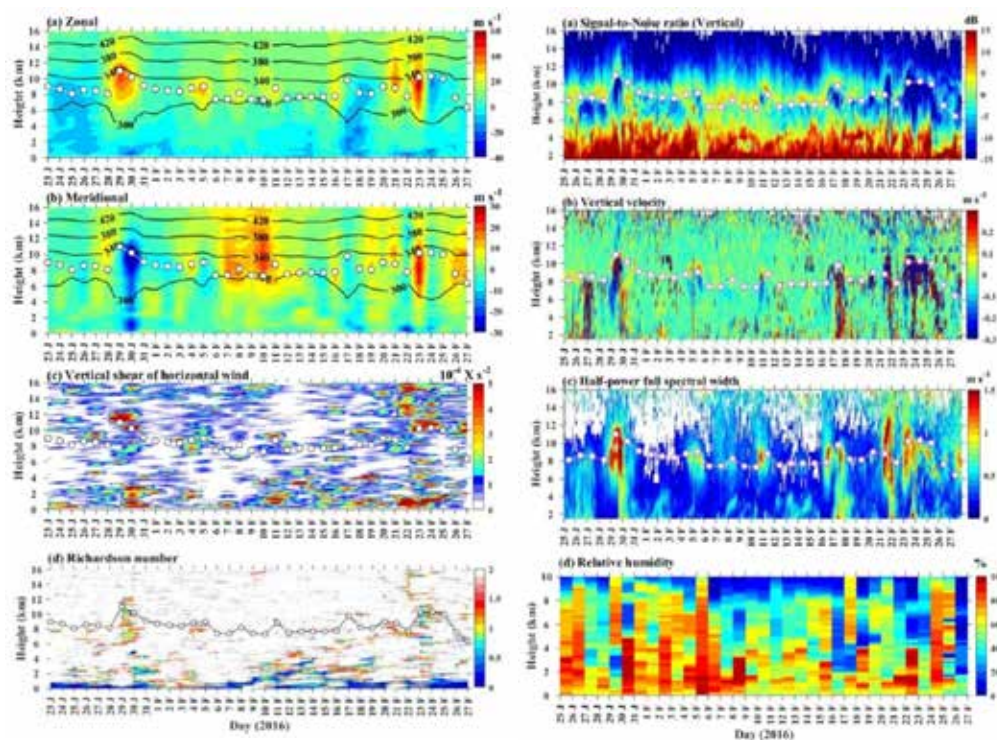


Figure 14: (Left) Height-time intensity plot of (a) zonal, (b) meridional wind, (c) square of vertical shear of horizontal wind and (d) Richardson number over Bharati station from 23 Jan. to 27 Feb. 2016. Black lines indicate the potential temperature. (Right) Height-time intensity plot of (a) signal-to-noise ratio (SNR) in zenith direction, (b) vertical wind, and (c) corrected half-power full spectral width obtained from VHF radar at the Davis station and (d) relative humidity measured from the radiosonde at Bharati station from 25 Jan. to 27 Feb. 2016. White circles indicate the radiosonde derived lapse-rate tropopause [Das et al., *J. Atmos. Solar. Terr. Phys.*, 2020].

propagation of stratospheric O_3 into the troposphere. Tower measurements shows low-pressure (~ 972 hPa) on 16 February, whereas high pressure was observed on 23 (~ 1005 hPa), and 25 (~ 995 hPa), February 2016 from its diurnal mean (~ 980 hPa), which is above the 1-sigma standard deviation. High and low-pressure systems are the favorable conditions for the intrusion of stratospheric air.

Strong zonal winds as high as $50\text{--}60\text{ ms}^{-1}$ are observed in the vicinity of the tropopause during 23-25 February and moderate winds of the order of $30\text{--}40\text{ ms}^{-1}$ are observed on 29-30 January and 16-17 February 2016 as shown in Fig. 14a (left panel). Wind direction is north-westerly during 29-30 January and south-westerly during 16-17 and 23-25 February in the vicinity of tropopause as shown in Fig. 14a and 14b (left panel). The strong southerly wind is also observed above tropopause during 7-12 February. The vertical shear of horizontal wind shown in Fig. 14c (left panel) is also high and it corresponds to $Ri < 1$ as shown in Fig. 14d (left panel) during 29-30 January and 23-25 February. However, we do not observe significant wind shear on 16 February. Thus the turbulence occurring in the vicinity of tropopause is the prime candidate for an increase in the tropopause altitude on 29-30 January and 23-25 February, which further plays a key role in the stratospheric air intrusion into the troposphere.

To confirm the stratospheric intrusion event, the data from VHF radar located at Davis were analysed. Interestingly strong downdrafts of -0.3 ms^{-1} followed by the updrafts of $+0.3\text{ ms}^{-1}$ from the lower troposphere to the tropopause were observed during all the three events. Enhanced turbulence activities are observed in the spectral width (which is a direct indicator of the turbulence) as depicted in Fig. 14c (right panel). The same enhancement is observed in the Richardson number (Ri) derived from the radiosonde profiling as shown in Fig. 14d (right panel). Low relative humidity is observed between 2 and 8 km. On the basis of these observations, it is concluded that the turbulence due to strong wind shear, the oscillation of tropopause due to the updraft and downdrafts and advection constitute to the stratosphere-troposphere exchange processes over Bharati, Antarctica. These observations constitute the first multi-instrumented experimental evidence for the stratospheric intrusions over the coastal Antarctica.

Effect of Deep Convection and Monsoon Dynamics on the UTLS Water Vapour over the Indian Region

Balloon-borne cryogenic frost-point hygrometer (CFH) observations conducted over three stations Trivandrum, Hyderabad and Kolkata in the Indian region during the period 2014-2017 are used to study the effect of deep convection and monsoon dynamics on the distribution of water vapour in the upper troposphere and lower stratosphere (UTLS) and to quantify the amount of water vapour transported to the LS during summer-monsoon

(June to September). Fig. 15 shows the seasonal mean altitude structure of water vapour in the UTLS measured using CFH in all the four seasons over Trivandrum and Hyderabad and in the pre-monsoon and summer-monsoon seasons over Kolkata. The mean Water Vapour Mixing Ratio (WVMR) in the UT shows a distinct seasonal variation and is relatively high during the summer-monsoon over all the stations. The altitude structure of WVMR almost resembles the altitude structure of the occurrence of deep convective cloud tops in all the seasons except the summer monsoon season. In summer monsoon season, the water vapour enhancement in the upper troposphere is significantly high and sometimes extend even beyond the cold point tropopause (CPT). In the UT region (10-16 km), water vapour shows an enhancement of $\sim 40\text{--}60\%$ at Trivandrum, $150\text{--}200\%$ at Hyderabad and $\sim 200\text{--}300\%$ at Kolkata during the summer-monsoon with respect to the pre-monsoon season. This study shows that the WVMR entering to the lower stratosphere (LS) during summer monsoon can be enhanced about 10-40%.

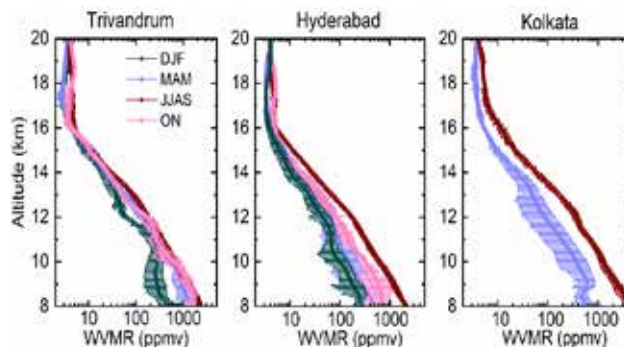


Figure 15: Seasonal mean altitude profiles of (a) water vapour mixing ratio (WVMR) in different seasons over Trivandrum, Hyderabad and Kolkata using CFH-radiosonde observations during the period 2014-2017. The horizontal bars in (a) and (b) represent standard error [Emmanuel et al., Atmos. Res., 2020].

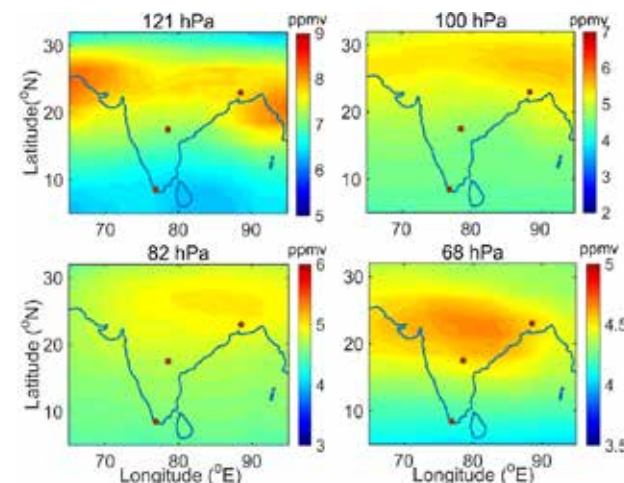


Figure 16: Spatial distribution of WVMR during summer monsoon season at 121 hPa, 100 hPa, 82 hPa and 68 hPa over the Indian monsoon region from MLS data during the period 2011-2017. The CFH launch locations are marked on the figure [Emmanuel et al., Atmos. Res., 2020].

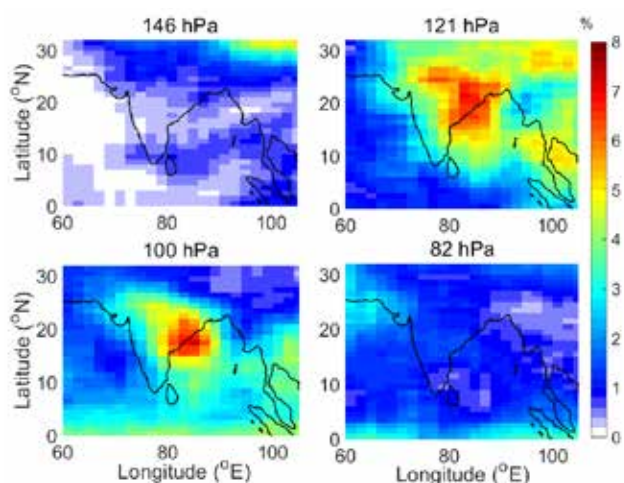


Figure 17: Spatial distribution of occurrence frequency of WVMR < 3 ppmv during summer monsoon season at 146 hPa, 121 hPa, 100 hPa and 82 hPa over Indian monsoon region from MLS data during the period 2011-2017 [Emmanuel et al., Atmos. Res., 2020].

In the summer monsoon season, WVMR at 100 hPa peaks north of the deep convection core over the head Bay of Bengal (BoB) as depicted in Fig.16. In the LS, the water vapour maximum shows a south westward shift with altitude in accordance with the anticyclonic circulation flow in the UTLS. In order to examine the effect of dehydration in the UT, the occurrence frequency of WVMR < 3 ppmv (amount expected during dehydration) are examined using MLS data at pressure levels 146 hPa (~14 km), 121 hPa (~15 km), 100 hPa (~16.5 km) and 82 hPa (~18 km), which are shown in Fig.17. The figure shows that the occurrence of WVMR < 3 ppmv is higher at 121 hPa and 100 hPa. The spatial pattern shows that the probability of dehydration is high along the fringes of deep convective core in the head BoB, but not directly above the peak occurrence of deep convection. The peak occurrence of WVMR < 3 ppmv shows a westward shift from the peak occurrence of deep convection confirming the influence of the TEJ on the formation of the anvil clouds and the associated dehydration. However, the occurrence of WVMR < 3 ppmv at 82 hPa is found to be small confirming that the

dehydration above the CPT altitude is comparatively less in this season.

Effect of Meteorology and Dynamics on the Variability of Ozone in the Troposphere and Lower Stratosphere over Thumba (8.5°N, 76.9°E)

The seasonal variability of the vertical distribution of ozone is investigated over the tropical station Thumba (8.5°N, 76.9°E) using nine-years (2011-2019) of ozonesonde data obtained as part of Tropical Tropopause Dynamics (TTD) campaign conducted under CAWSES-India Phase II and GARNETS programs.

In Figure 18, ozone exhibits a clear annual variation in the lower troposphere (0-2 km) with winter maximum (49.2±3.6 ppbv) and summer monsoon minimum (21.9±0.7 ppbv). In the middle (2-10 km) and upper (10-17 km) troposphere, ozone is maximum in pre-monsoon and minimum during summer monsoon. Ozone in the LS exhibits a clear annual variation with summer monsoon maximum and winter minimum in tandem with the temperature seasonal cycle.

The intra seasonal variability in the vertical distribution of ozone is examined by computing the relative standard deviation (RSD) at different altitudes. The seasonally grouped ozone profiles (Fig.19) show large variability during winter and summer monsoon compared to pre- and post-monsoon. The RSD of ozone is large in the troposphere (~20-30 %) compared to stratosphere (~5%) and is significant in the altitude region close to the surface and in the tropical tropopause layer (TTL) (>=30%). Maximum RSD is observed during summer monsoon (June-September) in the upper troposphere (~50%) close to cold point tropopause (CPT). In general, RSD in ozone and temperature profiles shows a sharp peak immediately above the CPT in all the seasons. The study shows that tropospheric ozone shows an in-phase relationship with temperature and opposite phase relationship with relative humidity. A significant negative correlation is observed between ozone and water vapour mixing ratios in the 2-5 km region.

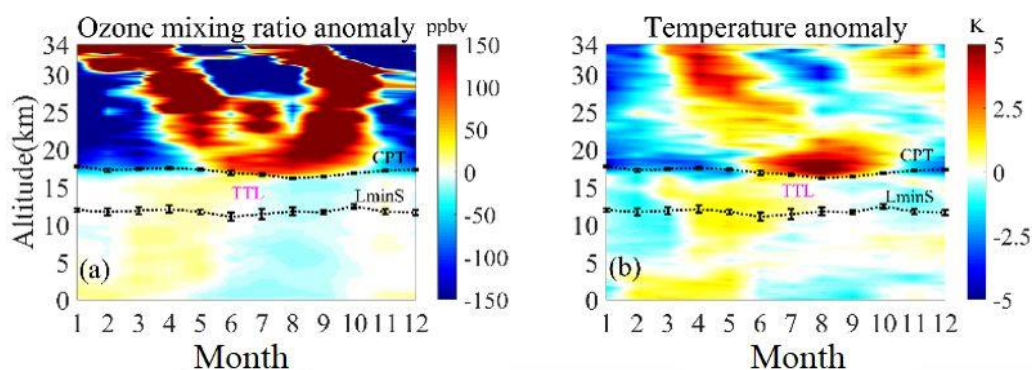


Figure 18: Monthly anomaly of (a) ozone mixing ratio and (b) temperature obtained from in situ (ozonesonde and radiosonde) observations during the period 2011-2019. Mean altitude of cold point tropopause (CPT) and level of minimum stability (LMinS) and their respective standard errors are super-imposed [Sateesh Chandran et al., J. Atmos. Sol. Terres. Phys., 2021].

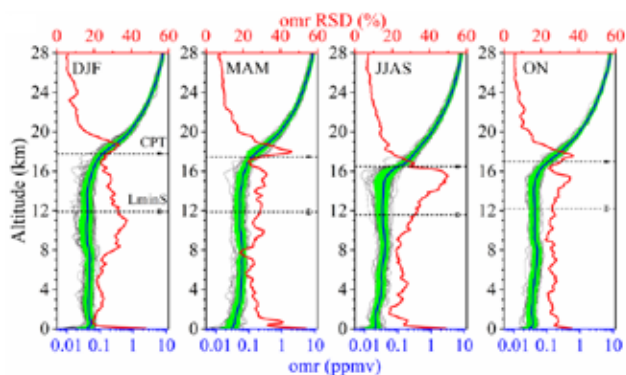


Figure 19: Seasonally grouped vertical profiles of ozone mixing ratio (omr) (grey colour) and its seasonal mean (blue colour) with one sigma standard deviation (green shade) in the altitude region 0-28 km. Relative standard deviation (RSD) of the same is shown in red colour [Satheesh Chandran et al., *J. Atmos. Sol. Terres. Phys.*, 2021].

The tropospheric column ozone over Thumba shown in Fig.20 depicts a semi-annual variation. The tropospheric contribution to the total columnar ozone is maximum during pre-monsoon (~16%) and minimum during summer monsoon (~7%). Mid-tropospheric ozone contributes more to the tropospheric column ozone (40-60%) compared to lower and upper tropospheric ozone. Tropospheric column ozone exhibits a similar seasonality as that of its precursors like NO_2 , CO and CH_4 . In order to check the role of long-range transport in the ozone variability, air-mass back-trajectories reaching over Thumba in the lower (LT: 0-2 km), middle (MT: 3-10 km) and upper troposphere (UT: 11 km-CPT) regions for monsoon season are estimated using HYSPLIT dispersion model. During this season, the vertical distribution of ozone over Thumba is mainly influenced by the monsoon dynamics, deep convection associated with monsoon and the upper tropospheric anti cyclonic flow. In the lower troposphere, the synoptic scale monsoon flow from the Indian ocean brings ozone poor marine air to the Indian sub-continent resulting in low ozone concentration, whereas, the transport of ozone poor air from Arabian Sea and western pacific dominates in the mid troposphere. The ozone distribution in the upper troposphere over Thumba is mostly influenced by the transport of air from western pacific along with a smaller contribution from south and Southeast Asian region. There is significant contribution from midlatitude lower stratosphere also. The trajectories from south and Southeast Asia ascend from lower altitudes (4-6 km) and reach the upper troposphere over Thumba.

Cloud Dynamics

The Vertical Structure of Latent Heating and their Association with Cloud Types during the Indian Summer Monsoon

Latent heat (LH) released in clouds plays a pivotal role in driving atmospheric circulations at various spatial scales ranging from mesoscale to synoptic scales. It is known

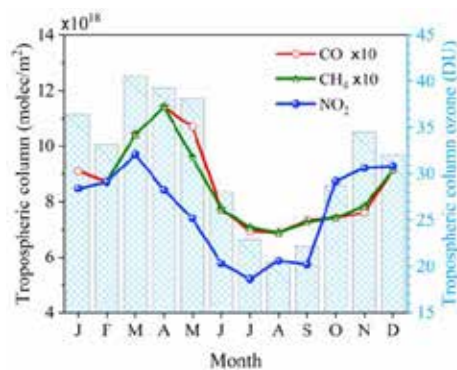


Figure 20: Annual variation of tropospheric column densities of NO_2 derived from OMI, CO and CH_4 from TES observations over Thumba during the period 2005-2015. CO and CH_4 data are scaled up by a factor of 10. The hatched bar represents the tropospheric column ozone in Dobson unit over Thumba derived from ozonesonde observations [Satheesh Chandran et al., *J. Atmos. Sol. Terres. Phys.*, 2021].

that various cloud types are typically governed by different cloud dynamical processes, which result in different microphysical properties. In the present study, the TRMM (Spectral Latent Heating data for LH profiles) and CloudSat (2B-CLDCLASS data for Cloud Type) observations were used to investigate the vertical structure of LH associated with various type of clouds during Indian summer monsoon period.

Figure 21 shows simultaneous observations of precipitating systems by CloudSat and TRMM on two typical days. Fig.21a depicts the cloud classification by CloudSat observations and Fig.1b shows the radar reflectivity structure as observed by TRMM-PR on 8th September 2006. The CloudSat overpass time was 19:13 UT and that of TRMM was 19:06 UT. The CloudSat classification of clouds depicted in Fig.21a readily reveals the presence of deep convective and Altostratus clouds over the observational locations. The LH profile corresponding to the deep convective (DC) cloud depicted in Figs. 21a and 21b is shown in Fig.21c. Another example of simultaneous observations of CloudSat (2306 UT) and TRMM (2256 UT) are shown in Fig.21d and 21e, respectively. In this case, the tops of the DC clouds are limited to 7 km in both the observations. LH profiles corresponding to DC and cumulus clouds are shown in Fig.21f.

Figure 22 shows the mean vertical profiles of LH for DC [over the Bay of Bengal (BoB) and the Central India (CI)], Stratocumulus [over the Arabia Sea (ARB)] and Cu [over the Western Ghats (WG)] clouds. Over the BoB and CI region, LH peaks around ~ 7 km altitude with slight variation in its magnitudes. In the DC clouds, LH is dominated by condensation as well as freezing process. The large vertical motions within in the DC clouds aid in the formation of ice and thus liberate relatively large LH, which is reflected in Fig.22a and 22c. One more interesting feature in these two figures is a dip in LH profile at around 5 km altitude. This altitude corresponds to 0°C isotherms

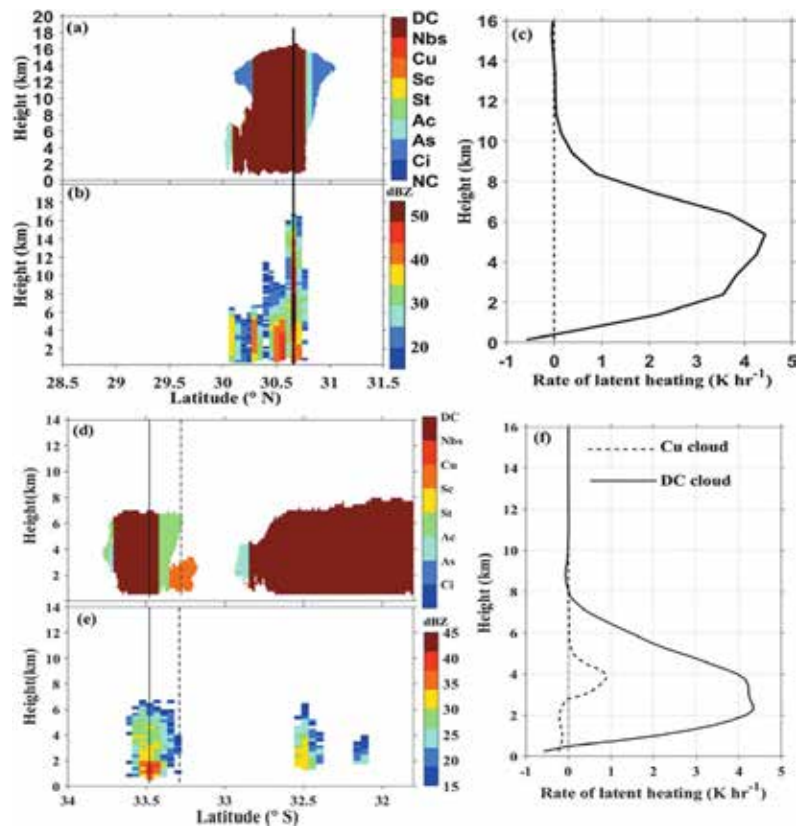


Figure 21: (a) Classification of the clouds observed by CloudSat, (b) TRMM-PR measured radar reflectivity and (c) vertical profile of LH derived from TRMM-PR on 8th September 2006. (d), (e) and (f) are same as (a), (b) and (c) but for 30 August 2006 [Subrahmanyam and Kumar, Remote Sensing Lett., 2021].

over the tropics where the melting of ice into water takes place in the DC clouds. The melting process absorbs the LH and thus there is net reduction in the heating. Over the ARB and WG regions, the LH structure is confined to lower troposphere and peaks at ~ 2km altitude. Over the ARB region, the Sc clouds are dominant with their cloud tops below 3 km altitude. Over the WG region, where Cu clouds dominate, the vertical profile of LH shows a peak around 2 km. The present study thus brought out the vertical structure of LH associated with various types of clouds over the Indian summer monsoon (ISM) region,

which is envisaged to have implications in assessing the role of various types of clouds in driving the circulation through diabatic heating during the ISM.

Validation of C-band Doppler Weather Radar at Thumba using Laser Precipitation Monitor and comparison with GPM observations

A C-band dual polarization Doppler weather radar (C-DWR) was installed at Thumba, a west coastal station in the southern peninsula of India known as “Gateway of Indian Summer Monsoon”. The C-DWR operates

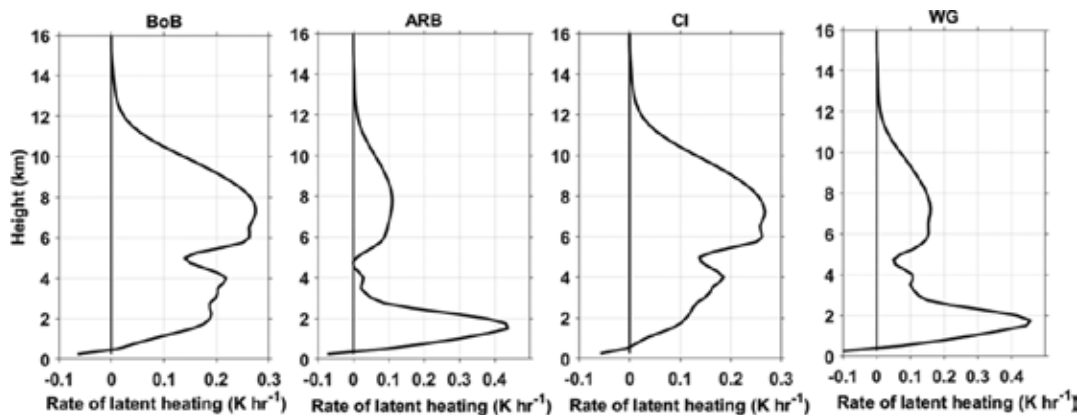


Figure 22: The mean vertical profiles of LH over the BoB, the ARB Sea, the CI and the WG regions derived from TRMM-PR observations [Subrahmanyam and Kumar, Remote Sensing Lett., 2021].

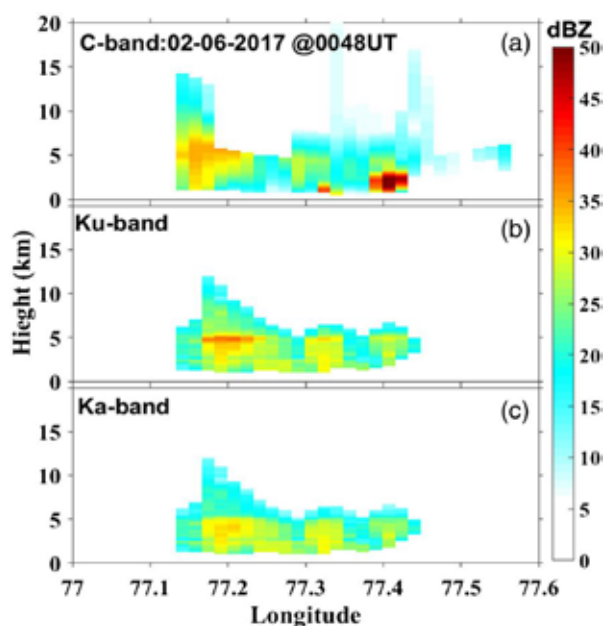


Figure 23: The height-longitude structure of radar reflectivity as observed by the ground-based C-DWR and space based Ku- and Ka-band radars [Kumar et al, J. Appl. Rem. Sens., 2021].

in the frequency range of 5.6 to 5.65 GHz with a peak transmitting power of 250 kW with 0.004 duty ratio. Simultaneous observations of precipitating systems by space- and ground-based radars are used for validation of C-DWR. The dual-frequency precipitation radars operating at Ku band (13.6 GHz) and Ka-band (35.5 GHz) on-board Global Precipitation Measurements (GPM) provide the three-dimensional distribution of clouds in terms radar reflectivity. A laser precipitation monitor (LPM) was installed at a distance of ~15 km from the C-DWR for periodically validating the radar-derived rainfall. Fig.23 shows the height-longitude structure of radar reflectivity as observed by the ground-based C-DWR and space-based Ku- and Ka-band radars onboard GPM. The three radar observations were brought to common grid points for the comparison. All the three radars, in general, show similar features of the precipitating system, and the reflectivity structure agrees very well. Except for a high reflectivity

observed in the low altitude at 77.4° E by the C-DWR, all other features are reproduced very well by the three radars though their sensitivity to the precipitation differ.

Some of the observed differences in the reflectivity of Ku and C-DWR can be attributed to the sensitivity of the respective radars to the size of precipitating droplets. These discrepancies as well as the differences in the radar sampling volumes also can be attributed to the observed differences in the radar reflectivities.

Figure 24a shows the time series of rainfall intensity measured by LPM and DWR on August 15, 2018. On August 15, 2018, C-DWR site experienced extreme precipitation and this observation was well captured by the radar. Before carrying out the quantitative analysis between the DWR and LPM, the LPM measurements are corrected for biases arising due to splashing of rain drops in to the field of view of the LPM, the rain drops falling at an angle to the laser sheet of the LPM and the drops falling through the edges of the laser sheet among others. The Z-R relation is employed to estimate the rainfall intensity from the C-DWR reflectivity observations. The coefficients used to retrieve the rainfall from the radar reflectivity are also provided in the figure. The C-DWR observations at 3° elevation are used for the comparison. From Fig.24a, it is very encouraging to note a very good agreement between the C-DWR and LPM measurements and thus providing credibility to the radar rain rate estimations. From Fig.24 b, it is evident that both the measurements agree very well with a correlation coefficient of 0.89. This study thus reported the initial observations of indigenously developed C-DWR and validated its observations using LPM measurements. It is envisaged that the present C-DWR located at the gate way of Indian summer monsoon will shed light on various aspects of precipitating clouds in details.

C-band Doppler Weather Radar Observations during the Passage of Tropical Cyclone ‘Ockhi’

The C-band DWR at Thumba provided an opportunity to investigate the spatial and vertical structure of ‘Ockhi’ cyclone during 29th November to 2nd December 2017 over

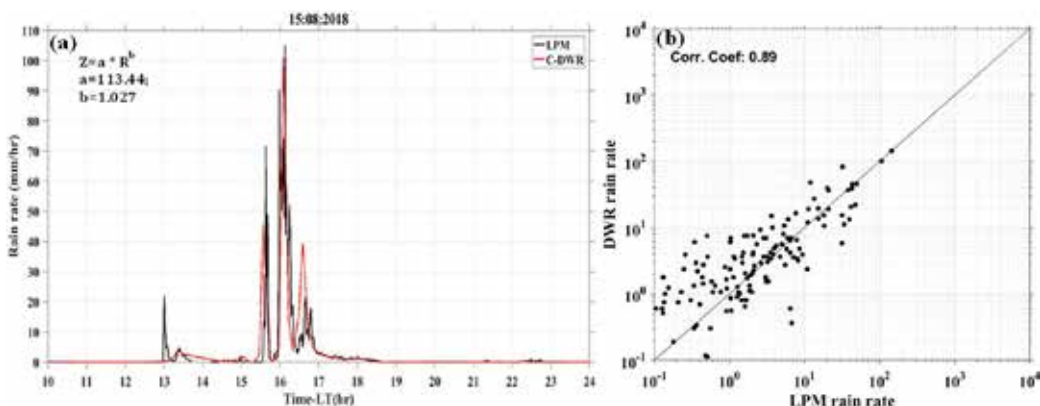


Figure 24: (a) The time series of rainfall intensity measured by LPM and DWR on August 15, 2018. (b) regression analysis of rainfall estimation using LPM and C-DWR measurements. The axes are in logarithmic scale [Kumar et al., J. Appl. Rem. Sens., 2021].

the south-west coast of Kerala. The C-band DWR captured various stages of ‘Ockhi’ cyclone passage and its rainbands as shown in figure 25. All these images are plotted at 2-degree elevation.

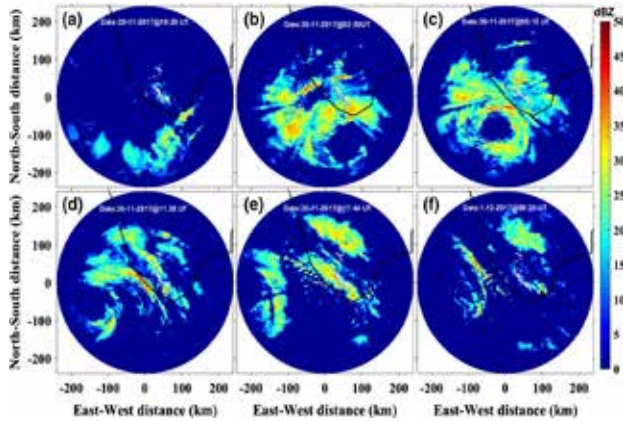


Figure 25: (a-f) DWR reflectivity images from 29th November to 1st December 2017 during the passage of ‘Ockhi’ cyclone. [Subrahmanyam and Baby, Natural Hazards, 2020].

The very first outer rainband of ‘Ockhi’ cyclone was observed at 19:29 UT on 29th November 2017 and was just 100 km away from the DWR station (Fig.25a). After 7 hrs, DWR observed the eye of ‘Ockhi’ cyclone partly and its inner and outer rainbands as seen in Fig. 25b. By 06:15 UT on 30th November 2017, cyclone eye was clearly captured by DWR (Fig.25c). At this time, the cyclone center was just about 20 km away from the coast of Thumba. The precipitation echoes, which were concentrated within inner and outer rainband regions, were clearly observed by the DWR. The intensity of inner rainband was about 45-50 dBZ in reflectivity. There are several convective systems having the maximum reflectivity of 45 dBZ embedded

inside the inner and outer rainbands (Fig.25c). At this time, the eye wall was affecting the south coast of Kerala, and isolated convective cells were moving across the Kerala (Fig.25c). After 5 hr, it moved away from the coast and was within DWR observation range as seen in Fig.25d. The cyclone continued to move north-westwards, and it was out of DWR range as seen in Figs.25e and 25f, where the outer fringes of the cyclone were captured by DWR on 30th November and 1st December 2017.

Figure 26 b-d shows the vertical structure of reflectivity, Z_{dr} and ρ_{hv} , respectively during passage of the cyclone across its eye represented by the white line shown in Fig.26a. From this cross-sections, it is evident the precipitating cloud-top heights are as high as around 10-12 km. The diameter of the eye is around 15 km, which was clearly seen in Fig.26. The present study thus provides the insights into the spatial as well as vertical structure of precipitating systems embedded within the ‘Ockhi’ cyclone by employing C-band polarimetric DWR observations over Thumba.

Convective Cell Identification and Tracking using C-band DWR Images based on Neural Network

Identifying and tracking the movement of the core of the convective clouds is of paramount importance to forecast extreme weather events such as thunderstorms. To study the initiation and development of convective core systems, an automatic tracking algorithm named ‘Convective cell Identification and TRacking (CITRA)’ has been developed to identify and track the convective cells in mesoscale convective systems (MCSs) using Doppler Weather Radar (DWR) reflectivity images. The algorithm is integrated with multiple methods of processing such as image threshold, pattern recognition,

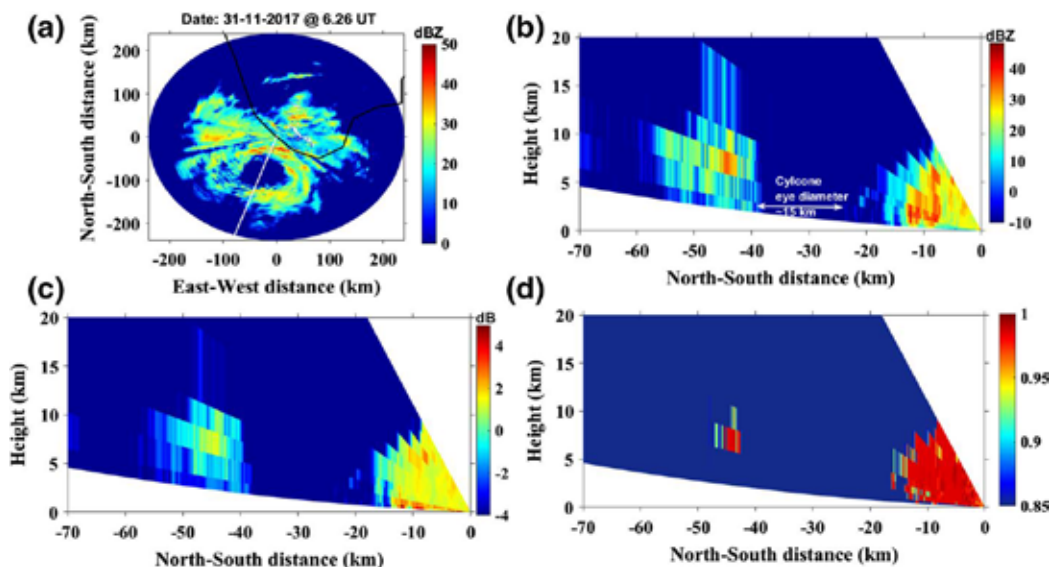


Figure 26: (a) The spatial distribution of reflectivity and vertical structure of (b) reflectivity, (c) differential reflectivity and (d) correlation coefficient corresponding to azimuth (200°) indicated in white in (a) on 30th November 2017 at 06:22 UT [Subrahmanyam and Baby, Natural Hazards, 2020].

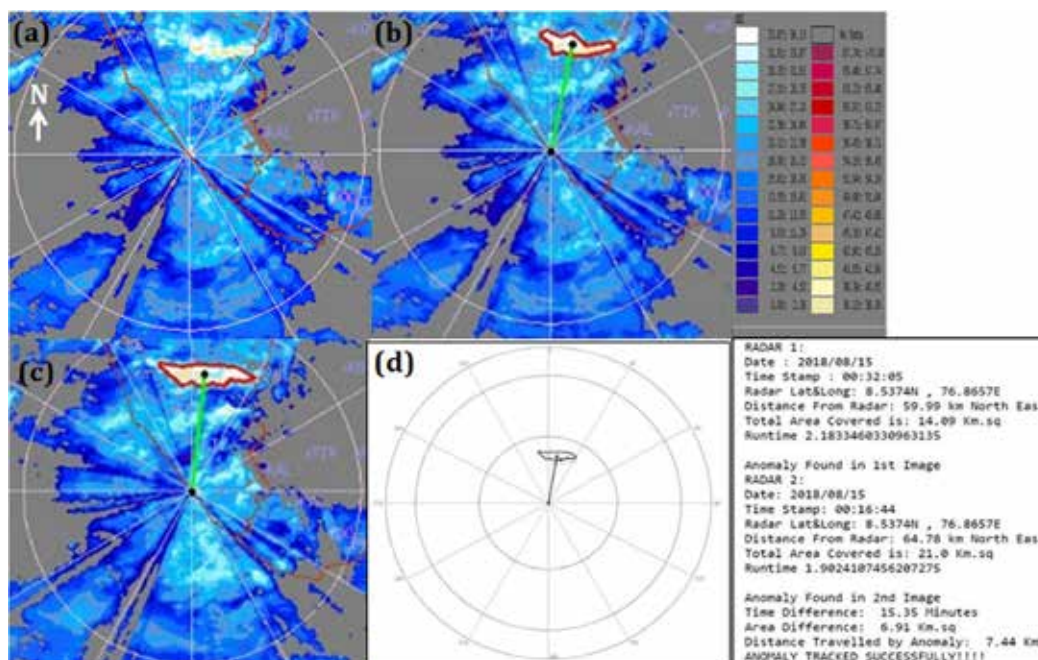


Figure 27: (a) Reflectivity image on 15th August 2018 at 00:16:44 UT, (b) & (c) Identified convective cell centroid (black dot) at 00:16:44 and 00:32:05 UT and area (red contour) superimposed on the original reflectivity image (d) Tracked convective cell shown by black contours. Distance from the convective cell centroid to the Radar centre is shown by a green line [Ranganakulu et al., *J. Electromag. Waves and Appl.*, 2021].

time series analysis, multiple convective cell patterns tracking, and optical character recognition using Long Short-term Memory (LSTM) Neural Network. It analyses the DWR reflectivity image pixel values and recognizes the intensities of the pixels (≥ 30 dBZ) and segregates convective cells along with other estimated cell physical properties such as centroid, convective core size and area, duration, maximum extent, distance and direction from the Radar centre. It identifies the convective cell and tracks the same with time. The performance of the CITRA algorithm was tested on 1255 convective cells identification and 90 distinct convective systems were tracked along with their physical properties during the monsoon periods of 2017, 2018 and 2019.

Figure 27 shows the tracking results for the convective systems, which occurred at 00:16:14 UT and 00:32:05 UT on August 15, 2017. Fig.27b and 27c shows the identified convective cell centroid (black dot) by CITRA and estimated area (red colour) superimposed on the original DWR reflectivity image. The distance from the convective cell centroid to the Radar centre is shown by the green line in Fig. 27b and 27c. Fig.27d shows the tracking of convective cells depicted by black contours for two different times. Also, the estimated physical properties are provided in the figure. At time 1 (i.e., 00:16:14 UT), the estimated convective cell area is around 14 km², while it is 21 km² at time 2 (i.e., 00:32:05 UT). The total distance travelled by convective cell is around 7.5 km in ~15 minutes time and the difference of cell area is 7 km².

Technical Development Activities

Solar Occultation Experiments (SOE) for Future Earth and Planetary Missions

Development of a payload for Solar Occultation Experiments (SOE) for future Earth and Planetary missions is a Technology Development Programme (TDP) of SPL/VSSC. The main objective of this TDP is the design and development of an instrument to obtain the vertical profiles of aerosols, trace gases and optically thin clouds in terrestrial and planetary atmospheres, at finer vertical resolution (1-2 km) using the solar occultation technique. The instrument consists of six co-aligned optical channels mounted on a high-precision sun-tracking mechanism (sun-sensor and 2-axis gimbal mechanism), for measuring the spectral characteristics of attenuated solar intensity in the visible-NIR regime, along the Line-of-Sight (LoS) at different tangent altitudes during sunrise and sunset events. The optical design layout of all the channels has been finalized considering the occultation-viewing geometry, field-of-view (FOV) requirements and detector specifications. A 3-dimensional laboratory model of the payload has been designed and motion simulations performed to analyze the simultaneous rotation of the gimbal system along elevation and azimuth axes. Steps have been initiated for the fabrication and realization of the prototype of the payload.

Simulation studies are carried out to determine the altitude profiles of expected attenuated solar flux to be measured by the instrument, by using the extinction profiles obtained

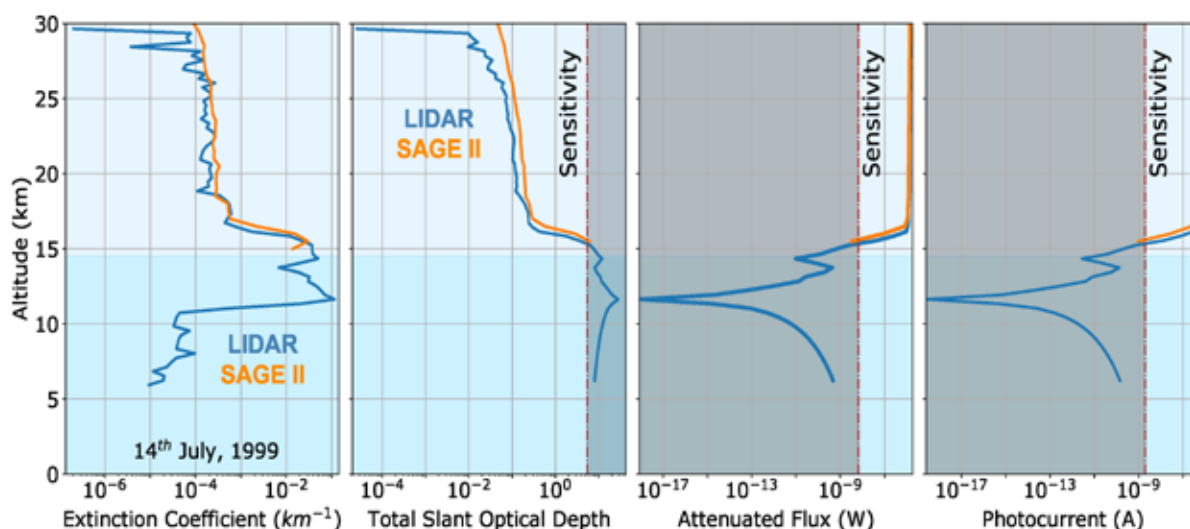


Figure 28: Simulation of expected attenuated solar flux and signal (photocurrent) in Earth atmosphere using the collocated aerosol extinction profiles obtained from ground-based lidar observations at 532 nm (blue), and space-based SAGE-II occultation measurements at 525 nm (orange) over Gadanki on 14th July, 1999. The boundary line of the gray-shaded region corresponds to the sensitivity of the SOE payload to be developed (in terms of maximum measurable optical depth, minimum detectable flux and minimum detectable signal).

from collocated space-based (SAGE-II) and ground-based (lidar) observations at Gadanki (Fig.28). While the ground-based lidar provides measurements well below 15 km altitude, SAGE-II is not able to provide measurements at low altitudes due to the high slant optical depth along the LoS during solar occultation measurements. Therefore,

the maximum slant optical depth to be measured by the SOE payload being developed at SPL is envisaged as ~ 5 , which corresponds to a minimum detectable signal of ~ 2 nano amperes. The flux simulations studies are utilized to optimize the required specifications of the optics and detectors for the development of SOE payload.

Future Projections/Ongoing

- Gravity wave momentum flux estimations using active aperture radar measurements.
- Stratopause elevation events during sudden stratospheric warming.
- Structure and dynamics of tropical cyclone/convection and associated Troposphere-Stratosphere Exchange using CUSAT-ST radar and Gadanki MST radar observations.
- Role of atmospheric circulation, ENSO and QBO in the exchange of minor constituents in the UTLS region.
- Signatures of regional dynamics in the variability of lower stratospheric water vapour over the Indian Peninsula from *in situ* and satellite observations.
- Effect of synoptic scale dynamics on the vertical structure of ozone in the troposphere lower stratosphere over the Indian Ocean.
- Origin and maintenance of Upper Tropospheric Inversion over the northern Indian Ocean during boreal winter.
- Characterization of Hadley cell dynamics at regional scales.
- Development and implementation of Artificial Intelligence model for forecasting the vertical profiles of monthly mean zonal winds using machine learning algorithms over Thumba.

Publications in Peer-Reviewed Journals

1. Das, S.S., G. Ramkumar, N. Koushik, D. J. Murphy, I. A. Girach, K. V. Suneeth, K.V. Subrahmanyam, V. K. Soni, Vivek Kumar, and M. Nazeer, "Multiplatform observations of stratosphere-troposphere exchange over the Bharati (69.41°S, 76°E), Antarctica during ISEA-35", *Journal of Atmospheric and Solar-Terrestrial Physics*, 211, 105455, <https://doi.org/10.1016/j.jastp.2020.105455>, 2020.
2. Emmanuel. M, S. V. Sunilkumar, M. Muhsin, K. Parameswaran, P. R. SatheeshChandran, B. Suneel Kumar, A. Maitra, A. N. V. Satyanarayana, N. Nagendra, "Effect of monsoon dynamics and deep convection on the upper troposphere lower stratosphere water vapour over Indian monsoon region", *Atmos. Res.*, <https://doi.org/10.1016/j.atmosres.2020.105336>, 2020.

3. Koushik, N., Kumar, K. K., Vineeth, C., Ramkumar, G., & Subrahmanyam, K. V., “Meteor radar observations of lunar semidiurnal oscillations in the mesosphere lower thermosphere over low and equatorial latitudes and their variability during sudden stratospheric warming events”, *Journal of Geophysical Research: Space Physics*, 125, e2019JA027736, <https://doi.org/10.1029/2019JA027736>, 2020.
4. Kumar, K K., K.V. Subrahmanyam, C Pradeep Kumar, Shanmugasundari, N Koushik, R P Ajith, and Girija Devi, “C-band dual-polarization Doppler weather radar at Thumba (8.50 N, 770 E): initial results and validation”, *Journal of Applied Remote Sensing*, 14(4), 044509, <https://doi.org/10.1117/1.JRS.14.044509>, 2020.
5. Kumar, K. K., “Is mesospheric quasi-biennial oscillation ephemeral?” *Geophysical Research Letters*, 48, e2020GL091033, <https://doi.org/10.1029/2020GL091033>, 2020.
6. Pramitha, M., Kishore Kumar, K. and Venkat Ratnam, M., “Observations and model predictions of vertical wavenumber spectra of gravity waves in the troposphere and lower stratosphere over a tropical station”, *Journal of Atmospheric and Solar-Terrestrial Physics*, 216, 105601, <https://doi.org/10.1016/j.jastp.2021.105601>, 2021.
7. Pramitha, M., Kishore Kumar, K., Venkat Ratnam, M., Praveen, M. and Rao, S. V. B., “Disrupted stratospheric QBO signatures in the diurnal tides over the low-latitude MLT region”, *Geophysical Research Letters*, 48, e2021GL093022, <https://doi.org/10.1029/2021GL093022>, 2021.
8. Pramitha, M., Kishore Kumar, K., Venkat Ratnam, M., Praveen, M., and Rao, S. V. B., “Stratospheric Quasi Biennial Oscillation Modulations of Migrating Diurnal tide in the Mesosphere and Lower Thermosphere over the Low and Equatorial Latitudes”, *Journal of Geophysical Research: Space Physics*, 126, e2020JA028970, <https://doi.org/10.1029/2020JA028970>, 2021.
9. Pramitha, M., Kumar, K. K., Ratnam, M. V., Praveen, M., and Rao, S. V. B., “Gravity wave source spectra appropriation for mesosphere lower thermosphere using meteor radar observations and GROGRAT model simulations”, *Geophysical Research Letters*, 47, e2020GL089390, <https://doi.org/10.1029/2020GL089390>, 2020.
10. Ramesh, K., Smith, A. K., Garcia, R. R., Marsh, D. R., Sridharan, S., and Kishore Kumar, K., “Long-term variability and tendencies in middle atmosphere temperature and zonal wind from WACCM6 simulations during 1850-2014”, *Journal of Geophysical Research: Atmospheres*, 125, e2020JD033579, <https://doi.org/10.1029/2020JD033579>, 2020.
11. Ramesh, K., Smith, A. K., Garcia, R. R., Marsh, D. R., Sridharan, S., and Kishore Kumar, K., “Long-term variability and tendencies in migrating diurnal tide from WACCM6 simulations during 1850-2014”, *Journal of Geophysical Research: Atmospheres*, 125, e2020JD033644, <https://doi.org/10.1029/2020JD033644>, 2020.
12. Ranganayakulu, S.V., K. V. Subrahmanyam and A. Niranjana, “A Novel Algorithm for Convective cell Identification and Tracking based on Optical Character Recognition Neural Network”, *Journal of Electromagnetic Waves and Applications*, <https://doi.org/10.1080/09205071.2021.1941299>, 2021.
13. Satheesh Chandran. P. R, S. V. Sunilkumar, M. Muhsin, M. Emmanuel, Geetha Ramkumar, Prabha R Nair, “Effect of meteorology on the variability of ozone in the troposphere and lower stratosphere region over a tropical station Thumba (8.5°N, 76.9°E)”, *Journal of Atmospheric and Solar Terrestrial Physics*, 215, 105567, <https://doi.org/10.1016/j.jastp.2021.105567>, 2021.
14. Subrahmanyam, K.V. and K. Kishore Kumar, “The Vertical structure of latent heating and their association with cloud types during the Indian summer monsoon”, *Remote Sensing Letters*, <https://doi.org/10.1080/2150704X.2020.1820615>, 2020.
15. Subrahmanyam, K.V., and Sruthy Rose Baby, “C-band Doppler weather radar observations during the passage of tropical cyclone ‘Ockhi’”, *Natural Hazards*, <https://doi.org/10.1007/s11069-020-04268-2>, 2020.
16. Uma, K. N., S. S. Das, M.V.Ratnam, and K.V. Suneeth, “Assessment of vertical air motion among reanalyses and qualitative comparison with direct VHF radar measurements over the two tropical stations”, *Atmospheric Chemistry and Physics*, 21, 2083-2103, <https://doi.org/10.5194/acp-21-2083-2021>, 2021.
17. Vishnu, R., Y. Bhavani Kumar and Anish Kumar Nair, “An Investigation of the Elevated Aerosol Layer Using a Polarization Lidar Over a Tropical Rural Site in India”, *Boundary-Layer Meteorology*, 178, 323-340, <https://doi.org/10.1007/s10546-020-00573-2>, 2020.
18. Vineeth, C., K. M. Ambili, T. K. Pant and K. V. Subrahmanyam, “Role of Equatorial Fountain for the Delayed Response of Thermosphere O1D 630.0 nm Day-glow over the Dip Equator during an X-class Flare”, *Journal of Geophysical Research: Space Physics*, 126, <https://doi.org/10.1029/2020JA028624>, 2021.

Presentation in Symposium/Conferences/Workshops

1. Satheesh Chandran P. R, S. V. Sunilkumar, Muhsin. M and Maria Emmanuel, “Effect of monsoon dynamics on the variability of ozone in the upper troposphere lower stratosphere region from balloon borne observations”, 43rd COSPAR scientific Assembly, Sydney, Australia, 28 Jan-04 Feb 2021.
2. Subrahmanyam, K.V. and Karanam Kishore Kumar, “C-band Polarimetric Doppler Weather Radar observations during an extreme precipitation event and associated dynamics over Peninsular India”, ISRSNS-2020, Space Application Centre (SAC), Ahmedabad, 18-19 December 2020.
3. Subrahmanyam, K.V. and Karanam Kishore Kumar, “Characterizing the diurnal variation of precipitating clouds as observed by C-band Polarimetric Doppler Weather Radar at Thumba, India”, National E-Symposium on Cloud and Precipitation Processes, IITM, Pune, 18-20 January 2021.
4. Subrahmanyam, K.V. and Karanam Kishore Kumar, “Diurnal evolution of the vertical structure of precipitating clouds over the southernmost part of the Western Ghats of India during summer and winter monsoons”, TROPMET-2020, North East Space Application Centre (NESAC), Shillong, 14-17 December 2020.
5. Subrahmanyam, K.V., C. Ramsenthil, D. Bala Subrahmanyam, Aniket Chakravorthy, R. Sreedhar, E. Ezhilrajan, Radhika Ramachandran, C. S. Jha and M. Rajasekhar, “Forecasting of time series of geophysical parameters using Artificial Intelligence, Virtual conference on TROPMET-20”, North East Space Application Centre (NESAC), Shillong, 14-17 December 2020.
6. Subrahmanyam, K.V., C. Ramsenthil, D. Bala Subrahmanyam, Aniket Chakravorthy, R. Sreedhar, E. Ezhilrajan, Radhika Ramachandran, C. S. Jha and M. Rajasekhar, “Forecasting of time series of geophysical parameters using Artificial Intelligence”, Virtual conference on Young Scientist Conference (YSC), Indian International Science Festival (IISF)-2020, Delhi, 22-24 December 2020.

Invited Talks

K. Kishore Kumar

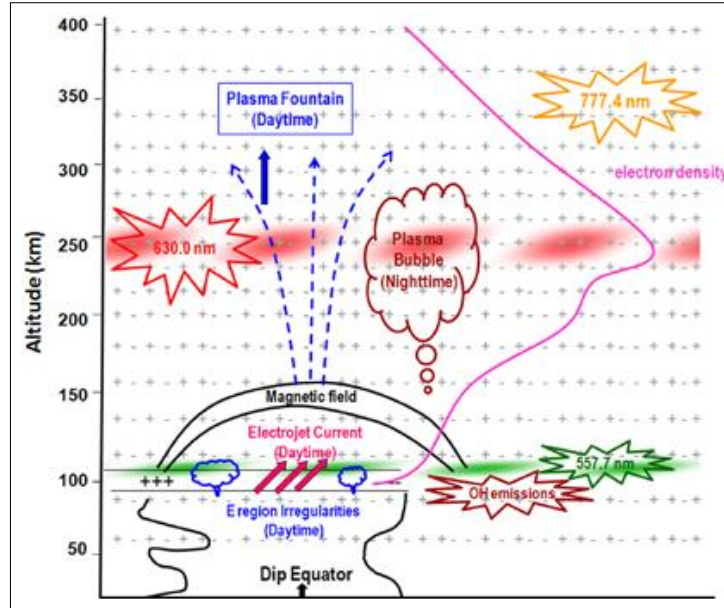
1. UGC Refresher course on “Middle Atmospheric Dynamics” organized by Department of Atmospheric and Space Sciences, Savitribai Phule Pune University, 4-18 January 2021.
2. “Are large-scale atmospheric circulations Accelerating in Present climate”, Webinar on Recent Advances in Atmospheric Sciences, National Center for Earth Science Studies, 30 April 2021

Training Programme

Kandula V Subrahmanyam

- Phase-III & Phase-IV of Artificial Intelligence (AI) organized by Directorate for Technology Development and Innovation (DTDI) during October 2020 (Phase-III) and December- 2020 (Phase-IV).

आयनमंडल तापमंडल एवं चुंबकमंडल भौतिकी IONOSPHERE THERMOSPHERE MAGNETOSPHERE PHYSICS



आयनमंडल, तापमंडल एवं चुंबकमंडल भौतिकी (आइटीएमपी) शाखा का लक्ष्य, (क) बदलते अंतरिक्ष मौसम एवं भूचुंबकीय परिस्थितियों तथा इसके अक्षांशीय असमानताओं पर चुंबकमंडल तापमंडल आयनमंडल प्रणाली की अनुक्रिया का अध्ययन (ख) तापमंडल-आयनमंडल का उसके नीचे प्रसरित वायुमंडल के साथ गतिकीय युग्मन पर अध्ययन (ग) ऊपरि वायुमंडलीय प्रक्रमों का प्रतिनिधित्व करने के लिए तापमंडल-आयनमंडल मॉडलों का आंतरिक विकास व उपयोग, और प्रौद्योगिक अनुप्रयोगों के लिए बेहतर इनपुट प्रदान करने हेतु इन अध्ययनों का उपयोग करने पर ध्यान केंद्रित करते हुए, भौमिक ऊपरी वायुमंडल की ऊर्जिकी तथा गतिकी की जाँच करना है। आइटीएमपी शाखा का यह प्रयास रहता है कि वह इन अनुसंधान लक्ष्यों को भूमि, रॉकेट तथा अंतरिक्ष आधारित मंचों में प्रयोग हेतु क्षमता रखनेवाले स्वदेशी तौर पर विकसित परीक्षणों के माध्यम से तथा अनुसंधान की व्याप्ति को अन्य सौर प्रणाली पिंडों के चुंबकमंडल, तापमंडल तथा आयनमंडल तक भी बढ़ाकर पूरा करे।

Ionosphere Thermosphere Magnetosphere Physics (ITMP) branch aims at investigation of the energetics and dynamics of terrestrial upper atmosphere, with focus on (a) Study of the response of the magnetosphere thermosphere ionosphere system to varying space weather and geomagnetic conditions and its latitudinal differences, (b) Study of the dynamical coupling thermosphere-ionosphere has with the atmosphere below it, (c) In house development and use of thermosphere-ionosphere models to represent the upper atmospheric processes and make use of these studies to provide better input for technological applications. ITMP strives to meet these research objectives through indigenous development of experiments capable of being used on ground, rocket and space-based platforms and extending the scope of its research to the magnetospheres, thermospheres, and ionospheres of other solar system bodies as well.

वैज्ञानिक टीम / Science Team

तरुण कुमार पंत / Tarun Kumar Pant
राज कुमार चौधरी / Raj Kumar Choudhary
मंजू जी / Manju G.
विनीत सी / Vineeth C.
मो. मोसारफ होस्सेन / Md. Mossarraf Hossain
संध्या के नायर / Sandhya K. Nair
मृदुला एन / Mridula N.
अंबीली के एम / Ambili K. M.
अजय अनिल पोटडार / Ajay Anil Potdar[§]

तकनीकी टीम / Technical Team

अनुमोद पी जी / Anumod P. G.
मणिकंठन नायर एन / Manikantan Nair N.
मोहम्मद नजीर एम / Mohammad Nazeer M.
उत्तम एस पूर्ती / Uttam S. Purty

इंस्पायर फैकल्टी / Inspire Faculty

अंकुष भास्कर / Ankush Bhaskar

अनुसंधान सहयोगी / Research Associates

अजेष ए / Ajesh A.
अश्वती आर पी / Aswathy R. P.*
दीप्ती रंजन रौत / Dipti Ranjan Rout #
जयलेक्ष्मी जी एल / Jayalekshmi G. L.
शमयता रेय / Shamayita Ray
राम सिंग / Ram Singh

अनुसंधान अध्येता / Research Fellows

केशव राम त्रीपाठी / Keshav Ram Tripathi
ललिता जी / Lalitha G
रिचवा नाजा जैन / RichaNaja Jain
सचिन एस / Sachin S
श्रुती टी वी / Sruthi T.V.

* Relieved in February 2021

Relieved in August 2020

§ Joined in January 2021

Equatorial Thermosphere Ionosphere Processes

The Post Sunset Equatorial F- region Zonal Drift Variability, its Linkage with Equatorial Spread- F Onset and duration over Indian Longitudes

The seasonal and solar activity variation of the post sunset F- region zonal plasma drift, at the magnetic equatorial region over Indian longitudes is examined using satellite data, namely data obtained onboard the Republic of China Satellite-1 for period January 2000 to April 2004. The dependence of the F region peak vertical drift on the zonal plasma drift at 18.5 IST (Indian Standard Time) and the time difference of the conjugate points sunset times, are quantitatively analysed. Further an integrated parameter (incorporating the above mentioned two independent factors), which is able to predict the peak vertical drift and growth rate of Rayleigh Taylor instability is proposed (Fig.1). The other major outcome of the study is the successful prediction of the Equatorial Spread-F (ESF) onset time and duration using the new integrated parameter at 18.5 IST. The present methodology for the prediction of the characteristics of these nocturnal irregularities becomes significant in mitigating the hazardous implications of the same for communication and navigation.

Ionospheric Planetary Wave Activity and Its Role in Equatorial Spread-F Day-to-day Variability

An analysis on the ionospheric Planetary Wave (PW) activity is undertaken using ionosonde data at Trivandrum and Thermosphere Ionosphere Mesosphere Energetics

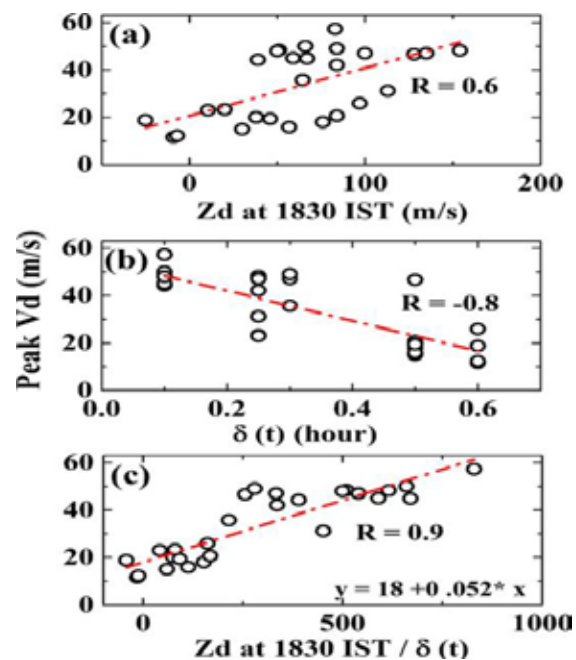


Figure 1: (a) Variation of monthly mean peak vertical drift V_d with peak zonal drift Z_d (b) Variation of the same with time difference 'dt' (c) Variation of the same with the integrated parameter [Aswathy and Manju, *Adv. Space Res.*, 2021].

and Dynamics satellite (TIMED) observations of off-equatorial E- region. The study reveals that the dominant PW is of 16- day periodicity and its strength is maximum in winter solstice/ autumnal equinox and minimum in summer solstice in high solar activity conditions. In low solar activity years, PW activity is more or less comparable in vernal equinox, autumnal equinox and winter solstice, while it is observed to be least in summer solstice. Further,

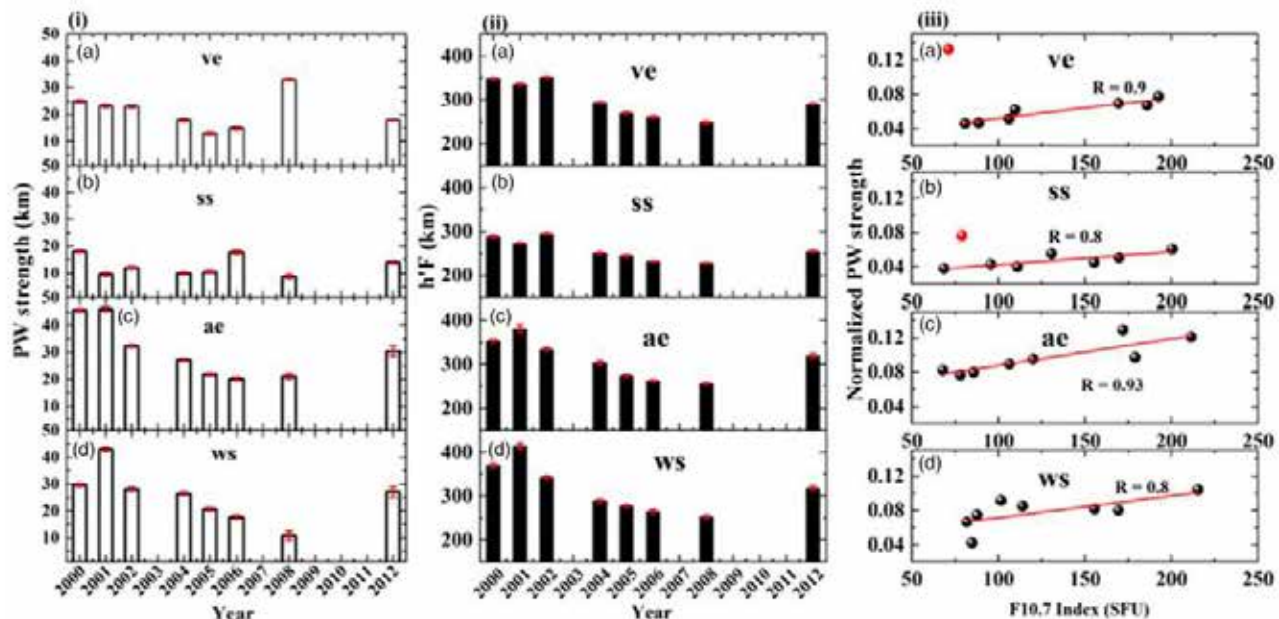


Figure 2: (i) Yearly variation of the seasonal average of the extracted power (strength) of planetary waves from h'F fluctuations. (ii) Yearly variation of the seasonal mean of h'F. (iii) The correlation of seasonal mean of F10.7 index and seasonal mean of normalized planetary wave strength [Manju and Aswathy, *J. Geophys. Res.*, 2021].

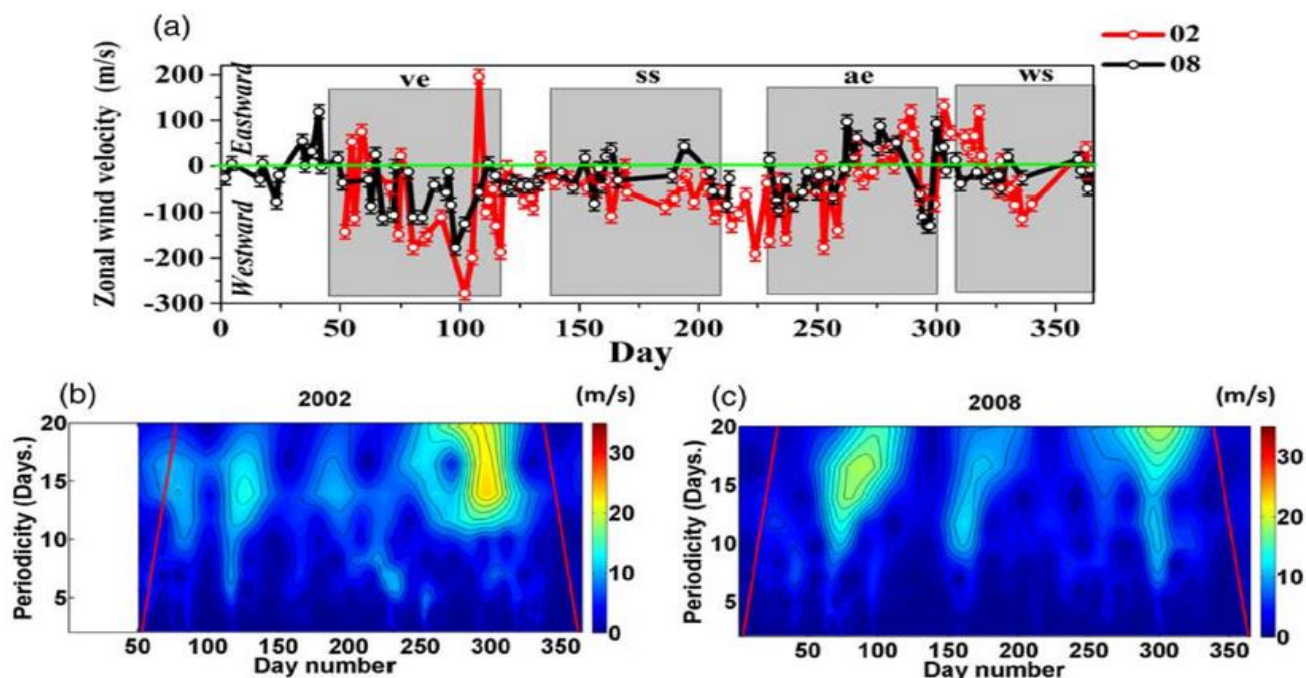


Figure 3 (a) TIMED satellite observations of off-equatorial zonal wind at 90 km for the years 2002 and 2008. Negative values represent westward winds, and positive values represent eastward winds. (b) Wavelet periodogram of off-equatorial zonal wind fluctuations for the year 2002. (c) Wavelet periodogram of off-equatorial zonal wind fluctuations for the year 2008 [Manju and Aswathy, *J. Geophys. Res.*, 2021].

the PW activity shows direct correlation with solar activity for the different seasons (Fig.2). TIMED observations of off-equatorial E-region zonal winds confirm the fact that they are strong westward in high solar activity years compared to low solar activity years. The strong westward winds (Fig. 3a) aid the upward propagation of westward propagating PWs in high solar activity years. The PWs reaching the off-equatorial E-region modulate the equatorial F-region via the coupling along the magnetic field lines. The role of PWs in modulating the pre-reversal enhancement, equatorial spread F duration and its spread range on a day-to-day basis is brought out quantitatively for both high and low solar activity conditions. This study emphasizes importance of ionospheric PW studies for the prediction of equatorial spread F characteristics.

Role of Equatorial Fountain for the Delayed Response of Thermosphere O¹D 630.0 nm Dayglow over the Dip Equator during an X-class Flare

This study reveals, for the ‘first time’, a delayed response of O¹D 630.0 nm dayglow emissions over Thumba, geomagnetic dip equatorial station in India, to the noontime X-class solar flare event of July 30, 2005. The dayglow measurements were made using the unique dayglow photometer operating at three wavelengths. The Equatorial Electrojet (EEJ) induced magnetic field, measured using a proton precession magnetometer, showed a magnetic spike having ~90 nT enhancement during this flare with a time delay of ~7.2 minutes. A noteworthy observation is that, unlike to the conventional belief, the O¹D 630.0 nm

dayglow over the dip equator exhibited a fourfold enhancement during the noontime flare after a time delay of ~45 minutes as shown in Fig.4. Analysis of satellite measured electron density and simulations using a quasi 2D ionospheric model (Fig. 5) indicate that the thermospheric O¹D 630.0 nm dayglow emission over the dip equatorial region during a solar flare is primarily driven by the

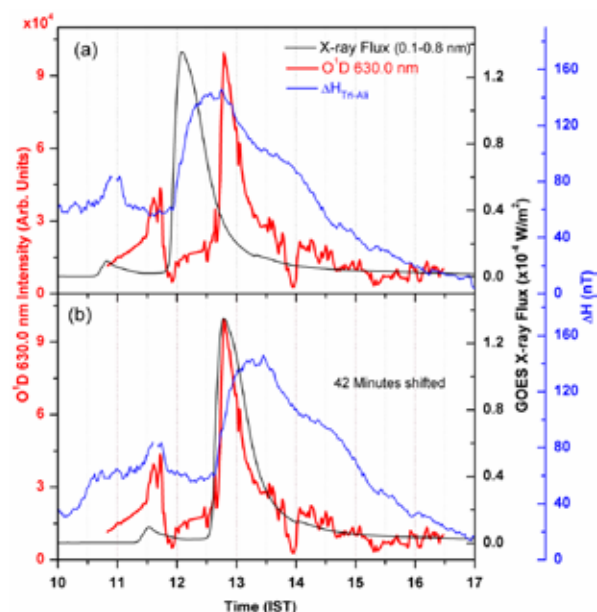


Figure 4: Time variation of (a) O¹D 630.0 nm dayglow emissions, X-ray flux and EEJ induced magnetic field on July 30, 2005, (b) same as Figure 2a but for the X-ray flux and EEJ induced magnetic field forward time shifted by 42 minutes [Vineeth et al., *J. Geophys. Res.*, 2021].

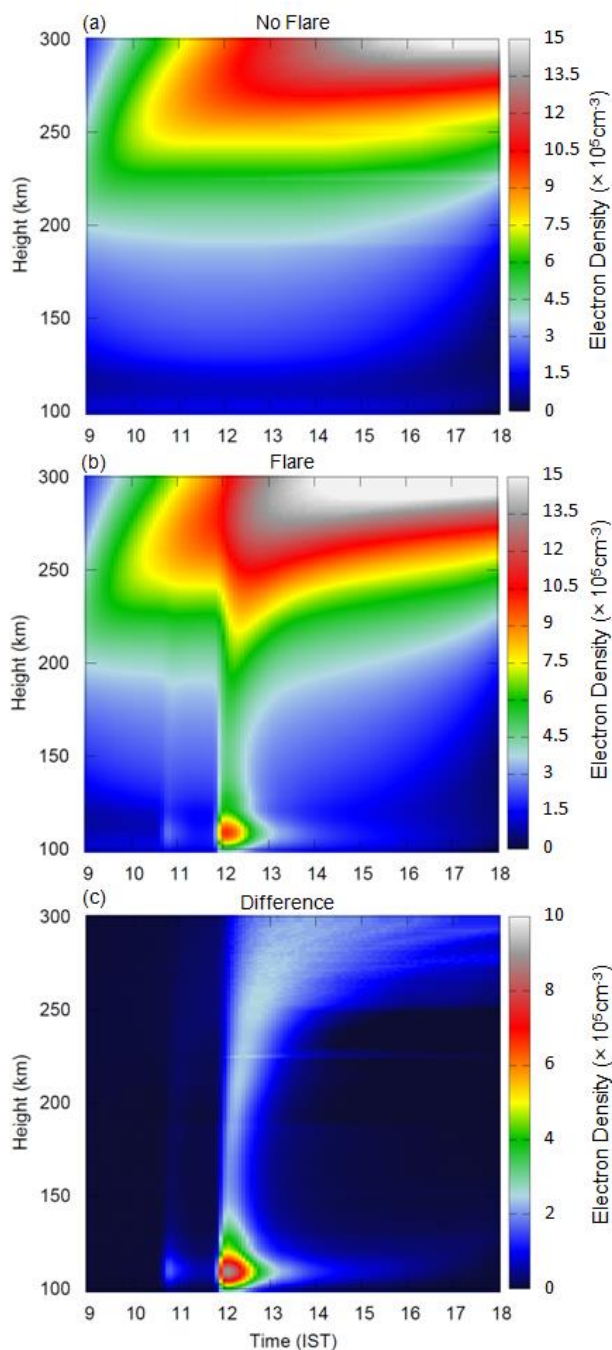


Figure 5: The modelled electron density profile on July 30, 2005 (a) without flare (b) with flare and (c) the difference between the flare and without flare [Vineeth et al., J. Geophys. Res., 2021].

electrodynamics, rather than the direct solar control. This finding is new, unique and very important for the studies related to plasma-neutral coupling and also for modelling studies on the equatorial thermosphere-ionosphere region.

Nighttime Enhancement in the Ionospheric Electron Density Over the Equatorial Anomaly region

Extending the study on the anomalous enhancement in the nighttime electron density over the equatorial ionosphere,

referred as the ionospheric nighttime enhancement (INE), their characteristics and occurrence probability was studied in the Appleton anomaly zone. The INE near equatorial ionization anomaly crest region in the Indian ionospheric sector was studied during May 2016 to August 2017, a solar minimum period using the VTEC data obtained from a multi-frequency multi-constellation global navigation satellite system (GNSS) receiver installed at Bhopal (23.2°N, 77.4°E & MLAT 14.2°N) under InSWIM program. A couple of examples of INE at Bhopal are shown in Fig.6. Only those enhancements which show VTEC enhancement $\sim 10\%$ compared to the background has been considered in the study. Out of the total 105 cases of enhancement recorded during this period, 86 events occurred during pre-midnight and 19 during post-midnight hours. Enhancements in VTEC occurred in all seasons; more frequent however during summer than winter and equinox months. Some of the nighttime enhancements in VTEC resulted in the scintillations in the satellite signals as well. Peak amplitude of the enhancement maximizes in summer whereas its half amplitude duration maximizes during equinox month. The number of occurrences of nighttime enhancement in VTEC shows negative correlation with peak amplitude while they are positively correlated with half amplitude duration. It has been found that the peak amplitude of nighttime enhancements in VTEC shows strong positive correlation while percentage occurrence shows strong negative correlation with solar and magnetic activities respectively. Other characteristics like half amplitude duration, time of peak and occurrence time of nighttime enhancement in VTEC show positive correlation with solar activity while they are insignificant with magnetic activity. The peak amplitude of pre-midnight enhancements in VTEC is highly correlated with the strength of Equatorial Electrojet (EEJ) strength (Fig.7). To conclude, it has been found that electrodynamic drift and plasma motion due to neutral air winds along with EEJ are the main cause behind the nighttime enhancement in vertical total electron content (VTEC) in the anomaly crest region, Bhopal.

Development of a Neural Network based TEC Model for Equatorial Ionospheric Anomaly Region

A Neural Network (NN) has been developed for the prediction of Vertical Total Electron Content (VTEC) over Bhopal (23.2°N, 77.4°E & MLAT 14.2°N), an equatorial Ionization anomaly crest region. The study is based on the VTEC data recorded by a multi-frequency, multi-constellation GNSS receiver installed at Bhopal during May 2016 to August 2017. The NN consists of artificial neurons that are used to learn data patterns, adjusting weights between input, hidden and output layers by computational modeling (Fig. 8). In order to obtain the optimal number of neurons in the hidden layer, the

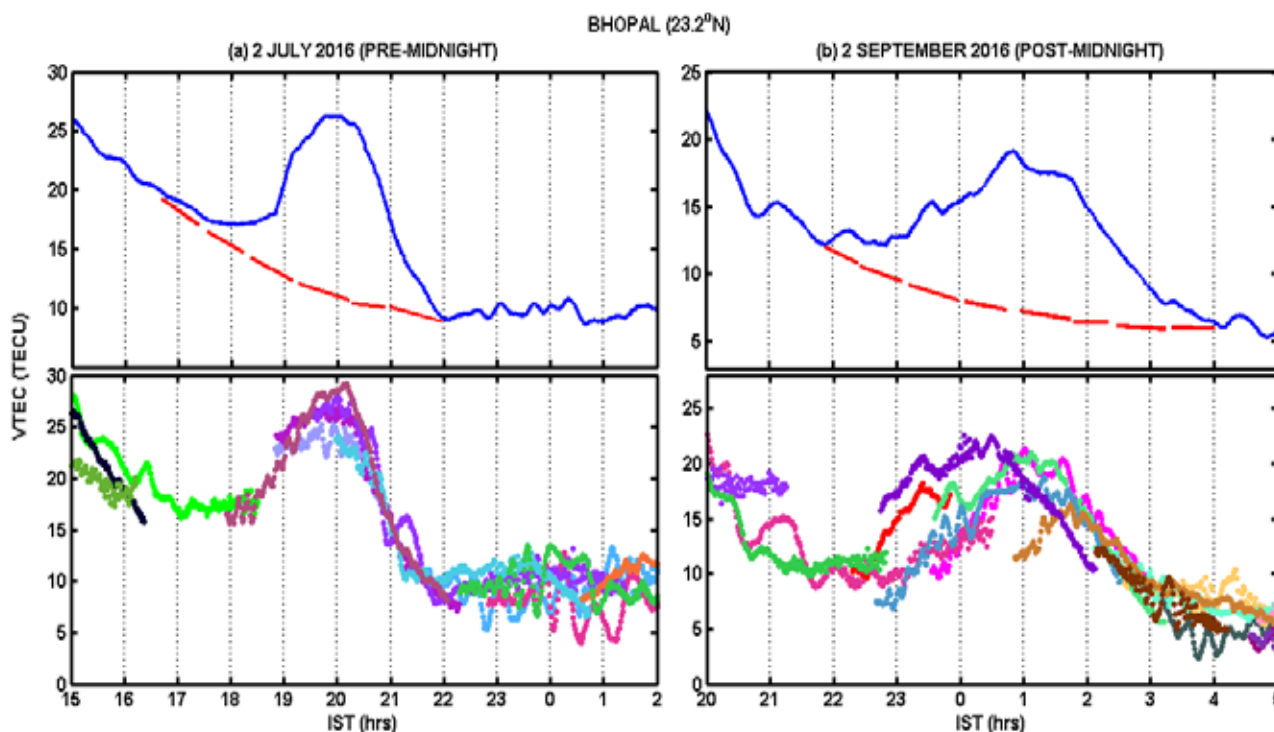


Figure 6: Examples of nighttime enhancement in VTEC for (a) pre-midnight (July 2, 2016) and (b) post-midnight (September 2, 2016) hours. Top panel represents the running average of VTEC for all PRNs and bottom panel represents the nighttime enhancement in VTEC for individual PRNs. The dashed line in the top panel shows the background VTEC content [Sahu et al, Adv. Space Res., 2020].

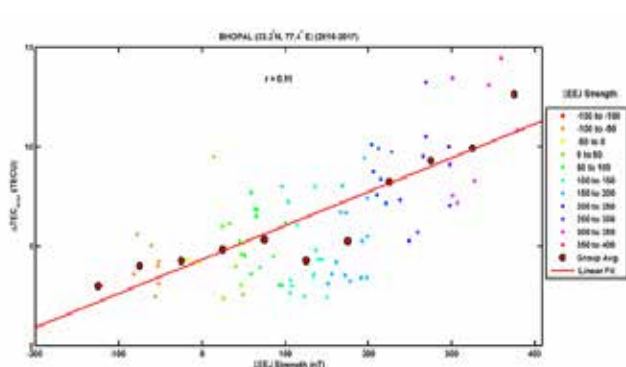


Figure 7: Variation of peak amplitude with ΣEEJ strength. (The colour dots show all data points in the respective groups of ΣEEJ strength and the average values are also shown with red circles on linear fit line) [Sahu et al, Adv. Space Res., 2020].

performance of four systems of neural network have been tested. Out of which, the fourth neural network has been used to predict VTEC with 7 input neurons in the present study. The number of hidden layer neurons is a factor that affects the performance of the trained networks. The input layer of the network includes the year, day of the year, hour of the day, geographic latitude, geographic longitude, Sun spot number and NmF2 from International Reference Ionosphere (IRI) model. The TEC obtained from the neural network prediction (NN TEC) has been compared with the GPS derived TEC (GPS TEC) and TEC from IRI-2016 model (IRI TEC) and depicted in Fig 9. It has been observed that the Root Mean Square Error (RMSE) decreases with increase in the number of hidden layer neurons. The RMSE

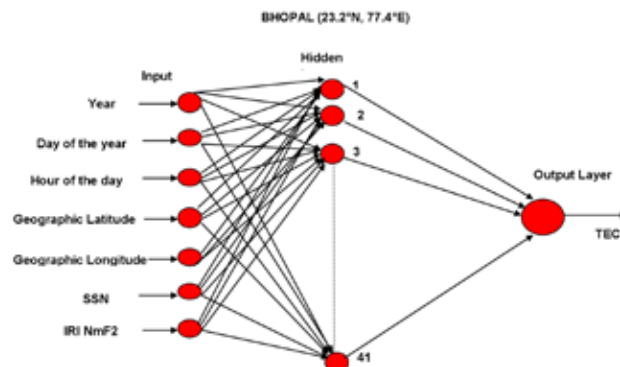


Figure 8: Schematic diagram showing the neural network used in the present study [Sahu et al, Adv. Space Res., 2021].

comes out to be lowest (1.96 TECU), when the number of hidden layer neurons are 41. The TEC predicted from the NN model and estimated from GPS receiver have same trend at 01:00 and 07:00 UT. The modelled NN TEC values are in good agreement with GPS TEC values for all seasons and 0.99 correlation coefficient was calculated for summer months, but IRI TEC always underestimates GPS TEC in all seasons. The NN model excellently predicted the TEC values of August 2017 by putting the credentials of August 2016 and only 0.55–32.16% relative errors were estimated between them whereas it reaches up to 93.86% with IRI TEC. Thus, the result shows that the proposed NN model can predict the diurnal and seasonal GPS TEC more accurate than IRI over anomaly crest region Bhopal. However, the inclusion of IRI-NmF2 as input layer neuron increases the network performance.

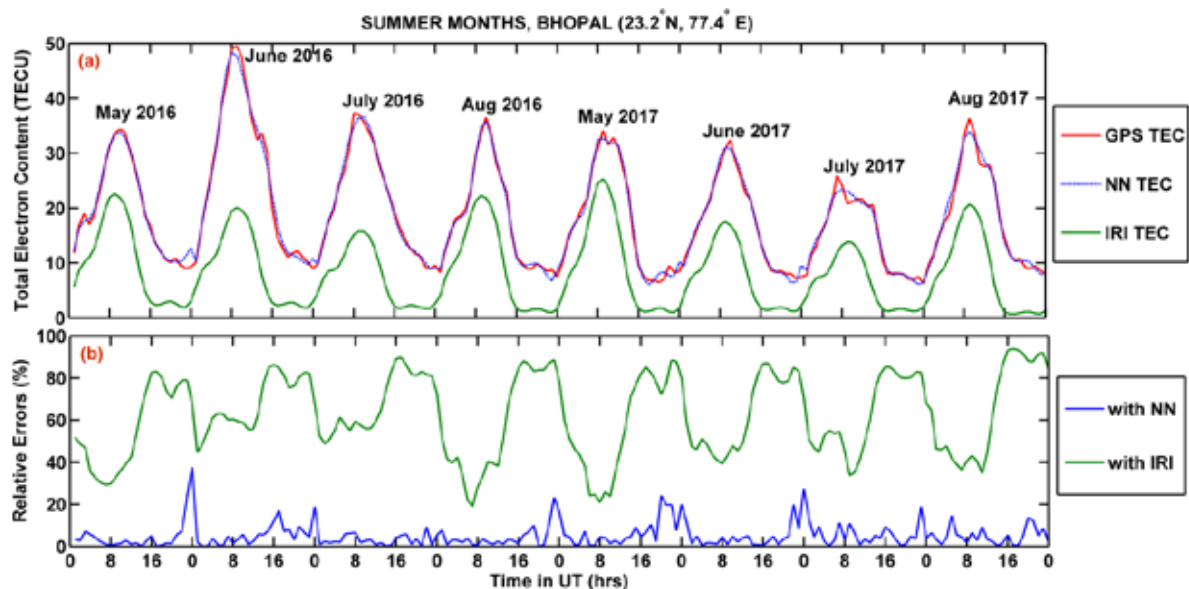


Figure 9: (a) Comparison of GPS TEC with the corresponding predictions from modelled NN TEC and IRI TEC (b) represents relative errors of NN TEC and IRI TEC with GPS TEC respectively for summer months at Bhopal (2016–2017) [Sahu et al, Adv. Space Res., 2021].

Studies on Planetary Ionospheric Processes

First Estimations of Gravity Wave Potential Energy in the Martian Thermosphere: An Analysis using MAVEN NGIMS Data

Precise aero-braking operations are extremely important for the safety of Mars lander missions. These operations depend on the atmospheric background conditions like wind and temperature. Gravity waves (GWs) have the potential to slow down or reverse the mean flow (wind) in the upper thermosphere through momentum exchange processes and thereby modulate the energy budget. It is therefore important to quantify the spatio-temporal evolution of the longitudinal distribution of GW Potential Energy (GWPE) in the Martian thermosphere. In this context, the first time estimations of GWPE for the Martian thermosphere are reported herein. The GWPE obtained from CO₂ density derived temperature fluctuations in the altitude region of 160–220 km corresponding to all Martian seasons during the 33rd Martian year (earth year: 2015–2017) have been analysed. Explicit diurnal evolution of GWPE (for 62° to 72° North latitude bin) with a post sunset maximum is delineated for summer (Fig. 10). The higher values of GWPE, during morning hours, compared to post mid-night period in the 40°–50° latitude bin for summer, is another important observation. Further, it is seen that GWPE in autumn is 6 times higher during the night time compared to day time for the 67° to 55° latitude bin. The analysis of the latitudinal variation of GWPE for the 3–4 LT bin of summer reveals near doubling of GWPE as the latitude increases from 9.6° to 44°. For the day LT bins (in the -56° to 67°

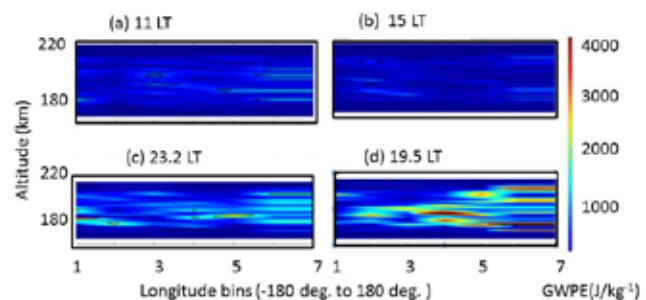


Figure 10: GWPE for four local times of the 6 longitude bins for the northern latitude bin of 52° to 73°, as a function of altitude (panels a–d) [Manju and Mridula, Monthly Notice Roy. Astron. Soc., 2021].

latitude bin) there is a clear decrease in the GWPE in autumn compared to spring for all longitudinal regions.

On the Seasonal Evolution of the Diurnal Pattern of the Longitudinal Structures in MAVEN NGIMS derived CO₂ Densities over Martian Upper Atmosphere

The Martian thermosphere system is coupled strongly to the lower atmosphere from below and the solar wind from above. Vertically propagating tides from lower atmosphere modulate the thermospheric energy budget and dynamics. Hence understanding the mean structure and variability of Martian thermosphere is essential to effectively comprehend the escape processes and eventually the planetary atmospheric evolution. In this scenario, an analysis on the longitudinal structures in the martian upper atmospheric CO₂ densities during the 33rd Martian year (earth year: 2015–2017) is carried out. The CO₂ densities in the altitude region of 165–220 km corresponding to

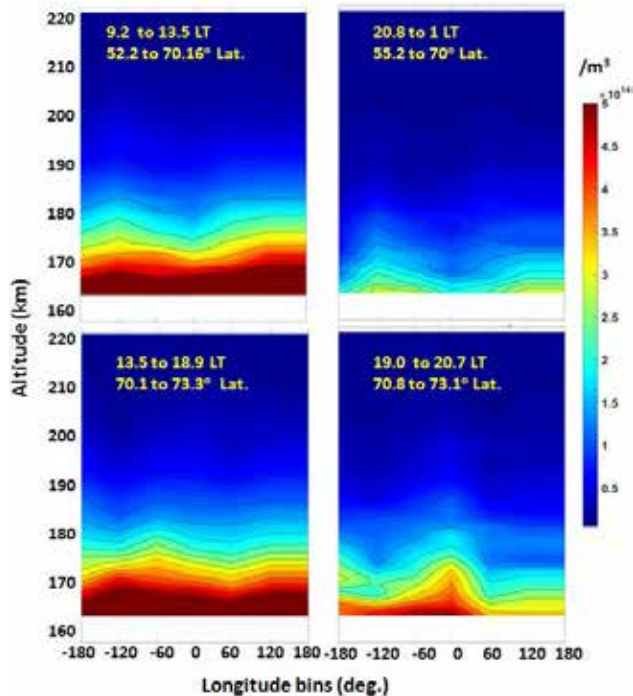


Figure 11: Local time variation of neutral density in Martian thermosphere during summer [Mridula and Manju, *J.Atmos.Sol. Terr. Phys.*, 2021].

the in-bound periapsis orbits of MAVEN NGIMS during different martian seasons have been considered for this study. The data used spans over a longitude region of -180° to 180° , the entire available latitude region (within 75°) and local time range of 0–24 h. The analysis reveals that there exists large longitudinal wave structure in CO_2 density which shows seasonal and local time variation (Fig.11).

The amplitude of the tidal waves are lower during day compared to night at the altitude region of 165–220 km for spring and summer. Seasonally based on the data available, the densities maximize in summer/autumn and attain minimum values in spring. Considering the entire martian year comprising all seasons (based on the availability of data), the wave-2 structure is found to manifest in the CO_2 densities. Theoretically predicted increased neutral density during southern summer nights in relation to autumn nights is experimentally demonstrated in this study. Thus the present analysis provides a clear picture of the diurnal evolution of the longitudinal structure in CO_2 densities for the martian seasons of Martian year.

Ongoing Scientific studies/Campaigns

Sounding Rocket Experiment(SOUREX-Phase-II)

The second phase of SOUREX campaign had been conducted successfully by launching a RH 560 MkIII rocket from SHAR on 12 March 2021, with ENWi and LP payloads being operated in dual modes along with TMA for the study of ion drifts, neutral winds, electron density and irregularities in the upper ionospheric region. For this purpose, the required quantity of TMA for successfully imaging using ground based cameras was estimated theoretically and the imaging locations & camera system needed for the experiment were finalized in collaboration with the LEOS, Bangalore. The TMA trail, released from 96 km to 155 km altitude, was imaged successfully from four locations as seen in Fig. 12. During this experiment, the TMA measurements covered 96 to 155 km altitude region in the upleg phase, while ENWi and LP covered 75 to 512 km



Figure 12: The TMA trail as imaged from the four ground stations. The station name is mentioned at the top of the column.

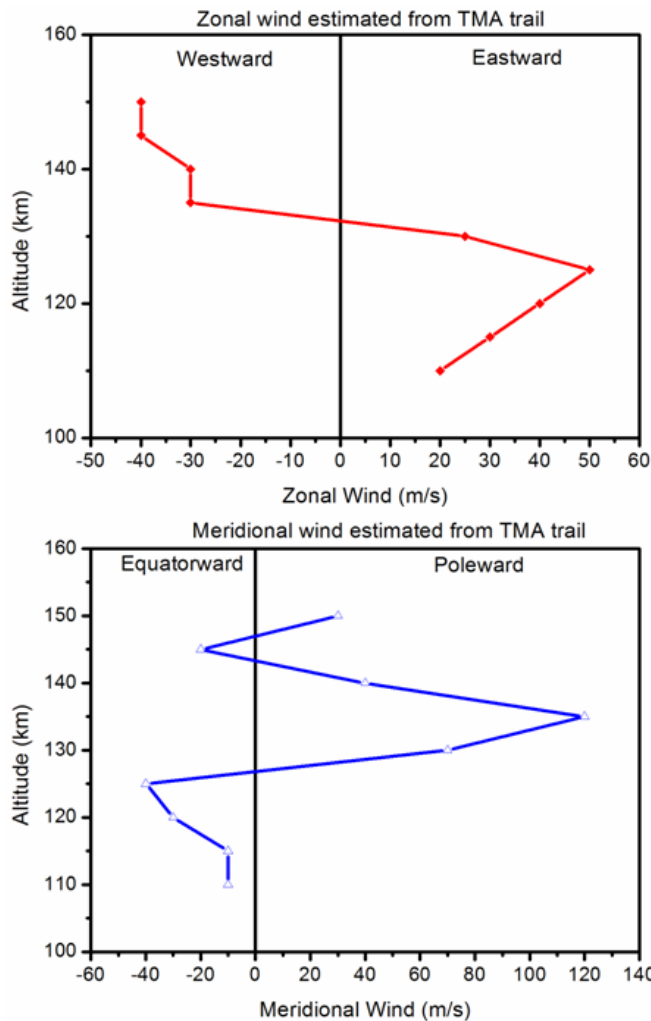


Figure 13: Altitude variations of zonal and meridional winds deduced from TMA trails.

altitude. This activity led by ATVP Project and SPL, had major contributions from MVIT, ASOE, AVN, MSA, MME, PCM, AERO and SPRE entities of VSSC, and launch support from SDSC, SHAR.

Analysis of the TMA data for SOUREX Phase-II revealed that there existed a large altitudinal gradient in the wind that was more pronounced for the meridional wind component. The altitudinal variations of the zonal and meridional components of the wind are shown in Fig.13. Interestingly, no significant large overturning features in the TMA trail existed at altitudes above 120 km.

The Electron density and neutral wind (ENWi) and Langmuir probe (LP) instruments were operated in different modes during the mission and the electron densities were derived from the altitude of 80 km to 510 km. The electron density profiles from cylindrical and spherical modes show good correspondence in terms of the broad features while the irregular structures are more prominent in cylindrical probe (Fig.14). The very steep bottom side electron density gradient is a remarkable feature. The uniqueness of these observations is that the altitudinal variation of the plasma

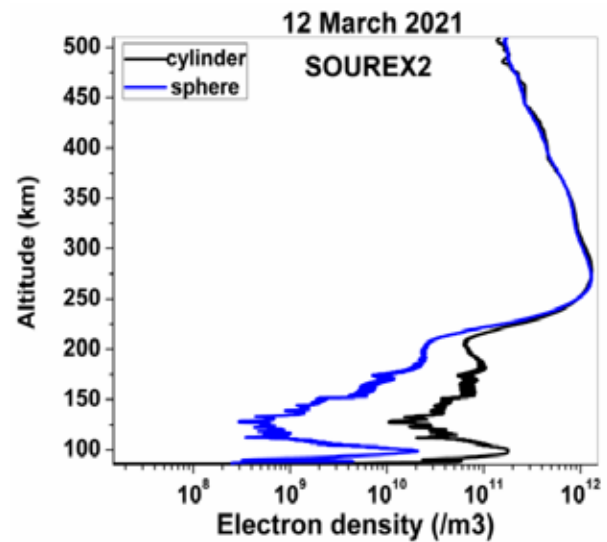


Figure 14: Electron density profiles obtained from LP cylindrical and spherical probes.

densities is revealed with excellent altitude resolution from around 80 km to 510 km. Ground based electron density measurements are capable of providing information only in the range of about 150-300 km during night time, which is the region of bottom side ionosphere wherefrom detectable reflected signals are obtained during night time. These profiles will help to investigate the vertical propagation characteristics of waves in the post sunset ionosphere. The plasma drift measurements were obtained from ENWi payload data. Detailed analysis is underway.

Investigations of Sun Earth Connections from Magnetospheric-Ionospheric Perspective

The long term variability exhibited by the solar activity in terms of magnetic flux, sunspot numbers, sunspot area at different solar latitudes is being investigated. The North-South asymmetry in the solar activity has been investigated. The results indicate that certain long period oscillations appear to be very effective in modulating the overall solar activity and the North-South asymmetry, ultimately manifesting in solar wind interactions with Earth's magnetosphere. Further, the magnetosphere is the environment in which the solar wind particle's acceleration, transport, and loss occurs. These are the fundamental processes that are very important for understanding how the solar wind energy gets distributed in the inner magnetosphere. Solar wind energy or stored energy in the magnetosphere sometimes manifests as particle injections. At times, after injections a bunch of particles has been observed drifting around the Earth, which is known as a "drift-echo". These drift-echoes, especially the ones induced by interplanetary shocks, are being investigated. Since, the ionosphere is intrinsically connected with the processes in magnetosphere, it responds to magnetospheric changes through electric fields and currents. For instance, the under-shielding and over-shielding electric fields in the magnetosphere are known to be governed by solar

wind changes and southward and northward turnings of interplanetary magnetic field (IMF Bz). The high latitude electric field penetrates to low and equatorial ionosphere whenever there is a sudden disruption in the shielding. In our recent studies, evidences of penetration and quasi-periodic oscillations of shielding electric fields associated with reorientations of IMF By under the steady northward IMF Bz condition have been shown. Detailed analysis is in progress.

Modelling of Planetary Ionospheres

In the area of the Ionospheric modelling, the recent progress has been the development/augmentation of: a) the Quasi Two-Dimensional (QTD) model for the terrestrial ionosphere, b) the one dimensional model for the Venusian ionosphere, and c) the three-dimensional model for the Lunar ionosphere. The QTD model includes all the chemistry from 70 km onwards till 600 km and the vertical drift. Currently, the model is employed to understand ionospheric features observed during different conditions such as electron density profiles and electrojet strength during the solar flare, variability in airglow intensity during midnight in context of the Midnight Temperature Maximum. The 1-Dimensional Photochemical Model (1D-PCM) developed for the Venusian ionosphere is able to predict electron density and V2 and V1 layer features during different solar activity phases. Detailed studies are being carrying out using this model and data from PVO, Venera, VeRa and Akatsuki missions. Another major activity had been the development of a model for calculating latitudinal, longitudinal and altitudinal variation of electron density over Moon. The model is being employed for generating the plasma density profiles for varying latitudes and longitudes of the moon to be used in conjunction with the data from CHACE-2, Apollo, LRO and LADEE missions.

Payloads/ New activities

RAMBHA-LP Payload on Chandrayaan-3

The Chandrayaan-3 RAMBHA-LP payload configuration remains similar to that flown on Chandrayaan-2. The RAMBHA-LP is a Langmuir probe (LP) onboard Lander for in situ measurements of ambient electrons, ions, densities and their temperatures. The basic operational parameters and the mechanical/ electrical systems of RAMBHA-LP have therefore been kept unchanged. The RAMBHA-LP payload consists of the mechanical module i.e. probe and a boom and the control electronics module. The required designer level tests of the flight models of control electronics and the mechanical system are completed. Post these tests, the end to end test and evaluation plan is being finalized. The integrated level tests and clearance are expected to be obtained by the end of September 2021. The characterization of probe for flight integration, realization of boom at CMSE, routing of RF cable on boom

and unit level test of actuator in thermo-vacuum have been completed. RAMBHA-LP is being developed with the help of several entities of VSSC including AVN, MVIT, MME, SR, CMSE, STR, PCM and AERO.

Development of Atomic Oxygen Sensor Payload onboard PS4 Mission

The atomic oxygen [O] is the most abundant constituent of the residual atmosphere in the Low Earth Orbit (LEO) altitudes and plays a significant role in many of the natural reactions in terrestrial upper atmosphere. It also exerts significant aerodynamic drag resulting in the degradation of the spacecraft's orbit, especially at LEO altitude in the high solar activity period. Hence, [O] has received considerable attention in the space science and engineering community. Despite being an important constituent of the thermosphere, there have been very few direct measurements of [O] owing to its highly reactive nature. In this context, a semiconductor oxide based [O] sensor (ATOXS) is being developed at SPL to measure the atomic oxygen concentration in the terrestrial upper atmosphere using PS4 and rocket platforms. During last year, the layout of ATOXS has been completed. The mask for sputtering the electrodes and ZnO films over Alumina is designed. Initiated the activities with MME, VSSC to sputter the electrodes and ZnO films over inert alumina and the development of the control electronics is in progress.

Upper-atmospheric Visible Airglow Spectral Imager (UrVASI)

UrVASI is a diffraction grating based spectral Imager proposed for studying the Earth's near space. The spectral band of the instrument is 530-780 nm and the resolution envisaged is 0.1 nm. The primary scientific objectives of this experiment are, the investigation of (i) *Coupling between different atmosphere regions through lower atmosphere wave forcings*, (ii) *manifestations of such processes in the evolution of large-scale processes like the Equatorial Ionization Anomaly, Equatorial Spread-F (ESF) and Midnight Temperature Maximum (MTM)*. The Baseline Design Report of UrVASI had been submitted and the BDR completed last year. Science compliance matrix was prepared and presented to a review committee constituted by SSPO. The preliminary optical design of the UrVASI has been performed using Zemax software in collaboration with SAC Ahmedabad and IIT, Roorkee. The optimization of the optical design of UrVASI is in progress.

Neutral Mass Spectrometer (NMS)

A Neutral Mass Spectrometer (NMS) has been proposed for measuring the composition in Earth's near space environment. The NMS is a quadrupole mass spectrometer based payload capable of measuring the neutral composition (1-100 amu), and the total pressure/neutral density. The sensor probe consists of a built-in electron impact ionizer along with a Bayard-Alpert collector catered by

a common emission circuit to measure the total pressure; a set of four quadrupole rods and a detector assembly. It draws its heritage from CHACE/MIP, MENCA/MOM and CHACE-2/Chandrayaan-2 missions. The primary mode of NMS instrument will use a well established mode of

operation where it is capable of measuring the neutral composition of the prevailing medium. However, an effort is being made to enhance the capability of the existing NMS, by suitably augmenting it to be able to measure not only the neutral but also the thermal ion composition.

Future Projections

- The first set of near surface, direct plasma measurements from Lunar polar region using the indigenously developed RAMBHA-LP payload aboard ISRO's forthcoming Chandrayaan-3 Lander will bring forth a new understanding of the surface bound ionosphere of Moon.
- To study the thermosphere-ionosphere system during varying geophysical conditions over the Indian region, five indigenously developed multi-wavelength nightglow photometers will be installed at the INSWIM chain of stations.
- The temporal changes in the ratio of the thermospheric Oxygen airglow emissions at 630 & 557.7nm will be used to infer changes in the thermospheric energetics.
- Investigation of the variability of the Equatorial Electrojet in terms of HF radar-measured (a) drifts, and (b) inferred changes in the prevailing electric field, in the current low solar activity epoch, will be carried out.
- The role of changes in the interplanetary magnetic field (IMF) orientations, especially that of the By component, in affecting the magnetospheric shielding and triggering the prompt penetration of electric field to low and equatorial latitudes will be explored in detail.
- The problem of day-to-day variability in the Equatorial Spread-F onset, evolution and duration will be addressed with focus on the seeding perturbations.
- Results concerning the Lunar atmospheric composition from the limited data from Dual Frequency Radio Science Experiment onboard CH-2 have to be further ascertained with more observations.
- As we continue to be actively participating in ISRO's forthcoming planetary missions through developing (a) experiments/payloads in-house, (b) ionospheric models, it is aimed to enhance the scope of our studies to planetary ionospheres involving both measurements and models.

Publications in peer reviewed journals

1. Manju G. and N. Mridula, "First estimations of gravity wave potential energy in the Martian thermosphere: An analysis using MAVEN NGIMS data", *Monthly notices of the Royal Astronomical Society*, 501, 1072-1077, <https://doi.org/10.1093/mnras/staa3491>, 2021.
2. Aswathy, R. P. and G. Manju, "The post sunset equatorial F-region zonal drift variability and its linkage with equatorial spread F onset and duration over Indian longitudes", *Advances in Space Research*, 67 (4), 1254-1260, <https://doi.org/10.1016/j.asr.2020.11.024>, 2021.
3. Manju G. and Aswathy R. P., "Ionospheric Planetary Wave Activity and Its Role in equatorial Spread F Day-to-Day Variability", *Journal of Geophysical Research*, <https://doi.org/10.1029/2020JA027960>, 2020.
4. Mridula N. and G. Manju, "On the seasonal evolution of the diurnal pattern of the longitudinal structures in MAVEN NGIMS derived CO₂ densities over Martian upper atmosphere", *Journal of Atmospheric and Solar-Terrestrial Physics*, 212, 105508, <https://doi.org/10.1016/j.jastp.2020.105508>, 2021.
5. Vineeth, C., Ambili, K. M., Pant, T. K., and Subrahmanyam, K. V., "Role of equatorial fountain for the delayed response of thermosphere O_{1D} 630.0 nm dayglow over the dip equator during an X-class flare", *Journal of Geophysical Research: Space Physics*, 126, 2020JA028624, <https://doi.org/10.1029/2020JA028624>, 2021.
6. Sahu, S., Pal, A., Choudhary, R.K., Jain, A. and Jain, S., "Nighttime enhancements in the VTEC at anomaly crest region Bhopal: Solar and magnetic activity effects", *Advances in Space Research*, 66(10), 2289-2301, <https://doi.org/10.1016/j.asr.2020.08.016>, 2020.
7. Sahu, S., Trivedi, R., Choudhary, R.K., Jain, A. and Jain, S., "Prediction of Total Electron Content (TEC) using Neural Network over Anomaly Crest Region Bhopal", *Advances in Space Research*, <https://doi.org/10.1016/j.asr.2021.05.027>, 2021.
8. Yadav, V., Rathi, R., Gaur, G., Sarkhel, S., Chakrabarty, D., Krishna, M.S., Chaitanya, P.P., Patra, A.K., Choudhary, R.K., Pant, T.K. and Upadhyaya, A.K., "Interaction between nighttime MSTID and mid-latitude

field-aligned plasma depletion structure over the transition region of geomagnetic low-mid latitude: First results from Hanle, India”, *Journal of Atmospheric and Solar-Terrestrial Physics*, 217, 105589, <https://doi.org/10.1016/j.jastp.2021.105589>, 2021

9. Saha, S., D. Pallamraju, T. K. Pant, S. Chakraborty, “The cause of nocturnal OI 630 nm airglow variability over low-latitude thermosphere”, *Journal of Geophysical Research: Space Physics*, <https://doi.org/10.1029/2021JA029146>, 2021
10. Manga, N.A., K. Lakshmana, A. D. Sarma, T. K. Pant, “Analysis of Correlation Between Roti and S4 Using GAGAN Data”, *Progress In Electromagnetics Research M*, 99, 23-34, 10.2528/PIERM20101405, 2021
11. Singh, P.R., A.I.S. Farid, A. K. Singh, T. K. Pant, A.A. Aly, “Predicting the maximum sunspot number and the associated geomagnetic activity indices aa and Ap for solar cycle 25”, *Astrophysics and Space Science*, 366, 48, <https://doi.org/10.1007/s10509-021-03953-3>, 2021.
12. Singh, P. R., A. I. S. Farid, T. K. Pant, A. K. Singh, “Signature of the 27-day variation in hemispheric sunspot activity and asymmetry during 2010–2015”, *Research in Astronomy and Astrophysics*, 21 (4), <https://doi.org/10.1088/1674-4527/21/4/106>, 2021.
13. Bhaskar, A., David G. Sibeck, Shrikanth G. Kanekal, Howard J. Singer, Reeves Geoffrey, Denny M. Oliveira, Suk-Bin Kang, Colin Komar, “Radiation Belt Response to Fast Reverse Shock at Geosynchronous Orbit”, *Astrophysical Journal*, 910 (2), <https://doi.org/10.3847/1538-4357/abd702>, 2021.
14. Koushik, N., Kumar, K. K., Vineeth, C., Ramkumar, G., and Subrahmanyam, K. V., “Meteor radar observations of lunar semidiurnal oscillations in the mesosphere lower thermosphere over low and equatorial latitudes and their variability during sudden stratospheric warming events”, *Journal of Geophysical Research: Space Physics*, 125, e2019JA027736, <https://doi.org/10.1029/2019JA027736>, 2020.

Book Chapter

- Miziya K., P. Pradeep Kumar, C. Vineeth, T. K. Pant, T. G., Anumod, Design and Implementation of Night Time Data Acquisition and Control System for Day and Night Glow Photometer. In: Patnaik S., Yang XS., Sethi I. (eds) *Advances in Machine Learning and Computational Intelligence. Algorithms for Intelligent Systems*. Springer, Singapore. https://doi.org/10.1007/978-981-15-5243-4_73, 2021.

Presentation/participation in Symposium/Conferences/Workshops

- C. Vineeth, Development of a Unique Airglow Photometer for measuring Extremely Faint Emissions from Planetary Atmospheres, India International Science Festival, New Delhi, December 22-24, 2020.

Trainings Programme

Tarun Kumar Pant

- “Space Weather Task Team (SWTT)”, CGMS-49 Working Group Meetings, Vienna, Austria, April 12-16, 2021

Manju G

- DTDI training program on Artificial Intelligence, ISRO HQ, Bangalore, August 2020 (online).

Invited Talks

Tarun Kumar Pant

- “अंतरिक्ष खोज का इतिहास”, विश्व हिन्दी दिवस व्याख्यान, विक्रम साराभाई अंतरिक्ष केंद्र, 22 फ़रवरी 2021

C. Vineeth

1. “Optical Remote Sensing of the Earth’s Near Space Environment”, International Webinar on Advances in Nonlinear Optics and Space Science, Department of Physics, Providence College, Kozhikkode, September 19, 2020 (online).
2. “Space Research in India”, Faculty Development Programme on “Skills for Next Generation Teachers” organized by Vimala College in collaboration with Guru Angad Dev Teaching Learning Centre of Ministry of Education (MoE), Govt. of India & Centre for European Studies, December 06, 2020 (online).

-
3. “The research activities of SPL and the SOUREX” at Radiation Safety Division (RASD), Indira Gandhi Centre for Atomic Research (IGCAR), Kalpakkam, March 12, 2021.

Ankush Bhaskar

1. “Space Weather impact on Asteroid”, orgnaized by Nehru Science Center on the International Asteroid Day event, June 30, 2021.
2. “Career in space Science”, organized by Indian National Young Academy of Sciences INYAS/INSA, New Dehi, June 19, 2021.
3. “Voyage through the Planetary Magnetospheres”, National Seminar on Astronomy and Climate Change, Department of Physics, Athalye-Sapre-Pitre Collge, Devrukh, Maharashtra, April 10, 2021.
4. “Dynamic Space Weather”, Gyan series lectures, Department of Physics, University of Mumbai, March 24, 2021.
5. “Space Weather and citizen science”, University of Mumbai, March 20, 2021.

Solar Wind and its Interaction with Planets and Planetary Bodies

Planetary Space Weather Studies Recurrent Solar Energetic Particle Flux Enhancements Observed near Earth and Mars

The period August 1 to November 15, 2016 was characterized by the presence of Corotating Interaction Regions (CIRs) and a few weak Coronal Mass Ejections (CMEs) in the heliosphere. It has been shown that recurrent energetic electron and proton enhancements occurred near Earth (1 au) and Mars (1.43–1.38 au) during this period. The observations near Earth use data from instruments onboard the Advanced Composition Explorer, the Solar and Heliospheric Observatory, and Solar Dynamics Observatory and those near Mars are from the Solar Energetic Particle,

Solar Wind Ion Analyser, and Magnetometer instruments onboard the Mars Atmosphere and Volatile Evolution (MAVEN). During this period, the energetic electron fluxes observed near Earth and Mars showed prominent periodic enhancements over four solar rotations, with major periodicities of ~27 days and ~13 days (Fig.1). Periodic radar blackouts/weakening of radar signals at Mars were observed by the MARSIS aboard Mars Express, and are associated with these solar energetic electron enhancements (Fig.2). These observations are unique, not only because of the recurring nature of electron enhancements seen at two vantage points, but also because they reveal the unexpected impact of the weak CME and interplanetary shock on the Martian ionosphere, which provides new insights into the impact of CME–CIR interactions on the Martian plasma environment.

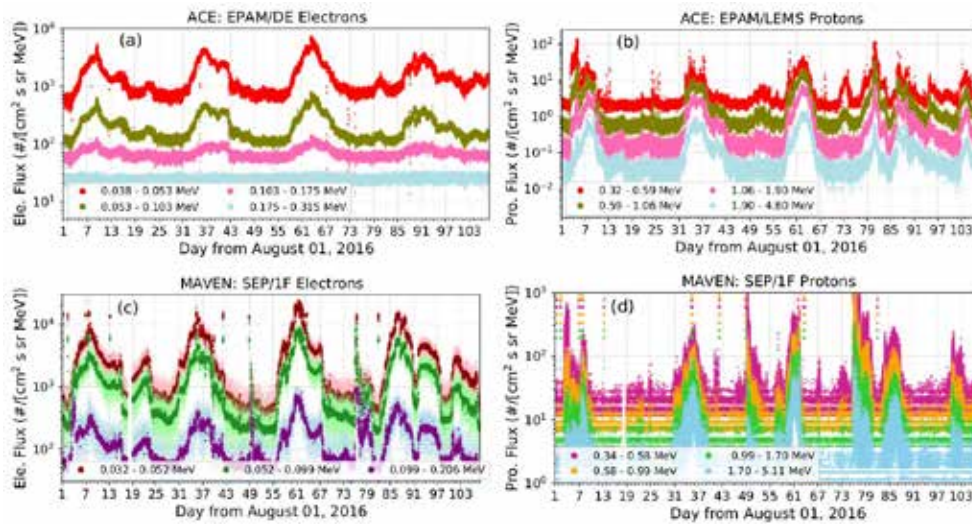


Figure 1: Temporal variation of the SEP fluxes during August 1–November 15, 2016. (a) Electron fluxes observed by ACE. (b) Proton fluxes observed by ACE. (c) Electron fluxes observed by MAVEN. (d) Proton fluxes observed by MAVEN [Krishnaprasad et al., *AstroPhys. J.*, 2020].

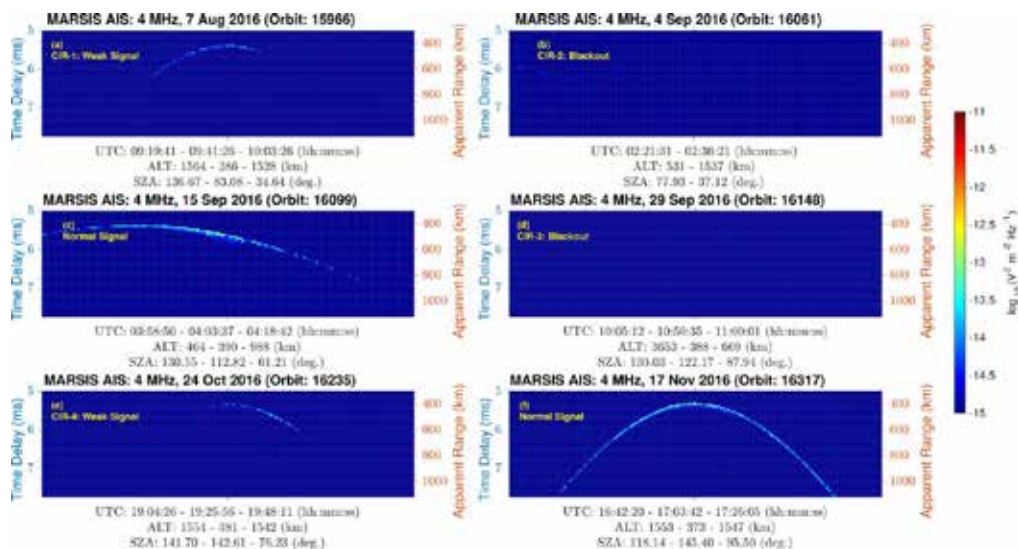


Figure 2: MARSIS/MEX Active Ionospheric Soundings. The time delay experienced by the signal at 4 MHz is shown in the left y-axis and the apparent range is shown in the right y-axis. The color bar represents the signal strength in units of electric field spectral density. Representative examples showing normal signals, blackouts and weak signals are given. [Krishnaprasad et al., *AstroPhys. J.*, 2020].

The Impact of a Stealth CME on the Martian Topside Ionosphere

Solar cycle 24 is one of the weakest solar cycles recorded, but surprisingly the declining phase of it had a slow coronal mass ejection (CME) that evolved without any low coronal signature and is classified as a stealth CME that was responsible for an intense geomagnetic storm at Earth ($Dst = -176$ nT). The propagation of this CME beyond 1 AU and its impact on other planetary environments have been studied using the data from the Sun–Earth L1 point and from the Martian orbit (near 1.5 AU). The observations near Earth were performed using the data from the Solar Dynamics Observatory (SDO) and the Advanced Composition Explorer (ACE) satellite located at L1 point, whereas those near Mars were from the instruments for plasma and magnetic field measurements onboard Mars Atmosphere and Volatile Evolution (MAVEN) mission. The observations show that the stealth CME has reached 1.5 AU after 7 days of its initial observations at the Sun (Fig.3) and caused depletion in the nightside topside ionosphere of Mars, as observed during the inbound phase measurements of the Langmuir Probe and Waves (LPW) instrument onboard MAVEN (Fig.4). These observations have implications on the ion escape rates from the Martian upper atmosphere.

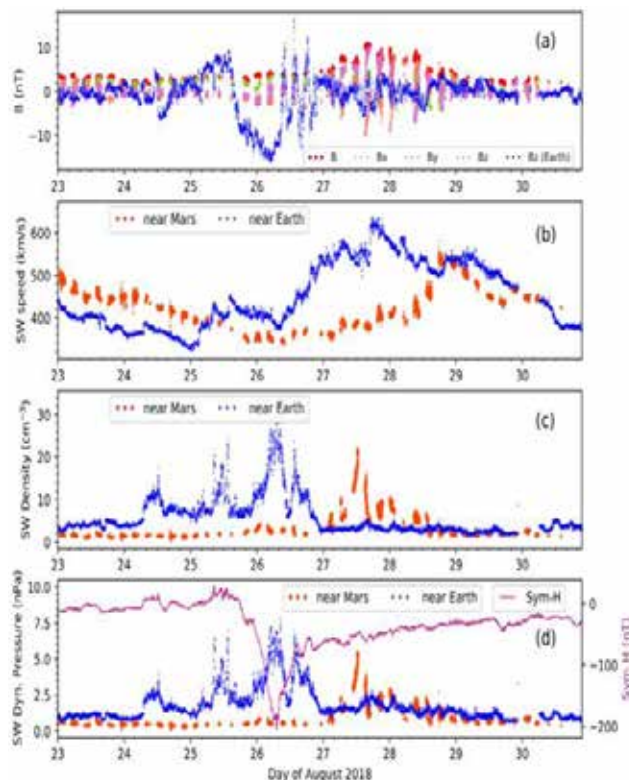


Figure 3: (a) IMF, (b) solar wind speed, (c) solar wind density, and (d) dynamic pressure observations during 2018 August 23–30, near Earth and Mars. The SYM-H variation indicating the occurrence of an intense geomagnetic storm at Earth is also shown in panel (d) [Smitha et al., Monthly Notice Roy. Astrono. Soc., 2021].

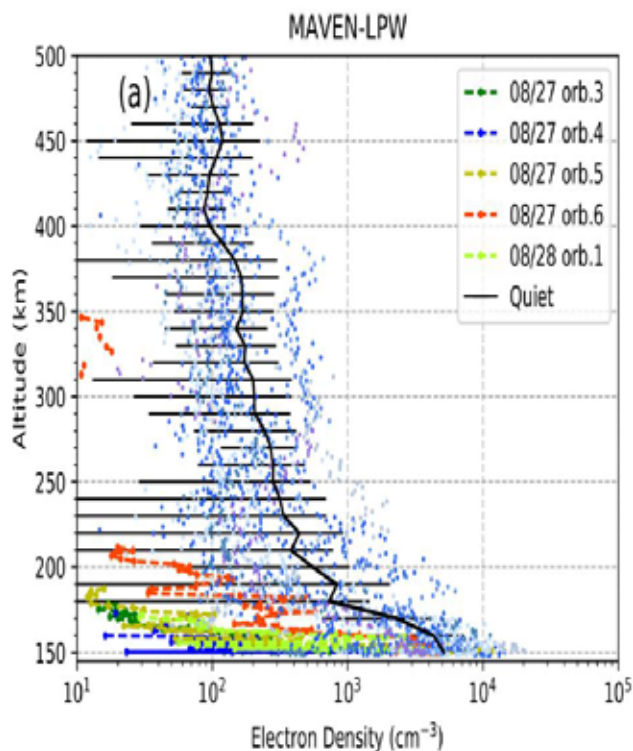


Figure 4: The Langmuir Probe and Waves (LPW) observations during 2018 August 27–28, along with the typical quiet time variation. The seven quiet orbits on 2018 August 24, 25, and 26 are shown as blue dots. The mean of the quiet time profiles is shown (black line) along with standard deviation [Smitha et al., Monthly Notice Roy. Astrono. Soc., 2021].

Ionospheric Plasma Energization at Mars During the September 2017 ICME Event

During September 2017, the solar active region (AR) 12673 produced several flares and Coronal Mass Ejections (CMEs). On 10 September 2017, a strong and wide CME was erupted from AR 12673, which was directed towards Mars. This ICME caused a major space weather event at Mars on 12–13 September. The impact of this event on Martian topside ionosphere has been investigated by using the observations made by Langmuir Probe and Waves (LPW) and Suprathermal and Thermal Ion Composition (STATIC) instruments onboard Mars Atmosphere and Volatile Evolution (MAVEN). LPW observations showed that the ionopause signature is at lower altitudes during the event period. This topside ionospheric compression/depletion observed by LPW was found to be associated with enhanced electron temperatures. STATIC observed significant energization of ionospheric heavy ions such as O^+ and O_2^+ to higher energies. Intense solar wind penetration to lower altitudes was also observed (Fig.5). The increased energies for heavy ions and increased spread in energy for the lighter species were found even at lower altitudes such as ~ 300 km, suggesting that significant heating and acceleration process is acting at these altitudes during severe solar events.

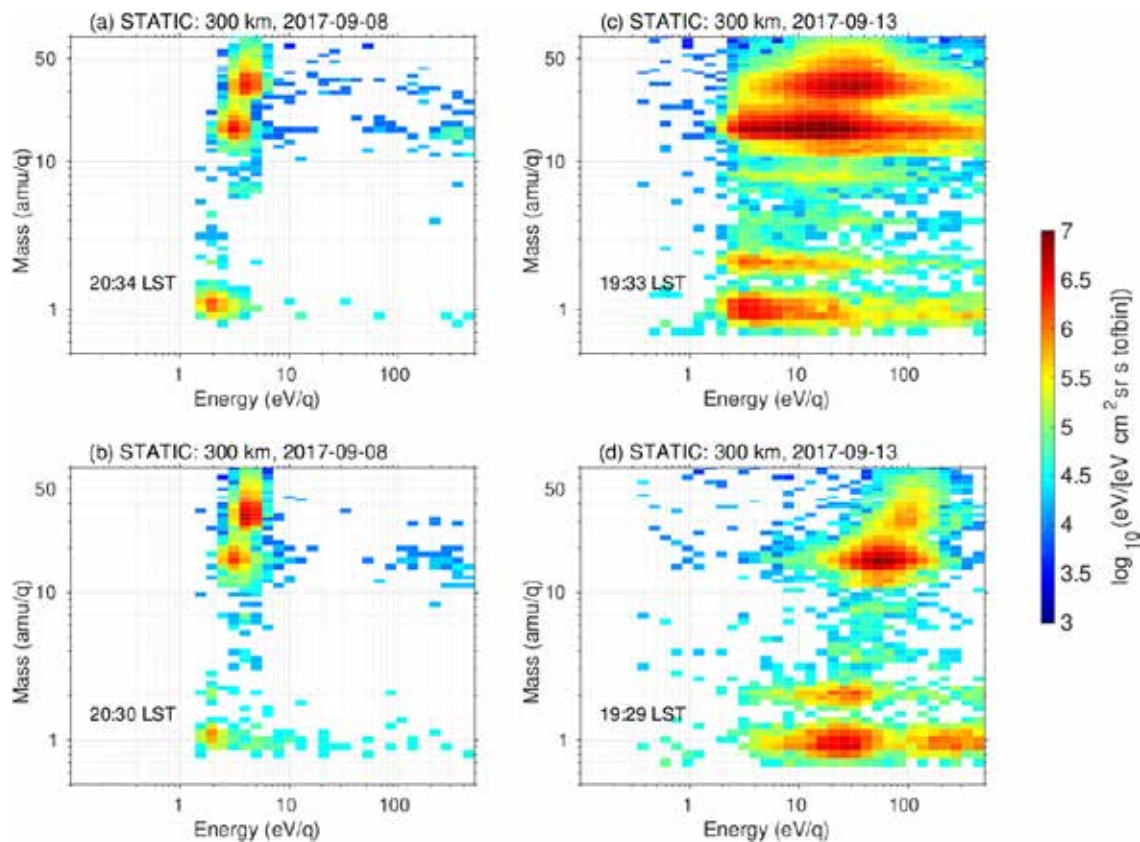


Figure 5: The MAVEN/STATIC outbound measurements at 300 km altitude during (a) 8 September - orbit 2, (b) September - orbit 3 (representing “Quiet” orbits) along with (c) 13 September - orbit 1, and (d) 13 September - orbit 3 (“Event” orbits) showing acceleration of ions to higher energies due to the enhanced solar wind-induced electric field during ICME [Krishnaprasad et al., Planet. Space Sci., 2021].

Impact of the 2018 Mars Global Dust Storm on the Martian Ionosphere: A Study Using a Photochemical Model

Mars has the greatest dust storms in our solar system, which are able to obscure the planet’s surface and last for several months. Such Planet encircling dust events affect all regions of the Martian atmosphere, including the thermosphere. In this context, an investigation has been carried out to study the impact of the 2018 Mars global dust storm on

the ionosphere, in particular, its peak altitude during the onset and growth phases of the event. A one-dimensional photochemical model is applied to estimate the ionospheric electron densities below 200 km using the measurements of in situ neutral densities and ionizing solar radiation by the Mars Atmosphere and Volatile Evolution (MAVEN) mission. The model simulations showed that on the dawn side, the altitude of the ionospheric layer peak during the dust may be lifted by ~10 km (Fig.6).

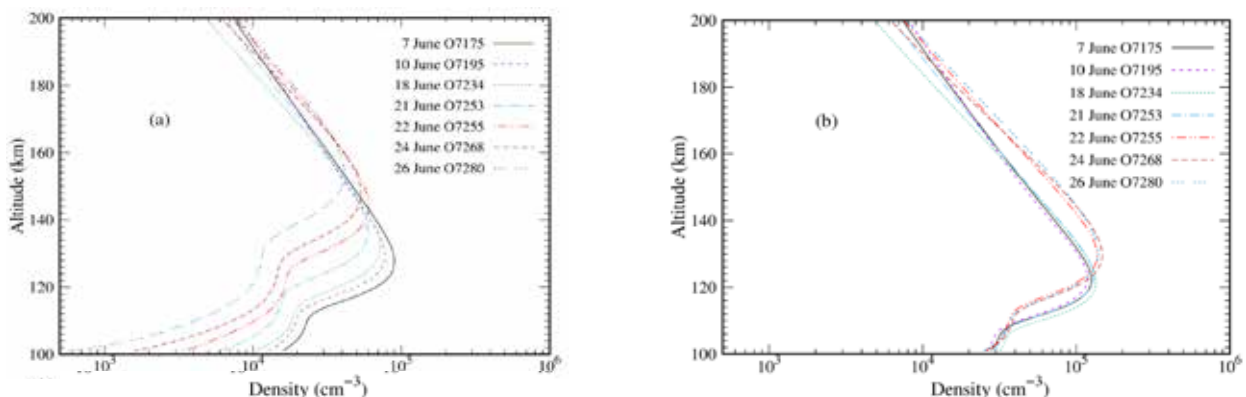


Figure 6: Electron density simulated using the model for (a) the solar zenith angles corresponding to the MAVEN observations (b) for 0-degree solar zenith angles, for dust storm and non-dust storm conditions. The enhancement in the ionospheric peak occurs during the dust storm conditions [Vrinda et al., J. Geophys. Res., 2021].

Planetary Neutral Atmospheres Through In-Situ Observations

The normal phase observations of CHACE-2 (Chandra's Altitudinal Composition Explorer-2) on Chandrayaan-2 Orbiter commenced in September 2019. CHACE-2 has provided the first global measurements of lunar exosphere. The observations have clearly shown the presence of Argon-40, Ne, CO₂ among others. Detailed analysis is in progress.

Distribution of Argon-40 in Lunar Exosphere from CHACE-2 (Chandra's Altitudinal Composition Explorer-2) on Chandrayaan-2 Orbiter

CHACE-2 has unambiguously detected of Argon-40 (40 amu) in lunar exosphere. Being a condensable gas, number density of Ar-40 is expected to vary with respect to local solar time, or equivalently the solar longitude. Since it is in a polar orbiting platform, different local times will be covered as the orbital plane of Chandrayaan-2 rotate with respect to the Sun. During September-October 2019, the orbit was in a dawn-dusk geometry and during December 2019 - January 2020, the orbital was in the noon-midnight plane, and the dawn-dusk geometry repeated in March-April 2020. Making use of these observations for almost one year (September 2019 to October 2020), the variability of Ar-40 was studied. The number density variation with respect to solar longitude, clearly showed peaks during sunrise (dawn) and a secondary peak during sunset (dusk). Also, the number density falls off on the nightside showing a nightside minima, which is in agreement with the condensable nature of Ar-40. The low-latitude observations from CHACE-2 was compared with LACE/Apollo observations and was found to be in agreement with each other. The mid-latitude observations also showed features similar to that of low-latitudes. Further, Ar-40 was found to have spatial variability by showing localised enhancements over certain longitude sectors. Some of the regions of Ar-40 enhancements coincide with KREEP (K-Potassium, REE-Rare Earth Elements and P-Phosphorus) as well as South Pole Terrain. These are the first observations over the mid-latitude region of Moon and reveals a wider source distribution for Ar-40.

Development of Payloads and Experimental Facilities for Planetary Exploration

SPL is developing different scientific payloads for the planetary and space missions of ISRO. The payloads are conceived, conceptualised, simulated (using ion-optics simulations), developed, tested and calibrated in-house in close coordination with AVN and other entities of VSSC. In order to do the testing and calibration of these scientific payloads a state-of-the-art High Vacuum Space Simulation Facility (HVSSF) has been set up and is being augmented to cater to the payload testing requirements. In addition, the ground segment activities of payloads are being carried

out at the Payload Operation Centre of SPL. Some of the major activities carried out during the report period are summarised below.

Plasma Analyser Package for Aditya (PAPA) Onboard Aditya-L1 Engineering Model - Full Integration Test Results

PAPA payload Engineering Model (EM) was subjected to full sequence of tests and calibration at the HVSSF. The tests were conducted to verify the Energy, Mass and Angular resolutions as well as the field of view for both SWEEP (Solar Wind Electron Energy Probe) and SWICAR (Solar Wind Ion Composition Analyser) sensors. The payload was exposed to electron and ion fluxes for the full spectrum of energy and incident angles. The test results were presented to a national level science review committee constituted by Critical Design Review committee of Aditya-L1 mission.

CEM Detector Qualification: 500 hours Burn-in Test Results

As part of the detector qualification plan for PAPA payload, three Channel Electron Multiplier (CEM) detectors were made to undergo 500 hours of burn-in tests, wherein they are kept ON with HV biases throughout the period. The three detectors were exposed to intermitted electron flux at a rate of 10,000 counts per second. The pulse height distribution of the CEMs were plotted before and after the burn in operation to evaluate their performance. Performance was satisfactory and burn in tests were successfully completed. Fig.7 shows the results of the burn in tests.

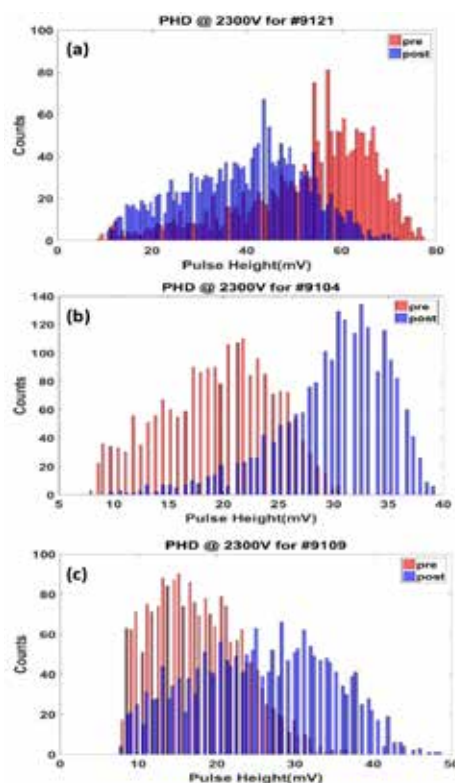


Figure 7: Burn-in test results for CEM detectors.

PAPA Qualification Model Sensor Test Results

PAPA qualification model sensor was tested with the benchmarks obtained from EM. These tests were carried out with the actual flight mechanical chassis and the lab electronics, and they serve to establish mechanical integrity prior to electrical integration. Various parameters such as energy resolution, angular resolution and field of view were

determined and all of them were within the specified values. Fig.8 shows the angular resolution at various angular bins and also the net azimuthal field of view of PAPA payload (128°). Time of flight spectrum of hydrogen ions at different energies when a post acceleration voltage of 2 kV applied to the TOF cell is shown in Fig.9. This shows the normal functioning of the payload QM sensor.

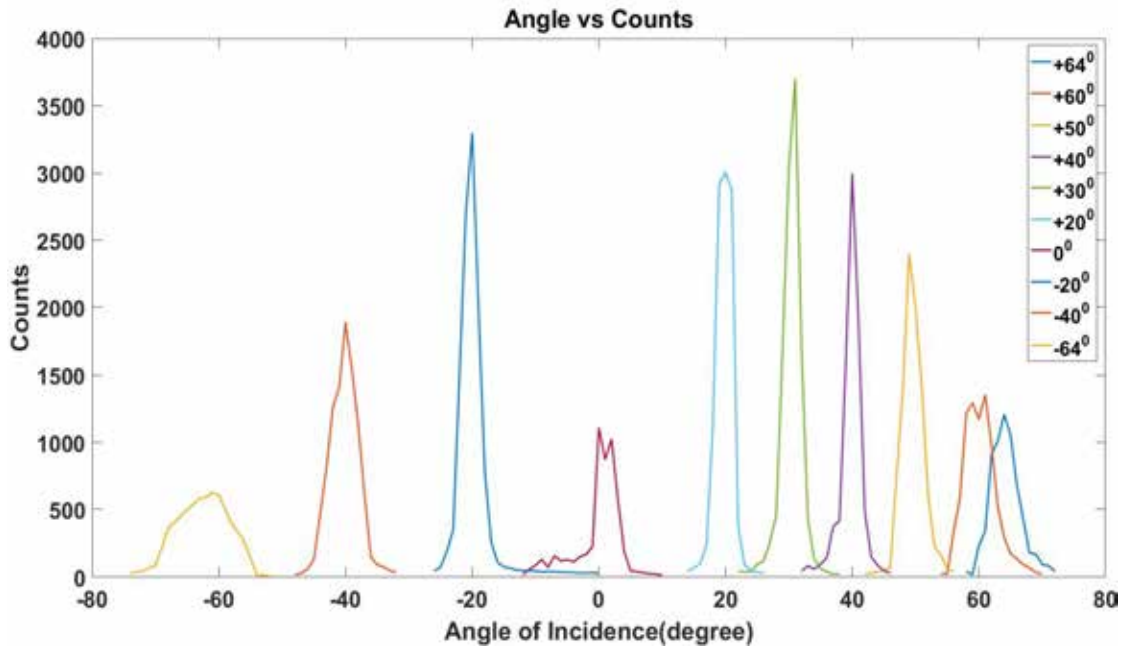


Figure 8: Angular resolution at various angular bins and the net azimuthal field of view of PAPA payload (128°).

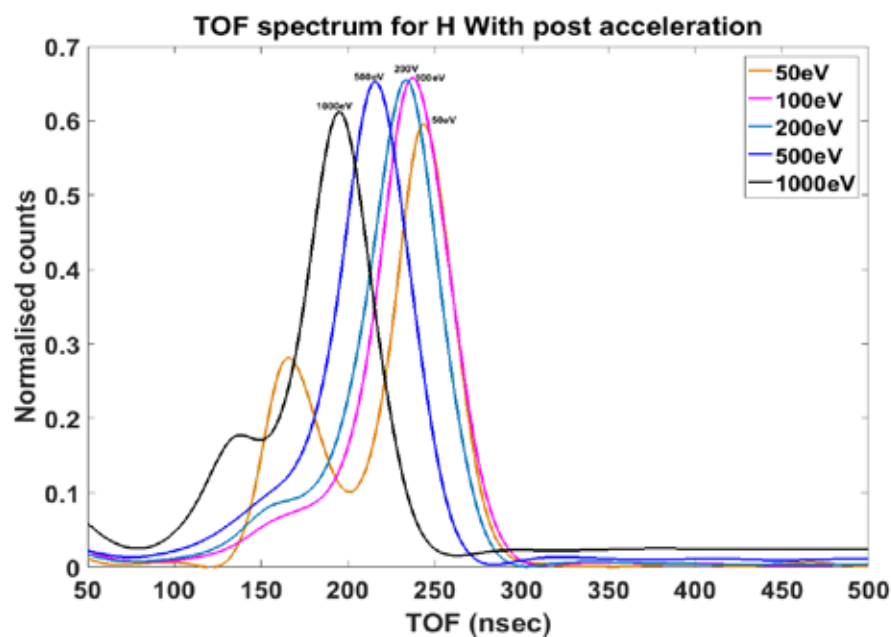


Figure 9: Time of flight spectrum of Hydrogen ions at different energies when a post acceleration voltage of 2 kV was applied to the TOF cell.

Estimation of UV Induced Photoelectrons in the Qualification Model of PAPA

SWICAR and SWEEP sensors of PAPA payload have Electrostatic Analysers (ESA) for measuring the energy of charged particles. The UV photons from the Sun can undergo multiple reflections within the analyser plates and generate photoelectrons that in turn adds noise to the CEM detector counts. Hence the internal surface of the analyser plate was coated with low reflectivity copper oxide (CuO) coating for reducing the photoelectron generation. The entrance aperture of the QM of PAPA was illuminated with a vacuum UV lamp for estimating the UV induced photoelectrons after coating the internal surfaces of the analyser and guiding plates with CuO. The CEM detector count was noted while sweeping the voltage of the analyser plates. This exercise was done for the SWICAR and SWEEP sections of the payload separately. In the SWICAR section the potential of the analyser plates were suitably changed for estimating the photoelectrons in both the electron and ion modes. The photoelectron suppression which is defined as the ratio of the photoelectron counts in the uncoated and coated cases were found to be around 10^7 .

Simulations for the development of a Quadrupole Ion-Mass Spectrometer

For the development of Quadrupole Mass Spectrometer (QMS) electronics for planetary atmospheric composition studies, a comprehensive design simulation was performed. Starting from a basic mechanical configuration and design, the simulation was able to derive the voltages required for proper operation of QMS. These voltages will serve as the starting inputs for the electronics development team.

The key task involved is simulating particle behaviour over one full RF cycle i.e. $0.43 \mu\text{s}$. The particles were fired in 11 shots at uniform intervals over $0.43 \mu\text{s}$. Fig.10 shows how the targeted mass passes through the Quadrupole rods at the pass band voltages.

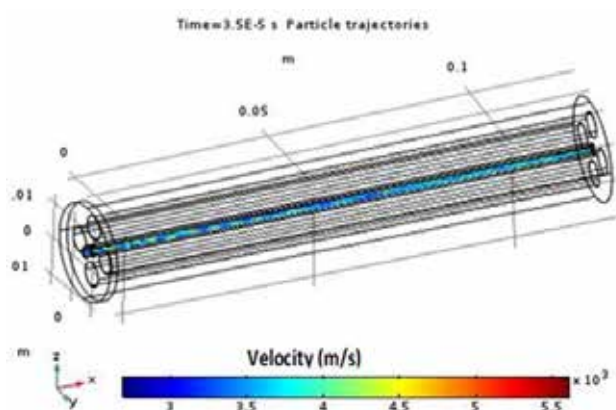


Figure 10: Mass transmission through the Quadrupole rods at the pass band voltages

Augmentation of High Vacuum Space Simulation Facility (HVSSF)

Installation of Low Energy Fine-Focus Ion Source

A new state of the art differentially pumped fine focus ion source, featuring high current range operation over the energy range between 5 eV and 5 keV was installed in HVSSF (Fig.11). The source is compatible with a wide spectrum of gases and can be used for various applications such as simulation of solar wind, sputter cleaning of samples and for charge neutralisation in electron spectroscopy. The source with an Yttria coated tungsten filament is capable of maintaining a spot size of $300 \mu\text{m}$ at 5 keV energy at a working distance of 30 mm inside the vacuum chamber.



Figure 11: Photograph of High Vacuum Space Simulation Facility.

Sensitivity Tests of Payloads for Chandrayaan-2 and SOUREX Mission

The sensitivity tests of RAMBHA LP probe and SOUREX ENWi and LP probes were carried out at HVSSF. Four different types of probes underwent characterisation and testing. The low energy ion and electron guns in HVSSF were used as plasma input for evaluating the probe sensitivity. The characterisation was done at electron energies ranging from 4 eV to 10 eV. The EM and FM of SOUREX electronics with corresponding checkout system were used for this activity.

Ground Segment Activities of Payloads in Planetary and Space Missions of ISRO

CHACE-2 Onboard Chandrayaan-2 Orbiter

The ground segment activities for CHACE-2 include processing of data from normal phase observation of CHACE-2, operation planning, long term archival of data and its public release. Following the review of CHACE-2 data products by the peer review committee, the first public release of CHACE-2 data in PDS4 standards happened on 24 December 2020 and the second release was done on 01 July 2021. The work towards third release is in progress.

PAPA Payload Onboard Aditya-L1 Spacecraft

The development of software pipelines for the quick look display and level-1 data products are in progress.

Payload Operation Centre at SPL

The payload operation centre in SPL is currently handling the data from CHACE-2 and DFRS payloads on Chandrayaan-2 orbiter and MENCA on Mars Orbiter Mission.

Level-0 data sets from normal phase observations of CHACE-2 have been regularly received from ISSDC via NKN-VRF link. These data sets are processed using automated software pipelines in POC; quick look plots are generated to verify the payload functionality. The performance of CHACE-2 has been found to be satisfactory and the housekeeping parameters are within limits. Also, a chain to generate the data products for archival also runs in POC.

Figure 12 shows the variation of total pressure measured by CHACE-2 Bayard Alpert Gauge from the day of the launch, which includes both dayside as well as nightside observations. These are indicative of the pressure of all the constituents observed by the instrument. The major component of this total pressure comes from the

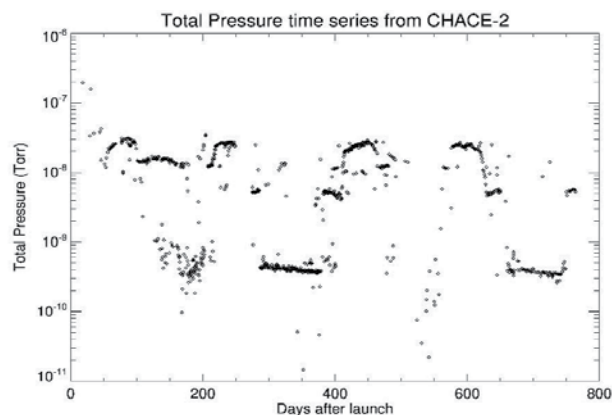


Figure 12: The variation of total pressure measured by CHACE-2 Bayard Alpert Gauge.

contribution from amu 18 and amu 17, which are primarily non-lunar origin. Therefore, the long-time variation of total pressure provides the information on how the background varies (reduces) in time.

MENCA had limited observations in 2020 due to higher periapsis altitude. The data sets are being received in POC and processed through automated pipelines. The detailed analysis is in progress.

Future Projections

- To develop and qualify the PAPA payload QM and FM and its integration with the Aditya-L1 spacecraft, and development of data processing algorithms
- Design and development of plasma analysers and space weather monitoring payloads for future planetary missions.
- Analysis of variability of lunar exospheric composition using CHACE-2 data.
- Investigations on the space weather impact on Venus and Mars using multi-year satellite (Venus Express, MoM – MENCA, MAVEN) data
- Study of Polycyclic Aromatic Hydrocarbons in Comets
- Development of Electron Temperature Analyser (ETA)
- Augmentation of High Vacuum Space Simulation Facility.
- Investigation of plasma waves in the space environment.
- Investigations on the propagation of space weather events from Sun to planetary environments and their impacts on planetary atmospheres and ionospheres.

Publications in Peer-Reviewed Journals

1. Krishnaprasad, C., Smitha V. Thampi, A. Bhardwaj, C. O. Lee, K. Kishore Kumar and T. K. Pant, “Recurrent Solar Energetic Particle Flux Enhancements Observed near Earth and Mars”, *The Astrophysical Journal*, <https://doi.org/10.3847/1538-4357/abb137>, 2020.
2. Yadav, Vipin K., “Plasma Waves around Venus and Mars”, *IETE - Technical Review*, 2020, 1-40, <https://doi.org/10.1080/02564602.2020.1819889>, 2020.
3. Thampi, Smitha V., Krishnaprasad C., Govind G. Nampoothiri, and T. K. Pant, “The Impact of a Stealth CME on the Martian Topside Ionosphere”, *Monthly Notices of the Royal Astronomical Society*, <https://doi.org/10.1093/MNRAS/stab494>, 2021.
4. Mukundan, V., Smitha V. Thampi, Bhardwaj, A., & Fang, X, “Impact of the 2018 Mars global dust storm on the ionospheric peak: A study using a photochemical model” *Journal of Geophysical Research: Planets*, 126, e2021JE006823, <https://doi.org/10.1029/2021JE006823>, 2021.

5. Krishnaprasad, C., Smitha V. Thampi, Anil Bhardwaj, Tarun K. Pant, R. Satheesh Thampi, Ionospheric plasma energization at Mars during the September 2017 ICME event, Planetary and Space Science, 105291, <https://doi.org/10.1016/j.pss.2021.105291>, 2021.

Publications in Proceedings

- Arijit Roy, Venkataraman V, and Bhalamurugan S, “Spectroscopic investigation of Comet 46P Wirtanen at UV wavelengths”, EPSC abstracts, Vol. 15, EPSC2021-777, 2021.

Scientific / Technical Reports

1. User Manual for Chandra’s Atmospheric Composition Explorer-2 (CHACE-2) onboard Chandrayaan-2; Ver. 1.2, 2020.
2. User Handbook for Plasma Analyser Package for Aditya (PAPA) Payload; SPL/UHB/PAPA/01/2020; August 07, 2020.
3. Commissioning sequence of PAPA payload onboard Aditya-L1 Mission, PAPA Team, SPL/VSSC; August 17, 2020.
4. PAPA Payload Assembly Procedure Document, PAPA Team, SPL/VSSC; August 21, 2020.
5. PAPA CDR Document, PAPA Team, SPL/VSSC; PAPA-CDR/SPL/VSSC/SEPT.2020/Ver.1; September, 2020.
6. Critical Design Review (CDR) Document for Magnetometer (MAG) Payload; SPL/VSSC; MAG-CDR-01-2020, September 2020.
7. Screening and Qualification Procedure for CEM (Channel Electron Multiplier) Detector; VSSC/QDAC/SL/TP/07/2020; September 24, 2020.
8. Magnetometer (MAG) payload for Aditya-L1 Handbook; SPL/LEOS/URSC/USO-PRL/IIG, SPL/VSSC; MAG-Aditya_L1-Handbook-2020, September 2020.
9. Engineering Model (EM) test results for Plasma Analyser Package for Aditya (PAPA) payload onboard Aditya-L1 Mission; SPL/VSSC; PAPA-EM_Results/Sept2020/Ver.1; November 02, 2020.
10. Test & evaluation plan for Plasma Analyser Package for Aditya (PAPA) Payload, QDTP/TP/PAPA/486/Ver2; February 22, 2021.

Presentations in Symposia/Workshops/Conferences/Seminars

1. V. Venkataraman, “Tentative detection of vibrationally excited Polycyclic Aromatic Hydrocarbons in Comets”, Europlanet Science Congress 2020 (CEST), September 22, 2020.
2. Vipin K. Yadav, “Solar Flares and Particle Acceleration - Theory”, 2nd Aditya-L1 Workshop, ISRO HQ, Bengaluru, December 17, 2020.
3. Vipin K. Yadav, “Fluxgate Magnetometer (MAG) onboard Aditya-L1”, IIA-50 Conference on Advances in Observations and Modelling of Solar Magnetism & Variability; Indian Institute of Astrophysics (IIA), Bengaluru, India, March 02, 2021.
4. Vipin K. Yadav, “CME Science from Aditya-L1 - MAG view”, 3rd Aditya-L1 Workshop, April 19-20, 2021.

Session Chair/Convener in Conferences/Symposia/Workshops

Smitha V. Thampi

- Session Chair; Session 4: Solar Science & Instrumentation, Indian Planetary Science Conference, (IPSC-2021), Virtual meeting by PRL, Ahmedabad, February 25-26, 2021.

Invited Talks

R. Satheesh Thampi

1. “Solar wind - A journey to its knowns and unknowns”, Aditya-L1 Science Working Group (ASWG) Meeting, July 8, 2020.
2. “Mass spectrometry and its applications to Space Science”, Christ College, Rajkot, Gujarat, January 13, 2021.

Vipin K. Yadav

1. “Magnetic field measurements at L-1 Point”, Aditya-L1 Science Working Group Meeting, July 15, 2020.
2. “Magnetic Field Measurements at the first Lagrangian (L1) Point”, National Conference on Recent Advances in Science and Technology (NCRASST 2020); Assam Science and Technology University, Guwahati, Assam, India, August 18, 2020.

-
3. “The Magnetic Field and Plasma Parameter Measurements in Space”, Recent Trends in and its Applications (Webinar); Department of Physics, Sikkim Manipal Institute of Technology (SMIT), Rangpo, Sikkim, India, October 09, 2020.
 4. “Plasma waves near the Moon”, 4th Asia-Pacific Conference on Plasma Physics (AAPPS-DPP 2020), Remote E-conference, October 26-30, 2020.

Smitha V. Thampi

- “In-situ particle dynamics with Aditya-L1 during Flare driven SEPs – Linking the source driven particles: Observations”, 2nd Aditya-L1 Workshop, ISRO HQ, Bengaluru, December 17, 2020.

Training Programme

Smitha V. Thampi

- ASCI Two-week Online Training on “General Management for Women Scientists”, 23 November 2020 – 04 December 2020.

Abhishek J.K.

- Environmental safety and hazardous waste management, VSSC, Thiruvananthapuram, March 02, 2021.

वायुमंडल प्रौद्योगिकी प्रभाग ATMOSPHERE TECHNOLOGY DIVISION



वायुमंडल प्रौद्योगिकी प्रभाग (एटीडी) गुब्बारे, रॉकेट तथा अंतरिक्ष उन्मुख प्रदायधारों की अवधारणा स्तर से लेकर अभिकल्पना, विकास तथा परीक्षण सहित वायुमंडलीय, अंतरिक्ष तथा ग्रहीय विज्ञान क्षेत्रों के लिए अभिकल्पित प्रयोगात्मक प्रणालियों के प्रौद्योगिकी पक्ष पर तथा स्वस्थाने अन्वेषण हेतु भू-आधारित प्रणालियों के विकास और वायुमंडल के सुदूर संवेदन पर ध्यान केंद्रित करता है। सक्रिय प्रयोगात्मक प्रणालियों के संवर्धन तथा रखरखाव, एसपीएल के वैज्ञानिक गतिविधियों को तकनीकी समर्थन देने तथा सामान्य तकनीकी सुविधाओं के अनुरक्षण के लिए भी एटीडी उत्तरदायी है। यह एसपीएल की वैज्ञानिक शाखाओं के साथ निकट समन्वय करते हुए कार्य करता है तथा वैज्ञानिक विचारों को मूर्तरूप देने हेतु तकनीकी विशेषज्ञता प्रदान करता है।

Atmosphere Technology Division (ATD) focuses on the technological aspects of experimental systems designed for atmospheric, space and planetary science areas, including the design, development and testing of balloon-, rocket-, and space-borne payloads from the proof-of-concept and development of ground-based systems for in-situ probing and remote sensing of the atmosphere. ATD is also responsible for the augmentation and maintenance of the ongoing experimental systems, providing technical support to the scientific activities of SPL and maintenance of the common technical facilities. It works in close coordination with the scientific branches of SPL and provides technical expertise for realization of scientific ideas.

वैज्ञानिक/इंजीनियर / Scientists/Engineers

राजीव के / Rajeev K.*
दिनकर प्रसाद वज्जा / Dinakar Prasad Vajja
मणिकंठन नायर एन / Manikantan Nair N.
प्रमोद पी पी / Pramod P. P.
मोहम्मद नजीर एम / Mohammad Nazeer M.
लाली पी टी / Lali P. T.
अनीष ए एन / Aneesh A. N.

तकनीकी टीम / Technical Team

अनुमोद पी जी / Anumod P. G.
सतीश कुमार बी / Satheesh Kumar B.
उत्तम एस पूर्ती / Uttam S. Purty

* till February, 2021

Executive Summary

Atmosphere Technology Division (ATD) has made significant contributions to the scientific and technical activities of SPL during the reporting period. These include contributions to the following ongoing activities: (i) Development of onboard electronics for the ChaSTE payload of the Chandrayaan-3 Lander, (ii) Testing of QM modules of the PAPA payload onboard the Aditya-L1, (iii) Development of data acquisition and processing GUI software for all-sky airglow imager, (iv) Design of front-end electronics for the solar occultation experiment and processing electronics for atomic oxygen sensor payload as part of the Technology Development Programmes (TDP), (v) Augmentation, operation and maintenance of HF Radar and Digisonde, (vi) Operation and maintenance of clean room, (vii) Installation and maintenance of experimental systems, and (viii) Fabrication of mechanical mounts/fixtures for various scientific instruments. ATD has also carried out the operation, maintenance and upgradation of the common facilities and looked after the safety aspects of SPL.

Payloads for Space Missions

Development of Onboard Electronics of Chandrayaan-3 ChaSTE Payload

Chandra's Surface Thermophysical Experiment (ChaSTE) is one of the payloads to be flown in Chandrayaan-3 Lander. It is identical to the one flown onboard Chandrayaan-2. The payload is being developed jointly by SPL/VSSC in collaboration with other entities of VSSC (PCM, STR, MVIT, AVN, SR, SPRE, AERO, MME) and PRL, Ahmedabad. The prime objective of the experiment is to make in-situ observations of the thermal behaviour of the outermost 100 mm layer of the lunar surface.

The electronics module of ChaSTE consists of processing electronics card, front-end electronics card and a DC-DC converter. The processing electronics developed at SPL/VSSC, drives BLDC motors for the probe deployment and penetration, acquires digitized sensor data through the front-end card and interfaces to Lander for data transfer, telecommand reception and telemetry generation. The front-end electronics was designed and developed at PRL and does the signal conditioning of RTD sensors and digitization of the signals. Both the cards are powered using a 30W output DC-DC converter, designed and developed at URSC.

The electronics package has been realized with the support of AMFF, APFD, EPCF and QID at VSSC. The package has been closed after final electrical and mechanical QC clearances and submitted to QDTE/VSSC for test and evaluation (Fig. 1). As part of realization of the electronics, various activities were carried out. These include, components soldering, conformal coating and filleting of the processing card, fabrication of electronics

chassis, assembly of the front-end card and the processing card with chassis, inter connection wiring among the front-end card, the processing card, motor driver, heater driver and DC-DC converter, mounting of electrical interface connectors with chassis, functional verification tests in disassembled mode and assembled mode. QC inspection was done in every stage of the realization. Specifications of the onboard electronics of ChaSTE are given in Table 1.



Figure 1: Onboard Electronics of the ChaSTE Payload

Table 1: Specifications of the Onboard Electronics

Weight	1.5 kg
Dimensions	214 x 208 x 57 mm ³
Power Consumption	20W max. (@28-42V)
Operating Temperature	-25 to +65°C
Storage Temperature	-40 to +70°C

Qualification Activities of Aditya-L1 PAPA Payload

Plasma Analyser Package for Aditya-L1 (PAPA) is one of the scientific payloads of ISRO's forthcoming Aditya-L1 mission. It is being jointly developed by SPL in association with AVN and various entities of VSSC.

Qualification of Channel Electron Multiplier (CEM) Detectors

As part of qualifying the CEM detectors for flight use, burn-in test for 20 days has been carried out for 3 CEM detectors with 2000V continuous bias at HVSSF/SPL (Fig. 2). After the burn-in test, the detectors have undergone thermal soak (cold) for 10 days at QDVF/VSSC. The V-I characteristics and pulse height distribution of these detectors were evaluated. All parameters of the detectors are found to be within the acceptable limits.

A python script was developed for operating high voltage power supply and for recording the V-I characteristic of each detector continuously. The program turns off the high voltage CEM bias power supply if vacuum drops, by monitoring turbo molecular pump's health continuously. A LabVIEW



Figure 2: CEM detectors kept inside vacuum chamber for burn-in test.

program was used for recording the CEM output pulses which are required for pulse height distribution calculation.

Radiation Testing on Industrial Grade Components of the PAPA Processing Unit

Single Event Latch-up (SEL) and Single Event Upset (SEU) tests were carried out on three non-rad components (charge discriminator, FIFO memory, time to digital converter), at the Inter-University of Accelerator Centre (IUAC), Delhi by using titanium beam (22.9 MeV.cm²/mg), nickel beam (31.1 MeV.cm²/mg), silver beam (50.7 MeV.cm²/mg) and gold beam (67.4 MeV.cm²/mg). Necessary technical support was provided for testing the same.

Testing of Qualification Model (QM) of PAPA

CEM detectors were assembled with chassis and performance of ion optics was evaluated before undergoing the copper oxide coating at URSC. Energy resolution and time of flight measurements were performed, as there were a few modifications in its mechanical design based on the observations from engineering model testing.

UV exposure test was carried out after coating the internal electrodes with copper oxide. A UV lamp connected at one of the ports of the vacuum chamber is used for this activity. Both Solar Wind Ion Composition Analyser (SWICAR) and Solar Wind Electron Energy Probe (SWEEP) sensors were tested and the corresponding counts were recorded for different analyser bias values upto 3000V.

Development Activities for Ground-based Systems

Refurbishment of Digisonde System

Digisonde is an ionospheric radar that uses high frequency radio waves (2 to 20 MHz) for monitoring the electron density in the ionosphere. Due to intense lightning, Digisonde's output power amplifier was damaged. This has been refurbished by in-house designed and developed 300 W power amplifier and normal functionality of the Digisonde was restored.

300 W RF Power Amplifier

A dual broadband amplifier with 300 W peak output power and 2 to 20 MHz frequency range for Digisonde has been



Figure 3: 300 W RF power amplifier developed for Digisonde.

realized (Fig. 3). The peak power has been achieved during the transmission of 532.8 μ S (16 chirps of 33.3 μ s) in both channels. The amplifier consists of a broadband Class-A pre-amplifier followed by a Class-AB power amplifier with transformer coupling. The power amplifier was designed by using LDMOS transistors. The average current rating is 600 mA in the transmission time and 80 mA in power down mode with a working voltage of 24 VDC.

Broadband Filter for Digisonde

To minimize noise, a 2-30 MHz fifth order Chebyshev broadband filter has been designed, developed and tested (Fig.4). This front-end filter rejects the harmonics and improves the signal-to-noise ratio and hence sensitivity of the receiver. The circuit design and simulations were carried out using ADS software and compared the values with the actual VNA measurements.



Figure 4: Populated view of the Broadband Filter.

An example of the ionogram obtained from Digisonde after refurbishment with the 300 W power amplifier and the broadband filter is shown in Fig. 5. The Digisonde system is fully operational now and the system has been shifted to a newly procured container laboratory (Fig. 6).

Development of Signal Blanking RF Switch for HF Radar System

A high isolation blanking switch circuit for HF radar system has been developed, tested and interfaced (Fig. 7). It is a Single-Pole Double-Throw (SPDT) RF switch, which isolates the sensitive radar receiver from the powerful radar transmitter. Transmit-Receive (T/R) switch protect the sensitive radar receiver during transmission. The blanking switch is used for an additional protection against strong interference during the transmission time. Insertion loss and receiver isolation of the blanking switch are \sim 0.71 dB and \sim 50 dB respectively.

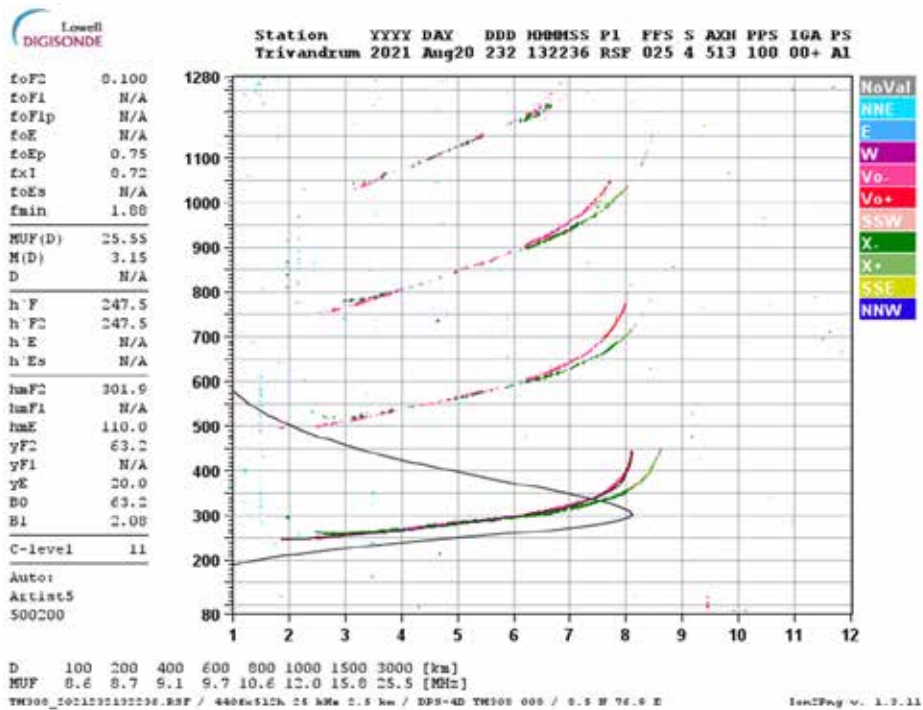


Figure 5: Ionogram obtained after the refurbishment of Digisonde with 300 W power amplifier and the broadband filter.



Figure 6 : Container laboratory for Digisonde.



Figure 7: HF Radar Signal Blanking RF Switch Module.

Design and Development of User Interface (UI) for the HVSSF Automation Software

As part of automation and remote operation of various sub-systems of the HVSSF, a client-server model using HTTP socket as a communication link has been designed. Client side is designed as a web application which runs in any modern web browser. Web app is being developed using Flutter UI tool kit in Dart programming language. Server side is being developed in Python. It is featured with a database for storing the configuration and instrument parameter values of all instruments. Mongo DB is used as database engine. In addition to that, server side driver programs were also developed in Python for 30 keV Electron gun power supply and Keithley source meter. Fig. 8 shows the HVSSF automation software scheme.

Refurbishment of Weather Monitoring Systems

Operation and periodic maintenance of 32m tower with meteorological sensors, ISRO's automatic weather station (AWS), micro-rain radar and disdrometer have been carried out. Data has also been provided to the meteorological facility (METF, VSSC) during the RH-200 launches. As part of periodic verification of the meteorological sensors, wind speed, wind direction, temperature and humidity sensors of the meteorological tower were compared with the newly procured calibrated standby sensors. The faulty sensors were replaced. Fig. 9 shows the arrangement of the verification set-up for the sensors. Also, sensors of ISRO's AWS were compared with the co-located meteorological tower sensors. It was found that the AWS data are in good agreement with that of the meteorological tower data.

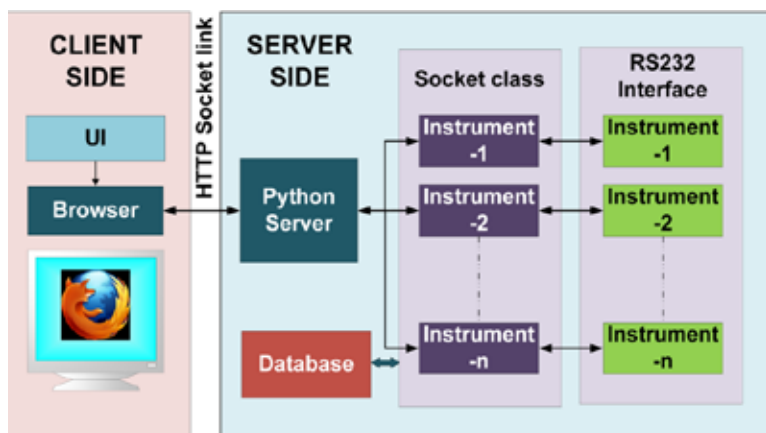


Figure 8: HVSSF Automation Software Scheme.



Figure 9: Set-up for comparing the meteorological sensors.

Operation and Maintenance of Experimental and Common Facilities

Operation and Maintenance of HF Radar System

HF radar is a phase coherent, monostatic, pulsed radar operating at 18.1 MHz. It is a powerful tool to study the ionosphere plasma instability processes. In addition to the daily operations, the HF radar was operated in campaign mode during SOUREX-II and Solar Eclipse experiments. The system maintenance was carried out for the trouble-free operation of HF radar. Fig.10 shows the time-height variations of the signal to noise ratio of HF radar signal during its operation on 12 March, 2021 (in support of the SOUREX-II experiment).

Operation and Maintenance of HVSSF

The High Vacuum Space Simulation Facility (HVSSF) is maintained and augmented with sub-systems for the development, testing and calibration of scientific payloads. The HVSSF facility has been extensively utilized for the characterization of RAMBHA LP probe and SOUREX ENWi and LP probes (Fig. 11). Necessary technical support was provided for carrying out the probe sensitivity tests using low energy ion and electron gun. Also, the facility is being utilized for testing and calibration activities of the PAPA payload.

Operation and Maintenance of Clean Room Facility

The Clean Room facility at SPL (with class 10000 and class 100000 clean rooms equipped with work benches of class 100 and class 1000 Laminar flow tables) has been utilized for the testing and development activities for scientific payloads of SPL and for the requirements from other entities of VSSC. Regular up-keep and maintenance of the facility have been carried out. The Clean Room is being extensively utilized for the realization and testing of the ChaSTE payload onboard the Chandrayaan-3 mission and PAPA payload onboard the Aditya L1 mission.

Technology Development Programmes (TDPs)

Development of Data Acquisition and Processing GUI Software for All-Sky Airglow Imager

All-sky airglow imager is a TDP of SPL for studying the spatio-temporal variability of thermospheric airglow emission for upper atmospheric research. As part of this, a PC based data acquisition and processing GUI software has been developed using LabVIEW. The software acquires CCD captured image in multiple frames at the desired integration time, processes the image by removing dark noise

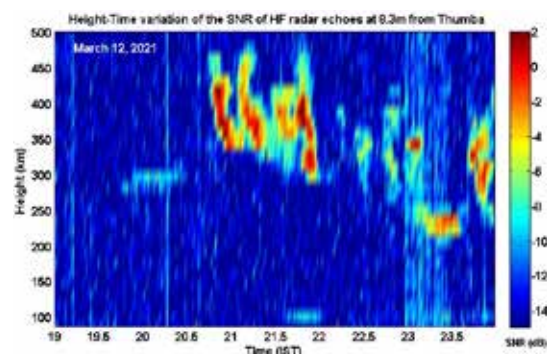


Figure 10: Time-height variation of SNR of HF radar signal

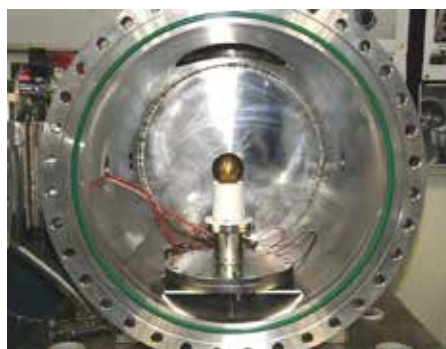


Figure 11: LP probe kept inside the vacuum chamber for characterization

and stores the processed image in a specified format. The GUI has features for selecting integration time and CCD's temperature control. The software has been successfully tested with the instrument (Fig. 12).

Development of Onboard Electronics for Solar Occultation Experiment

Development of a payload for solar occultation experiment is an ongoing TDP of SPL. The electronics package for this experiment is being developed in-house at SPL. It consists of three cards: front-end, processing and motors driver cards. The front-end card is used for signal conditioning of photodetectors and its digitization. The processing card acquires digitized data and packetizes with necessary information. It also has necessary interfaces for payload data transfer, telecomm and reception and telemetry generation. The motor drive card is for driving the azimuth and elevation motors of the gimbal unit, which is used for tracking the Sun.

Front-end Electronics

The front-end card has ten signal conditioning chains and two high resolution Analog to Digital Converters (ADC) to cater for one 2×2 element photodiode, four 1×1 element photodiodes and two 1×128 element linear photodiode arrays. Each signal conditioning channel includes pre-amplification with multiple gains, noise filtering, single-ended to differential conversion and charge reserving for the ADC. Low Voltage Differential Signaling (LVDS) is used for driving high speed clock and data signals with low jitter and less noise. Required operating voltages (+5 V, +3.3 V and +1.8 V) for the front-end card are derived by regulating the supply voltage. An external precision +2.5 V voltage reference is used as voltage reference for the ADCs.

Block diagram of the front-end electronics is shown in Fig. 13. The design of the front-end card circuits has been completed. Open-loop SPICE simulations have been carried out to assess any stability issues for operational amplifier based circuits. The simulated parameters (phase margin and rate of closure) for all the circuit sections are tabulated in the Table 2. The simulations have shown that all the circuits satisfy the stability criteria.

Table 2: Open-loop SPICE Simulations of the Front-end Card.

Circuit Section	Phase Margin (degree)	Rate of Closure (dB/decade)
Trans-impedance amplifier (1x1 photodiode)	60.7 (@ 2.3 MHz)	20
Voltage bias amplifier (1x1 photodiode)	60.4 (@ 2.3 MHz)	20
Trans-impedance amplifier (2x2 photodiode)	65.5 (@ 2.5 MHz)	20
Voltage bias amplifier (2x2 photodiode)	64.1 (@ 2.6 MHz)	20
Non-inverting amplifier stage (Single-ended to differential converter)	66.2 (@ 2.3 MHz)	20
Inverting amplifier stage (Single-ended to differential converter)	87.6 (@ 1.1 MHz)	20

Simulations were also carried out for ADC input circuit sections to know the signal settling time errors in its sampling period. ADC switched input load was considered for the simulations. The simulations have shown that settling error for the combination of ADC analog inputs, charge reservoir and single-ended to differential converter is 12 μV and settling error for the combination of ADC reference input, external voltage reference and its output capacitors is 3 μV. These errors are not significant for the required 14-bit resolution.

Development of Sensor and Electronics for Atomic Oxygen Sensor

Development of Atomic Oxygen Sensor (ATOXS) is an ongoing TDP of SPL/VSSC. Scientific objective of the sensor is to measure the atomic oxygen density in the earth's upper atmosphere. Zinc Oxide (ZnO) based film is used as the sensing element in ATOXS. The payload system consists of sensor unit and electronics unit. The laboratory prototype of the electronics has been designed. The sensor unit has also been designed and its fabrication is in progress (Fig. 14).

Design and Development of Rocketsonde Temperature Sensor (RTS)

Development of rocketsonde temperature sensor for vertical profiling of temperature in the stratosphere and the lower



Figure 12: All-Sky Airglow Imager and its Data Acquisition and Processing GUI Software.

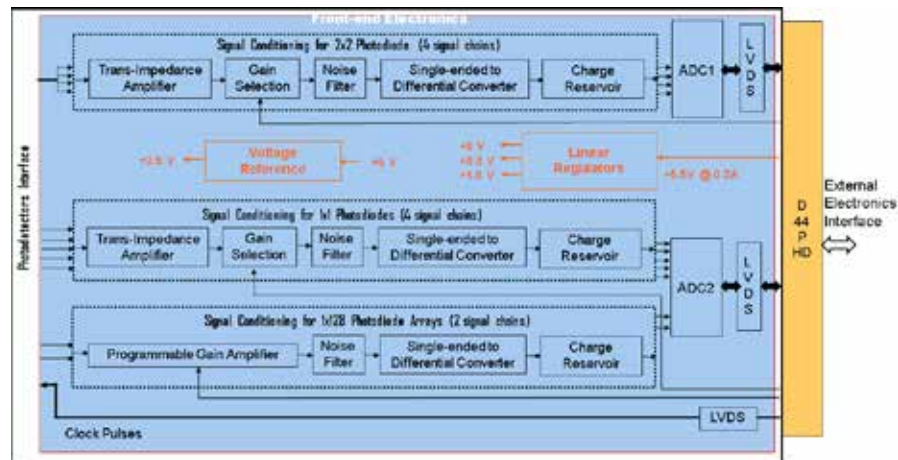


Figure 13: Block Diagram of the Front-end Electronics for Solar Occultation Experiment.

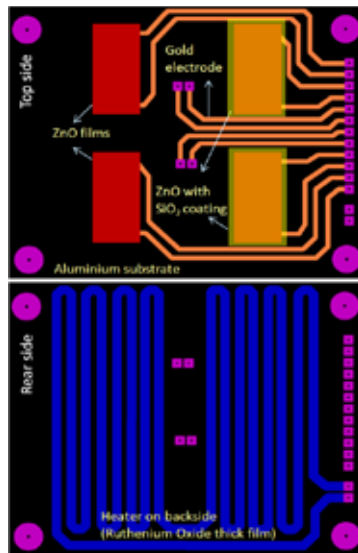


Figure 14: Proto-model of Atomic Oxygen Sensor Unit.

mesosphere regions up to ~ 65 km altitude has been initiated and the background work required for its development has been completed. This is essential to understand the vertical coupling of the atmosphere from troposphere to mesosphere. The Russian 'M-100' meteorological rocket soundings from the Thumba during the period 1970 to 1991 provided upper air data on winds and temperature up to ~ 65 km. Indigenous sounding rocket, RH-200, is being launched on a regular basis for wind measurements in the upper atmosphere regions with copper chaff as payload. There are no direct in-situ measurements of temperature using rocket observations since 1991 which is an important parameter along with wind measurements to understand the middle atmosphere dynamics.

Measurement of temperature in the upper stratosphere and mesosphere is a major challenge as the conventional thermistors and RTDs will not be responding to the temperature changes in these regions due to less density. Extensive review of the available literature has been made, but could find only a little information on the

hardware. Studies on the temperature sensors used in rocket observations elsewhere and the corrections required for minimization of errors through various sources of radiation and heat transfer were carried out for the in-house design and development of a Rocket-borne Temperature Sensor (RTS) for upper atmospheric observations with better reliability. Specially made thermistor-based rocketsondes were used for upper atmosphere temperature profiles up to ~ 65 km altitude. These have many advantages which include small size, less weight, less power consumption, low cost and easy telemetry requirements. In addition, properly mounted sensors have a fast response time and reasonably good temperature accuracy at higher altitudes. Specifications and design of the RTS proposed for development are given below.

Specifications of Proposed RTS

The basic components of the rocketsonde are thermistor sensor, thermistor mount, electronic system and power supply. The sonde will be ejected from the rocket after reaching its peak altitude by using an ejection system and decelerated to ground in vertically downward position by using a parachute for making measurements.

Thermistor

Design parameters in choosing a particular bead thermistor are its dimension and lead wire length. Heat transfer coefficients are greater for smaller dimension sensors than for the large sensors and hence smaller radiation error. Also, smaller dimension sensors have smaller lag errors compared to larger dimension sensors due to a faster time response. The advantage of the long lead wires is to reduce conduction errors caused by heat flowing from the sonde structures to the thermistor through short leads. But, the radiation effects would be larger and aerodynamic heating corrections would be more complex. The bead thermistor and lead wires will be coated with aluminum to reduce their sensitivity to radiation. The added mass of aluminized thermistors increases their time constant values over the equivalent black beads. A trade-off between radiation and lag errors dictate the use of

beads for a particular sounding system to minimize overall error. This trade-off would be a function of maximum measurement altitude and the sonde descent velocity. A small aluminum coated bead thermistor with short lead wires have been used to obtain atmospheric temperature profiles up to 65 km. Specifications of the proposed thermistor sensor are given in Table 3.

Table 3: Specifications of temperatures sensor of the RTS

Sensor	10-mil spherical bead thermistor
Sensor lead wire	Platinum alloy wire of 0.3 cm length and 1-mil diameter
Coating material	Aluminum (solar absorption coefficient equal to 0.1)

Thermistor Mount

The thermistor mount is a crucial factor due to heat transfer from the body to the sensor. A proper mount for the thermistor sensor is essential to make temperature measurements with reasonably good accuracy in the upper atmosphere. In the beginning of thermistors use with rocketsondes, reasonably accurate profiles were obtained up to about 45 km and this ceiling has been gradually raised to 65 km by improvements in the mounting arrangements for the thermistors and the sounding systems. Based on the detailed evaluation, film mount is chosen for the RH-200 rocket. Its specifications are mentioned in Table 4. It consists of a plate, mounting posts and a thin film.

Table 4: Specifications of sensor mount of the RTS

Mounting type	Film mount
Mounting structure	Plate with woven glass fabric and epoxy resin material, circular in cross-section of 6.4 cm diameter
Mounting posts	Two hollow cylindrical Nylon tubes each with 0.3 cm outside diameter
Mounting film	Mylar polyester film of 1×10^{-3} cm thickness, 1.3 cm height and 3.2 cm ² surface area
Film coating	Aluminum (solar absorption coefficient equal to 0.1)

Technical Reports

1. Pramod PP, Configuration Control Document (CCD) of Onboard Electronics of ChaSTE Payload, Chandrayaan-3 Mission, March 2021, Doc. No.: TTCP-S-0319
2. Dinakar Prasad Vajja, Specifications of Rocketsonde Temperature Sensor (RTS) onboard RH-200 Rocket, Doc. No.: SPL-ISRO-VSSC-TR-0448-0-21, June 2021.

Training Programmes

Pramod P.P. and Mohammed Nazeer M.

- Technology Update Programme on “Electronics Packaging Technology”, conducted by HRDD, 4-5 March, 2021.

Anumod P. G.

1. Safety Training Programme, National Safety Week 2021, 2-3 March, 2021.
2. Training on Quality Control and Assurance, 22-23 September, 2020.

Electronic System

The electronics consists of data acquisition block and RF transmitter block. The data acquisition block measures resistance of the thermistor (which varies with atmospheric temperature) at regular intervals. It also acquires temperature data of the thermistor mount by using supplementary thermistors and packetizes the acquired data in a proper format. The RF transmitter telemeters the rocketsonde data to ground station in real-time. The electronic system has linear voltage regulators for deriving the required voltages from battery powered input.

Temperature Corrections

Temperature of the ambient low density air of the upper atmosphere as measured by the thermistor differs from actual temperature because of low efficiency of heat exchange among the thermistor, the mylar film and the surrounding environment. This requires corrections for the measured temperatures. The correction factors include aerodynamic heating, solar and long wave radiation effects, conduction of heat from the rocketsonde mount structure to the thermistor through its leads, thermal time lag, electrical heating of the thermistor, RF heating due to the rocketsonde transmitter and measurement circuit error. Detailed simulations of these effects are being carried out.

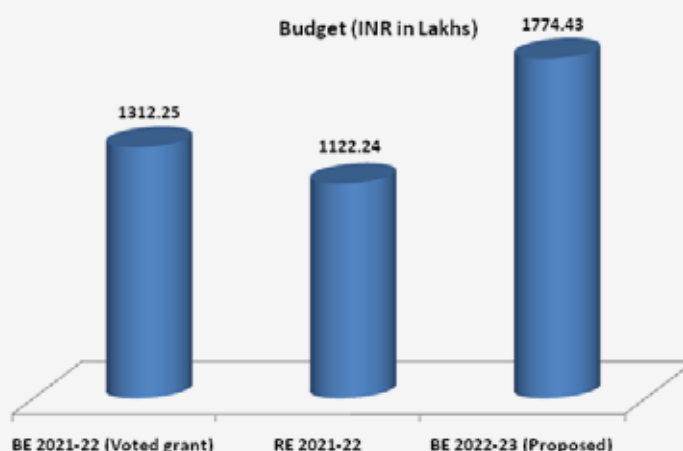
Mechanical Engineering Activities

The following mechanical engineering activities were carried out at SPL workshop and CAD design unit: (1) Fabrication of mounting fixtures for fish-eye lens, interference filter, CCD, temperature control and power supply of the in-house developed All-sky Airglow Imager, (2) Fabrication of mounting poles for installation of soil moisture and temperature sensors and aluminum enclosure for data logger and battery, (3) Fabrication of fixture for optical dome of photometer with provision for vertical alignment of its periscopic assembly, (4) Design and generation of CAD drawings for stepper motor fixture of scanning monochromator.

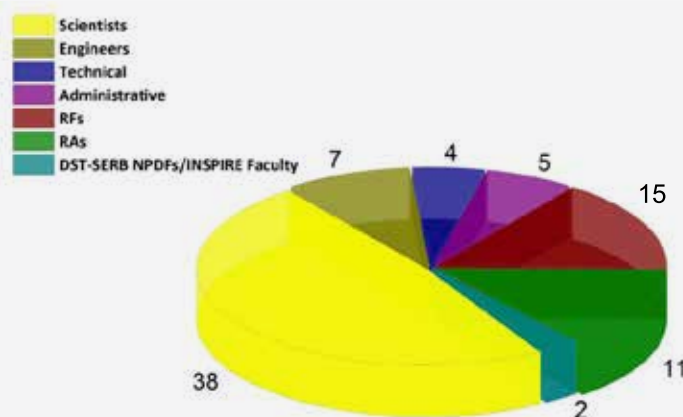
योजना और समन्वय प्रकोष्ठ PLANNING AND COORDINATION CELL

The Planning and Coordination Cell of SPL (SPL – PCC) is responsible for the overall planning of the activities at SPL, annual budget preparation and presentations for approval, coordination of need aspect review of scientific and technical items required for SPL activities, monitoring of procurement status and budget utilisation, coordination with other entities of VSSC and ISRO HQ and the periodic progress report preparation of the laboratory for submission to higher management.

Annual Budget of SPL



Manpower Status (as on June 2021)



एसपीएल-पीसीसी टीम/SPL-PCC Team

सुरेश बाबू एस, प्रधान पीसीसी / Suresh Babu S, Head PCC
 विजयकुमार एस नायर / Vijayakumar S Nair
 अजीषकुमार पी एस / Ajeeshkumar PS
 शिजी एन डी / Shiji ND

कार्यालय और प्रशासनिक सहायता Office and Administrative Support



एसपीएल कार्यालय टीम / SPL Office Team

गीता सी / Geetha C

षाजहान जे / Shajahan J *

शालिनी एम एल / Salini MS

शिजी एन डी / Shiji ND

सिमी इस्माइल / Simi Ismail

यूसफ एन / Yoosaf N

SPL administration facilitates the administrative and secretarial requirements for a smooth and effective functioning of SPL by providing co-ordination, communication and logistics. Besides the general administration, office management and housekeeping of SPL, it caters to the necessary official assistance to different ISRO projects such as ARFI, ICARB, RAWEX and NOBLE. It co-ordinates and provides logistic support for different national observation campaigns of SPL. Also SPL administration is responsible for coordinating activities within SPL, involving other Divisions, Facilities of VSSC and/or other ISRO centers and different Institutions/Universities. It meets the administrative requirements of different payload such as ChaSTE, RAMBHA and PAPA development for ISRO's space missions.

Research programme facilitated by ISRO fellowship program including research fellowship program and research associate program is a major activity of SPL. SPL administration provides the required assistance in terms of documentation and organizing Ph.D. Synopsis/Defence, Doctoral Committee meetings, student reviews, regular student/faculty seminars and Central Level Monitoring Committee meeting of VSSC. It also supports for arranging Seminar Talks/Invited Talks in SPL by leading scientists from India and abroad and arranges necessary logistics required during their visit and stay.

* Relieved in May 2021

शैक्षणिक परियोजनाएं / ACADEMIC PROJECTS

M.Sc. Projects

1. Aayush Barmase, Institute for Excellence in Higher Education, Bhopal, "Satellite observed distribution of carbon monoxide over India", January-June, 2021 [Supervisor: Dr. Girach Imran Asatar].
2. Abhirami Ajith, Government College for Women, University of Kerala, Kerala, "Variability of Earth's radiation belt during solar minimum", September-December, 2020 [Supervisor: Dr. Smitha V. Thampi].
3. AdityaPrajapati, Institute for Excellence in Higher Education, Bhopal, Madhya Pradesh, Investigation of the response of Martian Atmosphere to the passage of Interplanetary Coronal Mass Ejection"; February- June, 2021 [Supervisor: Dr. V. Venkataraman]
4. Afili S., Department of Physics, MSM College, Kayamkulam, "Measurements of aerosol phase function by using Polar Nephelometer", March-April, 2021 [Supervisor: Dr. Mukunda M. Gogoi].
5. Aiswarya, P.K., Union Christian College, Aluva, "A study on laser-induced incandescence technique for aerosol black carbon size distributions", November-December, 2020 [Supervisor: Dr. Sobhan Kumar Kompalli].
6. Amrutha K., School of Pure and Applied Physics, Kannur University, Kerala, "Study of Venusian Plasma Environment using Venus Express data", April- June, 2021 [Supervisor: Dr. Smitha V. Thampi].
7. Anjana S., St. Aloysius College, Thrissur, Kerala, "A study on the surface mineralogy of a sample of Comets"; August 2020 – January, 2021 [Supervisor: Dr. V. Venkataraman].
8. Anusree Vijayan, School of Pure and Applied Physics, Kannur University, "Estimation of concentration of atmospheric carbon dioxide", April-June, 2021 [Supervisor: Dr. Girach Imran Asatar].
9. Arya Babu M.K., Kannur University, Payyanur, Kerala, "Ion plasma parameter measurement with cylindrical Langmuir probe", April- May, 2021 [Supervisor: Dr. Vipin K. Yadav].
10. Ayisha M. V., Kannur University, "Soil moisture studies from microwave remote sensing observations", April -June, 2021 [Supervisor: Dr. Renju R].
11. Divyalekshmi S.V.,Vellore Institute of Technology, "Spectroscopic studies on a sample of Comets", February – June, 2021 [Supervisor: Dr. V. Venkataraman].
12. Jecy Mathew, St. Xavier's College, Thumba, "Study of Thermophysical Properties of the Moon and the Lunar Missions", April-June, 2021 [Supervisor: Dr. Nizy Mathew].
13. Kavya Manikandan, Vimala College, Thrissur, "Seasonal variations of Atmospheric CO2 using model estimates", May 2021 [Supervisor: Dr. S. Sijikumar].
14. Krishnapriya M., St. Aloysius College, Thrissur, Kerala, "A study on the surface mineralogy of a sample of Asteroids", August 2020 – January 2021, [Supervisor: Dr. V. Venkataraman].
15. Megha Thapak, Institute of Excellence in Higher Education, Bhopal, "Sodar observations of the Morning Rise of Inversion over Thumba", March-June, 2021 [Supervisor: Dr. N.V.P. Kiran Kumar].
16. Mini Rajput, Institute for Excellence in Higher Education, Bhopal, "Morphological evolution of the total electron content (TEC) of the ionosphere over near equatorial crest region, Hyderabad during 2004-2013", January – June, 2020 [Supervisor: Dr. R. K. Choudhary].
17. Reshma B, Fatima Mata College for Women, Kollam, "Morphology of tropical cyclone VARDAH", July-September, 2020 [Supervisor: Dr. K. N. Uma].

-
18. Sahana Dermal, Vellore Institute of Technology, Vellore, "Altitude distribution of aerosols over India using space-borne LIDAR observations", January – June, 2021 [Supervisor: Dr. S. Suresh Babu].
 19. Shivangi Sharma, Institute for Excellence in Higher Education, Department Of Physics and Electronics, Bhopal, "Detecting the Climatological Shift in Time Series of Rainfall over the Central Indian Region", January-April, 2021 [Supervisor: Kandula V Subrahmanyam].
 20. Soofiya Hakkim, MSM college, Kayamkulam, Alappuzha, Kerala "Surface layer characteristics over coastal station, Thumba", February-May 2021 [Supervisor: Dr. N.V.P. Kiran Kumar].
 21. Sreeraj R, Karpagam Academy of Higher Education, Coimbatore, "Microwave interaction with atmospheric constituents – Extinction by hydrometeors", December 2020 - February 2021 [Supervisor: Dr. Renju R].
 22. Srishti Guru, Institute for excellence in higher education, Department of Physics and Electronics, Bhopal, "Speed of Coronal Mass ejection (CME) events and ensuing geomagnetic disturbance effects during solar cycles 23 and 24", March-June, 2021 [Supervisor: Dr. Manju G.].
 23. Vandita Thakur, Institute for Excellence in Higher Education, Bhopal, "A morphological study on the Total Electron Content (TEC) of the ionosphere over equatorial crest region, Bhopal during 2004-2013", Jan 2020–June 2020 [Supervisor: Dr. R. K. Choudhary].

Thanks to Dr. Radhika Ramachandran

Dr. Radhika Ramachandran was the director of SPL during March 2017 to January 2021, and laid down office on 31 January 2021. Dr. Radhika joined ISRO, in the erstwhile Space Physics Division (SPD), in January 1984 and started her research career in the field of 'Atmospheric Boundary Layer Physics'. She initiated numerical weather prediction activity for the launch campaigns in ISRO and commissioned numerical atmospheric models at SPL for the operational weather prediction in ISRO. We sincerely thank and acknowledge the services of Dr. Radhika Ramachandran for the progress of SPL.



Brainstorming session on "Thrust Areas in Atmospheric, Space and Planetary Sciences"

SPL organised a two-day Brainstorming session, focussing on the recent developments, thrust areas and future requirements in the various disciplines pursued at SPL, during 21-22 January 2021. Eminent personalities from across the globe delivered talks and shared their thoughts in the thrust areas in Atmospheric, Space and Planetary Sciences.

Speaker	Topic
Prof. Dev Niyogi , University of Texas at Austin, USA	Atmospheric Boundary Layer and Modelling
Dr. R. Krishnan Indian Institute of Tropical Meteorology, Pune	Modelling of Weather and Climate
Prof. A. Jayaraman Former Director, NARL & ISRO Chair, Bangalore University	Atmospheric Aerosols
Prof. S. Gurubaran Indian Institute of Geomagnetism, Mumbai	Middle Atmosphere Dynamics
Dr. A.K.Patra Director, National Atmospheric Research Laboratory	Earth's Ionosphere
Prof. Pallam Raju , Physical Research Laboratory, Ahmedabad	Space Weather
Prof. Takeshi Imamura , The University of Tokyo, Japan	Venusian Atmosphere Dynamics
Prof. Yoden Shigeo Kyoto University, Japan	Stratospheric Influences on the Tropical Troposphere
Prof. Dhiren Kataria Mullard Space Science Laboratory, University College London, UK	Low Resource In-situ Particle Instruments for Space Science and Space Weather
Prof. Martin Patzold Dept. of Planetary Research, University of Cologne, Germany	Structure of the Ionosphere of Venus from Radio Occultation
Dr. Yoshifumi Futaana Swedish Institute of Space Physics (IRF), Sweden	Venus Express Results on Solar Wind Interaction





SPL uses various instruments & platforms to profile the atmosphere



SPACE PHYSICS LABORATORY

Vikram Sarabhai Space Centre, Thiruvananthapuram - 695 022, INDIA

Email: directorspl@vssc.gov.in, Ph: +91 471 256 3663, Fax: +91 471 270 6535

<https://spl.gov.in>